Advances in Multicolor Ultrafast Spectroscopies: Utilizing Theory and Experiment to Explore Vibronic Coupling in Molecular Systems from the Infrared to the X-ray

Robert B. Weakly

A dissertation
submitted in partial fulfillment of the
requirements for the degree of

Doctor of Philosophy

University of Washington

2022

Reading Committee:
Munira Khalil, Chair
Anne McCoy
Stefan Stoll

Program Authorized to Offer Degree:
Chemistry

University of Washington

Abstract

Advances in Multicolor Ultrafast Spectroscopies:
Utilizing Theory and Experiment to Explore Vibronic Coupling in Molecular Systems from the Infrared to the X-ray

Robert B. Weakly

Chair of the Supervisory Committee:
Munira Khalil
Chemistry

Multicolor ultrafast spectroscopies enable the simultaneous and/or sequential interrogation of dissimilar degrees of freedom relevant to the inter- and intramolecular interactions that drive natural and artificial chemical phenomena on the atto- to nanosecond timescale.

Two-dimensional electronic-vibrational (2D EV) and vibrational-electronic (2D VE) spectroscopies expand on the multidimensional spectroscopic landscape as the cross of infrared (IR) and electronic spectroscopies. They provide a window into the coupling of nuclear and electronic degrees of freedom. Each peak position and amplitude gives a direct measure of how specific IR active modes are coupled to specific electronic transitions. Both of these spectroscopies can be described by the same model Hamiltonian that consists of multiple high-frequency vibrational modes, each uniquely coupled in both the ground and electronically excited state, giving rise to a coupling between the electronic states. Polarization-selective spectra and modeling can determine shifts in the electronic excited state potential, and measure dipole orientations, Duschinsky mixing, and non-Condon effects. Spectroscopic and therefore chemical information can be isolated through a host of time-frequency analysis tools. Model analysis demonstrates the strength of these techniques used in tandem. This generalized approach can be applied to a host of molecular systems including mass and charge transfer systems.

Because 2D EV is specifically sensitive to the couplings between nuclear and electronic degrees of freedom it is an effective method for uncovering non-Condon, non-adiabatic, and non-Born–Oppenheimer effects. A model proton transfer system (10-hydroxybenzo[h]quinoline) exhibits non-Born-Oppenheimer behavior, manifested through a coherence transfer following optical excitation. Rather than propagating a coherence between the ground and excited state enol geometries, there is experimental evidence that the coupled behavior of the proton and electron motions creates a coherence between the ground state enol geometry and the excited state keto geometry. This experimental evidence of a coherence transfer presents in multiple ways. First, 2D EV spectra show an excited state emission at a pump frequency lower than the electronic transition frequency. Second, coherent oscillations of that signal in the time domain match the character of the vibrational motions previously shown to be coupled to the proton transfer.

Multicolor X-ray pump X-ray probe transient absorption spectroscopy of molecular systems in solution directly reports on valence–core interactions by probing a core-to-core absorption measurement in a spectrally isolated area. Specifically, in third-row transition metals, the 1s→3p transition can undergo an absorption event in the wake of an Auger–Meitner cascade following the removal of a 1s electron which produces the necessary vacancy in the 3p. The first of two coincident X-ray pulses removes a 1s electron. The second pulse monitors the 1s→3p transition energy — the absorption corollary to Kβ fluorescence.

Markov-chain Monte-Carlo simulations can predict the core-excited electronic states present during the cascades. Further, they can describe the time evolution of those states, providing explanations for the types of peaks present and their temporal response profile. In the presence of additional core and valence holes, each orbital relaxes in energy due to the change in electrostatic shielding. Additional interactions due to 3p–3d exchange, spin–orbit coupling, and crystal–field effects further perturb these orbitals. Time-dependent density functional theory calculations predict that the 1s→3p transition energies shift ≈ 2 eV with

each sequential hole in the valence (t_{2g}), reporting on the strength of core–valence interactions. These predictions are tested and confirmed with measurements made on $K_4Fe^{II}(CN)_6$ and $K_3Fe^{III}(CN)_6$ in H_2O. We utilize both the density functional theory and Markov-chain Monte-Carlo simulations in peak assignment, and experimentally measure the predicted $\approx$2 eV shift in 1s$\rightarrow$3p transition energy as a function of valence hole density. This technique's first demonstration in solution is chronicled here.

TABLE OF CONTENTS

LIST OF FIGURES

LIST OF TABLES

GLOSSARY

AS: Attosecond (10^{-18})

BOA: Born Oppenheimer Approximation

CXI: Coherent X-ray imaging, experimental hutch at LCLS

DHO: Displaced harmonic oscillator

ESA: Excited-state absorption

(2D) ES: (two-dimensional) electronic spectroscopy

ESE: Excited-state emission

(2D) EV: (two-dimensional) electronic-vibrational spectroscopy

FC: Franck–Condon

FS: Femtosecond (10^{-15})

FTIR: Fourier transform infrared spectroscopy

GSB: Ground-state bleach

HBQ: 10-Hydroxybenzo[h]quinoline

HHG: High harmonic generation

(2D) IR: (two-dimensional) infrared spectroscopy

IRF: Instrument response function

K-SHELL: Relating to the N=1 electron shell

KB (MIRRORS): Kirkpatrick—Baez (mirrors)

L-SHELL: Relating to the N=2 electron shell

LCLS: Linac coherent light source

M-SHELL: Relating to the N=3 electron shell

MCMC: Markov-chain Monte-Carlo

MIR: Mid-infrared

MRAD: milliradian

NIR: Near-infrared

NR: Non-rephasing

NS: Nanosecond (10^{-19})

PS: Picosecond (10^{-12})

R: Rephasing

RIXS: Resonant inelastic X-ray scattering spectroscopy

TDDFT: Time-dependent density functional theory

TIR: Transient infrared (spectroscopy)

(2D) VE: (Two-dimensional) vibrational-electronic spectroscopy

XAS: X-ray absorption spectroscopy

XES: X-ray emission spectroscopy

(X)FEL: (X-ray) free electron laser

XPP: X-ray pump probe, experimental hutch at LCLS

XPXP: X-ray pump X-ray probe (spectroscopy)

ACKNOWLEDGMENTS

The work done by the end of a Ph.D. is very different from what it appears at the onset. It is influenced in both direction and success by so many dedicated and talented scientists. So many people have worked professionally to make this science happen, too many to list here. I owe so much to so many of them, the successes outlined here are collaborative and would be impossible if attempted in isolation

I'll start with my advisor, Munira Khalil, to whom I owe such an incredible mountain of gratitude. She has encouraged me to tackle problems I initially shied from, shared expertise, and taught me how tackle problems independently with both grand hopes and realistic expectations, all while modeling such a keen drive to better understand the universe. Her leadership in our department and in our group has been nothing short of empowering.

Jason Sandwisch is the most excitable scientist I know. His passion for learning and tinkering have created a gold standard of an optical scientist against whom I pity anyone being measured. We started this journey together, and your continual presence, and friendship have been a rock through and lab's triumphs and pitfalls. Hey Jason, "I did a thing!" I have spent many long hours in lab with Caroline Loe, who is undeterrable and perplexingly optimistic in her quest for progress. The pain of slow and arduous progress is better in her company fueled by an angsty soundtrack. Lab 1 could not be in better hands. James Gaynor has the magical ability to call all around him to strive for a level of excellence they did not think possible. It was my privilege to learn from and work with him developing the bulk of this thesis. A stunning example of a human and a scientist. Zach Fox, thank you for being my first mentor in graduate school. You tolerated my abundance of questions and patiently guided my understanding of the whole system. You taught me how to trust the

things I am sure of and question the things of which I am not. Chelsea Liekhus-Schmaltz, thank you for teaching me what it looks like to be a person who does science. Ben Poulter is going to become an amazing X-ray scientist and the molecules will quiver in fear, or quiver appropriately according to the carefully developed experimental design. To all members of the Krew, past and present, I have learned from each of you. I know each of you individually to be smart and capable people. I am nothing if not excited to see the heights to which you will each climb.

Whether it was escaping into an elaborate dinner plan, routing on the sounders, or simply retreating from the chaos that is a Ph.D., I am so thankful or the love and support of my friends and family. Thank you for the long rainy runs, and the exciting game nights. Thank you for listening, and your understanding. Heidi, I do not know the words to write here to express the gratitude in the wake of the debt I owe for your never-ending patience, understanding and encouragement; May I spend the rest of my life searching for them. To all those who have taught me, all those who have encouraged me, all those who have been patient with me, all those have been kind to me, thank you. Someone else taught me most of what I know. The rest came from long hours spent being wrong. Go teach someone else.

DEDICATION

For my family.

Chapter 1

INTRODUCTION

1.1 Degrees of Freedom in Photochemical Interactions

From the synthesis of small molecules in large industrial vats to photosynthesis in microscopic chloroplasts, many of the chemical reactions we care about are multi-step and involve a host of players (degrees of freedom). These could be separate parts of a single molecule, groups or individual atoms, individual electrons, or protons acting intramolecularly. They could be entire molecules, large lattice structures, or solvents that govern how molecules interact with each other intermolecularly. Any attempt to understand, manipulate or eventually control these reactions requires understanding each of these players' different roles in governing the molecules' behavior.

Figure 1.1 shows, that many of these players evolve over drastically different timescales. If not for its own relaxation, the vibrational motion which takes place is 10^{-13} seconds could occur tens or hundreds of thousands of times over the course of a long-lived electronic relaxation. Looking at just the lifetime of vibrations and electronic states, a long-lived vibration might last tens of times longer than a short-lived electronic excitation but a short-lived vibrational state could be created and destroyed ten thousand times during a long-lived electronic state. While the precise location and energy of valence electrons are primarily determined by the geometry of each atom's nucleus, vibrational motions are constantly changing that geometry in response to solvent effects and other long-range motions on a timescale bridging the timescale of vibrational motion and electronic relaxation. In the intervening years since originally published, the bounds of these timescales have shifted.

In addition to the wide range of timescales on which each of these players act, one unavoidable fact of the diversity found in the contributing degrees of freedom is the corre-

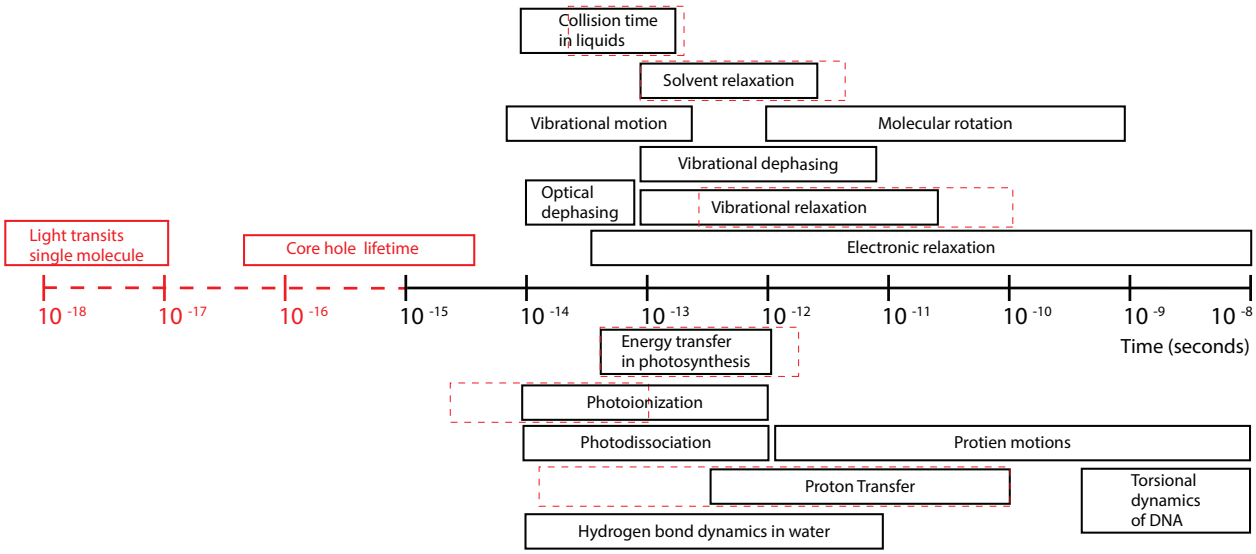

Figure 1.1: **Timescales of Studied Systems:** The relevant timescales of cutting-edge optical experiments in 1990 (black) and 2006 (red dashed) extended from the femto- to the nano-regimes. This was coincident with the advent of pump–probe and multidimensional techniques (see Fig. 1.2). The pertinent systems and processes are informed by the capabilities of the time and definitions of boxed bounds shifted as new experiments demonstrated behavior on previously unobserved timescales. The extended (red) timescale axis shows the next domain of experimental capabilities. Adapted from [1, 2]. The red–dashed extension of proton transfer represents the timescale of Excited State Intramolecular Proton Transfer (ESIPT) explicitly considered in Ch. 4, as measured by Kim and Joo [3, 4].

sponding range in energies of each motion. Electronic motions like a charge transfer of a valence electron or the promotion of an electron into a higher-lying orbital typically require photons with energy near or around the visible spectrum. One convenient unit for energy on the atomic and molecular scale is the electron volt (eV). It relates well to the small amounts of energy carried by individual photons. For example the entire visible spectrum of light, from low energy red light to higher energy blue light spans from $\approx$1.5 to $\approx$3 eV. Molecular vibrations, conversely, consist of the motion of comparatively slow and heavy nuclei. This slower motion is resonant with, lower energy, infrared light (reaching down to less than 10^{-3} eV). On the other end of the spectrum, electrons tightly bound to the nucleus (core electrons) require immense amounts of energy on the atomic scale to move or remove. These electrons

are typically studied with photons in the extreme ultraviolet, extending out the hard X-ray regime (reaching upwards of 10^5 eV). The wavelength of that low-energy MIR photon is 10^8 times longer than the high-energy X-ray so this range of energies and timescales also manifests as a range of length scales. What might be the most pertinent connection here is that none of those players act independently of the others. Understanding how dissimilar degrees of freedom interact, with their wildly different characteristics, is key in taking steps to control those interactions.

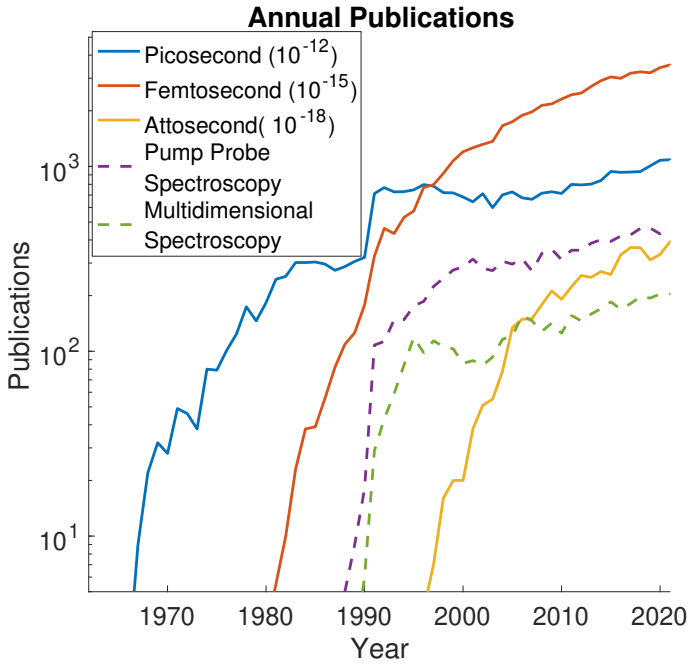

Figure 1.2: **Publication history of timescales from Pico- to Atto-:** Each line corresponds to the number of citations in a given year containing the phrase in the legend. The techniques which investigate the femtosecond dynamics of molecular systems came about in the wake of the development of the relevant optical pulses. Counts produced by Web of Science search for publications including the legend word or phrase under "topic".

One can imagine a molecule vibrating in just the right way, to lengthen or shrink a key bond. In response, the electrons in the molecule subtly rearrange, changing the symmetry of the electron cloud. Whether an electronic transition is favorable depends on that symmetry,

which triggers a second bond, elsewhere in the molecule, to break more easily. The easily broken bond allows for another change in geometry, creating a new species, which is more reactive or more effective at absorbing another photon. The key was getting the first vibration just right. We could look at the vibrational spectroscopic signature to note its importance in the process. Frustratingly, it is challenging to know if the success in the case above was due to exactly the story that accompanied it. This could be the wrong order of events. There could be a contributing effect that we missed like the solution the molecule is in. There could be some intermediate state through which the system passes.

The example of a bond breaking could be any goal: forming a bond, prolonging an excited state, harvesting a photon in a solar cell, or preventing damaging buildup in a new battery. The goal is not to make that one bond break, but to identify the key players and understand their specific roles. The goal is to learn how to design and build systems where we know who is doing what, and we can change their behavior. This creates an outstandingly challenging question: Can we understand the causality and the connection (coupling) between each of these degrees of freedom and leverage that knowledge for specific control over molecular species? Stopping short of direct control, we start by simply looking for connections. e.g. Were that first vibration and the electronic transition coupled in the first place? We start by looking for connections with ultrafast multi-color multidimensional spectroscopies.

Investigations of these processes require techniques that cover the wide range of timescales presented above. Crucially, the experiment needs to be fast enough to resolve the fastest action which we wish to observe. Specifically, we will reach into the femtosecond (10^{-15}) regime, and discuss simulations/future works in the attosecond (10^{-18}). Experimentally producing, controlling, and detecting each energy regime of photons requires distinct equipment, expertise, and considerations. while the first continuous-wave ruby laser was developed in 1960 [5], the community needed to wait until the mid-1980s for the short duration, high-intensity pulses required to perform these sorts of experiments [6, 7].

Pump–probe spectroscopy grew quickly following the development of high energy pulsed lasers in the optical regime. The ability to spatially and temporally separate, recombine,

and detect those pulses allowed for numerous studies, shown over time in Fig. 1.2. While the advent of pump–probe spectroscopy quickly followed these advancements, multidimensional spectroscopy was a rapid next step.

1.2 Multicolor and Multi-Pulse Spectroscopies

Fundamentally pump–probe experiments work by utilizing two independently controlled short-duration pulses of light. The first, called the pump, interacts with the system to perturb a particular degree of freedom. The second pulse, the probe, is delayed in time so the system can evolve and respond to the pump. It is the system's behavior as a function of this time (called τ) that is what we are studying. The probe pulse could assess a wide array of measurements, but in each experiment, it is carefully tuned to probe a specific degree of freedom. The experiment is repeated with and without the pump and the extracted data is the difference between the two measurements, over the course of many different delay times, we can build up an idea of what the system is doing.

The general concepts of a pump and probe do not require photon-based actions, however, the generation of a quickly changing electric field is intrinsically tied to photons in some way. The key is that the pump and probe are fast in relation to the action that is being measured (τ). Additionally, there is nothing limiting us to pumping and probing the same degree of freedom. A common infrared technique, transient infrared spectroscopy (t-IR), relies on initiating an experiment with an optical pulse to change the system's electronic state and monitors the vibrational response as a function of time. Comparisons of the vibrational characteristics of the ground and electronically excited state have been used to report on an exhaustive list of phenomena.

We can improve the quality of the information in these spectroscopies by gaining resolution about the pump pulse. This answers the question "what aspect of the pump mattered?" Considering the vibrational spectroscopy case, by restricting the frequency distribution of the pump to a narrow bandwidth, and progressively stepping through those frequencies, we can build a correlation map. Pumped at X frequency, the probed difference spectrum is Y. While

the time-bandwidth product of these pulses stipulates that we can only use this method to study long-lived (picosecond) dynamics, this serves as a method to reach two-dimensional infrared spectroscopy with only two pulses [8–10].

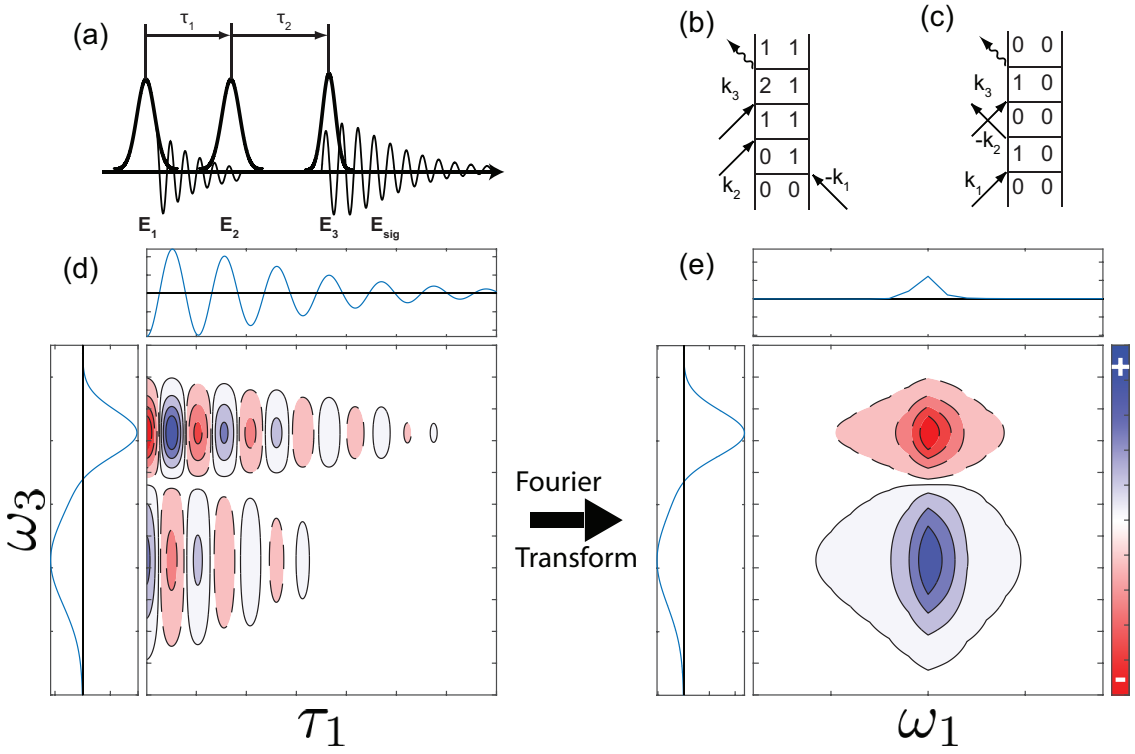

Figure 1.3: **Pulse sequence and Experimental Description of Multidimensional Experiments:** shown via pulses in the time domain (a) and a double-sided Feynman diagram (b-c). Descriptions of the pulse order interactions are found in the main text. Experimental durations are shown as height in the Feynman diagrams. (b) and (c) represent an excited state absorption and a ground state bleach respectively. They carry separate signs (positive and negative) in the spectrum, which nearly cancel out in the linear spectrum, represented as rectangular plots directly beneath the Feynman diagrams. For a given (τ_2) delay, a series of (τ_1) are collected over which a Fourier transform is performed to retrieve the frequency domain information, depicted in (d-e). Each small rectangle plot surrounding the square plots represents the summation of the plot along that dimension.

We could continually increase the number of pump pulses. With each additional pump pulse, the system undergoes further changes, enriching the spectrum with more information, but at a cost of increased experimental complication, requiring more sophisticated data

analysis. Two-pulse (frequency domain) two-dimensional infrared spectroscopy resolved the pump frequency dependence of the pump and enabled measurements of coupling between vibrational modes. Three-pulse (time domain) two-dimensional infrared [11–15] and electronic [16–18] spectroscopy allowed for understanding temporal population and coherence dynamics with improved resolution thanks to advancements in pulse generation and compression. That has led to the development of experiments with more and more pulses [19–23] limited only by our ability to produce, control, and detect the independent pulses of light. Each experimental improvement must be met with corresponding progress in our ability to extract information from preexisting experimental procedures [24–28]. Sometimes these theoretical advancements occur years before the experiment and serve as a call for and guide the development of experimental capabilities. Other times they arise out of necessity, prompted by confusing or unexpected experimental results.

Both nuclear (vibrational) and electronic motions have been heavily studied by pump–probe and multidimensional methods. The fundamental conception of those experiments is the same regardless of the system or the type of motion, so the experiment can be described in general and then applied to the degree of freedom that requires investigation. A brief description of a multidimensional four-wave mixing experiment is given in Fig. 1.3. The first pulse ($\boldsymbol{E_1}$, $\boldsymbol{k}_1$) creates a coherence state between the 0^{th} and 1^{st} state which lasts for a duration (τ_1). The second pulse ($\boldsymbol{E_2}$, $\boldsymbol{k}_2$) collapses that coherence into a population in the 1^{st} excited state. This population, similarly, evolves for a duration (τ_2) before a third interaction ($\boldsymbol{E_3}$, $\boldsymbol{k}_3$) probes the system, which emits ($\boldsymbol{k}_{sig}$) as the detectable signal of the experiment. Each signal in the presented field shows the coupling strength between two degrees of freedom. For example pathway (b) accesses state (2) while pathway (c) only accesses states (0) and (1).

The great advantage of these techniques is the resolution along both the pump and probe axis, (ω_1 and ω_3). The ability to take incredibly short steps in time correlates with the ability to resolve high-frequency oscillations in the pumped domain. Consider the example in Fig. 1.3 as a 2D IR experiment. The linear FTIR measurement (approximated as the

rectangular panel above plot (1.3 e)) carries vibrational information but only shows a single weak signal. By gaining the second dimension of data, both of the pathways shown in the Feynman diagrams above can be accessed, separated, and measured.

1.3 Multidimensional Vibronic Spectroscopies

It appears oddly formal to simply refer to states (0, 1, 2) in Fig. 1.3. There is good reason to remain painfully general in this description. In 2D IR spectroscopy, all of these states are vibrational modes, and we could replace each numbered state with a corresponding bra or ket representation $|\nu_i\rangle$ and $|\nu_i\rangle$. In 2D ES these states are electronic in nature, generally tracking the motion of valence electrons. For this experiment, we would write states as $|g\rangle$ or $|e\rangle$ for ground and excited electronic states. To properly describe a vibronic state, simultaneous description of the electronic and vibrational quantum states is required ($|g;\nu_i,\nu_j\rangle$ and $|e;\nu_{i'},\nu_{j'}\rangle$) for multiple vibrations in multiple electronic states.

Figure 1.4 shows that this multidimensional experiment can, and has, been performed across a wide range of energies. Each colored box represents the spectral window of a performed multidimensional experiment. Experiments along the diagonal of the figure measure the coupling between similar degrees of freedom. The off-diagonal experiments, measure the coupling between dissimilar degrees of freedom. Similar to the t-IR experiment mentioned above, these off-diagonal experiments, two-dimensional electronic-vibrational (2D EV) and two-dimensional vibrational-electronic (2D VE), measure the interaction between nuclear and electronic motions. However, they benefit from the multidimensional separation of peaks shown in Fig. 1.3.

Importantly, signals in these spectroscopies do not simply represent the separation of vibrational stretches, or electronic states, but report directly on the coupling between those two degrees of freedom. Fig. 1.5 (a) shows the ω_1 projection of a 2D VE experiment performed on a model metal-to-metal charge transfer system with four vibrational modes. The difference in intensity between the linear FTIR (grey) and the 2D VE (black) results from the vibronic coupling strength between the degrees of freedom.

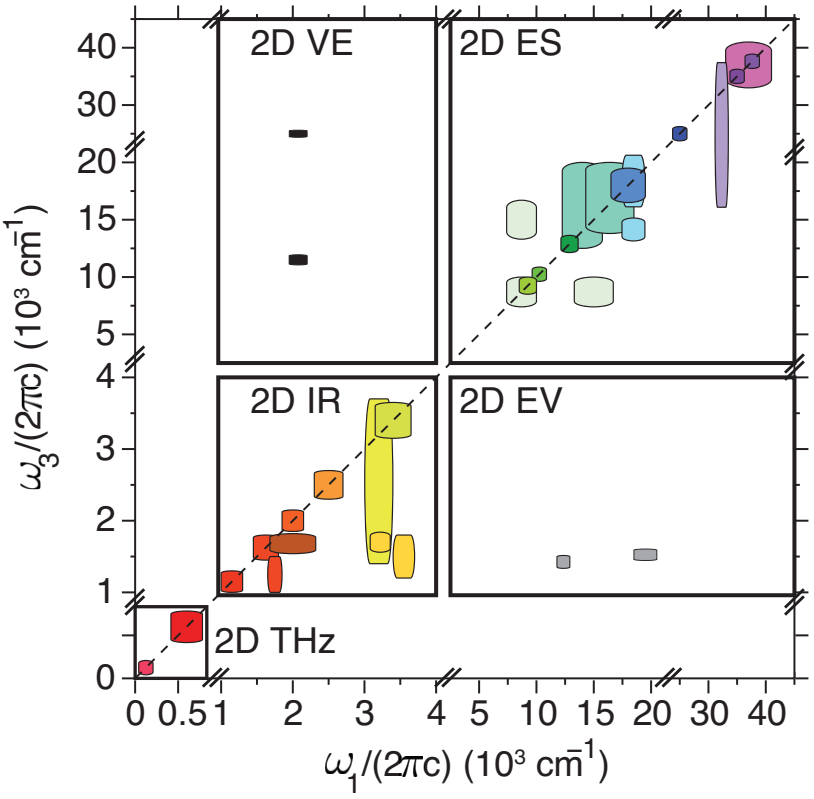

Figure 1.4: **Multidimensional Energy Landscape:** Colored regions represent the reported spectral windows of distinct experiments. Boxed regions separate experiments by type and energy. Experiments which lie along the diagonal line of this plot pump and probe similar degrees of freedom. The off-diagonal boxes labelled VE and EV constitute the vibronic spectroscopies explored here. Reproduced from [29].

The 2D analog of the t-IR experiment (2D EV) is shown in Fig. 1.5 (b). Wherein, distinct electronic states coupled to specific vibrational modes can be readily seen. It is easy to see how this approach holds great value when the excited state electronic manifold consists of multiple states, impossible to separate without both axes of resolution.

These vibronic spectrscopies are comparatively young, first demonstrated in the mid 2010's [29,32]. To date they have been harnessed to study correlated motions of atomic nuclei and electrons in systems ranging from biological light harvesting complexes [33, 34] to synthetic dyes and charge/energy transfer systems [31,35]. Separately, results from polarization-

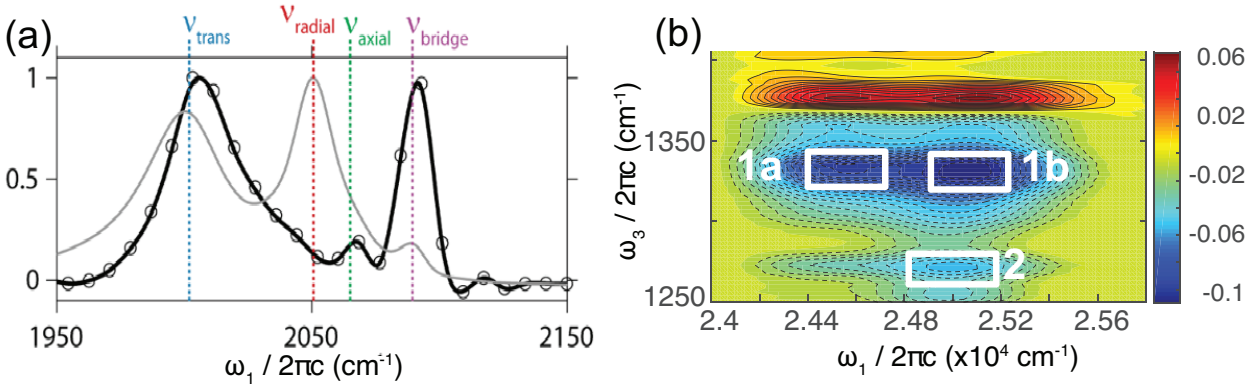

Figure 1.5: **Example of Vibronic Spectra Isolating Signals:** (a) ω_1 projection of 2D VE spectrum of a model metal-to-metal charge transfer system consisting of four high frequency IR active vibration modes. Grey line shows the linear FTIR. Black line shows the 2D VE projection. The discrepancy between the two demonstrates how vibronic spectroscopies do not simply separate and clarify signals, but report directly on the vibronic coupling within a system. Reproduced from [30]. (b) Sample 2D EV spectrum of a model metal-to-ligand charge transfer system. Because of the separation of signals along both the ω_1 and ω_3 axes and the inherent measurement of coupling shown in (a), this spectrum allows for the observation and measurement of vibronic couplings across the entire vibrational spectrum and multiple distinct electronic excited states. The vibrational mode (horizontal line) labeled (1) is has two peaks (a and b), showing coupling to multiple electronic states. However, vibrational mode 2 is significantly more coupled to the higher energy electronic state. Adapted from [31].

selective 2D VE have mapped the orientations of a metal-metal-charge-transfer relative to multiple vibrations [29, 36, 37], and 2D EV results have reported on similar mappings in model dyes to differentiate orientations of multiple electronic transitions relative to a host of vibrations and have tracked the time evolution of those vibrations and electronic states acting in concert [38]. These experimental achievements are realized in tandem with theoretical and computational work [39–41] that allows us to build up our understanding of the chemical information they hold and answer new questions: What approximations are valid when you combine quantum mechanical descriptions of nuclear and electronic degrees of freedom? What role does the three-dimensional orientation and configuration of the system play? What experimental explanations are feasible, probable, or completely ludicrous?

1.4 X-ray Pump X-ray Probe Spectroscopy

So far alluded to, but left largely not discussed, are the core electrons. Given that they are localized to a single atom, and moving them requires immense effort, they play a much different role in molecular behavior than their valence counterparts. Nonetheless, each and every electron in an atom interacts with every other electron. Inner electrons partially shield outer electrons from the highly charged nucleus and the size of that shielding determines the radius of the atom and ultimately governs how it interacts electronically with other atoms. Each shell of electrons is in a push–pull equilibrium with the shell of electrons above and below it and pump–probe spectroscopy can help explain how these different shells interact. Specifically, measuring the time-evolving interactions of 3p and 3d electrons is crucial for understanding, accurately modeling, predicting, and synthesizing electronic correlations in transition metal complexes used in catalytic, magnetic, and information storage applications [42, 43]. Notably, as the 3p and 3d electrons interact, they shift in energy not only relative to each other but also relative to all of the surrounding shells as well.

These interactions are encoded in numerous transitions connecting the K- (n=1), L- (n=2), or M- (n=3) edge X-ray absorption and emission spectra of transition metal complexes measured at synchrotrons, X-ray Free Electron Lasers (X-FELs) and with table-top high harmonic generation (HHG) based sources. Each shell of core electrons (labeled in Fig. 1.6) is well separated and the vast distance between energetic edges means that we can easily separate signals from different types of atoms and different electron shells. At the K-edge, a fluorescence experiment connecting the K- and M-shells (called Kβ X-ray emission spectroscopy [XES]) probes the 3p–3d exchange energy through the relative intensities of the spectral features sensitive to spin and 3d occupancy [44–46]. Similarly, L-edge spectroscopy has been used extensively to monitor the electron orbital characteristics like covalency, spin, and back-bonding in transition metals [47–50]. The extraction of core electronic state-specific information from equilibrium and optically-pumped X-ray absorption spectroscopy (XAS) and XES spectral features at the K-, L- and M-edges has fundamental limiting challenges.

Vacancies in the K- or L-shell are incredibly short lived which results in spectrally broad features [51]. That leaves the M-edge, where the spectra directly measure 3p→valence transitions [52–54]. The fundamental problem with this approach is that there are so many vacant orbitals around the valence energy that it is incredibly difficult to nail down exactly which transition is which. They are packed close together and are not differentiable. The challenge in accessing these 3p–3d interactions is to design an experiment where: 1) The pumped state can live for a long time, i.e. the hole lifetime is long enough to allow for meaningful dynamics to evolve. 2) The probed transition involves two specific states, avoiding the continuum of states at the valence edge, to create separable data.

Just as the pump–probe transient absorption experiment was the precursor to the multidimensional optical experiment, the X-ray pump X-ray probe (XPXP) Spectroscopy experiment is a precursor for multidimensional X-ray spectroscopy, enabling the study of how core electrons interact both with each other and with valence electrons. To fit the XPXP experiment the landscape of Fig. 1.4 without using a log-scale would require over 250 sheets of paper laid out in a grid. To describe the experiment on a heavier metal of interest, Ruthenium, would require 2,500 sheets of paper. To expand on the axis seen in Fig. 1.1, lifetimes of core holes are on the attosecond (10^{-18}) to ones of femtoseconds timescales [51, 55]. This extends the scale of the figure three steps to the left, shown in red. While Fig. 1.2 shows publications in the attosecond regime arising in the late-1990s, experimental implementation of their use has lagged behind the theoretical work. Robust femtosecond lasers are available for purchase, while attosecond optical setups are still burgeoning.

Conceptually, this experiment is similar to the pump–probe experiments discussed thus far. Pump: remove a 1s electron from a molecule. Probe: monitor some aspect of the 3p–3d interaction as a function of time. However, there are some significant differences. Pump–probe spectroscopy in the laboratory was enabled by the development of robust high repetition rate femtosecond laser systems. Tremendous progress has been made in recent years at the world's XFELs to enable the technical ability to generate multiple time-delayed hard X-ray pulses of different colors with novel detection schemes [56–61].

Just as the t-IR experiment can excite multiple electronic states the generation of a deep core hole results in an overabundance of outcomes. For the electronic excitation, each of those states might be conceivably tracked, often modeled as the progression of 3-10 states over the course of thousands of femtoseconds. Rather than a single electron moving around, when a 1s electron is removed, a cascade of all the higher-lying electrons occurs. Through radiative and non-radiative processes each progressive hole is filled and new ones, sometimes multiple, are generated. An iron atom with up to six vacancies would have more than 300,000 possible states. The ruthenium atom from earlier would have more 8.2 million, not a directly calculable process.

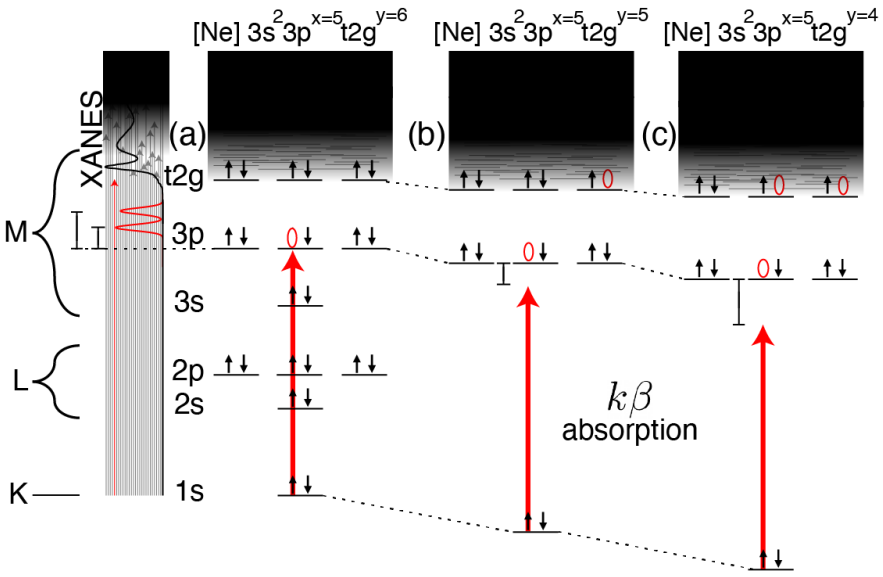

Figure 1.6: **Energy diagram of accessed states in XPXP experiment:** Red arrows (labeled kβ absorption) show the absorption event correlated with the probe pulse between the K- and M-shells. One of the two electrons in the filled 1s orbital is promoted to the vacancy in the 3p (Kβ absorption). All orbitals shift and relax in energy due to a reduction of shielding from 3p and valence holes, but they each respond differently. The progression from (a) to (c) shows that for each additional hole in the valance (t_{2g}) orbital, the energy of the 1s$\rightarrow$3p transition rises. Arrow thickness corresponds to the strength of the transition. This is contrasted with the transient XANES experiment, shown to the left, which is tasked with distinguishing a single weak (thin red) transition at the edge of the filled orbitals from the dense continuum of transitions forming the edge.

Fortunately, we restrict observation of these states using the characteristics of the X-ray pulses we control. Specifically tuning the frequency of the probe to the 1s→3p transition allows us to be selectively sensitive to states that carry a 3p vacancy. The probed states are represented in Fig. 1.6, where additional holes in the valance shell of the iron atom (labeled t_{2g}) have caused the energy of the 1s→3p transition to rise, creating different 1s-3p energy gaps for each configuration of elections shown in (a)-(c). Molecules in exclusively those states absorb that light and we measure the change in intensity of the X-ray probe pulse. The probe pulse does not significantly interact with molecules unless they have that 3p vacancy. Those are the same states which slightly shift energetically in response to the valence occupancy, which is sensitive to the 3p–3d interaction strength. Rather than attempt to model the cacophony of cascading states perfectly, we simply design an experiment that probes exclusively the states that carry the chemical information we need. No doubt, the next steps of this experiment include tracking the initial states of the cascade and correlating them with specific behavior. That will require multidimensional resolution of the core hole coherence, which is not currently available to researchers.

1.5 Dissertation Overview

In part I of this dissertation, chapters 2 and 3 explore the third-order orientational response function jointly governing 2D VE and 2D EV spectroscopy and chapter 4 details recent experimental work informed by that exploration. Chapter 2 draws on the first publication in a series of theoretical works [62], to focus on the formalism and analytical expressions governing all possible signals in the two spectroscopies. It covers the relaxation of assumptions made in diagonal multidimensional spectroscopies and includes implications for leveraging anisotropic analysis to reveal non-Condon effects and Duschisnky mixing. Chapter 3 extends that approach, chronicling the second paper in that series [63], to explore the implications of applying a model Hamiltonian to the model system from the previous chapter. The Hamiltonian description is accompanied by a discussion of constituent terms, relating them to previous literature. The interaction Hamiltonian is applied and model vibronic analysis is

performed on joint simulations of polarization selective 2D VE and 2D EV experiments. Specific analysis of classically forbidden transitions shows promise for the isolation and detection of non-Condon processes. Together chapters 2 and 3 provide a road map for how these two spectroscopies can and should be used in tandem to measure the coherent behavior of coupled nuclear and electronic degrees of freedom in a wide range of systems. Chapter 4 continues by presenting a brief perspective of new work featuring 2D EV spectroscopy of a model proton transfer system. Data and analyses are presented which show strong experimental evidence of τ_1 coherence transfer. This constitutes concrete evidence for the breakdown of the Born–Oppenheimer approximation. Much of the formalism of the previous work is based on that approximation; this work prompts discussion about the validity of treating nuclear and electronic degrees of freedom separately under the very formalism, used to describe their coupling. Much of the progress made in experimental technique does not relate to publishable experimental results. For that reason, technical notes on the successful performance of these spectroscopies can be found in Appendix E.

Part II of this dissertation, chapters 5 and 6, presents work on the development of a novel hard X-ray pump X-ray probe spectroscopy and chronicles its first-ever implementation in solution phase. Both chapters relate to the same two works [64], — the second, not yet published —, but divide the descriptions along theoretical and experimental lines. Chapter 5 outlines the process of modeling, proposing, and simulating the XPXP experiment. Following the removal of a 1s electron, determining a full molecular response is complicated. Separate approaches are detailed for describing the plethora of electronic states which result in two oxidation states of a model third-row transition metal [Fe^{II} and Fe^{III}]. An electronic-structure calculation approach, which preserves core hole vacancy, is utilized to determine the chemical shifts and dipoles present in those resulting states. Finally, preliminary calculations are performed to show the feasibility of the XPXP both at the valence edge and at the 3p level. The benefits of this experiment compared to the study of other relevant spectroscopic edges are also put forth. Given the overwhelming advantage of the increased dipole strength of the 1s→3p transition over the quadrapole nature of the 1s→3d transitions,

chapter 6 recounts the performance of the XPXP experiment on both oxidation states of iron in model salts [$K_4Fe^{II}(CN)_6$ and $K_3Fe^{III}(CN)_6$]. In addition to describing the particulars of the experimental setup and discussion of results, a new filtering approach is discussed and conceptual improvements for subsequent experiments are posited. Data are presented that account for distinct electronic states — those sensitive to the predicted 3p–3d interaction — and correlate well with the simulated cascade.

Chapter 2

MULTIMODE TWO-DIMENSIONAL VIBRONIC SPECTROSCOPY I: ORIENTATIONAL CORRELATION FUNCTIONS AND POLARIZATION SELECTIVITY

Relevant publications, with the permission of AIP publishing:

- [62] James D. Gaynor, Robert B. Weakly, and Munira Kahlil. "Multimode two-dimensional vibronic spectroscopy. I. Orientational response and polarization-selectivity", *Journal of Chemical Physics*, Vol. 154, no. 18, p. 184201-20, 2021

2.1 Introduction

This chapter is the first of two which primarily convey work [62, 63] published with the intent of building upon previous work [40] with the intent of expanding the single mode picture to consider n coupled oscillators. The work takes advantage of the naturally occurring difference in dipole orientation and vibrational shifts in electronically excited states to provide a model for multiple vibrations coupled both amongst themselves and to a specific electronic transition. The majority of that work is reproduced here. Additionally, the groundwork for these results can be found in a previous thesis [65].

The seminal work of Ernst and co-workers [66] laid a foundation for the development of multidimensional Fourier-transform (FT) spectroscopy, first using pulses in the radio frequency spectral region to map correlated nuclear spin phenomena. In the decades since, advancements in laser technology have enabled a spectral exploration of this technique which now reaches throughout the terahertz, mid-infrared, visible, and ultraviolet spectral regions. [67] Coherent multidimensional spectroscopy is now capable of measuring chemical dynamics occurring on the femtosecond (fs) and picosecond (ps) timescales, in non-

equilibrated ground and excited states, that involve complex molecular couplings between many different degrees of freedom.

Two-dimensional electronic spectroscopy (2D ES) and two-dimensional infrared spectroscopy (2D IR) are well-established coherent multidimensional techniques that are used extensively to investigate chemical and physical processes in the condensed phase. An effective probe of electronic couplings, 2D ES has been critical for understanding photosynthetic energy transfer, [68–73] charge transfer, [74] excitonic phenomena, [75–77] and quantum coherences in dimers and aggregates. [78–80] The sensitivity of vibrations to molecular structural parameters has made 2D IR an essential tool for measuring chemical exchange, [81–83] vibrational anharmonicity and couplings, [11, 84–87] spectral diffusion in liquids, [28, 88–91] and structural dynamics in proteins. [8, 92–96] Incorporating polarization-selectivity into 2D ES and 2D IR experiments has significantly enhanced our ability to obtain molecular-frame structural insight and to deconvolve congested spectra. By experimentally controlling the polarization of the three incident electric fields and the detected signal field, specific transition dipole moments can be isolated and cross-peaks describing interactions between different dipole moments can be enhanced. [97–100] In 2D ES, polarization-selectivity can distinguish different electronic states through its sensitivity to the orientation of the dipole moment. [68, 99, 101] In some instances, polarization-selective 2D ES has also been able to map observed electronic dynamics onto specific vibrational coordinates. [26,102] Polarization-selective 2D IR spectroscopy can be used to measure angles between coupled vibrational coordinates, [24,103–105] to extract hydrogen bond jump angles during chemical exchange, [106] to observe reorientation-induced spectral diffusion, [107] and to determine secondary protein structure. [108] The 2D IR and 2D ES techniques are primarily sensitive to correlated dynamics involving vibrational and electronic motion, respectively. Direct measurements of correlated motion involving both electronic and vibrational degrees of freedom — known as vibronic couplings — require resonant techniques that interact with both electronic and vibrational transitions.

Two-dimensional electronic-vibrational (2D EV) spectroscopy and its mirrored analog

two-dimensional vibrational-electronic (2D VE) spectroscopy are among the most recent additions to the coherent multidimensional spectroscopy toolbox. [29, 32, 109, 110] These multicolor, coherent FT techniques include both electronically-resonant interactions in the UV-visible spectral domain and vibrationally-resonant interactions in the mid-infrared domain (see Fig. 2.1 pulse sequences) and are uniquely sensitive to vibronic coupling. [40] Recent 2D EV and 2D VE investigations have produced new insight into ultrafast charge transfer in transition metal complexes, [30, 31, 37, 38] proton transfer, [111] photosynthetic light-harvesting, [33, 112–114] and dynamics at conical intersections. [115, 116] Polarization-selectivity has also been experimentally incorporated into both techniques to better understand congested spectra [31, 33] and separate orientational response from the vibronic molecular response. [37] Theoretical treatments are actively developing an infrastructure to fully understand the information content of the measured spectra for model systems including one vibronically coupled anharmonic oscillator on two electronic states, [40] a vibronically coupled molecular dimer containing a vibrational frequency resonant with the excitonic energy gap, [39] and investigations into the origin of 2D EV line shapes. [41,117,118] Of particular interest for ultrafast excited-state phenomena is the role those vibronic couplings, non-Condon effects, and Duschinsky mixing play in determining relaxation trajectories. [25, 27, 102, 119–123] By exploiting direct sensitivity to both electronic and vibrational motions, 2D EV and 2D VE spectroscopies are well-suited for such investigations. Other works have used the term "vibronic" to describe strong coupling between multiple excited electronic states. [25, 39] Here the term is used to explicitly describe a ground and single excited state coupling through the vibrational modes of interest in the weak coupling limit. This chapter is the first in a series of two that investigates the 2D EV and 2D VE spectral signatures of a model system involving two vibronically coupled anharmonic vibrations in two electronic states, but it is readily extendable to multiple vibrational modes. We leave the inclusion of multiple excited electronic states for a future publication. For brevity, we will collectively refer to both 2D EV and 2D VE spectroscopies as 2D "vibronic" spectroscopies.

The emphasis in this first chapter is on the nonlinear orientational response of the model

system with generally defined vibronic system eigenstates. A complete treatment of the vibronic system Hamiltonian is reserved for the second chapter in this series,3 which provides a detailed account of how non-Condon effects, the Huang–Rhys parameter, [124, 125] and Duschinsky mixing are measured in the 2D vibronic spectra for this specific multimode system.

This chapter is organized as follows: Section 2.2 briefly outlines the model system discussed here and introduces the nonlinear orientational response. In Section 2.3, the 2D Vibronic peak positions, amplitudes, and line shapes are discussed and a nomenclature is developed to facilitate the discussion of the 2D vibronic spectra such that each of the contributing transition pathways and the involved transition dipole moments in each polarization-selective 2D spectrum can be specified. The system-bath interactions for this model system are treated in the homogeneous dephasing limit. Section 2.4 treats the orientational response functions within the framework of orientational diffusion, assuming the dipole moments behave as symmetric diffusers in isotropic media, and gives expressions for the generalized 2D vibronic nonlinear orientational response functions. After constructing the complete set of response functions, the orientational responses for polarization-selective signals are calculated in Section 2.6.1 and observables such as spectral anisotropy and the depolarization ratio are derived and discussed. The orientational response of 2D vibronic spectroscopies inherently contains angular dependence of at least one angle, and can have up to four angles in the framework discussed here. Section 2.6 extends the discussion of the polarization-selective 2D Vibronic spectroscopic observables. Importantly, new insights from a systematic anisotropy analysis are shown which can involve multiple peaks measured in either one of these techniques. Further, anisotropy ratios between specific vibronic pathways in both spectroscopies increases the set of dipole moments whose relative orientations can be determined. In principle, this systematic analysis could directly identify and quantify the presence of non-Condon effects and Duschinsky mixing. Comparisons between 2D vibronic spectral observables and those of other ultrafast spectroscopies are then made to contextualize the capabilities of these newer techniques. Specific polarization schemes are discussed which can help to selectively enhance

particular pathways of interest when spectra are congested with overlapping features. Finally, we discuss how time-dependence can be used to deconvolve the complete third-order vibronic response probed in 2D vibronic spectroscopies. One goal of this chapter is for this discussion to serve as a field guide for other researchers wishing to perform polarization-selective 2D vibronic experiments on more widely varied molecular systems. Finally, Sec. 2.7 concludes the first part of this two-part series, and introduces chapter 3.

2.2 Polarization-Selective Third-Order 2D Vibronic Spectroscopy: A Model Multimode System

The multimode vibronic system considered in this chapter consists of two coupled anharmonic vibrational coordinates, i and j, in two different electronic states, $|g\rangle$ and $|e\rangle$. The vibronic couplings result in excited-state displacement along vibrational coordinates, vibrational frequency shifting, and vibrational mode mixing (known as Duschinsky mixing). Generalized eigenstates for such a model system are depicted in Fig. 2.1 (a) along with analytical expressions for the energy separations of the eigenstates. The electronic ground and excited eigenstates are specified by $|g;\nu_i,\nu_j\rangle$ and $|e;\nu_{i'},\nu_{j'}\rangle$, respectively, where primes denote electronically excited state vibrations. The pulse sequences for the 2D EV and 2D VE spectroscopies are given in Fig. 2.1 (b) and (c), where the electronically-resonant and vibrationally-resonant electric fields are identified in blue and green, respectively.

In the limit that the orientational dynamics such as rotational diffusion occur on much slower timescales than vibronic dynamics of a molecule in solution, the complete third-order material response tensor ($\overleftrightarrow{\boldsymbol{R}}^{(3)}$) may be expressed as the product of the orientational response tensor ($\overleftrightarrow{\boldsymbol{Y}}$) and the vibronic response ($\boldsymbol{R}$). [98, 126, 127] The third-order material response function consists of eight distinct Liouville pathway types that group into four pairs of complex conjugate field-matter interaction pathways. Therefore, summing over all possible third-order transition pathways, α, $\overleftrightarrow{\boldsymbol{R}}^{(3)}$ is expressed as:

$$\overleftrightarrow{\boldsymbol{R}}^{(3)}(\tau_3,\tau_2,\tau_1) = \sum_{\alpha=1}^{4}\sum_{IJKL}\sum_{a,b,c,d}(Y_\alpha)_{IJKL}^{abcd}(\tau_3,\tau_2,\tau_1) \times R_\alpha^{abcd}(\tau_3,\tau_2,\tau_1). \tag{2.1}$$

The nonlinear tensorial orientational response $Y_{IJKL}^{abcd}(\tau_3,\tau_2,\tau_1)$, which specifies elements of the generalized orientational tensor ($\overleftrightarrow{\boldsymbol{Y}}$), accounts for sequential projections of the four linearly polarized electric fields in the fixed laboratory frame onto the fixed molecular frame for each successive field-matter interaction. The indices (a,b,c,d) denote the vibronic eigenstates involved in each pathway as defined by a vibronic system Hamiltonian. The time dependence of $Y_{IJKL}^{abcd}(\tau_3,\tau_2,\tau_1)$ includes the molecular diffusion between field-matter interactions. The indices $[I,J,K,L] \in [X,Y,Z]$ are a permutation of the electric field polarization over the laboratory frame coordinates (X,Y,Z).

The third-order response function for 2D vibronic spectroscopies measures the couplings between vibronic and vibrational transition dipole moments (see Fig. 2.1 (d)). These transition dipole moments describe either vibronic transitions, where changes in both the electronic state and vibrational state can occur, or vibrational transitions occuring in the same electronic state. An illustration of the molecular transition dipole moments that can be selectively probed in a polarization-selective 2D vibronic spectroscopy is given in Fig. 2.1 (d) using oscillator i as an example. It is the interaction Hamiltonian, $H_{int} = -\boldsymbol{M}\cdot\boldsymbol{E}(\boldsymbol{k},\omega,t)$, that explicitly describes the light–matter interaction itself, where the transition dipole operator is $\boldsymbol{M}$ and the time-dependent electric field is defined by its wavevector, $\boldsymbol{k}$, and its angular carrier frequency, ω. The system dipole operator is defined in terms of the vibronic system eigenstates ($|a(r,Q)\rangle$ and $|b(r,Q)\rangle$) and the transition dipole moment matrix element between eigenstates a and b given by $\mu^{a,b}$. Here, the generalized vibronic eigenstates are written as functions of the electron coordinates, r, and the nuclear coordinates, Q. The transition dipole moment vector connecting eigenstates a and b is represented by $\boldsymbol{\mu}^{a,b} = \hat{\mu}^{a,b}\times\mu^{a,b}$; that is, the dipole moments possess a direction in the molecular frame, expressed by the unit vector $\hat{\mu}^{a,b}$, as well as the magnitude of the dipole moment expressed by $\mu^{a,b}$. Therefore, H_{int}

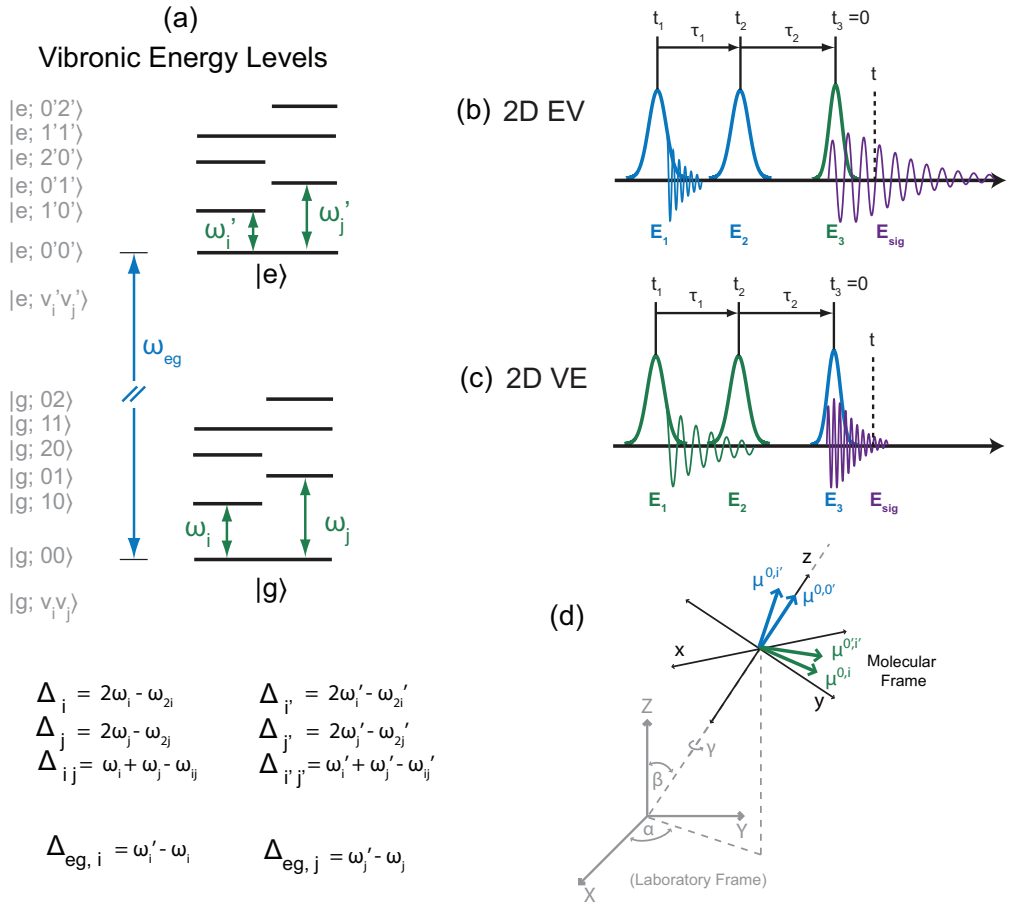

Figure 2.1: **2D Spectroscopy Overview of a Multimode Vibronic System.** The vibronic eigenstates of a coupled multimode molecular system are shown schematically in (a) where the electronic state (e or g) and the vibrational quanta (ν_i and ν_j) of the two coupled oscillators, i and j, are specified by $|g;\nu_i,\nu_j\rangle$ and $|e;\nu_{i'},\nu_{j'}\rangle$; primes indicate electronically excited state vibrations. Analytical expressions for eigenstate separation are also given. Experimental pulse sequences for (b) 2D Electronic-Vibrational (2D EV) and (c) 2D Vibrational-Electronic (2D VE) spectroscopies are shown; the four electric fields are denoted $\boldsymbol{E}_1$, $\boldsymbol{E}_2$, $\boldsymbol{E}_3$ and $\boldsymbol{E}_{sig}$, with corresponding wavevectors $\boldsymbol{k}_1$, $\boldsymbol{k}_2$, $\boldsymbol{k}_3$, and $\boldsymbol{k}_{sig}$ (blue = electronically-resonant, green = vibrationally-resonant, and purple = signal). The molecular orientation within the laboratory frame is exemplified in (d) using dipole moments for oscillator i for the electronic ($\boldsymbol{\mu}^{0,0'}$, $\boldsymbol{\mu}^{0,i'}$) and vibrational ($\boldsymbol{\mu}^{0,i}$, $\boldsymbol{\mu}^{0',i'}$) transitions. The relative angles of these dipole moments can be accessed experimentally as well as all other combinations of dipole moments contributing to any of the quantum transition pathways in either 2D spectroscopy. See text for definitions of dipole moments. The molecular frame basis vectors are lower case, $(\hat{x},\hat{y},\hat{z})$ while the laboratory frame basis vectors are upper case, $(\hat{X},\hat{Y},\hat{Z})$.

can be written as

$$H_{int} = (\hat{\mu}^{a,b} \cdot \hat{E}_Z) \times (\mu^{a,b} e^{i(\boldsymbol{k}\cdot\hat{X}-\omega t)}) \tag{2.2}$$

for the light–matter interaction of an electric field propagating along in the $\hat{X}$ direction with a linear polarization in the $\hat{Z}$ direction of the laboratory frame that is defined by the vector $\hat{E}_Z$. The first part of Eqn. 2.2 containing the scalar product is related to the nonlinear orientational response, while the second part is related to the nonlinear vibronic response through the transition probability between the system eigenstates given the spectral intensity of the incident electric fields. As previously shown for a single mode case, [40] expanding the dipole moment operator to explicitly treat the electronic and vibrational transitions that are probed in these spectroscopies demonstrates the direct sensitivity to the measurement of non-Condon effects and electrical anharmonicity. For example, both 2D EV and 2D VE spectroscopies have access to vibronic transition dipole moments which only affect the electronic state ($|g;00\rangle \leftrightarrow |e;0'0'\rangle$) and to those which affect both the electronic and vibrational degrees of freedom ($|g;00\rangle \leftrightarrow |e;1'0'\rangle$). The development of a vibronic Hamiltonian resulting in the vibronic eigenstates shown in Fig. 2.1 (a), and the connection between vibronic coupling parameters and the relative orientations of the vibronic transition dipole moments shown in Fig. 2.1 (d), is detailed in Sec. 3.2.

In this work, we employ a simplified transition dipole moment notation for $\boldsymbol{\mu}^{a,b}$: a prime denotes the excited electronic state (no prime indicates ground state), superscript index 0 indicates the common ground state (zero quanta of each oscillator), and the superscript index i, j, or ij specifies the vibrational quanta in either i, j, or a common state with nonzero vibrational quanta in each oscillator, respectively. For example, the fundamental electronic transition $\boldsymbol{\mu}^{|g;00\rangle,|e;0'0'\rangle}$ is expressed $\boldsymbol{\mu}^{\mathbf{0,0'}}$, and $\boldsymbol{\mu}^{|g;10\rangle,|e;1'1'\rangle} \equiv \boldsymbol{\mu}^{i,i'j'}$. The angle between the two dipole moments $\boldsymbol{\mu}^{a,b}$ and $\boldsymbol{\mu}^{c,d}$ is denoted $\theta_{a,b}^{c,d}$ using the same simplified notation for the transition dipole moments. For example, the angle formed between $\boldsymbol{\mu}^{0,0'}$ and $\boldsymbol{\mu}^{0,i}$ is defined $\theta_{0,0'}^{0,i}$. Here, the molecular frame is defined such that $\boldsymbol{\mu}^{0,0'}$ is parallel to $\hat{z}$ with all transition

dipole moments defined in the yz-plane; this orientation sets all dipole moments relative to $\boldsymbol{\mu}^{0,0'}$. We note that $\boldsymbol{\mu}^{0,0'}$ expresses the same dipole moment as $\boldsymbol{\mu}^{e,g}$ used previously. [40] The laboratory frame coordinates (X,Y,Z) are shown in gray with the Euler angles (α, β, γ) that describe the relative orientation of the molecular frame and the laboratory frame. Using polarizers to control the linear polarization of the incident electric fields allows the experimentalist access to specific molecular frame orientations and dipole angles. Typical polarization combinations include the parallel configuration, in which all incident fields have linear polarization that are parallel to one another (ZZZZ), and the perpendicular (or "crossed") configuration in which the first two electric fields are parallel to one another and the last two electric fields are rotated 90^o from the first two fields (YYZZ). Many other polarization combinations have also been exploited in 2D spectroscopy to isolate specific signals. [100] Importantly, performing 2D EV and 2D VE experiments with polarization-selectivity can facilitate signal isolation in otherwise congested spectral regions and potentially separate the orientational signal contributions from the vibronic molecular signal contributions.

2.3 2D Vibronic Spectral Features: Positions, Amplitudes, and Line Shapes

Establishing a self-consistent system of reference for pathway types and peak characteristics is crucial for furthering the present discussion. Additionally, the determination of a particular vibrational mode's role in a vibronic pathway greatly aids the interpretation of the polarization-selective data as the relative orientations of vibrational modes dictate the strength of the vibronic response. This section should be used as an informative reference in denoting pathways for both EV and VE spectroscopy throughout both chapters in this series. Each peak measured in a 2D EV or 2D VE spectrum of a multimode system reports on the simultaneous contribution of multiple vibronic pathways with overlapping spectral locations. Each pathway may be described by a symbol written as:

$$\mathsf{N}^{\mathsf{m_3}}_{\mathsf{m_1},\mathsf{m_2}} \tag{2.3}$$

for pathway types N where $\mathsf{N} \in \mathsf{I} - \mathsf{VII}$, and vibrational indices $\mathsf{m_1}, \mathsf{m_2}, \mathsf{m_3}$. The pathway labels in the Feynman diagrams of Figs. 2.3 and 2.4 connote the type of signal (ground state bleach (GSB), excited state absorption (ESA), or excited state stimulated emission (ESE)) and a description of the transition pathway responsible for the signal. All pathways originate in the ground state as we assume the low temperature (T) limit such that one vibrational quantum is much greater than $K_B T$, where K_B is the Boltzmann constant.

The two subscript values $(\mathsf{m_1}, \mathsf{m_2})$ denote the vibrational part of the vibronic state that is involved with the first two respective light–matter interactions. For example, in the pathway $\mathsf{VI}^{\mathsf{ij}}_{\mathsf{i,j}}$, $\boldsymbol{k}_1$ induces a change in vibrational quanta of mode i and $\boldsymbol{k}_2$ induces a change in vibrational quanta of mode j. Similarly, the superscript (ij) indicates the vibrational part of the vibronic state accessed by $\boldsymbol{k}_3$. When $\mathsf{m_1}$, $\mathsf{m_2}$, or $\mathsf{m_3}$ are equal to zero, this indicates that the light–matter interaction has brought the system to the lowest energy eigenstate (e.g., $|g;00\rangle$ or $|e;0'0'\rangle$). Importantly, this labeling scheme is generalizable to both techniques with a few exceptions detailed below. It applies to both the 2D EV and 2D VE transition pathways because the electronic part of the vibronic eigenstates is not directly specified, but rather inferred from whichever spectroscopy is being discussed. For comparison, the double-sided Feynman diagrams for pathways $\mathsf{VI}^{\mathsf{ij}}_{\mathsf{i,j}}$ are found in Fig. 2.3 for 2D EV spectroscopy and Fig. 2.4 for 2D VE spectroscopy. The main differences are that the τ_2 coherences occur in the electronically excited state for 2D EV ($|e;1'0'\rangle\langle e;0'1'|$) and the ground state for 2D VE ($|g;10\rangle\langle g;01|$), and that the τ_3 coherence period captures a purely excited state vibrational coherence in 2D EV spectroscopy ($|e;1'1'\rangle\langle e;0'1'|$) while the τ_3 coherence in 2D VE spectroscopy includes the two electronic states ($|e;1'1'\rangle\langle g;01|$). It should be noted that for systems including more than one excited electronic state, 2D EV spectroscopy is also sensitive to coherences involving different electronic states. [38]

Pathway numbers I-V are simple variations of previous pathway descriptions, [40] expanded to include possible interactions with multiple modes in the cases of pathways III and V. Pathways I and II are GSBs and ESAs that have $\mu^{0,0'}$ electronic transitions, respectively; all other pathway numbers have different electronic transitions, either greater or lesser in

energy than $\hbar\omega_{eg}$. Pathways III and IV are GSBs and ESAs that access higher-lying vibrational levels in $|e\rangle$, respectively. Notably, the two spectroscopies differ in the definition of pathways V. The 2D EV transition pathways include excited-state stimulated emissions for pathways labeled as V; 2D VE transition pathways do not permit stimulated emissions, and so pathways V are ESAs with electronic transitions between states with smaller energy gaps than $\hbar\omega_{eg}$. Pathways VI are the ESAs which access the shared vibrational state $|e;1'1'\rangle$, either through a coherence or population in τ_2. Pathways VII only occur in 2D VE spectroscopy and are defined by the electronic transition driving a change of vibrational quanta in both modes ($\Delta_{\nu_i} = -\Delta_{\nu_j}$). In general, a τ_2 coherence is indicated by any pathway in which $\mathsf{m}_1 \neq \mathsf{m}_2 \neq 0$.

Since the electronic information is not directly included in the pathway labeling scheme, a few important labeling distinctions between 2D EV and 2D VE pathways should be noted. First, the set of allowed transitions in 2D EV spectroscopy includes the case where $\mathsf{m}_1 = \mathsf{m}_2 = 0$ whereas the 2D VE pathways are such that m_1 and m_2 can never both equal 0. As a result, all pathways in 2D VE spectroscopy are uniquely described by label subscripts and superscripts. However, knowledge of the path type N may be required to distinguish the 2D EV pathway. For example, any 2D VE pathway in which $\mathsf{m}_2 = 0$ denotes a GSB, while the 2D EV pathway $\mathsf{N}^{\mathsf{i}}_{0,0}$ would reference a GSB ($\mathsf{N} = \mathsf{I}$) or an ESA ($\mathsf{N} = \mathsf{II}$).

The principal aim of this chapter is to account for the signal amplitude arising from the directionality of the dipole moments by using polarization-selective light–matter interactions in these 2D vibronic spectroscopies. The nature of the signatures measureable in 2D vibronic spectra will be introduced in the remainder of this section. 2D vibronic orientational response and polarization-selectivity are then be fully addressed beginning in Sec. 2.4 after this groundwork has been established.

This pathway labelling scheme can result a single point of ambiguity when distinguishing between rephasing and non-rephasing pathways that are spectrally separated and which access a common vibrational state (e.g., $|e;0'0'\rangle$). The two pathways differ by the phase of the τ_1 coherence period since $\boldsymbol{k}_1$ is a bra-side interaction in the rephasing pathway and a ket-

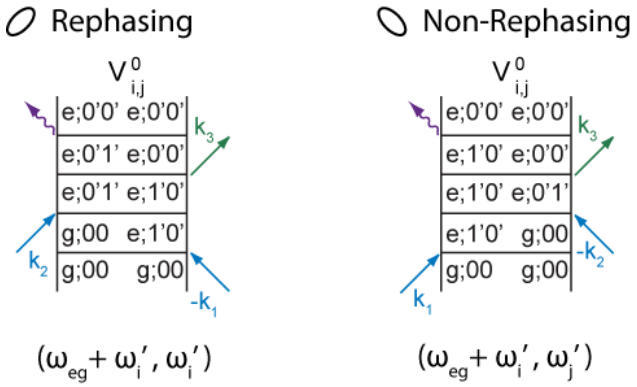

Figure 2.2: **Signal Positions for Separated R and NR Pathways.** The rephasing and non-rephasing pathways for 2D EV pathways $V^0_{i,j}$ are given, along with the 2D coordinates of the pathway position in (ω_1, ω_3).

side interaction in the non-rephasing pathway. This is compensated for in the τ_3 coherence in order to achieve the phase-matched condition and end in a population. As an example, the double-sided Feynman Diagrams for 2D EV pathways $V^0_{i,j}$ are given below. This is also the case for the 2D EV pathways contributing to pathways $V^0_{j,i}$. The same ambiguity arises in 2D VE pathways $VI^{ij}_{i,j}$, $VI^{ij}_{j,i}$, $VII^{i}_{j,i}$, $VII^{j}_{i,j}$, $V^0_{i,j}$, and $V^0_{j,i}$.

2.3.1 2D Electronic-Vibrational Signatures

A cartoon schematic of an absorptive 2D EV spectrum for a multimode molecular system is shown in Fig. 2.3. The pathways depicted are those which would arise from electronically resonant electric fields ($\boldsymbol{E}_1$ and $\boldsymbol{E}_2$) with center frequency ω_{eg} and bandwidth $2\omega_j$ to allow resonant transitions into higher lying vibrational states of both the vibrational coordinates Q_i and Q_j (where $\omega_i < \omega_j$). The vibrationally resonant field ($\boldsymbol{E}_3$) is assumed to have sufficient bandwidth to excite one-quantum transitions only and spans the vibrational transition frequencies of interest. The fully absorptive spectrum results from the sum of the rephasing (R, $\boldsymbol{k}_{sig} = -\boldsymbol{k}_1 + \boldsymbol{k}_2 + \boldsymbol{k}_3$) and non-rephasing (NR, $\boldsymbol{k}_{sig} = +\boldsymbol{k}_1 - \boldsymbol{k}_2 + \boldsymbol{k}_3$) signal pathways, which differ by the phase of the oscillation propagating during the τ_1 coherence period. When a R and NR signal pathway with the same (ω_1, ω_3) coordinates are equally

weighted and the dynamics can be described within the homogeneous limit, their sum results in a symmetric pathway without any phase twist, as shown in Fig. 2.3 (e.g., pathway $I^{j}_{0,0}$). Likewise, pathways arising from unequally weighted R and NR contributions will result in elongated features with either positive (R) or negative (NR) slopes.

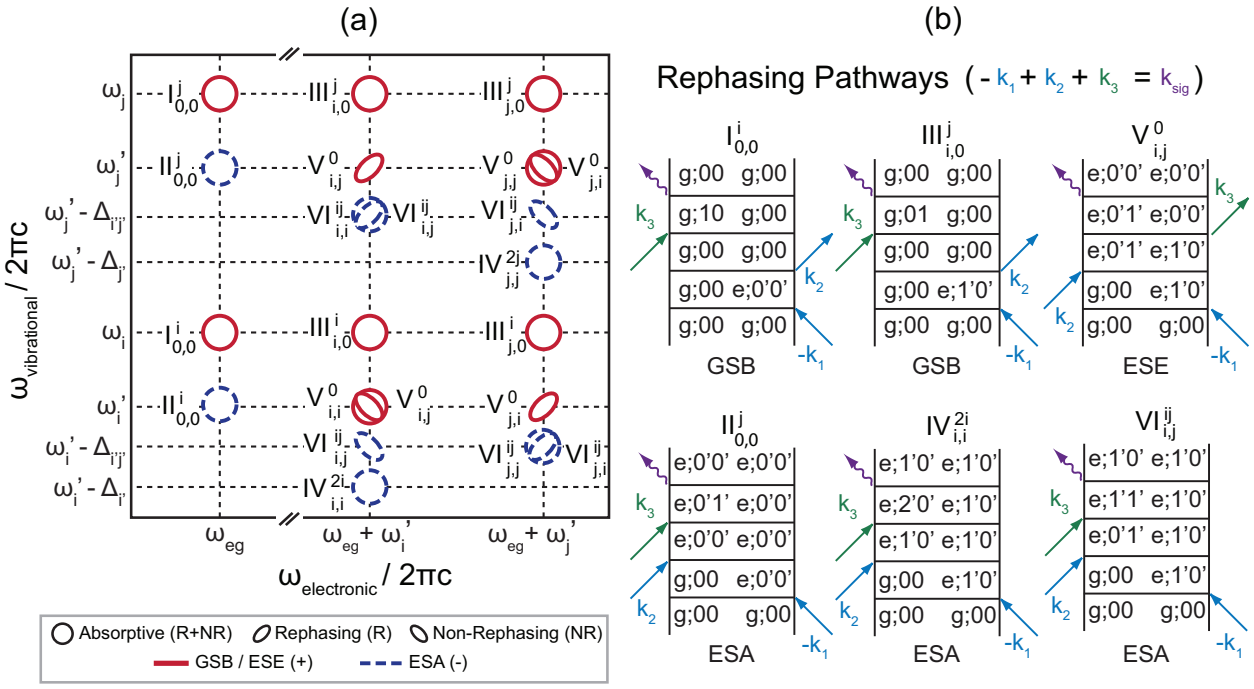

Figure 2.3: **Multimode 2D EV Signals Schematic.** (a) A schematic illustration of the dipole allowed 2D EV signals appearing for a two-mode vibronically coupled system and the energy level schematic described in Fig. 2.1. The absorptive pathways are symmetric and result from equally weighted rephasing (R) and non-rephasing (NR) pathways, generating signals at the same (ω_1, ω_3) coordinates; phase twisted pathways result from unequally weighted R and NR signals; red = positive signal [ground state bleaches (GSB) and excited state stimulated emissions (ESE)], blue = negative signal [excited state absorptions (ESA)]. The pathway numbering scheme is described in the main text. (b) Double-sided Feynman diagrams of selected 2D EV rephasing pathways. Electronic excitations ($\boldsymbol{k}_1$ and $\boldsymbol{k}_2$, blue); vibrational interactions ($\boldsymbol{k}_3$, green); emitted signal ($\boldsymbol{k}_{sig}$, purple).

The specific pathway positions correspond to the transition frequencies between vibronic eigenstates of the molecular system being studied. In general, a system Hamiltonian determines the nature of the eigenstates for the system of interest. In this discussion, the

vibronic system consists of two electronic states (the ground g and excited e states) and two coupled anharmonic vibrations whose frequencies and couplings change in the excited state. As shown in Fig. 2.3 (and Fig. 2.4 for 2D VE), the frequency separations of the pathways are expressed as a combination of system transition frequencies ω and energy shifts Δ (with appropriate indices, defined in Fig. 2.1) resulting from the system Hamiltonian. A 2D EV spectrum of a two-mode system includes two blocks of pathways I-V corresponding to each of the vibrational modes (e.g., the i^{th} mode pathways: $\mathsf{I}^{\mathsf{i}}_{0,0}; \mathsf{II}^{\mathsf{i}}_{0,0}; \mathsf{III}^{\mathsf{i}}_{\mathsf{i},0}; \mathsf{IV}^{\mathsf{i}}_{\mathsf{i},\mathsf{i}}; \mathsf{V}^{\mathsf{i}}_{\mathsf{i},\mathsf{i}}$). Each of these pathways have equal R and NR contributions which evolve as a decaying population during τ_2. The electronic excitations to $|e; 0'0'\rangle$ will appear at $\omega_1 = \omega_{eg}$ and the oscillator i excitations to $|e; 1'0'\rangle$ will have $\omega_1 = \omega_{eg} + \omega_{i'}$ coordinates; the oscillator j excitations follow similarly. New pathways also appear due to the system including two coupled vibrational modes from pathways utilizing the shared vibrational states $|g; 00\rangle$, $|e; 0'0'\rangle$ and $|e; 1'1'\rangle$. These pathways are distinguished by the first two light–matter interactions involving one vibration and the third light–matter interaction involving a different vibration, and they also have matched R and NR pathways (e.g., $\mathsf{III}^{\mathsf{i}}_{\mathsf{j},0}$). Additional pathways that excite different vibrations during the $\boldsymbol{k}_1$ and $\boldsymbol{k}_2$ interactions result in τ_2 coherences. The phase matching conditions necessarily separate the R and NR pathways spectrally (e.g., $\mathsf{V}^{\mathsf{0}}_{\mathsf{i},\mathsf{j}}; \mathsf{V}^{\mathsf{0}}_{\mathsf{j},\mathsf{i}}; \mathsf{VI}^{\mathsf{ij}}_{\mathsf{i},\mathsf{j}}; \mathsf{VI}^{\mathsf{ij}}_{\mathsf{j},\mathsf{i}}$) resulting in phase-twisted line shape (see Fig. 2.2 and 2.7).

The amplitudes of the 2D EV pathways are dependent on the ground state population of molecules, (i.e., in $|g; 00\rangle \langle g; 00|$, assumed to be all molecules in this work) and the strength of the four transition dipole moments accessed by the field-matter interactions during a vibronic transition pathway. The explicit treatment of the electronic and vibrational transition dipole moments in the interaction Hamiltonian incorporate the nuclear dependence of the electronic transition and the electrical anharmonicity of a vibration in an excited electronic state; a complete description of dipole moments within $H_{vibronic}$ can be found in Sec. 3.3.1 of Ch. 3 [63]. Not only are the signal amplitudes governed by the magnitude of the electronic and vibrational dipole moments, but the vectorial nature of the dipole moments in the molecular frame contributes amplitude that depends upon their relative orientation with

each other and with the incident electric fields.

Spectral lineshapes in the homogenous dephasing limit are based on the analytical expressions for energy gap correlation functions used in previous work [40] and follow the work of Sung and Silbey. [126] Here they have been expanded to include multimode effects and are reported in the Supplementary Material. Recent investigations into inhomogeneous line shapes and dynamics of 2D EV peaks may be found elsewhere. [118] Interestingly, the correlated (or anti-correlated) line shapes may occur in a multimode 2D EV spectrum even within the homogeneous limit as a result of spectrally separated R and NR pathways with respect to ω_3 in the 2D spectrum. For example, consider pathway $\mathsf{VI}^{\mathsf{ij}}_{\mathsf{i,j}}$ which has a positively correlated line shape when τ_2 is such that the $|e;0'1'\rangle\langle e;1'0'|$ coherence is constructively interfering. As discussed above, these contributions will necessarily oscillate at the $|\omega_{j'} - \omega_{i'}|$ difference frequency producing a dynamic center line slope across the bandwidth of this feature. The spectral resolution of the pathways with this dynamic is inherently linked to the magnitude of $\Delta_{i'j'}$ because the oppositely signed ESE, $\mathsf{V}^{\mathsf{0}}_{\mathsf{i,j}}$, will have the same oscillatory behavior and can cancel out part of the dynamic signal in pathway $\mathsf{VI}^{\mathsf{ij}}_{\mathsf{i,j}}$ if $\Delta_{i'j'}$ does not sufficiently separate these two pathways in the ω_3 dimension. In the next chapter, Sec. 3.2.3 connects the $\Delta_{i'j'}$ splitting to the Duschinsky mixing.

2.3.2 2D Vibrational-Electronic Signatures

A cartoon schematic of an absorptive 2D VE spectrum and corresponding Feynman pathways are shown in Fig. 2.4. The pathways depicted meet analogous criteria as those listed above for 2D EV. The 2D VE spectrum assumes the same spectral properties of the electronically- and vibrationally-resonant electric fields as described above for 2D EV. However, the temporal ordering of these electric fields are opposite in the 2D VE experiment, where $\boldsymbol{E}_1$ and $\boldsymbol{E}_2$ are vibrationally-resonant and $\boldsymbol{E}_3$ is electronically-resonant. The 2D VE schematic shows pathways associated with the vibronic eigenstates shown in Fig. 2.1 (a) and demonstrates the same organization of R and NR pathways; for example, pathway $\mathsf{V}^{\mathsf{0}}_{\mathsf{i,i}}$ is symmetric while pathways $\mathsf{V}^{\mathsf{0}}_{\mathsf{i,j}}$ have spectrally separated, positively (negatively) sloped R (NR) components.

The ω_1 pathway positions are determined by the first light–matter interaction, which resonantly excites a vibrational transition in oscillator i or j yielding pathways centered at $\omega_1 = \omega_i$ or ω_j. The probed ω_3 positions are determined by the frequencies of the final vibronic transitions. Hence, the ω_3 pathway positions in 2D VE spectroscopy contain the information regarding the vibrational structure of excited electronic states. Several pathways arise from the participation of multiple vibrational modes as shown in Fig. 2.4. Such pathways may be observed in the probe domain with ω_3 positions at different frequencies from ω_{eg}, as is the case for pathway $\mathsf{III}^{\mathsf{j}}_{\mathsf{i},0}$. Another set of pathways, $\mathsf{VI}^{\mathsf{ij}}_{\mathsf{i},\mathsf{j}}$ and $\mathsf{VII}^{\mathsf{i}}_{\mathsf{i},\mathsf{j}}$ result from the two excitation pulses creating a vibrational coherence. With exception to pathways $\mathsf{IV}^{\mathsf{2i}}_{\mathsf{i},\mathsf{i}}$ and $\mathsf{IV}^{\mathsf{2j}}_{\mathsf{j},\mathsf{j}}$, the ESA features in 2D VE spectra appear in blocks of six pathways. For example, the lower energy ESA manifold consists of two pairs of R ($\mathsf{V}^{\mathsf{0}}_{\mathsf{i},\mathsf{j}}, \mathsf{V}^{\mathsf{0}}_{\mathsf{j},\mathsf{i}}$) and NR ($\mathsf{V}^{\mathsf{0}}_{\mathsf{i},\mathsf{j}}, \mathsf{V}^{\mathsf{0}}_{\mathsf{j},\mathsf{i}}$) pathways at opposite sides of the box and a pair of absorptive pathways ($\mathsf{V}^{\mathsf{0}}_{\mathsf{i},\mathsf{i}}, \mathsf{V}^{\mathsf{0}}_{\mathsf{j},\mathsf{j}}$) at two corners of the box. We note that the R pathways and the fully absorptive peaks are spectrally overlapping. The ESA blocks are identifiable by having frequency separations of $|\omega_j - \omega_i|$ between peaks in both the ω_1 and ω_3 dimensions. This structure arises because the τ_2 coherence pathways access an identical set of vibronic states that either differ by the interaction order of $\boldsymbol{k}_1$ and $\boldsymbol{k}_2$ with respect to the vibrations, or by the phase of the τ_1 coherence. Each of the R and NR coherence pathway pairs (such as $\mathsf{V}^{\mathsf{0}}_{\mathsf{i},\mathsf{j}}$ (R and NR)) interact with the same four transition dipoles, exhibit identical time-dependent behavior during τ_2, and share the same orientational response functions.

The faster dephasing times of condensed phase electronic transitions result in 2D VE spectral features with typically broad line shapes with respect to ω_3, yielding significant overlapping of oppositely-signed features and a unique sensitivity to vibronic coupling parameters. For example, the 2D VE spectra are sensitive measurements of the Franck–Condon factors and Huang–Rhys parameters for the system of interest as we discuss in Sec. 3.2.2 and 3.5.3 of Ch. 3, Specifically in Eqs. 3.6 and 3.15 and Figs. 3.2, 3.3, and 3.7. This is especially true when the features of interest have electronic transition frequencies of $\omega_3 \geq \omega_{eg}$ because these regions of the 2D VE spectrum contain GSB features and ESA features of similar

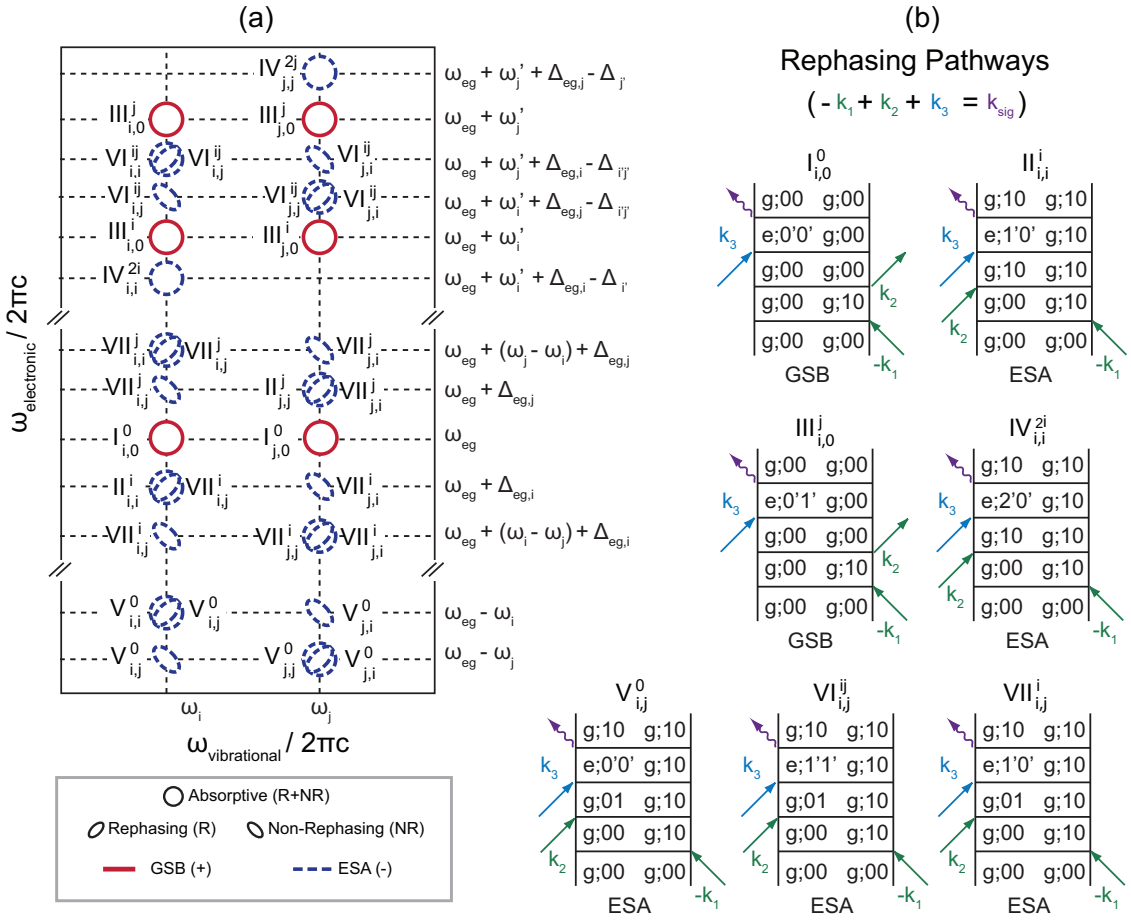

Figure 2.4: **Multimode 2D VE Signals Schematic.** (a) A schematic illustration of the dipole allowed 2D VE signals appearing for a two-mode vibronically coupled system and the energy level schematic given in Fig. 2.1. The absorptive pathways are symmetric and result from equally weighted rephasing (R) and non-rephasing (NR) pathways, generating signals at the same (ω_1, ω_3) coordinates; phase twisted pathways result from unequally weighted R and NR signals; red = positive signal [ground state bleaches (GSB)], blue = negative signal [excited state absorptions (ESA)]. The pathway numbering scheme is described in the main text. (b) Double-sided Feynman diagrams of selected 2D VE rephasing pathways. Vibrational excitations ($\boldsymbol{k}_1$ and $\boldsymbol{k}_2$, green); electronic interactions ($\boldsymbol{k}_3$, blue); emitted signal ($\boldsymbol{k}_{sig}$, purple).

transition pathways which overlap significantly. The sign of the observed signal immediately indicates which of the Franck–Condon factors has greater magnitude. More generally, the 2D VE transition pathways access a greater variety of vibronic transitions than the 2D EV

experiment because of the initial vibrational excitation used in the 2D VE technique. Hence, 2D VE can sample more of the coordinate space for the projection between the ground and excited electronic potentials.

The 2D VE line shapes also encode the same electronic-state-dependent vibrational dephasing as 2D EV spectroscopy does, and the same considerations discussed above apply here to the 2D VE discussion. However, the larger combination of vibronic transitions allowable in the 2D VE pulse sequence affords a larger sampling of energy gap correlation functions for a given molecular system. In principle, the 2D VE line shapes contain a large sampling of frequency fluctuations between ground and excited vibrational levels in both the ground and excited electronic states. For example, the 2D line shape of pathway $\mathsf{VI}^{\mathsf{ij}}_{\mathsf{i,i}}$ is determined by the combination of auto-correlations and cross-correlations between many vibronic eigenstates: the zero-point energies of the ground and excited electronic states ($\Gamma_{eg,eg}$), the ratio of the electronic-state-dependent vibrational fluctuations for both vibrations i and j (Γ_{ν_i,ν_i}, Γ_{ν_j,ν_j}, and the respective λ_k proportionality constants), and the vibronic frequency fluctuations relating the electronic energy gap and the vibrational energy gaps in both electronic states (Γ_{eg,ν_i} and Γ_{eg,ν_j}). Full lists of analytic dephasing functions for 2D EV and 2D VE spectroscopies are given in Appendix C.

2.4 Nonlinear Orientational Response for 2D Vibronic Spectroscopies

From the initially isotropic orientational distribution of molecules in an ensemble, each linearly polarized electric field in the experimental pulse sequence selects a subset of molecules from the evolving orientational distribution. Given a combination of three incident pulses with fixed linear polarization, the orientational response for a specific transition pathway depends upon the directionality of the transition dipole moments in a fixed molecular frame. In our description of these 2D vibronic spectroscopies, we explicitly include both the electronic and vibrational coordinates in the set of transition dipole moments accessed experimentally (See Sec. 3.3 and Fig. 3.3 in Ch. 3.) Thus, the orientational response for a particular vibronic transition pathway is calculated by defining the orientation of the four time-ordered

vibronic transition dipole operators within the molecular frame and performing an orientational average to transform the motion of the molecular frame into the laboratory frame.

The orientational response function, $\left(Y_\alpha\right)^{a,b,c,d}_{IJKL}$, can be described within the framework of orientational diffusion. The orientational response is represented as the product of the directional cosines for all four molecular dipole moments ($\hat{\mu}$) and the molecular frame basis vectors ($\hat{i},\ \hat{j},\ \hat{k},\ \hat{l}$) which is scaled by an orientational average ($\widetilde{Y}^{ijkl}_{IJKL}$). The solutions to orientational diffusion equations and the accompanying conditional probability functions are well known, [85,128,129] and the resulting analytical expressions are given in Eqs. 2.4a-2.4d for use in calculating $Y^{abcd}_{IJKL}\left(\tau_3,\tau_2,\tau_1\right)$. These factors transform the molecular orientational diffusion into the laboratory frame.

For a specific transition pathway involving four vibronic eigenstates (a,b,c,d), the orientational response is determined by expressing the orientation of the four involved transition dipole moments in a fixed molecular frame, projecting each transition dipole moment onto the molecular frame basis vectors $[\hat{i},\hat{j},\hat{k},\hat{l}\in\hat{x},\hat{y},\hat{z}]$ and then selecting the set of laboratory frame polarization directions of the incident electric fields $(\hat{I},\hat{J},\hat{K},\hat{L}\in\hat{X},\hat{Y},\hat{Z})$ over which to orientationally average.

$$\left(Y_1\right)^{a,b,c,d}_{IJKL}\left(\tau_3,\tau_2,\tau_1\right)=\sum_{ijkl}\widetilde{Y}^{ijkl}_{IJKL}\left(\tau_3,\tau_2,\tau_1\right)\left[\hat{\mu}^{c,d}\cdot\hat{i}\right]\left[\hat{\mu}^{b,c}\cdot\hat{j}\right]\left[\hat{\mu}^{a,b}\cdot\hat{k}\right]\left[\hat{\mu}^{d,a}\cdot\hat{l}\right] \tag{2.4a}$$

$$\left(Y_2\right)^{a,b,c,d}_{IJKL}\left(\tau_3,\tau_2,\tau_1\right)=\sum_{ijkl}\widetilde{Y}^{ijkl}_{IJKL}\left(\tau_3,\tau_2,\tau_1\right)\left[\hat{\mu}^{c,b}\cdot\hat{i}\right]\left[\hat{\mu}^{d,c}\cdot\hat{j}\right]\left[\hat{\mu}^{b,a}\cdot\hat{k}\right]\left[\hat{\mu}^{a,d}\cdot\hat{l}\right] \tag{2.4b}$$

$$\left(Y_3\right)^{a,b,c,d}_{IJKL}\left(\tau_3,\tau_2,\tau_1\right)=\sum_{ijkl}\widetilde{Y}^{ijkl}_{IJKL}\left(\tau_3,\tau_2,\tau_1\right)\left[\hat{\mu}^{c,b}\cdot\hat{i}\right]\left[\hat{\mu}^{b,a}\cdot\hat{j}\right]\left[\hat{\mu}^{d,c}\cdot\hat{k}\right]\left[\hat{\mu}^{a,d}\cdot\hat{l}\right] \tag{2.4c}$$

$$\left(Y_4\right)^{a,b,c,d}_{IJKL}\left(\tau_3,\tau_2,\tau_1\right)=\sum_{ijkl}\widetilde{Y}^{ijkl}_{IJKL}\left(\tau_3,\tau_2,\tau_1\right)\left[\hat{\mu}^{a,b}\cdot\hat{i}\right]\left[\hat{\mu}^{b,c}\cdot\hat{j}\right]\left[\hat{\mu}^{c,d}\cdot\hat{k}\right]\left[\hat{\mu}^{d,a}\cdot\hat{l}\right] \tag{2.4d}$$

The Eqs. 2.4a-2.4d differ only by the ordering of vibronic eigenstates interacting with the electric fields, as labeled by α. Typically, orientational diffusion timescales are much longer than the vibronic dynamics of interest, so the orientational parts of the response function can be simplified even further [24, 98] to facilitate calculations of the orientational response measurable with 2D EV and 2D VE spectroscopies.

By assuming that orientational dynamics are sufficiently slow with respect to τ_1, τ_2, and τ_3, we remove the time dependence of the orientational response, written in the examples given in Eqs. 2.12 and 2.13. Further discussion of anisotropic diffusion [129] non-diffusive orientational dynamics, [130] the scrambling of the orientational response due to vibronic coherence and population transfer processes, [15] and orientational relaxation occurring on the timescale of vibronic dynamics can be found elsewhere. [24, 98, 131]

2.5 Anisotropy

The polarization-selective signals for specific 2D EV and 2D VE pathways may be calculated using Eqn. 2.1, where the multimode vibronic response, $R_{\alpha}^{abcd}(\tau_3, \tau_2, \tau_1)$, is determined by the physics of the system of interest, and the orientational response, $\left(Y_{\alpha}\right)_{IJKL}^{a,b,c,d}$, is detailed in Sec. 2.4 above. The 2D signals for parallel and perpendicular polarized experiments on the multimode vibronic systems can now be calculated directly, as well as any other arbitrary polarization combination. In this section, generalized analytical relationships are given for the orientational responses with varying degrees of angular dependence. The orientational responses generally can include angular dependence of one, two, and four angles. In contrast to 2D IR spectroscopy and other degenerate third-order techniques, 2D EV and 2D VE spectroscopies do not include transition pathways involving four interactions with the same transition dipole moment. Therefore, each 2D EV and 2D VE pathway must possess angular dependence on at least one angle between electronic and vibrational dipole moments, albeit $\theta = 0^o$, corresponding to parallel with $\boldsymbol{\mu}^{0,0'}$, is fully allowed. Using these expressions, specific polarization-selective signals can be simulated and meaningful parameters such as the depolarization ratio and the anisotropy parameter can be derived.

The general expression for the orientational response functions for parallel ($\boldsymbol{Y}_{ZZZZ}(\theta_1)$) and perpendicular ($\boldsymbol{Y}_{YYZZ}(\theta_1)$) polarized signals of 2D vibronic signal with a single angle dependence are given in Eqns. 2.5 and 2.6.That is, $\boldsymbol{Y}_{YYZZ}$ represents the result for Eqs. 2.4 for which the laboratory frame polarization of electric fields $[\hat{I}, \hat{J}, \hat{K}, \hat{L}] = [\hat{Y}, \hat{Y}, \hat{Z}, \hat{Z}]$.

$$\boldsymbol{Y}_{ZZZZ}(\theta_1) = \frac{1}{15}\big[2\cos^2(\theta_1) + 1\big] \tag{2.5}$$

$$\boldsymbol{Y}_{YYZZ}(\theta_1) = \frac{1}{15}\big[2 - \cos^2(\theta_1)\big] \tag{2.6}$$

Signals that depend on one angle will result from transition pathways where interactions of $\boldsymbol{k}_1$ and $\boldsymbol{k}_2$ access the same transition dipole moment, which is separate from the same transition dipole moment accessed by the interactions of $\boldsymbol{k}_3$ and $\boldsymbol{k}_{sig}$. Thus, the angle between the dipole moments accessed by $\boldsymbol{k}_2$ and $\boldsymbol{k}_3$ is the one on which the orientational response depends and it is distinguished by the vibrational character. Since it is a requirement that $\boldsymbol{k}_1$ and $\boldsymbol{k}_2$ interact with the same dipole moment for pathways with single angular dependence, these transition pathways may be GSBs or ESAs (or ESEs in 2D EV only) which evolve in a population during the τ_2 evolution time period. In 2D EV spectroscopy, this is the angle between a vibrational dipole moment in either $|g\rangle$ or $|e\rangle$ and the electronic transition dipole moment. However, in 2D VE spectroscopy this will only be the angle between a vibrational dipole moment in $|g\rangle$ and the electronic transition dipole. While the electronic transition dipole moments may explicitly include nuclear coordinate dependence in $|e\rangle$ (e.g., through linear vibronic coupling and non-Condon effects), 2D VE spectroscopy is only directly resonant with vibrational transitions in the ground electronic state through $\boldsymbol{k}_1$ and $\boldsymbol{k}_2$.

The transition pathways which depend on two dipole angles have the same requirement for $\boldsymbol{k}_1$ and $\boldsymbol{k}_2$ as the single angle pathways but the electronic transition must be different in energy than $\hbar\omega_{eg}$. In the case of 2D EV, this occurs when a vibrationally "hot" state in $|e\rangle$ is excited and for 2D VE when an electronic excitation from a vibrational "hot" state in $|g\rangle$ occurs. The dependence on a second angle arises when the electronic transition has a dipole moment with a different vibrational character or directionality than the $|g;00\rangle \leftrightarrow |e;0'0'\rangle$

transition dipole. When this is not the case, the analytical form of the angular dependence for such pathways reduces to the expression for a single angle. The general expressions for the polarization-selective orientational response for signals with two-angle dependencies are shown in Eqs. 2.7 and 2.8.

$$\boldsymbol{Y}_{ZZZZ}(\theta_1,\theta_2) = \frac{1}{15}\big[\cos(2(\theta_1-\theta_2))+2\big] \tag{2.7}$$

$$\boldsymbol{Y}_{YYZZ}(\theta_1,\theta_2) = \frac{1}{30}\big[3-\cos(2(\theta_1-\theta_2))\big] \tag{2.8}$$

Orientational response functions which depend on four separate dipole moment angles arise if each light–matter interaction involves a different transition dipole moment. Necessarily, these pathways produce a coherent superposition that propagates during the τ_2 evolution time. Within the multimode molecular system considered here, the electronic transition must also change the vibrational quantum numbers (i.e., $\boldsymbol{\mu}^{0,i'}$ or $\boldsymbol{\mu}^{0,j'}$) for the pathway to carry angular dependence on four dipole angles. However, a similar angular dependence may also arise in systems composed of multiple electronic excited states which is not discussed here. The orientational response functions for pathways with four-angle dependency are:

$$\begin{aligned}\boldsymbol{Y}_{ZZZZ}(\theta_1,\theta_2,\theta_3,\theta_4) = \frac{1}{15}\big[&\cos(\theta_1+\theta_2-\theta_3-\theta_4)\\ &+\cos(\theta_1-\theta_2+\theta_3-\theta_4)\\ &+\cos(\theta_1-\theta_2-\theta_3+\theta_4)\big]\end{aligned} \tag{2.9}$$

$$\begin{aligned}\boldsymbol{Y}_{YYZZ}(\theta_1,\theta_2,\theta_3,\theta_4) = \frac{1}{20}\big[&\cos(\theta_1-\theta_2+\theta_3-\theta_4)\\ &+\cos(\theta_1-\theta_2-\theta_3+\theta_4)\big]\\ &-\frac{1}{30}\big[\cos(\theta_1+\theta_2-\theta_3-\theta_4)\big]\end{aligned} \tag{2.10}$$

While a pathway involving four distinct dipole moments will have an orientational response dependent upon four angles, the analytical form of this dependence may be simplified if some of the dipole moments are parallel. Algebraically, Eqs. 2.9 and 2.10 simplify to Eqs. 2.7 and 2.8, respectively, when $\theta_1 = \theta_2$ and $\theta_3 = \theta_4$. Likewise, the orientational response is simplified to Eqs. 2.5 and 2.6 if $\theta_2 = 0$. The angular dependence for each 2D EV and 2D VE pathway as defined for the multimode vibronic system of interest considered here is given in Appendix D.

Signals collected with particular polarization dependence can be used to extract meaningful parameters such as depolarization ratios and anisotropies. While the measured signals will be dependent on both the orientational response and the vibronic response, the following discussion focuses only on the orientational response. In the pump-probe experimental geometry, the depolarization ratio for any 2D pathway can be obtained from the signals which depend on the appropriate expressions for $\boldsymbol{Y}_{ZZZZ}$ and $\boldsymbol{Y}_{YYZZ}$ in Eqs. 2.5 - 2.10 using the relation $\frac{\boldsymbol{Y}_{YYZZ}}{\boldsymbol{Y}_{ZZZZ}}$. The anisotropy parameter, $r(\theta)$, can be derived from the ratio of the anisotropic response ($\boldsymbol{Y}_{ZZZZ} - \boldsymbol{Y}_{YYZZ}$) and the isotropic response ($\boldsymbol{Y}_{ZZZZ} + 2\boldsymbol{Y}_{YYZZ}$). For pathways carrying single angle dependency, the familiar range of anisotropies of $r = 0.4$ for parallel transition dipole moments and $r = -0.2$ for orthogonal dipole moments is obtained,

$$\begin{aligned} r(\theta) &= \frac{\boldsymbol{Y}_{ZZZZ} - \boldsymbol{Y}_{YYZZ}}{\boldsymbol{Y}_{ZZZZ} + 2\boldsymbol{Y}_{YYZZ}} \\ &= \frac{1}{5}(3\cos^2(\theta) - 1). \end{aligned} \tag{2.11}$$

As described in Eqn. 2.11, the angle between two different dipole moments can be extracted directly from the anisotropy. In general, the pathways that depend on a single angle are the most directly quantifiable. The correct determination of dipole angles for pathways with two- and four-angle dependencies may require a systems-of-equations approach where one or more of these angles are first determined from other pathways with fewer angle dependency or informed by other experiments. It is also important to note that a direct and accurate determination of a dipole angle from experimental spectra relies upon the pathway being fairly

isolated from other spectral features in order to exclude amplitude from different transition dipoles in the calculation of $r(\theta)$. As discussed below in Sec. 2.6.3, such a measurement of $r(\theta)$ is most direct when the orientational response is truly dependent on *one* angle since the magnitude of the isotropic response ($\boldsymbol{Y}_{ZZZZ} + 2\boldsymbol{Y}_{YYZZ}$) is not angularly independent when there exists non-zero angles between the first two dipole moments and the last two dipole moments in the transition pathway. In particular, these type of considerations matter when dealing with mismatched R and NR pathways, which should display τ_2-dependent coherences. We will discuss below and in Ch. 3, [63] how polarization-selectivity can be used creatively to enhance specific features in convoluted spectra.

2.6 Discussion

Using the orientational response described above, polarization-selective features of both techniques are calculated to better understand the molecular-level information that is obtainable from 2D EV and 2D VE experiments. It is assumed in this discussion that the signal characteristics from the vibronic part of the molecular response ($R^{a,b,c,d}$) are completely determined and are effectively unity in magnitude so that the analysis of the simulated spectral features is related directly to the orientational response, Y^{abcd}_{IJKL}. While separating these contributions can prove challenging in practice, it is achievable. As was shown in a recent polarization-selective 2D VE study of a cyanide-bridged mixed-valence transition metal complex, both the vibronic coupling strengths and the relative orientations between a metal-to-metal charge transfer dipole moment and the dipole moments of three vibrational coordinates were determined. [37] It is important to underscore the assumption that allows us to emphasize the orientational response because, in reality, the pathway amplitudes and amplitude ratios also depend upon the scalar part of the dipole moments which include contributions from excited state displacement (linear vibronic coupling) effects, non-Condon effects, and mechanical anharmonicity effects. However, considering only the orientational response will help to identify the orientational versus vibronic origins of signals measured experimentally. We note that, in principle, there is vibrational character in the $|g;00\rangle$ and $|e;0'0'\rangle$ states due

to the vibrational zero-point energies but our analysis assumes this to be the baseline orientation for the vibronic eigenstates and that the relative orientations between these states and those containing greater vibrational quanta is the quantity of interest. This discussion builds a foundation for extracting and separating orientational and vibronic contributions to the total molecular response in 2D EV and 2D VE spectroscopy. In chapter 3, we discuss how non-Condon effects and Duschinsky mixing impact the extracted angles between vibronic transition dipoles in 2D EV and 2D VE spectra.

2.6.1 Molecular Insight from 2D Vibronic Anisotropy Analysis

In this section, a few simple examples are given for how anisotropy can be used to extract structural information relating various dipole moments in 2D vibronic spectra. First, the orientational responses for the fully absorptive (i.e., R + NR) 2D EV pathway $\mathsf{II}^{\mathsf{i}}_{0,0}$ are calculated where $a = |g;00\rangle$, $b = |e;0'0'\rangle$, $c = |e;1'0'\rangle$ and $d = |e;0'0'\rangle$, and $\alpha = 1$ specifies the Liouville pathway for this vibronic transition.

$$\begin{aligned}(Y_1)_{ZZZZ} &= \left[\widetilde{Y}^{zzzz}_{ZZZZ}(\cos^2(\theta^{0',i'}_{0,0'})) + \widetilde{Y}^{yyzz}_{ZZZZ}(\sin^2(\theta^{0',i'}_{0,0'}))\right]_R \\ &+ \left[\widetilde{Y}^{zzzz}_{ZZZZ}(\cos^2(\theta^{0',i'}_{0,0'})) + \widetilde{Y}^{yyzz}_{ZZZZ}(\sin^2(\theta^{0',i'}_{0,0'}))\right]_{NR} \\ &= \frac{2}{15}(2\cos^2(\theta^{0',i'}_{0,0'}) + 1).\end{aligned} \tag{2.12}$$

$$\begin{aligned}(Y_1)_{YYZZ} &= \left[\widetilde{Y}^{zzzz}_{YYZZ}(\cos^2(\theta^{0',i'}_{0,0'})) + \widetilde{Y}^{yyzz}_{YYZZ}(\sin^2(\theta^{0',i'}_{0,0'}))\right]_R \\ &+ \left[\widetilde{Y}^{zzzz}_{YYZZ}(\cos^2(\theta^{0',i'}_{0,0'})) + \widetilde{Y}^{yyzz}_{YYZZ}(\sin^2(\theta^{0',i'}_{0,0'}))\right]_{NR} \\ &= \frac{2}{15}(1 + \sin^2(\theta^{0',i'}_{0,0'})).\end{aligned} \tag{2.13}$$

The anisotropy of pathway $\mathsf{II}^{\mathsf{i}}_{0,0}$ is found using Eqn. 2.11, yielding the expected relationship for a pathway with an orientational response dependent upon a single angle. For a spectrally isolated pathway $\mathsf{II}^{\mathsf{i}}_{0,0}$, the 2D EV anisotropy directly reports on the angle between the excited state vibrational mode i and the fundamental electronic transition, $\boldsymbol{\mu}^{0,0'}$. Similarly,

pathway $\mathrm{II}^{j}_{0,0}$ has the same form of angular dependence and anisotropy relations, as do the corresponding GSB pathways, $\mathrm{I}^{i}_{0,0}$ and $\mathrm{I}^{j}_{0,0}$.

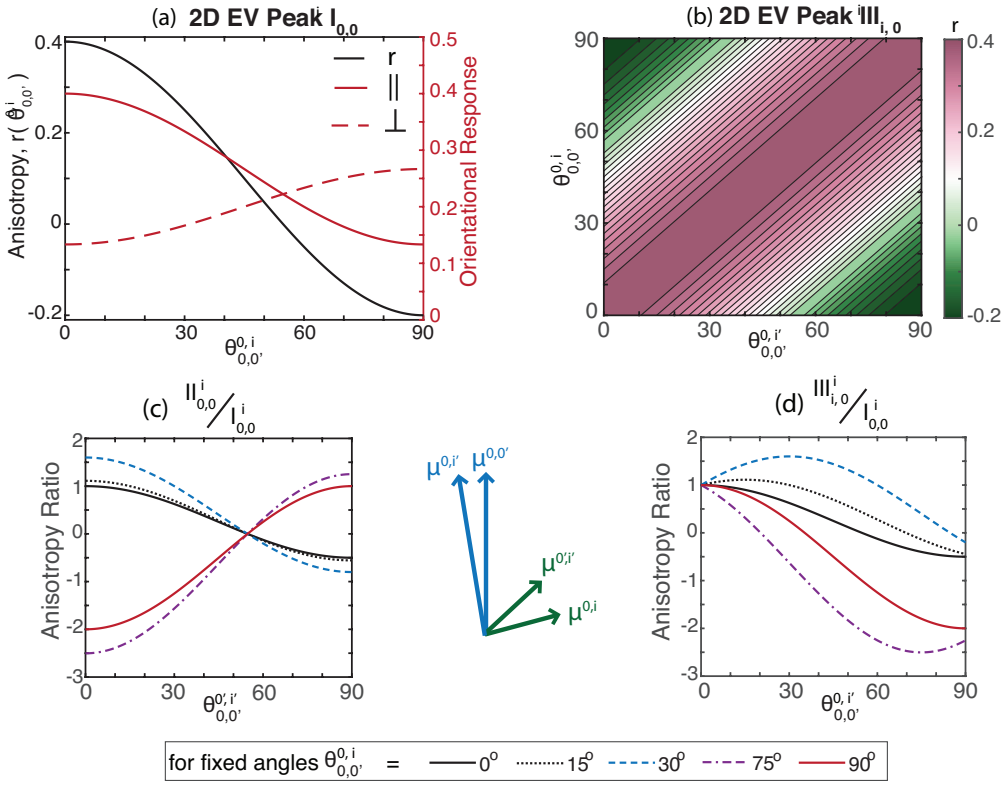

Figure 2.5: **Systematic Anisotropy Analysis using Multiple 2D Pathways.** (a) The orientational response and anisotropy for 2D EV pathway $\mathrm{I}^{i}_{0,0}$. (b) The anisotropy for 2D EV pathway $\mathrm{III}^{i}_{i,0}$ depends on two angles: the electronic dipole moment $\hat{\mu}^{0,i'}$ with angle $\theta^{0,i'}_{0,0'}$ and the vibrational dipole moment $\hat{\mu}^{0,i}_{0,0'}$ with angle $\theta^{0,i}_{0,0'}$ (contours given with five percent intervals). The anisotropy ratios of pathways with different dipole moments are plotted in (c) and (d) to illustrate how various angles may be extracted by considering multiple pathways in the 2D EV spectrum. For a determined angle $\theta^{0,i}_{0,0'}$, the relative angles between the ground and excited state vibrational mode can be obtained (as in (c)) and the relative angles between the electronic dipole moments $\hat{\mu}^{0,0'}$ and $\hat{\mu}^{0,i'}$ can be determined (as in (d)). Note that these figures and the discussion assumes the vibronic response is effectively unity such that the relative amplitudes are governed only by orientational response.

The anisotropy relations described above can be used systematically on different 2D EV and 2D VE pathways with different angle dependencies to obtain further insight into the

molecular frame. For example, consider the 2D EV pathways $\mathsf{I}^{\mathsf{i}}_{0,0}$, $\mathsf{II}^{\mathsf{i}}_{0,0}$, and $\mathsf{III}^{\mathsf{i}}_{\mathsf{i},0}$. The Y_{ZZZZ}, Y_{YYZZ}, and $r(\theta^{0,i}_{0,0'})$ are plotted in Fig. 2.5 (a) for 2D EV pathway $\mathsf{I}^{\mathsf{i}}_{0,0}$. The parallel and perpendicular responses are equal at the magic angle, 54.7^o, and the anisotropy parameter ranges from 0.4 when $\hat{\mu}^{0,i} \parallel \hat{\mu}^{0,0'}$ to -0.2 when $\hat{\mu}^{0,i} \perp \hat{\mu}^{0,0'}$. The unit vectors (i.e., $\hat{\mu}$) are specifically used in discussing the values of $r(\theta)$ to emphasize the assumptions made in the analysis and outlined above. We note that the magnitudes of the dipole moments may still distort $r(\theta)$ from this range of values as a result of non-Condon effects and Duschinsky mixing; this is thoroughly outlined in Secs. 3.3-3.5 of the second chapter in this series (3). From the experimental observable, $r(\theta^{0,i}_{0,0'})$, the angle between the ground state vibrational dipole moment of oscillator i ($\hat{\mu}^{0,i}$) and the fundamental electronic transition dipole moment ($\hat{\mu}^{0,0'}$) is determined. With $\theta^{0,i}_{0,0'}$ defined, the ground state vibrational transition dipole moment can be used as a molecular-frame point of reference for determining the relative orientation of other dipole moments. For example, the existence of a nonzero angle between $\hat{\mu}^{0,0'}$ and $\hat{\mu}^{0,i'}$ ($\theta^{0,i'}_{0,0'} \neq 0$) provides evidence that a vibrational coordinate dependence of the electronic transition is present in the molecular system under investigation. Since the GSB $\mathsf{III}^{\mathsf{i}}_{\mathsf{i},0}$ depends on both $\theta^{0,i}_{0,0'}$ and $\theta^{0,i'}_{0,0'}$, this pathway can be used to determine $\theta^{0,i'}_{0,0'}$. The two-angle dependent anisotropy for $\mathsf{III}^{\mathsf{i}}_{\mathsf{i},0}$ is plotted in Fig. 2.5 (b). Using the determined value of $\theta^{0,i}_{0,0'}$ from pathway $\mathsf{I}^{\mathsf{i}}_{0,0}$, this two-dimensional anisotropy is reduced to only a dependence on $\theta^{0,i'}_{0,0'}$ which can then be determined from the empirical anisotropy of pathway $\mathsf{III}^{\mathsf{i}}_{\mathsf{i},0}$.

Another way of quantifying angles between various dipole moments is through the ratio of anisotropies measured for different pathways. As shown in 2.5 (c) and (d), the anisotropy ratios between pathways which contain at least one common transition dipole moment can be used to identify the difference between the two pathways' angular dependence. The 2D EV GSB pathway $\mathsf{I}^{\mathsf{i}}_{0,0}$ and ESA pathway $\mathsf{II}^{\mathsf{i}}_{0,0}$ share the same electronic transition dipole moment, $\boldsymbol{\mu}^{0,0'}$; thus, these pathways can be used to determine the difference in the vibrational transition dipole moments involved in these transitions. Figure 2.5 (c) plots the 2D EV anisotropy ratio ($\mathsf{II}^{\mathsf{i}}_{0,0}/\mathsf{I}^{\mathsf{i}}_{0,0}$) for various values of $\theta^{0,i}_{0,0'}$ which are determined by Fig. 2.5 (a). Anisotropy ratios differing from 1 indicate that the vibrational motion of oscillator i changes

direction upon electronic excitation. The excited state angle can be read directly from the plot in Fig. 2.5 (c). A similar relationship between pathways $\mathsf{I}^{\mathsf{i}}_{0,0}$ and $\mathsf{III}^{\mathsf{i}}_{\mathsf{i},0}$ exists, as implied by 2.5 (b) and the discussion above. The common dipole moment of these two pathways is $\boldsymbol{\mu}^{0,i}$ and they differ by their electronic transitions. Recasting the anisotropy relationships between these two GSB pathways as a ratio yields Fig. 2.5 (d), where the nuclear coordinate dependence of the $\hat{\mu}^{0,i'}$ is readily identified through an anisotropy ratio differing from 1. While these examples have used specific 2D EV pathways, the analytical approach is generalizeable to any set of 2D vibronic pathways with the same relationships of angular dependence described above. This approach can also be extended to narrow down the angular dependence of pathways that depend on four angles.

Anisotropy analyses using both 2D EV and 2D VE features naturally increases the set of dipole moments that can be investigated when studying a molecular system. While the anisotropy ratios for the 2D EV pathways in Fig. 2.5 (d) use the GSBs to explore the presence of non-Condon effects, the analogous comparison in 2D VE spectroscopy lends a different perspective on non-Condon effects through the orientational response. In particular, the 2D VE pathway $\mathsf{II}^{\mathsf{i}}_{\mathsf{i},\mathsf{i}}$ uses the electronic dipole moment $\boldsymbol{\mu}^{i,i'}$ which is inaccessible to 2D EV spectroscopy. Since the 2D VE pathway $\mathsf{I}^{\mathsf{0}}_{\mathsf{i},0}$ accesses $\boldsymbol{\mu}^{0,0'}$, the anisotropy ratio of these two pathways is directly sensitive to how vibrational mixing in either electronic state affects the projection of the ground state vibrational coordinate onto the electronically excited state potential. In cases where spectral overlap in 2D VE features inhibits direct anisotropic analysis, the use of an analogous 2D EV GSB pathway that employs the same dipole moments can facilitate the anisotropy analysis. For example, since 2D EV pathway $\mathsf{I}^{\mathsf{i}}_{0,0}$ and 2D VE pathway $\mathsf{I}^{\mathsf{0}}_{\mathsf{i},0}$ both use $\boldsymbol{\mu}^{0,0'}$ and $\boldsymbol{\mu}^{0,i}$, the anisotropy ratios of each of these pathways with 2D VE ESA pathway $\mathsf{II}^{\mathsf{i}}_{\mathsf{i},\mathsf{i}}$ contain identical information. Additionally, better ω_3 spectral resolution of the 2D EV anisotropy afforded by vibrationally-resonant probing should help the comparison of these two anisotropy ratios to provide a more consistent analysis of the 2D VE anisotropy ratio. That is, by finding the ω_3 frequencies where these two ratios approach the same value would provide more confidence in the determination of $\theta^{i,i'}_{0,0'}$, which

is only accessible through 2D VE ESA pathways. For systems in which the Franck–Condon approximation is valid, it is expected that $\hat{\mu}^{0,0'} \cong \hat{\mu}^{i,i'}$. However, the presence of non-Condon effects and Duschinsky mixing will render $\theta_{0,i}^{0,0'}$ and $\theta_{0,i}^{i,i'}$ to have increasingly different values due to the different vibronic dipole moments on which these angles depend. This example suggests one way that an anisotropy comparison between specific pathways measured in 2D EV and 2D VE spectroscopy can be used in tandem to help quantify non-Condon effects. On a broader level, it is notable that the 2D EV and 2D VE spectroscopies can directly interrogate the $\boldsymbol{\mu}^{0,i'}$ and $\boldsymbol{\mu}^{0,j'}$ transition dipole moments in comparison to the fundamental electronic transition dipole moment $\boldsymbol{\mu}^{0,0'}$.

It is important to note that an absolute — as opposed to relative — determination of the dipole orientations can be ambiguous due to the π-periodic nature of the anisotropy relations. [24] For example, determining $\theta_{0,0'}^{0',i'} = 20^o$ using Fig. 2.5 (c) cannot distinguish between the full range of solutions $\theta_{0,0'}^{0',i'} = 20^o \pm 180^o$. Therefore, when the anisotropy ratios equal 1 in Fig. 2.5 (c)-(d), the dipole moments of interest may either be parallel or antiparallel to the shared dipoles between the two pathways being investigated. However, it is reasonable to assume that such large changes in dipole moments would not retain similar enough character to be comparable in the manner discussed here and so are outside the scope of this discussion; much smaller angles are expected in practice. Notably, the anisotropy ratios also become ill-defined and diverge asymptotically as the reference dipole moment angle approaches the magic angle where $r \to 0$. [132]

2.6.2 Brief Comparison Between Observables in 2D Vibronic Spectroscopies and Other Nonlinear Techniques

As 2D EV and 2D VE spectroscopies are more widely applied to a variety of scientific questions, it is useful to directly discuss how some of the observables in these newer techniques compare to other ultrafast nonlinear techniques that have been used to study molecular structural dynamics.

Transient-IR (tIR) Spectroscopy vs. 2D EV Spectroscopy

Transient-IR (tIR) spectroscopy — the one-dimensional analog to 2D EV spectroscopy — has employed polarization selectivity in femtosecond chemical dynamics investigations to better understand excited state chemical phenomena. [133] In principle, the tIR spectrum is obtained from a corresponding 2D EV spectrum by integrating over the excitation frequency domain. As a result, any discernment of excitation-dependent features in the 2D EV spectrum is lost. Generally, the differences between the tIR signal amplitudes and the ω_1-dependent 2D EV signal amplitudes shows that an inaccurate assessment of the excited-state molecular structure could be obtained from the tIR signal alone. This observation was emphasized for consideration of only one vibration studied using these 2D vibronic spectroscopies, [40] but the effect clearly worsens as more degrees of freedom are at play in the system of interest, and as polarization selectivity is deliberately employed to extract molecular-frame information. A multimode vibronic system has even more oppositely signed pathways with different orientational and vibronic responses which are all convolved in the tIR spectrum as the ω_1 dimension is integrated away. This fact is easily understood by considering the 2D EV cartoon schematic in Fig. 2.3. The molecular system described by this schematic spectrum is one in which all vibronic eigenstates assume the maximum degree of pathway separation through various intramolecular couplings; even in this case, there are only two spectral features that would not be convolved with at least one other pathway composed of very different molecular transitions in a tIR spectrum. The spectral intensities and the anisotropy values are affected for most 2D EV pathways, potentially making the tIR anisotropy values unreliable for extracting an accurate, quantitative picture of the molecular frame. For example, considering the anisotropy of a GSB feature in a tIR experiment at $\omega_3 = \omega_i$ would convolute the effects of dipole moment angles $\theta_{0,0'}^{0,i}$, $\theta_{0,0'}^{0,i'}$, and $\theta_{0,0'}^{0,j}$ by integrating signals from pathways $\mathsf{I}_{0,0}^{\mathsf{i}}$, $\mathsf{III}_{\mathsf{i},0}^{\mathsf{i}}$, and $\mathsf{III}_{\mathsf{j},0}^{\mathsf{i}}$. Consideration of the angular dependence for pathways with common ω_3 frequencies (shown in Appendix D) illustrates further sources of inaccuracy possible through a polarization-selective tIR experiment. Of course,

this effect becomes more problematic for tIR spectral interpretation as electric fields with broader bandwidths are used for excitation. Conversely, narrower band excitation sources used in tIR experiments would mitigate this spectral convolution. By separating out the ω_1-dependent pathways in the 2D EV experiment, the separation of spectral contributions arising from differently overlapped pathways in the ω_3 domain is achieved. Inevitably, for molecular systems in which some of the vibronic eigenstates are not well separated (e.g., if $\Delta_{eg,i}$ is much smaller than the vibrational line width), even the polarization-dependent 2D EV spectrum will contain spectrally overlapping features of very different character.

Transient-2D IR (t-2D IR) Spectroscopy versus 2D Vibronic Spectroscopies

One approach to measuring electronically excited state molecular structural dynamics is by incorporating an additional electronic excitation pulse that precedes the third-order 2D IR pulse sequence. This technique known as transient-2D IR (t-2D IR) spectroscopy has been successful in particular applications for studying excited state charge transfer of transition metal complexes. [20, 22, 134] The promise of t-2D IR spectroscopy lies in the measurement of excited state vibrational anharmonicities and frequency shifts through a difference measurement between 2D IR spectra of the ground and excited electronic states. However, the signal levels in t-2D IR spectroscopy are inherently much weaker due to their fifth-order dependence on the molecular response. As shown in the schematic spectra (Figs. 2.3 and 2.4), all of the same observables are accessible through 2D EV and 2D VE spectroscopies, which are third-order nonlinear techniques. From Figs. 2.3 and 2.4, we see that the pathway positions directly describe the excited state anharmonicities ($\Delta_{i'}, \Delta_{j'}, \Delta_{i'j'}$) and excited state vibrational frequency shifts ($\Delta_{eg,i}, \Delta_{eg,j}$). Noting that third-order nonlinear signals are stronger than fifth-order signals, we expect that the above information can be more easily accessed with 2D Vibronic spectroscopy as opposed to t-2D IR. It is important to note that the t-2D IR spectrum is capable of *simultaneously* measuring the vibrational anharmonicity in both the ground and the excited electronic states of a molecule. This information is not as directly discernible in 2D EV or 2D VE spectroscopy because neither of these

third-order techniques directly access the two-quantum manifold of the ground electronic state. Polarization-selective 2D EV and 2D VE spectroscopies provide very direct routes to measuring Duschinsky mixing. When excited-state vibrational frequency shifting is of interest, the 2D EV experiment has a notable advantage over t-2D IR because the degree of mechanical anharmonicity does not determine the signal strength in 2D EV spectra, as it does in t-2D IR. Thus, the $\Delta_{eg,i}$ or $\Delta_{eg,j}$ parameter is more directly measured with 2D EV. In principle, 2D VE spectroscopy also measures excited state frequency shifting more directly than t-2D IR, but the inherently overlapping features in ω_3 may limit the direct extraction of this information.

2.6.3 Selective Pathway Enhancement Through Polarization Schemes

The use of polarization schemes to enhance various signals compared to others is a common strategy in both 2D IR and 2D ES spectroscopies that has been treated in depth elsewhere. [11, 24, 85, 97, 98, 131, 135, 136] Specifically, polarization control in 2D IR has been used to enhance cross peaks and, more recently, perform bulk-forbidden, surface-specific experiments. [86,100,137] Many of these studies are focused on the cross peaks where two different dipoles interact. These strategies are directly applicable to 2D EV and 2D VE spectroscopies where every transition pathway includes at least two different dipole moments.

The $\boldsymbol{Y}_{ZYYZ}$ and $\boldsymbol{Y}_{ZYZY}$ polarization configurations can be used to isolate all pathways in both 2D EV and 2D VE spectroscopies which experience a τ_2 coherence. There is an inherent separation of purely vibrational and vibronic transitions between the $\boldsymbol{k}_1$ and $\boldsymbol{k}_2$ interactions relative to the $\boldsymbol{k}_3$ and $\boldsymbol{k}_4$ interactions in 2D EV and 2D VE spectroscopy. Assuming that rotational diffusion is negligible during the pulse sequence, the $\boldsymbol{k}_1$ and $\boldsymbol{k}_2$ ordering of the dipole projections into the laboratory frame (ZY vs. YZ) for the τ_2 population pathways is inconsequential because the same dipole is projected onto both axes. In fact, τ_2-dependent dynamics of population pathways could provide some measure of rotational diffusion during the experiment if the rotational diffusion timescale is comparable to the population relaxation timescale.

On the other hand, the pathways involving four unique dipole moments possess very different orientational responses. When separate transition dipole moments are driven by $\boldsymbol{k}_1$, $\boldsymbol{k}_2$, $\boldsymbol{k}_3$, and $\boldsymbol{k}_4$ interactions, the pathway amplitudes are sensitive to which dipole is projected onto the laboratory frame Z and Y axes. As discussed above, all pathways involving four distinct transition dipole moments propagate as coherent superpositions during τ_2. For example, pathways VII in 2D VE spectroscopy lie almost perfectly on top of pathways I and II. However, in the absence of Duschinsky mixing, pathways VII carry little intensity due to the inherently low Franck–Condon overlap of the vibronic transition resulting in a change of both vibrational quanta (e.g., $|g;01\rangle \rightarrow |e;1'0'\rangle$). Since pathways I and II have an identical response under the $\boldsymbol{Y}_{ZYYZ}$ and $\boldsymbol{Y}_{ZYZY}$ polarization schemes, the difference between these two spectra eliminates pathways I and II contributions and enhances those of pathways VII.

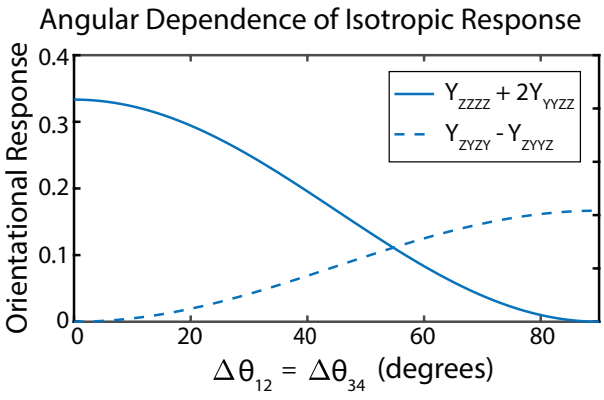

Figure 2.6: **Polarization-Selective Responses with ZYZY and ZYYZ Polarization Combinations.** The orientational response is compared for a system with four non-parallel dipole moments with the polarization combinations $\boldsymbol{Y}_{ZZZZ} + 2\boldsymbol{Y}_{YYZZ}$ (solid blue) and $\boldsymbol{Y}_{ZYZY} - \boldsymbol{Y}_{ZYYZ}$ (dashed blue). The responses are plotted as a function of $\Delta\theta_{12}$, the difference between angles θ_1 and θ_2, and of $\Delta\theta_{3,4}$, the difference between angles θ_3 and θ_4. The angles θ_1, θ_2, θ_3, and θ_4 are the respective angles formed between $\hat{\mu}^{0,0'}$ and the dipole moments driven by $\boldsymbol{k}_1$, $\boldsymbol{k}_2$, $\boldsymbol{k}_3$, and $\boldsymbol{k}_{sig}$. For simplification, the orientational responses are only plotted for the condition $\Delta\theta_{12} = \Delta\theta_{34}$.

The orientational responses for the $\boldsymbol{Y}_{ZZZZ} + 2\boldsymbol{Y}_{YYZZ}$ and the $\boldsymbol{Y}_{ZYZY} - \boldsymbol{Y}_{ZYYZ}$ polariza-

tion combinations for 2D EV and 2D VE pathways involving four different transition dipole moments are expressed in terms of $\Delta\theta_{12}$ and $\Delta\theta_{34}$ where $\Delta\theta_{12} = \theta_1 - \theta_2$ and $\Delta\theta_{34} = \theta_3 - \theta_4$ in Eqs. 2.14. The angular dependence of these polarization schemes is shown by plotting $\boldsymbol{Y}_{ZYZY} - \boldsymbol{Y}_{ZYYZ}$ and its comparison to $\boldsymbol{Y}_{ZZZZ} + 2\boldsymbol{Y}_{YYZZ}$ in Fig. 2.6. The angles θ_1, θ_2, θ_3, and θ_4 are the angles between $\hat{\mu}^{0,0'}$ and the transition dipole moments accessed by the light–matter interactions of $\boldsymbol{k}_1$, $\boldsymbol{k}_2$, $\boldsymbol{k}_3$, and $\boldsymbol{k}_{sig}$, respectively. As Eqn. 2.14a shows, the $\boldsymbol{Y}_{ZZZZ} + 2\boldsymbol{Y}_{YYZZ}$ response approaches the expected value of 1/3 as $\Delta\theta_{12}$ and $\Delta\theta_{34}$ approach 0^o, becoming parallel and yielding what is known as the isotropic response. This case clearly reduces the complexity of the system such that a measurement of an angle of interest between, for example, $\boldsymbol{k}_2$ and $\boldsymbol{k}_3$ could be reliably extracted from $r(\theta)$. However, it is clear that the $\boldsymbol{Y}_{ZZZZ}+2\boldsymbol{Y}_{YYZZ}$ response retains angular dependence for all pathways in a system with four non-parallel transition dipole moments.

$$\boldsymbol{Y}_{ZZZZ} + 2\boldsymbol{Y}_{YYZZ} = \frac{1}{6}\big[\cos(\Delta\theta_{12} + \Delta\theta_{34}) + \cos(\Delta\theta_{12} - \Delta\theta_{34})\big] \tag{2.14a}$$

$$\begin{aligned} \boldsymbol{Y}_{ZYZY} - \boldsymbol{Y}_{ZYYZ} &= \frac{1}{12}\big[\cos(\Delta\theta_{12} + \Delta\theta_{34}) - \cos(\Delta\theta_{12} - \Delta\theta_{34})\big] \\ &= -\frac{1}{6}\sin(\Delta\theta_{12})\sin(\Delta\theta_{34}) \end{aligned} \tag{2.14b}$$

This same angular dependence can be used productively in more creative polarization combinations; an example is described in Eqn. 2.14b. The angular dependence of the $\boldsymbol{Y}_{ZYZY} - \boldsymbol{Y}_{ZYYZ}$ polarization-dependent signal becomes zero for all pathways in which fewer than four dipole moment angles are non-zero. Observation of this particular polarization-dependent signal immediately confirms a more complicated orientational response than just a single angle dependence. The comparison of the $\boldsymbol{Y}_{ZYZY} - \boldsymbol{Y}_{ZYYZ}$ difference and the isotropic signal demonstrates the signal enhancement that is achievable. Spectral analysis taking advantage of these polarization combinations is discussed at more length in chapter 3 within the context of 2D vibronic spectral simulations.

The $\boldsymbol{Y}_{ZYZY} - \boldsymbol{Y}_{ZYYZ}$ polarization combination can be exploited in all regions of the 2D

VE spectrum. For example, eliminating pathways III, IV, and τ_2 populations in VI to isolate pathways VI with τ_2 coherence, or eliminating the τ_2 population pathways V to amplify the multimode pathways V. In 2D EV spectroscopy, it can be used to selectively interrogate pathways V and VI for identical reasons. In general, each τ_2 coherence pathway for both spectroscopies has a partner pathway. That is, for each of these pathways there exists another τ_2 coherence pathway sharing the same four dipole moments, but their temporal order of interaction is different resulting in spectral separation of these pathways in the (ω_1, ω_3) plane. In 2D VE spectra, pathways producing such signals contribute intensity to peaks that often overlap in ω_3 (e.g., those generating R and NR $\mathsf{V}^0_{i,j}$, see Fig. 2.4). The pathway pairs mentioned above acquire opposite signs in the $\boldsymbol{Y}_{ZYZY} - \boldsymbol{Y}_{ZYYZ}$ difference spectrum, resulting in more easily separated signals in the ω_3 dimension.

To date, the polarization conditions of ZYZY and ZYYZ have not been realized experimentally for 2D VE or 2D EV experiments. The experimental requirement of phase-stable interferometric precision for $\boldsymbol{k}_1$ and $\boldsymbol{k}_2$ lends the implementation of these polarization schemes more amenable to 2D VE spectroscopy over 2D EV spectroscopy. Studies using 2D EV spectroscopy has been performed with pulse shapers to generate two collinear pump pulses with complete amplitude and phase shaping control. [32,109,110] As a result, $\boldsymbol{k}_1$ and $\boldsymbol{k}_2$ necessarily must have the same linear polarization. [138] While there are examples of polarization-selective 2D ES experiments with independently controlled excitation fields, [68, 99] these actively phase-stabilized UV-Visible interferometers have yet to be incorporated into a 2D EV experiment. However, the Mach-Zender mid-IR interferometer used to generate pulse pairs in 2D VE spectroscopy may be readily adapted to such polarization schemes. [29,36,37] The partially collinear pump-probe geometry has been used in all cases of 2D EV and 2D VE spectroscopies published to-date; this is largely for convenience because the energetic discrepancy between the electronic and vibrational resonances will result in poor spatial separation of signals in a non-collinear geometry. A notable experimental challenge will be incorporating an external local oscillator as the ZYZY and ZYYZ polarization schemes require orthogonal $\boldsymbol{E}_3$ and $\boldsymbol{E}_{sig}$ fields - precluding the direct use of the self-heterodyned

detection with $\boldsymbol{E}_3$, as employed in the pump-probe geometry.

2.6.4 τ_2 Dependent Dynamics and Anisotropies

In 2D VE spectroscopy, pathways V-VII have an (ω_1, ω_3) coordinate mismatch between the R and NR pathway positions, complicating data interpretation. As discussed earlier, the spectrally separated R and NR pathway pairs propagate as a coherent superposition during τ_2. In cases where the R and NR pathway pairs form spectrally overlapped pathways with other 2D pathways (e.g., those with τ_2 populations), the τ_2-dependent amplitude oscillations characteristic of these R and NR pathway pairs can be used to target these pathway or selectively remove them from interfering with the τ_2 population pathways.

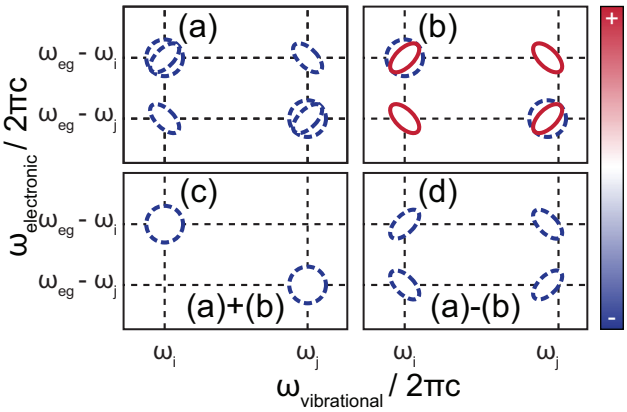

Figure 2.7: **Distinguishing Population and Coherence Pathways by τ_2-Dependence.** (a) 2D VE excited state absorption pathways V at $\tau_2 = n(\Delta\omega)^{-1}$ for integer values of n, where $\Delta\omega = |\omega_j - \omega_i|$ is the frequency difference between the two vibration. All pathways constructively interfere and contribute signal. (b) The same set of 2D VE pathways at $\tau_2 = (n + 1/2)(\Delta\omega)^{-1}$; the coherence pathways destructively interfere at these τ_2 delays. (c) Coherence pathways are eliminated by summing the panels (a) and (b); the positive and negative interferences of the coherence signals at these τ_2 points yields their elimination. (d) Likewise, population pathways are eliminated by the difference of the panels (a) and (b). See 2D VE schematic in Fig. 2.4 for referencing pathway labels.

In Fig. 2.7 the lower energy ω_3 manifold of a 2D VE schematic (i.e., the block of pathways V) is illustrated for two different series of τ_2 delays, as the τ_2-coherence pathways beat

repeatedly. The first schematic (Fig. 2.7 (a)) shows all pathways V plotted at $\tau_2 = n(\Delta\omega)^{-1}$ for any integer value of n where ($\Delta\omega = |\omega_j - \omega_i|$). The τ_2-coherence R contributions of $\mathsf{V}^0_{\mathsf{i,j}}$ and $\mathsf{V}^0_{\mathsf{j,i}}$) occupy the same (ω_1, ω_3) positions as the τ_2 population pathways $\mathsf{V}^0_{\mathsf{i,i}}$ and $\mathsf{V}^0_{\mathsf{j,j}}$, whereas the NR coherence pathways of $\mathsf{V}^0_{\mathsf{i,j}}$ and $\mathsf{V}^0_{\mathsf{j,i}}$) are spectrally isolated. As a result, the R pathways skew the line shape of the τ_2 population pathways. All four τ_2 coherence pathways oscillate in τ_2 with the same period because they all experience a coherence between the same two states ($|g;10\rangle\langle g;01|$). Theoretically, this means they all reach relative extrema simultaneously. The schematic in Fig. 2.7 (b) at $\tau_2 = (n + 1/2)(\Delta\omega)^{-1}$ shows the impact of simply choosing a value of τ_2 where the $\mathsf{V}^0_{\mathsf{i,j}}$ and $\mathsf{V}^0_{\mathsf{j,i}}$ destructively interfere to distinguish these pathways. The τ_2-dependent constructive and destructive interference of the coherence pathways can be used to further isolate signals of interest. Data from the τ_2 points represented in Figs. 2.7 (a) and (b) can be used to eliminate the coherence pathways by their sum (Fig. 2.7 (c)), thus enabling use of center line slope or other analyses [28] on the population pathways $\mathsf{V}^0_{\mathsf{i,i}}$ and $\mathsf{V}^0_{\mathsf{j,j}}$. Similarly, if the coherence pathways are of greater interest, the population pathways may be eliminated by the difference of the 2D VE signals collected at $\tau_2 = n(\Delta\omega)^{-1}$ and $\tau_2 = (n+1/2)(\Delta\omega)^{-1}$, as depicted in Fig. 2.7 (d). In practice, this analysis would be limited by the residual dispersion of the pulses used in the experiment, yielding the best results with well characterized, fully compressed broadband pulses.

The above analysis underscores the importance of obtaining 2D VE spectra at a series of linearly spaced waiting times over which a Fourier transform is performed to resolve the third-order molecular response of the system within the parameter space accessible to the experiment. The resultant three-dimensional (3D) spectrum consists of cross peaks in the $(\omega_1, \omega_2, \omega_3)$ coordinate space. Compared to using a well-chosen τ_2 delay time which enhances particular features of interest, 3D spectroscopy is effectively the frequency-domain equivalent of such spectral filtering. The τ_2 population peaks will approach the DC line ($\approx$0 cm^{-1}) in the 3D VE spectrum due to much slower lifetime decay by comparison to the faster oscillations characteristic of the τ_2 coherent oscillations. Employing these types of strategies will allow isolation of multiple coherences in the case where more than two vibrational modes exist,

including high frequency vibrations, low frequency vibrations, and even multiple electronic states.

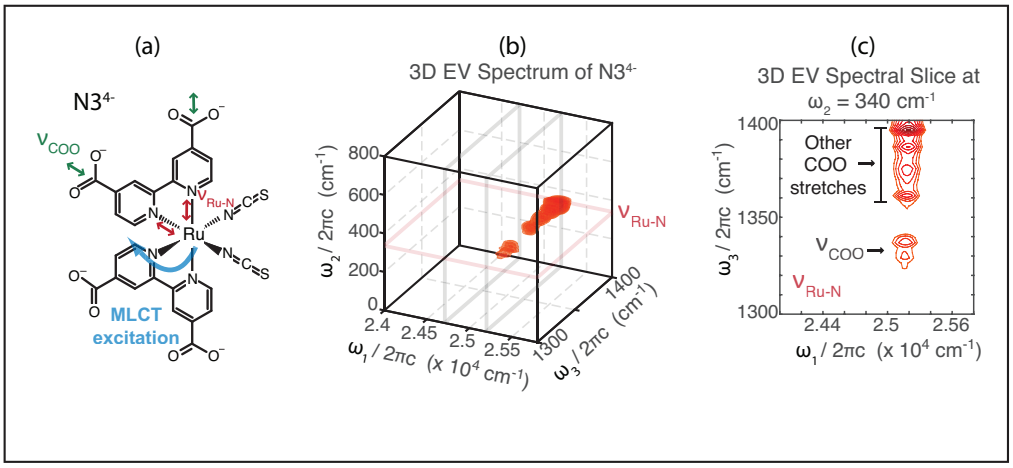

Figure 2.8: **Spectral Deconvolution with τ_2-Dependent 3D EV Amplitudes.** (a) The molecular structure of $[Ru-(dcbpy)_2(NCS)_2]$ (dcbpy = 4,4'-dicarboxy-2,2'-bipyridine), also known as $N3^{4-}$, with the relevant degrees of freedom highlighted: metal-to-ligand-charge-transfer (MLCT) excitation (light blue), a carboxylate symmetric stretch ν_{COO} (green), and a low frequency vibration involved in the excited state coherence evolution, ν_{Ru-N}. (b) The early time ($0 < \tau_2 < 600fs$) 3D EV spectrum of $N3^{4-}$ showing the vibronic couplings between all three degrees of freedom highlighted in (a). (c) A spectral slice of the 3D EV spectrum at the ν_{Ru-N} vibrational frequency (340 cm^{-1}) to demonstrate the deconvolution of the other excited state carboxylate symmetric stretches in the 1350 $cm^{-1} < \omega_3 <$ 1400 cm^{-1} region.

The three-dimensional approach has recently proven successful in EV spectroscopy with the report of a 3D EV spectrum in the aqueous deprotonated ruthenium-centered solar cell dye molecule, $N3^{4-}$ [38]. The τ_2-dependence of a prominent and spectrally-isolated charge accepting carboxylate symmetric stretch (ν_{COO}) that vibronically couples with specific metal-to-ligand-charge-transfer excited states was used to follow the excited state evolution of

vibronic coherences in $N3^{4-}$. The spectral isolation of this particular ν_{COO} reporter vibration enabled the success of this 3D EV experiment. However, calculations performed in the earlier polarization-selective 2D EV studies on $N3^{4-}$ indicate there are actually many near-degenerate carboxylate symmetric stretches that split in the excited triplet states such that the ν_{COO} becomes spectrally isolated while the other carboxylate modes remain spectrally overlapped with their corresponding GSB features [31]. Since the vibronic coherences evolve in the excited state in $N3^{4-}$, these ESA features should have a different τ_2-dependence than the corresponding GSBs and, thus, be separable in the 3D spectrum. Figure 2.8 shows the 3D EV spectrum of $N3^{4-}$ and a spectral slice at $\omega_2 = 340$ cm^{-1}, referred to as ν_{Ru-N} corresponding to a low frequency vibration involving the Ru-N stretch of the dcbpy ligands (highlighted in red). The fact that the ν_{Ru-N} is active during the vibronic coherence evolution through couplings with eigenstates of ν_{COO} character accounts for the observed τ_2-dependence during the first ≈600 femtoseconds of relaxation. Moreover, this is used to deconvolve the spectrally overlapped carboxylate symmetric stretches, which is represented by the peaks in the spectral slice in the $1350 < \omega_3 < 1400$ cm^{-1} region. This is one example of how specific τ_2-dependencies can be exploited to simplify the interpretation of complex 2D spectra.

2.7 Conclusions

A multimode vibronic system has been generally described in this study with emphasis on the orientational response. Various ways in which the orientational responses can be targeted to ascertain deeper insight into a multi-vibration, vibronically coupled molecular system using polarization-selective 2D EV and 2D VE spectroscopies have been thoroughly treated. This discussion may serve as a field guide to other groups interested in using 2D EV and/or 2D VE spectroscopies to directly measure vibronic dynamics in molecules. In comparison to other ultrafast nonlinear spectroscopies currently available, polarization-selective 2D EV and 2D VE spectroscopies provide unique opportunities to measure and characterize vibronic couplings, non-Condon effects, Duschinsky mixing, and electronic delocalization. Due to the complementary nature of these two techniques, an in-tandem approach to studying the

vibronic couplings of molecules should give direct access to the molecular-level vibronic dynamics of interest during many photochemical phenomena, such as excited state charge transfer and excited state proton transfer. This work builds upon an expanding foundation for 2D EV and 2D VE techniques to be applied to an increasingly diverse set of scientific investigations. Future studies of vibronic Hamiltonians with multiple electronic excited states and multiple vibrations will also prove useful for interpreting experimental spectra. In the second chapter of this series, the material Hamiltonian representing the system discussed here is fully described. The experimental methods and observables detailed in this chapter are some of the means by which the molecular machinery described in chapter 3 can be accessed directly. Taken together the work in this series of chapters provides a road map for obtaining a detailed view of vibronic dynamics at the molecular level.

Chapter 3

MULTIMODE TWO-DIMENSIONAL VIBRONIC SPECTROSCOPY II: SIGNATURES OF VIBRONIC COUPLINGS PARAMETERS FROM POLARIZATION-SELECTIVE SPECTRA

Relevant publications, with the permission of AIP publishing:

- [63] Robert B. Weakly, James D. Gaynor, and Munira Khalil. "Multimode two-dimensional vibronic spectroscopy. II. Simulating and extracting vibronic coupling parameters from polarization-selective spectra", *Journal of Chemical Physics*, Vol. 154, no. 18, p. 184202-18, 2021

3.1 Introduction

Polarization-selective two-dimensional infrared (2D IR) [15, 85, 97, 139] and two-dimensional electronic spectroscopy (2D ES) [16,68,99,101,135,140–142] are becoming routine tools in the nonlinear spectroscopy toolbox. Data from both spectroscopies are rich in information, often requiring model Hamiltonians to understand the connection between molecular structure and spectroscopic observables . [67, 79, 86, 143] Over the years, models of coupled vibrations and excitons have been developed, utilizing third-order nonlinear response theory to simulate and interpret 2D IR [12,100,144–148] and 2D ES [71,78,102,149,150] spectra. These simulations have revealed how the magnitude of anharmonic couplings and angles between transition dipoles of vibrational modes can be extracted from polarization-selective 2D IR spectra. [11,14,24,131,137] Similarly, simulations of polarization-selective 2D ES spectra have shown how couplings and angles between excitonic states are encoded in experimental spectra. There is also considerable interest in understanding how non-adiabatic couplings between

vibrations and electronic states are manifested in 2D ES spectroscopy. The concurrent development of experiment and computational methodologies have enabled the success of 2D IR and 2D ES to uncover new details of hydrogen bonding, protein structural dynamics, energy transfer in natural and artificial light-harvesting, and non-equilibrium vibrational relaxation in molecules and materials. [25–27, 151–154]

Fourier transform two-dimensional electronic-vibrational (2D EV) and two-dimensional vibrational-electronic (2D VE) spectroscopies, collectively referred to as "2D vibronic" spectroscopies in this work, have been developed in the last few years to directly quantify coupled vibrational and electronic motions in the condensed phase. These off-diagonal spectroscopies directly interrogate the interplay of vibrational and electronic degrees of freedom. The identification of coupled vibronic coordinates and measuring the magnitude of their coupling is necessary for developing predictive theory, [155] as well as new molecules and materials with targeted functionality. The term "vibronic" has been used in several technically specific contexts. Distinct from coupling between multiple excited electronic states, as explored elsewhere, [25,39] the term in this context refers specifically to a ground and single excited state coupling through the vibrational modes of interest in the weak coupling limit. A plausible extension of this work is to explore the impacts of additional additional coupled electronic excited states.

2D EV spectroscopy, was first demonstrated in 2014, [32] and 2D VE spectroscopy was demonstrated in 2015. [29] Since then, these techniques have been successfully employed to better understand biological light harvesting and

[112, 113, 156] the roles played by correlated vibrational and electronic motions during ultrafast charge- and energy-transfer in transition metal-centered molecular systems. [30–32, 36, 39, 117]

Polarization-selective 2D VE spectroscopy on a cyanide-bridged mixed-valence complex has mapped relative orientations of the coupled metal-to-metal charge transfer (MMCT) transition and cyanide stretching vibrations providing a method to spatially map vibronic couplings on the molecular frame. [37] Similarly, polarization-selectivity in 2D EV has led

to differentiating vibration orientations in a transition metal solar dye [31] and aided sate assignments of vibronic states in biological systems. [33]

Many experimental 2D EV and 2D VE investigations to date clearly highlight the selectivity of these techniques to vibronic couplings and also the need for developing tools to interpret the spectra at the molecular level. Previously, a model Hamiltonian consisting of a single anharmonic vibration coupled to a ground and excited electronic state was used to develop a set of selection rules for 2D VE and 2D EV spectroscopy. [40] Here, that description of 2D vibronic spectroscopy is advanced by considering vibronic coupling between multiple coupled anharmonic high-frequency vibrational modes and an excited electronic state, and by calculating the nonlinear orientational response of coupled vibronic coordinates. In the first chapter of this series, [62] a description of multimode polarization-selective 2D EV and 2D VE experiments was developed by defining generalized molecular system eigenstates and vibronic transitions within the molecular frame. The consideration of multiple vibrational modes resulted in additional vibronic pathways and new spectral features whose positions, amplitudes and line shapes were explored in detail. Orientational response functions for up to four unique vibronic transition dipoles were calculated and the use of experimental polarization conditions to enhance, suppress, or analyze specific vibronic pathways was discussed. Additionally, methods for isolating vibronic coherence and population relaxation pathways were described as a result of their τ_2 dependence.

This chapter explores the molecular basis for the vibronic eigenstates and transition dipole moments defined in chapter 2 by constructing a model Hamiltonian that encapsulates both vibrational and electronic coupling, and describes how vibronic couplings result in angular distortions of the electronic transition dipole moment in a mode-specific manner. Hamiltonian parameters are connected to spectroscopic observables here, which demonstrates how 2D EV and 2D VE spectroscopies can be used in tandem to map vibronic couplings in the molecular frame. The rest of the chapter is organized as follows. Section 3.2 presents a model Hamiltonian composed of two electronic states and two anharmonic oscillators that describes vibronic interactions and coupled vibrational interactions. Each term of the Hamiltonian is

explored, beginning with the relationship between the linear vibronic coupling term and the Huang-Rhys parameter in the Displaced Harmonic Oscillator (DHO.) model [124, 125]. The bilinear vibronic coupling is mapped to a specific angle of rotation in vibrational coordinate space and connected to Duschinsky mixing [154]. Section 3.3 utilizes the transformation matrix that was used to diagonalize the ground and excited state Hamiltonians to construct the vector form of the anharmonic vibrational transition dipole moments. The vibronic transition dipole moments measured in 2D EV and 2D VE spectra are constructed as a vector sum of the electronic and vibrational dipoles in the molecular frame. Next, the effect that the vibronic Hamiltonian terms have on the orientation and magnitude of the vibrational and vibronic transition dipoles in the molecular frame is elucidated. Non-Condon effects (NCEs) are calculated to first and second-order and their impact on the amplitude and direction of the vibronic dipoles measured in 2D vibronic spectra are explored. Section 3.4 simulates polarization-selective 2D EV and 2D VE spectra using the molecular Hamiltonian described above. Additionally, considerations of experimental design outline methods for isolating and extracting spectroscopic observables in congested spectra. Section 3.5 details how 2D peak positions and amplitudes can be used to measure mode-specific Huang-Rhys and Duschinsky mixing parameters and to extract relative angles between vibronic transition dipoles. Finally, we discuss the prospect of extracting and quantifying non-Condon contributions from 2D vibronic spectra.

3.2 Model Vibronic Hamiltonian: Bilinearly Coupled Anharmonic Oscillators

3.2.1 Material Hamiltonian

The vibronic material Hamiltonian, $H_{vibronic}$ shown in Fig. 3.1, is defined by the sum of the ground and excited state Hamiltonians: $H_{vibronic} = H_g + H_e$. Our previously described vibronic material Hamiltonian for a molecular system consisting of a single vibrational mode and two electronic states [40] (the ground, $|g\rangle$, and first excited, $|e\rangle$, states) is extended to describe the same system with two vibrational modes of interest (modes i and j). These

vibrations oscillate along vibrational coordinates q_i^0 and q_j^0 about an equilibrium position Q_0, and are described as a dimensionless coordinate system Q_k^0 in Eqn. 3.1. Each oscillator k has a reduced mass m_k and natural frequency ω_k^0 along the coordinate q_k^0 . The oscillator index k (not to be confused with the electric field wavevectors, $\boldsymbol{k}$) is used to describe the behavior of both vibrational modes where $[k_a, k_b, ...] \in [i, j]$. Throughout this work, the superscript $(^0)$ indicates an attribute of zeroth-order, before Hamiltonian diagonalization, when applied to eigenstates, energies, and dipole orientations.

$$Q_k^0 = \sqrt{\frac{m_k \omega_k^0}{\hbar}} q_k^0 \tag{3.1}$$

The ground electronic state Hamiltonian, H_g, takes the form of two bilinearly coupled anharmonic oscillators written in the Q_k^0 basis, as represented in Fig. 3.2, and it is expressed in terms of raising and lowering operators of the harmonic oscillator using the dimensionless coordinate system Q_k^0. The ground state Hamiltonian (Eqn. 3.2) is described as the sum of the kinetic energy, $(P_k^2/2m_k)$ and the potential energy, $V_g(Q_k)$ (Eqn. 3.3), with momentum given as P_k.

$$H_g(Q_i^0, Q_j^0) = \frac{P_i^2}{2m_i} + \frac{P_j^2}{2m_j} + V_g(Q_i^0, Q_j^0) \tag{3.2}$$

$$V_g(Q_i^0, Q_j^0) = \frac{\hbar\omega_i^0}{2}(Q_i^0)^2 + \frac{\hbar\omega_j^0}{2}(Q_j^0)^2 + B_{ij}Q_i^0 Q_j^0 + \frac{1}{6}\left(\hbar\omega_i^0 g_{iii}(Q_i^0)^3 + \hbar\omega_j^0 g_{jjj}(Q_j^0)^3\right) \tag{3.3}$$

The ground state potential, $V_g(Q_i, Q_j)$, is represented by two oscillators with cubic anharmonicity determined by (g_{iii} and g_{jjj}) and coupled through the bilinear mixing term, B_{ij}. The 2D IR community has used B_{ij} to describe mode coupling in the ground state, [11, 14, 84, 97, 157] which has the effect of rotating the potential relative to the Q_i^0 and Q_j^0 coordinates. The excited state Hamiltonian, H_e (Eqn. 3.4), is constructed similarly to H_g,

but varies in the potential V_e. Equation 3.5 describes the excited state potential lifted vertically from the ground state by the electronic transition energy $\hbar\omega_{eg}^0$ and perturbed by various vibronic coupling terms (V).

$$H_e(Q_i^0, Q_j^0) = \frac{P_i^2}{2m_i} + \frac{P_j^2}{2m_j} + V_e(Q_i^0, Q_j^0) \tag{3.4}$$

$$\begin{aligned} V_e(Q_i^0, Q_j^0) =& V_g(Q_i^0, Q_j^0) + \hbar\omega_{eg}^0 + \hbar\omega_i^0 V_i Q_i^0 + \hbar\omega_j^0 V_j Q_j^0 \\ &+ \frac{\hbar\omega_i^0}{2} V_{i,i} (Q_i^0)^2 + \frac{\hbar\omega_j^0}{2} V_{j,j} (Q_j^0)^2 + V_{ij} Q_i^0 Q_j^0 \end{aligned} \tag{3.5}$$

The subscript of each additional term describes its vibrational coordinate dependence. The term, V_k, is a linear perturbation in the direction Q_k^0. Vibrational mixing in the excited state, given by V_{ij}, is linear in both Q_i^0 and Q_j^0. The term, V_{kk}, which is quadratic in Q_k^0, is responsible for the excited state red or blue shifting of each vibrational mode, changing the curvature in each direction of the excited state potential. Vibrational mode anharmonicities are encoded in the ground state potential (Eqn. 3.3).

Figure 3.1 shows the eigenstates resulting from the system Hamiltonian in Eqs. 3.2-3.5. The zeroth-order vibrational states in the electronic ground state are described as $|\nu_i, \nu_j\rangle^0$. The excited state manifold is increased in energy by $\hbar\omega_{eg}^0$. Since the excited state potential energy surface is described as a perturbation of the ground state, the terms g_{iii} and B_{ij} induce the anharmonic shifts in both vibrational manifolds, leading to the states $|g; \nu_i\nu_j\rangle$. In the excited state, V_{kk} depicts a red-shifting of both vibrational modes, corresponding to a negatively signed perturbation term. The linear perturbation, V_k , displaces the excited state potential along coordinate Q_k^0 and lowers the excited electronic states by $\Delta\hbar\omega_{eg}$. Finally, V_{ij} couples and mixes the vibrational states in the electronic excited states in combination with B_{ij}. Diagonalizing the ground and excited state Hamiltonians results in the following parameters used throughout this work: ω_{eg} = electronic energy gap, $\omega_k(\omega_k')$ = fundamental ground (excited) state vibrational transition frequency, $\Delta_k(\Delta_k')$ = ground (excited) state anharmonicity, $\Delta_{eg,k}$ = excited state vibrational frequency shift, $\Delta_{ij}(\Delta_{i'j'})$ = ground

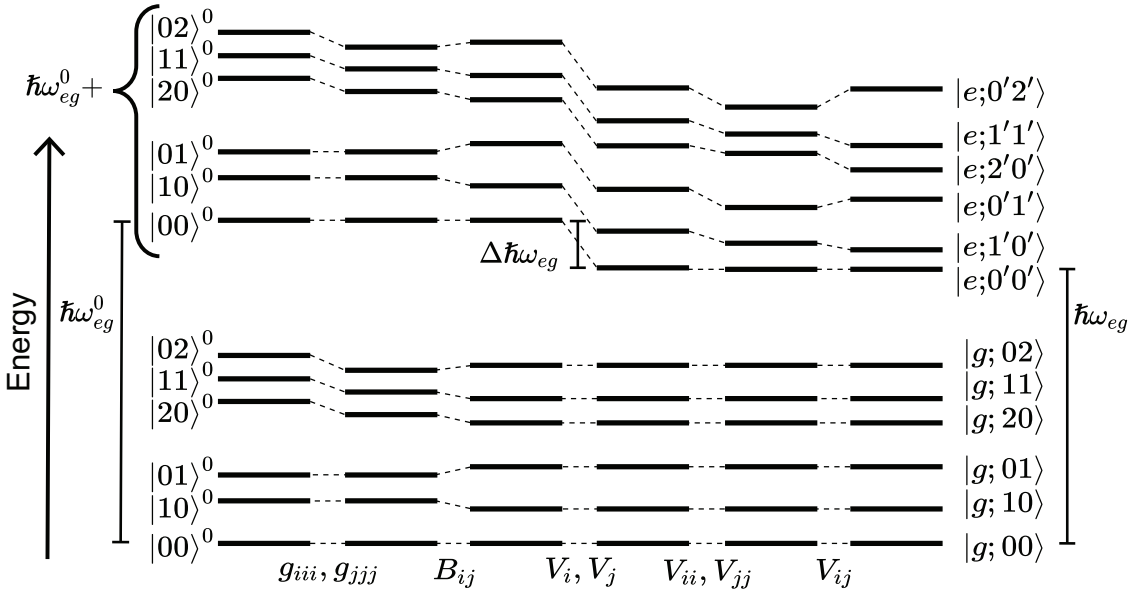

Figure 3.1: **Energy levels of the vibronic states obtained from the model Hamiltonian.** Zeroth-order states denoted as $|\nu_i, \nu_j\rangle^0$ in the electronic ground state and increased in energy by $\hbar\omega^0_{eg}$ in the electronic excited state. The effects of various couplings in the material Hamiltonian are displayed as energetic changes in the zeroth-order states moving from left to right. Symbols between each column of states indicate coupling terms from material Hamiltonian (see main text for details). The resultant vibronic eigenstates are shown on the right and are denoted as $|g;\nu_i\nu_j\rangle$ on the ground electronic state (g) with vibrational quanta in Q_k ($\nu_k = 0, 1, ...$). The vibronic eigenstates of the excited electronic state (e) with vibrational quanta in Q'_k ($\nu_{k'} = 0', 1', ...$) are denoted as $|e;\nu_{i'}\nu_{j'}\rangle$.

(excited) state mixed mode anharmonicity. The term, $\Delta_{i'j'}$ represents energetic shifts due to Duschinsky mixing. The vibronic eigenstates of the above Hamiltonian, $|a(r,Q)\rangle$, are written as Born–Oppenheimer adiabatic eigenstates, [158] which depend on both electronic coordinates, r, and the reduced vibrational coordinates for system vibrations, Q. The vibronic eigenstates used here may be considered eigenfunctions of a dynamical Schrödinger equation in a basis spanning a complete electronic space for each vibrational coordinate, as described by the Born Representation of Ballhausen. [159] As defined the Eqs. 7 of our

previous work [40], the wavefunction has separable electronic and nuclear components each defined for the equilibrium geometry of the system and expanded over each coordinate Q_k. This separation is what permits the expansion of the vibronic transition dipole moments in Sec. 3.3.

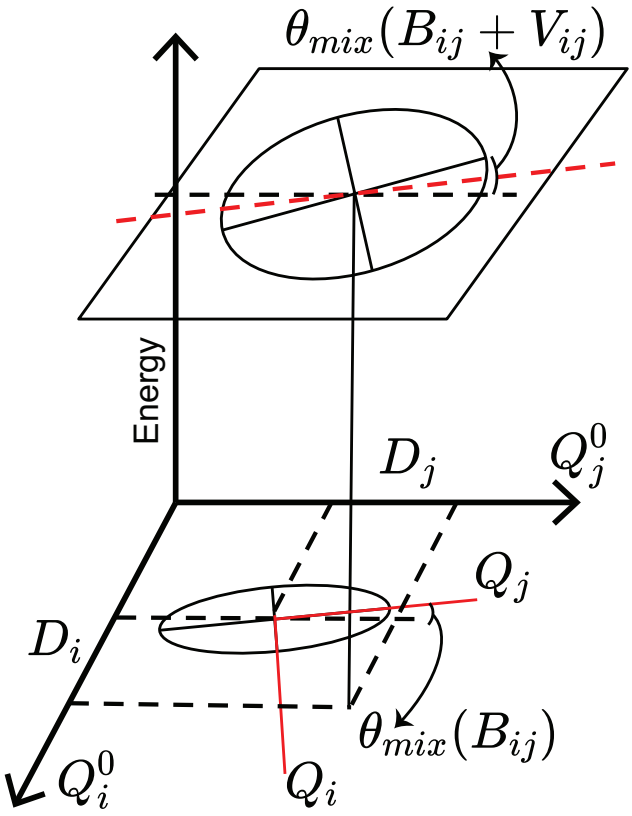

Figure 3.2: **Potential Energy Surfaces:** Ground and excited state potentials plotted against zeroth-order vibrational coordinates (Q_i^0 and Q_j^0). The ground state potential is rotated to some angle θ_{mix} (B_{ij}) relative to Q_i^0 and Q_j^0. The excited state is displaced along Q_i^0 and Q_j^0 by D_i and D_j as described in Sec. 3.2.2 and further rotated to θ_{mix} ($B_{ij}+V_{ij}$). The red dotted line is parallel to the potential in the ground state (Q_j); vibrational anharmonicity ($g_{iii} and\ g_{jjj}$) does not change between electronic states.

The complete material Hamiltonian includes $H_{vibronic}$ and Hamiltonians describing the bath (H_B) and the system-bath interactions (H_{SB}). Following our previous description [40] and that of Sung et al. [126] the dephasing functions, describing in appendix C are written

in the homogeneous limit. The interaction Hamiltonian (H_{int}) describes the light–matter interactions and is discussed at length in Sec. 3.3 below.

3.2.2 Linear Vibronic Coupling: Huang-Rhys Parameter

The linear coupling term, V_k, in Eqn. 3.5 serves a similar function to the displacement operator found in the Displaced Harmonic Oscillator (DHO.) model commonly used to explain a vibronic progression of Franck–Condon (FC) overlap integrals in both absorption and fluorescence spectra. [124, 125] In the case of the DHO. model, the strength of the vibronic coupling is measured by the unitless Huang-Rhys parameter, D_k , which is related to the square of the displacement.

Multiple representations of these parameters have been published, in both the momentum [160] and position basis [40,65,161,162]. A description of those representations, their mutual conversion, and Eqn. 3.6 and the electronic energy correction term $\Delta\omega_{eg}$ are derived for the single mode case in appendix A. The relationship between the Huang-Rhys parameter and the linear coupling term, is quadratic as shown in Eqn. 3.6.

$$D_k = \left(\frac{1}{\sqrt{2}}\frac{V_k}{\omega_k^0}\right)^2 \tag{3.6}$$

The above equaiton holds when $g_{iii},\ g_{jjj},\ B_{ij},\ V_{ij}$ are zero in the model Hamiltonian (Eqs. 3.2 and 3.4). We note that V_k is not an explicit horizontal displacement, but rather a shift of the excited state potential along a line with its slope in proportion to V_k, and therefore results in an additional shift of the electronic transition energy equivalent to $\Delta\hbar\omega_{eg} = \sum_k D_k\hbar\omega_k^0$ as shown in Fig. 3.1. To consider the Huang-Rhys factor in multiple coordinates, D_k is defined using Eqn. 3.6 as a displacement along the zeroth-order coordinates, Q_k^0 (see Eqn. 3.1), leading to a useful description of both D_i and D_j, as seen in Fig. 3.2. Because the linear coupling parameter translates the potential energy surface in Q coordinate space, and does not reorient the potential, applying either V_i or V_j does not shift the orientations of

vibrational dipoles relative to the ground state dipoles, as discussed in Sec. 3.3.1.

3.2.3 Bilinear Vibronic Coupling: Duschinsky Mixing

Vibrational mode mixing due to bilinear coupling terms, B_{ij} and V_{ij}, can be seen in Fig. 3.2, where both the ground and excited states are rotated relative to the (Q_k^0) zeroth-order basis. The total rotation of the excited state potential is dependent upon both B_{ij} and V_{ij}. In a 2D vibronic experiment, the Q_k^0 basis is not measurable, but the rotations of vibrational transition dipole moments between $|g\rangle$ and $|e\rangle$ are measureable, as discussed later. Here, the term Duschinsky mixing is reserved for the excited state bilinear coupling (V_{ij}). As a consequence of bilinear mixing, excited state vibrational modes are delocalized across the zeroth-order state basis, [163] manifested as a rotation in the zeroth-order basis seen in Eqs. 3.7.

$$|e;1'0'\rangle = \hbar\omega_{eg}^0 + \alpha\,|1,0\rangle^0 \pm \beta\,|0,1\rangle^0 \tag{3.7a}$$

$$|e;0'1'\rangle = \hbar\omega_{eg}^0 \mp \beta\,|1,0\rangle^0 + \alpha\,|0,1\rangle^0 \tag{3.7b}$$

In the above equations, each state, $\left|e;\nu_i'\nu_j'\right\rangle$, is represented as a new linear combination of the zeroth-order vibrations when the cubic anharmonic couplings (g_{iii} and g_{jjj}) and the linear vibronic couplings (V_i and V_j) reach a limit of zero. After mixing, the Q_j' coordinate is a linear combination of $\alpha Q_j^0 \pm \beta Q_i^0$ governed by the Duschinsky mixing. Both α and β represent the projection of the zeroth-order coordinate onto the rotated coordinate system by a fraction related to $\pm\alpha$ in direction Q_j' and to $\mp\beta$ in direction Q_i'.

The effects of of V_{ij} on the rotation of the excited state vibrational dipoles are calculated in Sec. 3.3.1 and extracted from simulated 2D EV and 2D VE spectra in Sec. 3.5.2. Additionally, V_{ij} influences the measurement of the Huang-Rhys parameter in the following manner. As the excited state potential is rotated relative to the ground state, the projection of each excited state vibrational mode onto its ground state analogue becomes more extreme

as shown in Sec. 3.5.3. As will be discussed later, the Duschinsky mixing term is responsible for mixed mode anharmonicity in the electronic excited state, given by $\Delta_{i',j'}$, and can be directly measured in 2D EV spectra. The bilinear coupling parameter, V_{ij}, is also crucial for seeing amplitude in 2D vibronic signal pathways involving forbidden transitions (e.g. pathways VII in 2D VE, as discussed in Sec. 3.5).

3.3 Interaction Hamiltonian: Vibronic Transition Dipoles

The interaction Hamiltonian (H_{int}) describes the light–matter interaction between the four electric fields ($\boldsymbol{E}(\boldsymbol{k},\omega,t)$) and the dipole operator ($\boldsymbol{M}$) of the molecular system of interest. In the first chapter of this series (2, ref. [62]) we derived the nonlinear orientational response functions resulting from the sequential projections of the four linearly polarized electric fields in the fixed laboratory frame onto the fixed molecular frame for each successive field-matter interaction in 2D EV and 2D VE spectroscopy. The system dipole operator is defined below in terms of the vibronic system eigenstates, $|a(r,Q)\rangle$ and $|b(r,Q)\rangle$, and the elements of the transition dipole matrix between eigenstates a and b given by $\mu^{a,b}$.

$$\boldsymbol{M} = \sum_{a}\sum_{b} |a(r,Q)\rangle\, \mu^{a,b}\, \langle b(r,Q)| \tag{3.8}$$

Here, the dipole operator of the model vibronic system is built up from the zeroth-order basis to understand how the vibronic Hamiltonian and the inclusion of NCEs impact the amplitude and orientation of the vibronic transition dipoles are measured in 2D EV and 2D VE spectra.

3.3.1 Orientation of Vibronic Dipoles

The complete transition dipole moment ($\boldsymbol{\mu}^{a,b}$) is a vector quantity, and is the product of a unit vector direction ($\hat{\mu}^{a,b}$) and a magnitude ($\mu^{a,b}$). The spatial orientation of each vibrational dipole vector in $|g\rangle$ or $|e\rangle$ is obtained by transforming the harmonic transition

dipole operators, $\boldsymbol{M}_i^0$ or $\boldsymbol{M}_j^0$ in the zeroth-order basis, where, $\boldsymbol{M}_k = T^{-1} \cdot \boldsymbol{M}_k^0 \cdot T$. [14] The transformation matrices, T_g and T_e, are obtained by diagonalizing H_g and H_e (Eqs. 3.2 and 3.4) respectively. The contributions of each zeroth-order vibrational transition dipole is calculated separately in both the ground and excited states as shown below:

$$\boldsymbol{\mu}^{a,b} = \hat{\mu}_i^0 \cdot \boldsymbol{M}_i^{a,b} + \hat{\mu}_j^0 \cdot \boldsymbol{M}_j^{a,b} \tag{3.9}$$

In the above expression, $\boldsymbol{\mu}^{a,b}$, the indices (a,b) refer to the corresponding matrix element. For brevity, the orientation of the vibrational transition dipole moment associated with the k^{th} mode is denoted as $\hat{\mu}^k$ in the ground electronic state and $\hat{\mu}^{k'}$ in the excited electronic state. In this manner, we connect the orientations of the zeroth-order (unmixed) vibrational dipoles to the vibrational transition dipoles described by the molecular vibronic Hamiltonian. As in chapter 2 dipole orientations, which are fixed within the molecular frame, are defined relative to one another through dipole moment angles, $\theta_{a,b}^{c,d}$. For example, the angle between $\boldsymbol{\mu}^{0,0'}$ and $\boldsymbol{\mu}^{0,i}$ is defined $\theta_{0,0'}^{0,i}$. We note that $\mu^{0,0'}$ expresses the same dipole moment as $\mu^{e,g}$ used in chapter 2 [62] and in previous treatments [40].

Based on the Born–Oppenheimer approximation, [164–166] the transition dipole is described explicitly as separate operators for the vibrational and electronic transitions. Each vibronic transition dipole may be expressed as $\boldsymbol{M} = \boldsymbol{M}_{elec}(r) + \boldsymbol{M}_{vib}(Q)$, the sum of the electronic $\boldsymbol{M}_{elec}(Q)$ and the vibrational $\boldsymbol{M}_{vib}(Q)$ dipoles. Thus, each vibronic transition which includes vibrational character nonparallel to the purely electronic transition necessarily carries additional angular dependence. The orientation of a vibronic dipole may be considered as the vector sum of electronic and vibrational components. Combining the electronic dipole ($\boldsymbol{\mu}^{e,g}$) and relevant vibrational dipoles ($\boldsymbol{\mu}^k$) results in the vector form of each vibronic dipole, represented in Fig. 3.3 (c). Vibronic dipoles $\boldsymbol{\mu}^{i,j'}$ and $\boldsymbol{\mu}^{0,i'}$ are formed by the corresponding vector addition.

Figure 3.4 demonstrates how Duschinsky mixing rotates the excited state vibrational transition dipoles relative to the ground state dipoles by comparing the extent to which each

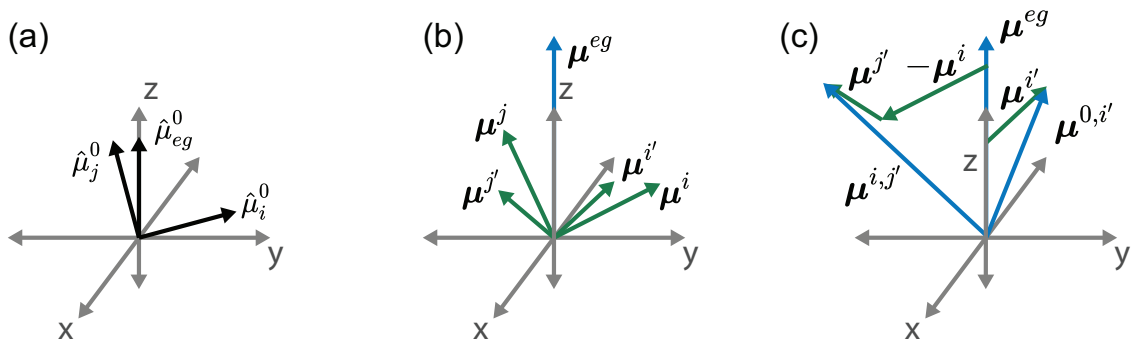

Figure 3.3: **Orientation of Dipoles:** a) Zeroth-order dipole unit vectors (black) plotted within the molecular frame (x,y,z, grey). b) Vibrational and electronic dipole vectors after transformation of the unit vectors. (see Eqn. 3.9 in the main text) The parameters of the system Hamiltonian used for the transformation are detailed in Sec. 3.3.1. c) Construction of vibronic dipole orientations under the Born–Oppenheimer approximation. Total vibronic dipole is the sum of both electronic and vibrational dipoles. ($\boldsymbol{\mu}^{i,j'} = \langle g;10|e;0'1'\rangle\, \boldsymbol{\mu}^{e,g} - \boldsymbol{\mu}^{i} + \boldsymbol{\mu}^{j'}$), ($\boldsymbol{\mu}^{0,i'} = \langle g;00|e;1'0'\rangle\, \boldsymbol{\mu}^{e,g} + \boldsymbol{\mu}^{i'}$).

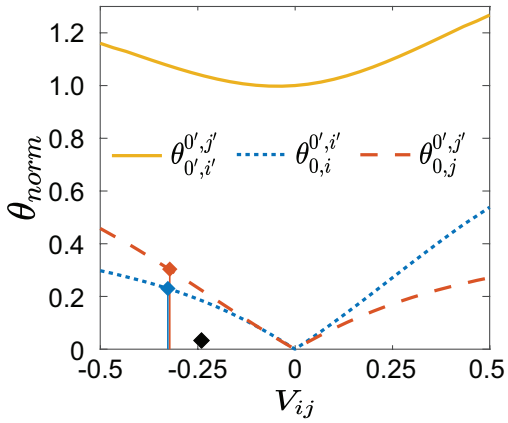

Figure 3.4: **Orientation of Dipoles:** Angular dependence of vibrational dipole moments on bilinear coupling, V_{ij}. Both vectors describing the transition dipole moment for $|e,0'0'\rangle \rightarrow |e,1'0'\rangle$ ($\theta^{0'i'}_{0,i}$) and $|e,0'0'\rangle \rightarrow |e,0'1'\rangle$ ($\theta^{0'j'}_{0,j}$) respond approximately equally but retain their relative angle. Angles are normalized to the angles between ground state vibrations dipoles, $\theta_{norm} = \theta/\theta^{0,i}_{0,j}$ with $B_{ij} = g_{iii} = g_{jjj} = 0$. Blue and orange diamonds represent the values of V_{ij} as calculated in Sec. 3.5.2. The black diamond, on lower axis, represents the input value used in the simulation.

mode k reorients in the excited state ($\theta_{0,k}^{0',k'}$), where the angles are normalized to the angle between ground state vibrational dipole moments ($\theta_{0,i}^{0,j}$). Both $\theta_{0,i}^{0',i'}$ and $\theta_{0,j}^{0',j'}$ increase as a function of increasing Duschinsky mixing. The sign of V_{ij} determines direction of rotation in the excited state. As the two zeroth-order vibrations in the present simulation are not perpendicular, their vector sum or difference reorient each vibrational mode asymmetrically. In the limit where $\hat{\mu}_i^0 \perp \hat{\mu}_j^0$, both vibrational modes respond symmetrically with respect to the sign of V_{ij}. The angle $\theta_{0',i'}^{0',j'}$ reports that the excited state vibrational modes largely retain their relative orientation through the transformation, rotating not only by similar magnitudes, also in the same direction. The rotation of the vibrational dipoles in space is the direct consequence of the rotation (θ_{mix}) relative to Q_k^0 as seen in Fig. 3.2. Figure 3.4 shows the response of zeroth-order dipole with a ground state angular separation of 45^o, as simulated in Sec. 3.4.1. In Sec. 3.5.2, the excited state vibrational dipole reorientation is used as a metric of Duschinsky mixing, which are indicated by the diamonds in Fig. 3.4.

3.3.2 Non-Condon Effects on Amplitude and Orientation of Vibronic Dipoles

In this section, the impact that NCEs have on the amplitude and orientation of the vibronic dipoles measured in 2D EV and 2D VE spectra is explored. The vibrational dependence of the electronic transition dipole moment is made more explicit by letting $\boldsymbol{M}_{elec}(r) \approx \boldsymbol{M}_{eg}(Q)$ and Taylor expanding over each specific vibrational coordinate in the harmonic basis set (Q_k^0) about the equilibrium nuclear configurations, Q_0.

$$\begin{aligned}\mu^{e,g} =& \mu^{(0)} \left\langle g;\nu_i\nu_j \middle| e;\nu_i'\nu_j' \right\rangle + \\ & \mu^{(1)} \sum_{k\in i,j} \left\langle g;\nu_i\nu_j \middle| Q_k^0 \middle| e;\nu_i'\nu_j' \right\rangle + ...\end{aligned} \tag{3.10}$$

In the above expression, the first two expansion coefficients ($\mu^{(n)}$) are expressed as $\mu^{(0)} = \boldsymbol{M}_{eg}(Q_0)$ and $\mu^{(1)} = (\partial \boldsymbol{M}_{eg}/\partial Q_k)_{Q_0}$. In the Condon approximation, $\mu^{(n>0)} = 0$, the FC overlap fully describes the vibronic transition of interest and the 2D vibronic pathway am-

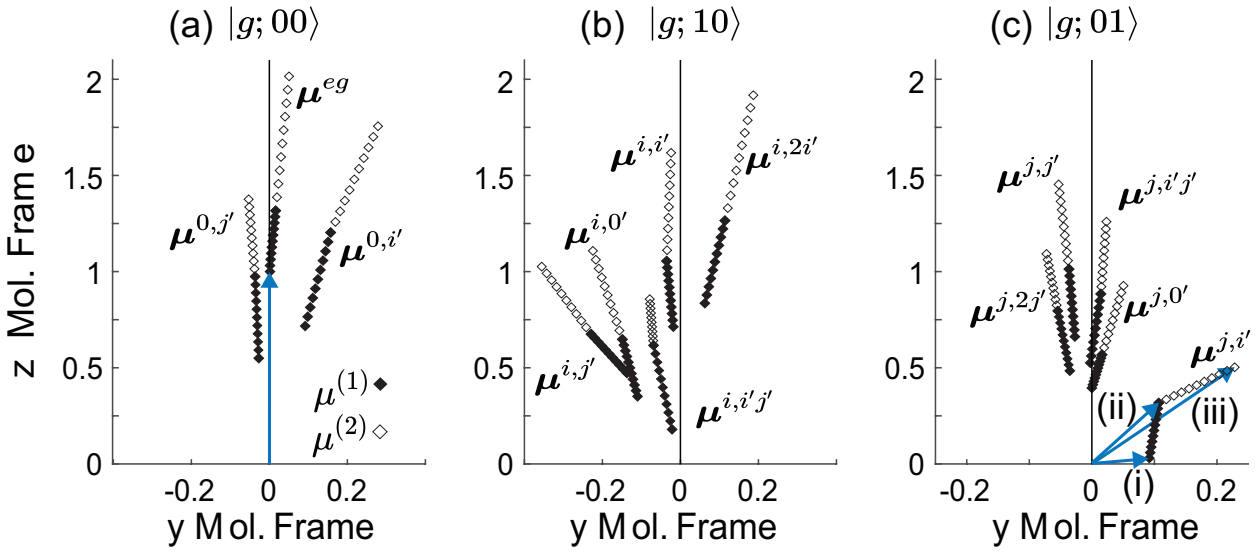

Figure 3.5: **Non-Condon Effects on Dipole Moments:** Each marker indicates terminal point of the labelled dipole vector ($\boldsymbol{\mu}^{a,b}$) for increasingly strong contributions of NCEs, plotted within the yz plane of the molecular frame. First $\mu^{(1)}$ is scaled from 0 to 0.25 (in increments of 0.025) (filled diamonds), then held constant while $\mu^{(2)}$ is scaled form 0 to 0.25 (open diamonds). All vectors are normalized to $\boldsymbol{\mu}^{e,g}$ under the FC limit ($\mu^{(1)} = \mu^{(2)} = 0$), shown as the blue vertical vector reaching the point (0,1), in panel (a) for reference. Panels (a), (b), and (c) represent dipoles originated from $|g;0,0\rangle$, $|g;1,0\rangle$, and $|g;0,1\rangle$, respectively. Dipoles (i, ii, and iii) shown in (c) all represent the same dipole ($\boldsymbol{\mu}^{j,i'}$) with varied strengths of NCEs. i) corresponds to the FC limit, ($\mu^{(1)} = \mu^{(2)} = 0$). ii) corresponds to substantial Herzberg–Teller coupling, ($\mu^{(1)} = 0.25,\ \mu^{(2)} = 0$). iii) corresponds the both first and second-order NCEs, ($\mu^{(1)} = \mu^{(2)} = 0.25$). Hamiltonian parameters are as described in Sec. 3.4. NCEs scale both amplitude and orientation of vibronic dipoles by non-uniform amounts. Both first- and second-order NCEs increase the magnitude of $\boldsymbol{\mu}^{j,i'}$ but each has oppositely signed orientational effects.

plitude is proportional to $|\mu^{e,g}|^2 = \left|\mu^{(0)}\right|^2 \left|\langle g;\nu_i\nu_j|e;\nu'_i\nu'_j\rangle\right|^2$. When the higher-order terms in Eqn. 3.10 become non-zero, the Condon approximation breaks down. The first-order expansion terms in $\boldsymbol{M}_{eg}(Q)$ are referred to as Herzberg–Teller vibronic coupling terms as this formalism parallels the Herzberg–Teller adiabatic approximation [159, 166–168] described in Eqn. 3.11.

$$\mu^{(1)} \sum_{k\in i,j} \langle g;\nu_i\nu_j|Q_k|e;\nu_i'\nu_j'\rangle = \mu^{(1)}\big[\,\langle g;\nu_i\nu_j|e;(\nu_i\pm 1)'\nu_j'\rangle + \langle g;\nu_i\nu_j|e;\nu_i'(\nu_j\pm 1)'\rangle\,\big] \tag{3.11}$$

The above equation shows that the first-order NCEs result in vibronic dipoles gaining transition intensity from neighboring transitions regardless of shared vibrational character. In other words, Herzberg–Teller coupling may drive intensity contributions to a vibronic pathway that primarily involves oscillator j through the displacement of oscillator i, and vice versa. Crucially, NCEs appear not only in amplitude modulation but also in the orientation of vibronic dipoles. Eqn. 3.10 can be written as an expansion of vector quantities over the same vibrational coordinates. The non-Condon contributions add scaled vectors while amplitudes are determined by the expansion coefficients, $\mu^{(n)}$. The full transition dipole moment connecting the ground state $|a\rangle$ to an excited state $|b\rangle$ is expressed in Eqn. 3.12 with vector contributions determined by the non-Condon vibronic dipole orientations $\hat{\mu}^{a,b}$.

$$\boldsymbol{\mu}^{a,b} = \langle a|b\rangle\,\hat{\mu}^{a,b} + \mu^{(1)} \sum_{k\in[i,j]} \left(\langle a|Q_k|b\rangle \cdot \hat{\mu}^{a,b\pm k} \right) + \mu^{(2)} \sum_{k\in[i,j]} \left(\langle a|Q_k^2|b\rangle \cdot \hat{\mu}^{a,b\pm 0,2k} \right) + \ldots \tag{3.12}$$

Figure 3.5 shows how first- and second-order NCEs influence vibronic dipoles, causing changes in orientation and amplitudes. We emphasize that simply scaling the magnitude of a vibronic dipole moment fails to capture the full impact of NCEs. Likewise, monitoring the relative amplitudes of pathways or individual dipole orientations is insufficient to accurately determine the NCEs. For example, in Fig. 3.5 (c), the relative amplitudes of dipoles $\boldsymbol{\mu}^{j,0'}$ and $\boldsymbol{\mu}^{j,2j'}$ do not change drastically over the course of this calculation, but the NCEs shift the orientation of those dipoles in opposite directions. Alternatively, dipoles of forbidden transitions with unexpectedly large amplitudes, would indicate the presence of NCEs as discussed later in Sec. 3.5.4.

Polarization-selective 2D EV and 2D VE experiments, simulated in Sec. 3.5, measure the relative angles of vibronic dipoles shown in Fig. 3.5, and give insight into the coupling of vibrational and vibronic transition dipole moments. The relative angles of vibrational dipoles in the ground and excited state manifest in the angular dependence of the excited state absorption (ESA) and ground state bleach (GSB) of the $|g;0,0\rangle \rightarrow |e;0'0'\rangle$ transitions in 2D EV spectroscopy (e.g., pathways I and II). See the first chapter of this series (2) for the definition of pathway symbol nomenclature (Sec. 2.3 and Figs. 2.3 and 2.4) [62] In 2D VE spectroscopy, direct measurement of many vibronic transition dipoles relative to $\boldsymbol{\mu}^{e,g}$ can be measured. Pathways III and V compare the relative impacts of the excited and ground state vibrations respectively by probing the transitions $|g;0,0\rangle \rightarrow |e;k'\rangle$ and $|g;k\rangle \rightarrow |e;0'0'\rangle$. Subsequent sections explore these measurements using simulated 2D vibronic spectra.

3.4 Results

In the following section we detail the calculation of eigenstates and transition dipole orientations for a model molecular system, following the procedures described in Secs. 3.2 and 3.3, respectively, and 2D EV and 2D VE spectra of that system are then simulated. These simulations map onto the schematic Figs. 2.3 and 2.4 in Ch. 2, [62] but they incorporate more realistic molecular signatures (e.g., non-zero line widths). Additionally, we discuss several points of experimental design which aid in accessing spectral information by either increasing peak separation or by enhancing weaker signals and diminishing stronger signals.

3.4.1 Simulation of Polarization-Selective 2D EV and 2D VE Spectra

The 2D EV and 2D VE spectra were simulated using all third-order nonlinear vibronic response functions for the molecular system described in this chapter. The third-order response function is described as the product of an orientational response, $\overleftrightarrow{\boldsymbol{Y}}_{\alpha}$, and vibronic response, $\boldsymbol{R}_{\alpha}^{abcd}$, summed over four vibronic states (a, b, c, d) for all considered Liouville pathways (α). The simulations incorporate (i) allowed vibronic pathways, (ii) a resonant electronic input pulse spanning frequencies $\omega_{eg} \pm \omega_k$, (iii) a resonant mid-IR pulse with sufficient bandwidth

to excite one-quantum vibrational transitions in the ground and electronic excited state and (iv) two forbidden vibronic transitions, ($|g;1,0\rangle \rightarrow |e;0',1'\rangle$ and $|g;0,1\rangle \rightarrow |e;1',0'\rangle$), explicitly discussed in Sec. 3.5. The orientational response is determined by the four angle response functions for the ZZZZ, YYZZ, ZYYZ, and ZYZY experimental polarization combinations as shown in Eqs. 2.9 and 2.10 of chapter 2 and Eqs. C.26 and C.27 of appendix C. The electric fields interacting with the sample are assumed to be in the delta function or impulsive limit, where the pulse duration is sufficiently faster than system dynamics. For these simulations we assume that the duration τ_2, is sufficiently short that $\tau_2 = 0$ dynamically, but $\tau_2 > 0$ in terms of laser pulse ordering. Dephasing functions for each vibronic pathway are written in the homogenous limit (see appendix C, Eqs. C.1-C.21).

Rephasing (R) and non-rephasing (NR) 2D EV and 2D VE spectra were calculated separately in the time domain using 0.5 and 4.0 fs steps over a full duration of 4.0 and 32.0 ps in the electronic and vibrational dimensions, respectively. Time-domain data were then fast Fourier transformed (FFT) in the τ_1 and τ_3 dimensions. The ω_{vib} and $\omega_{electronic}$ dimensions have resolutions of 2.0 cm^{-1} and 16.3 cm^{-1} respectively. Absorptive data are obtained by summing the real components of the 2D EV and 2D VE signals following an axis shift of the rephasing data. Data were simulated for four polarization conditions (ZZZZ, YYZZ, ZYYZ, ZYZY) and normalized to the global extreme before calculating isotropic spectra (ZZZZ+2YYZZ). In total, 36 (48) pathways were simulated for 2D EV (2D VE) respectively (i.e., 18 or 24 rephasing and non-rephasing pairs for the respective techniques). A list of vibronic pathways, orientational responses, and related dephasing functions included in these simulations are found in appendix D.

The simulated spectra originate from the material Hamiltonian, as described in Sec. 3.2.1 and diagonalized to produce the eigenstate energies and FC overlaps. Amplitudes and orientations of individual vibronic dipoles are determined using the method described in Sec. 3.3. Unless otherwise noted, the following parameters of the vibronic Hamiltonian were used to simulate all the spectra: $\omega_{eg}^0 = 16,500\ cm^{-1}$, $\omega_i^0 = 1,850\ cm^{-1}$, $\omega_j^0 = 2,100\ cm^{-1}$, $B_{ij} = 0$, $g_{iii} = 0.2$, $g_{jjj} = 0.3$, $V_i = 0.63 \rightarrow D_i = 0.2$ (Eqn. 3.6), $V_j = 0.77 \rightarrow D_j = 0.3$ (Eqn. 3.6),

$V_{ii} = -10\ cm^{-1}$, $V_{jj} = -30\ cm^{-1}$, and $V_{ij} = -0.24$. Unitless values are normalized to the corresponding ω_k^0, except V_{ij} is normalized to $|\omega_j^0 - \omega_i^0|$. Dephasing timescale parameters were defined as in previous work: [40] $\lambda_i = \lambda_j = 1.0$, $\Gamma_{eg,eg} = 40\ cm^{-1}$, $\Gamma_{eg,\nu_j} = \Gamma_{eg,\nu_j} = 4\ cm^{-1}$, $\Gamma_{\nu_i,\nu_i} = \Gamma_{\nu_j,\nu_j} = \Gamma_{\nu_i,\nu_j} = 4\ cm^{-1}$ $\mu^{(1)} = \mu^{(2)} = 0$. Expressions for the lineshape and dephasing functions for various 2D VE and 2D EV pathways are given in the Eqs. C.1-C.21 of appendix C. Orientations of the zeroth-order dipoles are $\boldsymbol{\mu}_{eg}^0 \measuredangle \boldsymbol{\mu}_i^0 = 45°$, $\boldsymbol{\mu}_{eg}^0 \measuredangle \boldsymbol{\mu}_j^0 = 0°$ by setting: $\hat{\mu}_{eg}^0 \parallel \hat{z}$, $\hat{\mu}_i^0 \parallel (\hat{z} + \hat{y})$, $\hat{\mu}_j^0 \parallel \hat{z}$.

The energies and transition dipole orientations of the vibrational eigenstates in the ground and excited electronic states are obtained by numerically diagonalizing both H_g and H_e, each expanded to 10 vibrational quanta. The resultant energies and orientations are: $\omega_{eg} = 15,457\ cm^{-1}$, $\omega_i = 1,834\ cm^{-1}$, $\omega_j = 2,058\ cm^{-1}$, $\omega_{i'} = 1,806\ cm^{-1}$, $\omega_{j'} = 2,042\ cm^{-1}$, $\Delta_i = 16.4\ cm^{-1}$, $\Delta_j = 46.5\ cm^{-1}$, $\Delta_{ij} = 0.0\ cm^{-1}$, $\Delta_{i'} = 15.0\ cm^{-1}$, $\Delta_{j'} = 38.2\ cm^{-1}$, $\Delta_{eg,i} = -28.2\ cm^{-1}$, $\Delta_{eg,j} = -14.8\ cm^{-1}$, $\Delta_{i'j'} = 10.8\ cm^{-1}$, $\theta_{0,0'}^{0,i} = +45.0°$, $\theta_{0,0'}^{0,j} = 0.0°$, $\theta_{0,0'}^{0',i'} = +35.1°$, $\theta_{0,0'}^{0',j'} = -12.5°$.

Table 3.1: Calculated orientations of vibrational (top panel) and vibronic (bottom panel) dipoles $\hat{\mu}^{a,b}$ in the molecular frame. Angles are described as $\theta_{0,0'}^{a,b}$ where a and b are the initial and final states of each transition as denoted in Eqn. 3.8. (e.g. $\hat{\mu}^{0,i'}$ forms an angles of $+7.3^o$ with $\hat{\mu}^{0,0'}$).

	$\|e;0',0'\rangle$	$\|e;1',0'\rangle$	$\|e;0',1'\rangle$	$\|e;2',0'\rangle$	$\|e;1',1'\rangle$	$\|e;0',2'\rangle$
$\|e;0',0'\rangle$	—	+35.1	-12.5	—	—	—
$\|e;1',0'\rangle$	—	—	—	+31.4	-6.0	—
$\|e;0',1'\rangle$	—	—	—	—	+56.1	-7.6
$\|g;0,0\rangle$	0.0	+7.3	-2.8	—	—	—
$\|g;1,0\rangle$	-17.4	-1.5	-16.2	+4.3	-6.8	—
$\|g;0,1\rangle$	0.0	+71.7	-2.3	—	-0.3	-4.2

Relative dipole orientations are listed in Table 3.1 for the excited state vibrations (top) and vibronic transitions (bottom). The excited-state rotation described in Fig. 3.4 is seen

here as mode i and j have both rotated approximately in unison away from their initial, ground state, orientations. Relative angles for vibrational dipoles involving transitions where $\Delta\nu_i = 1$ are negative as a result of vibration i gaining character of ground state vibration j and partially reorienting in the $-\hat{\mu}_j^0$ direction. The vibronic dipoles predominantly align with $\mu^{e,g}$ (i.e., $\hat{z}$). The exceptions ($|g;10\rangle \rightarrow |e;0'0'\rangle$ and $|g;01\rangle \rightarrow |e;1'0'\rangle$) reflect the weak FC overlap of the those transitions, allowing the vibrational component to more heavily influence the vibronic dipole orientation. As discussed in Sec. 3.3.1, the reorientation of the vibrational and electronic components of the vibronic dipole, is determined exclusively by the couplings present in the system Hamiltonian. Figures 3.6 and 3.7 show the simulated polarization-selective 2D EV and 2D VE spectra of the model molecular system using the parameters listed above. Here we use the pathway numbering formalism described in Ch. 2 and shown there in Figs. 2.3 and 2.4. However, we emphasize that the labels in Figs. 3.6 and 3.7 denote the dominant vibronic pathway contributing to each peak, leaving the weaker spectral features unlabeled.

The 2D EV spectra enables access to a wide swath of the excited state vibrational manifold. Each pathway represents a measure of coupling between distinct vibrational and electronic transitions. Polarization-selectivity enables the construction of a three-dimensional molecular frame describing coupled vibronic degrees of freedom and how vibrations change between electronic sates. Figure 3.6 shows polarization-selective 2D EV data in the ZZZZ and YYZZ configurations, respectively. Data are portioned into lower and upper manifolds (probing mode i and j, respectively) and vertically aligned along three separate ω_1 frequencies. Each ω_1 position corresponds to exciting initial coherences between the ground state ($|g;0,0\rangle$) and $|e;0',0'\rangle, |e;1',0'\rangle, |e;0',1'\rangle$, respectively. Each peak location in ω_3 is determined by a different transition within the excited state vibrational manifold (ESA) or ground state manifold (GSB). Measurement of excited state vibrational dipole orientations, as discussed in Sec. 3.5.2, provide a metric for the extent of Duschinsky mixing. In Sec. 3.5.1 we compare multiple pathway locations enabling the determination of the excited state anharmonicity, mixed mode anharmonicity and excited state frequency shifts, ($\Delta_{k'}, \Delta_{i'j'}$ and

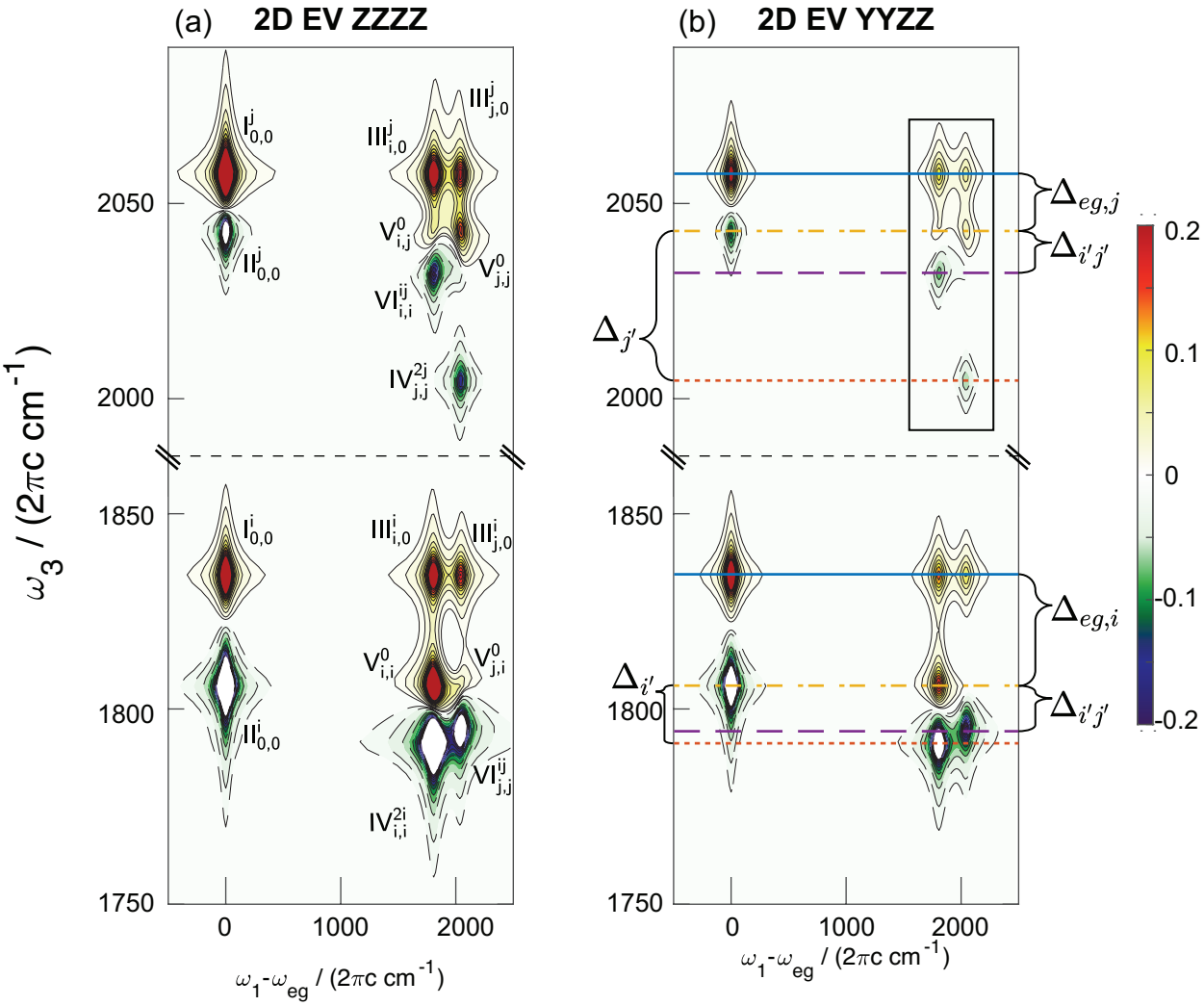

Figure 3.6: **Polarization-Selective 2D EV spectra:** (a) Simulation with ZZZZ polarization. Peaks are labelled with dominating vibronic pathway symbol. (b) Simulation with YYZZ polarization. Box corresponds to region plotted in Fig. 3.8 (b-e). Contours at ±(0.01, 0.02, 0.04, 0.08, 0.12, 0.16, and 0.20). Figures are plotted with a break in the ω_3 dimension to zoom in on the data.

$\Delta_{eg,k}$) respectively. Interactions between vibrational modes may be measured by considering regions of the 2D EV spectrum where the system is first excited at a frequency ($\omega_{eg} + \omega_{i'}$) and then probing behavior of the other vibrational mode at ($\approx \omega_{j'}$), or vice versa. Reported experimental 2D EV spectra have shown closely lying electronic states in the ω_1 dimension,

separated by hundreds of wavenumbers. [31, 32, 38, 113, 114] The simultaneous detection of ω_{eg} and $\omega_{eg}+\omega_{k'}$ peaks in the same electronic state has not been seen in experimental 2D EV studies to date. In this chapter, we discuss how such data would allow for analyses of mode specific Huang-Rhys parameters and vibronic dipole orientations (Secs. 3.5.2 and 3.5.3).

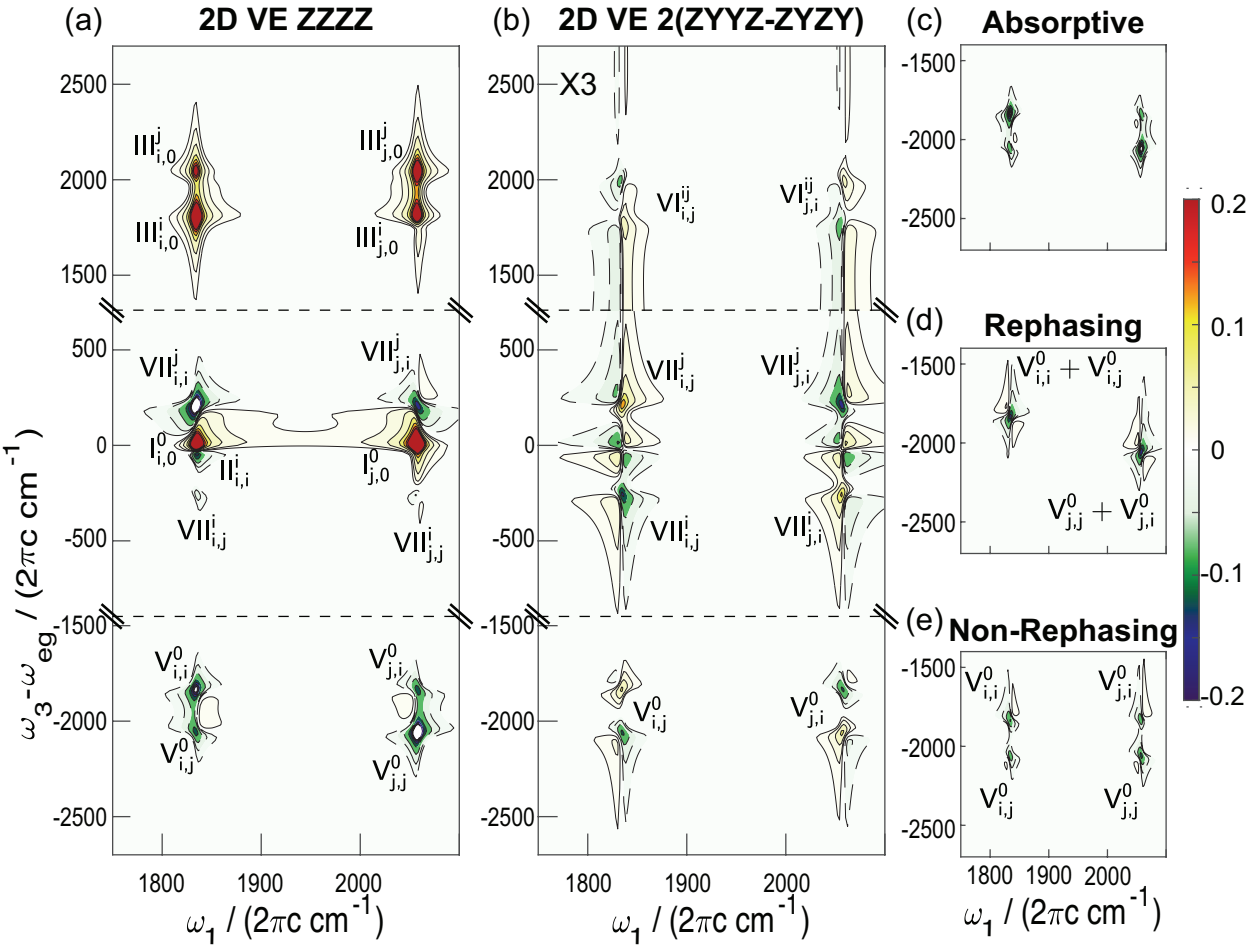

Figure 3.7: **Polarization-Selective 2D VE spectra:** (a) Simulation with ZZZZ polarization. Peaks are labelled with dominating vibronic pathway symbol. (b) Simulation with polarization combination ZYYZ-ZYZY. Contours at $\pm$(0.01 0.02 0.04 0.08 0.12 0.16 0.20). Figures are plotted with a break in the ω_3 dimension to zoom in on the data. (c-e) Isotropic 2D VE spectra of region containing pathways V. The rephasing (d) and non-rephasing (e) data are plotted separately using the same contours levels as other simulations above.

Figure 3.7 (a-b) shows the polarization-selective 2D VE spectra of the model molecular

system. Further discussion of Fig. 3.7 is detailed in Sec. 3.4.2. Generally, data are grouped into six regions, split into two columns, corresponding to an initial τ_1 coherence in mode i and mode j. In the higher manifold, vibronic transitions gained one quanta of vibrational energy so pathways cluster around $\omega_{eg} + \omega_i$ and $\omega_{eg} + \omega_j$. The middle region corresponds to vibronic transitions with $\Delta\nu_i + \Delta\nu_j = 0$. Thus, the intense GSB of pathway I appears convoluted with the many less intense ESAs which shift their vibrational character in the excited state (pathways VII). The lower manifold holds only pathways V which directly report on the coupling of the ground state vibrations to the electronic transition. Some pathways result from a τ_2 coherence and always experience a displacement in ω_3 between the rephasing/non-rephasing contribution. Positive and negative R and NR tilts appear at paired energies, most notably at pathways V and VII. The four peaks labelled III obscure direct visualization of pathways IV and VI. Many vibronic transitions lie close in energy; the fact that 2D VE accesses so many transition (13 in the two mode case) means that such convolution is inevitable. Conversely, the high density of pathways indicates that spectra are dense with information, if uncovered. In the middle manifold the obscured pathways are: $\mathsf{II}^{\mathsf{j}}_{\mathsf{j,j}}$, $\mathsf{VII}^{\mathsf{j}}_{\mathsf{i,j}}$, and $\mathsf{VII}^{\mathsf{i}}_{\mathsf{j,i}}$. Noting sign and NR or R tilts aids in pathway assignment. Rephasing pathways $\mathsf{V}^{\mathsf{0}}_{\mathsf{i,j}}$ and $\mathsf{V}^{\mathsf{0}}_{\mathsf{j,i}}$ are unlabelled but lie atop $\mathsf{V}^{\mathsf{0}}_{\mathsf{i,i}}$ and $\mathsf{V}^{\mathsf{0}}_{\mathsf{j,j}}$, respectively, as evidenced by the positively going tilt.

2D VE spectra report on the ground vibrational manifold coupling to a large progression of vibronic transitions. Isolating and assessing carefully chosen transitions reports on mode specific Huang-Rhys displacement, Duschinsky mixing, and NCEs. As discussed later, polarization-selectivity also aids the understanding of how vibrations affect the orientations of vibronic transitions. Thus far, published 2D VE spectra [29, 30, 36, 37] have been dominated by negatively going features. This is possibly a result of accessing more highly excited vibrational states, which may have greater overlap with highly excited ground state vibrations to more strongly weight to ESA pathways over GSB pathways. Experimental 2D VE data has primarily probed the $\omega_{eg} + \omega_k$ region of the electronic transition, with no data to date in the $\omega_{eg} - \omega_k$ region. Such data could aid in determining the source of the ESA

dominance in 2D VE spectroscopy.

3.4.2 Experimental Considerations

Molecular-level information held in 2D EV and 2D VE data are commonly congested by a host of factors including lifetime broadening and poor peak separation, which convolute amplitudes of neighboring pathways. Experimental 2D VE spectra often have little ω_3 definition, with spectral features broader than the probe bandwidth. [29,36,37] Here we discuss the use of experimental design to better isolate specific transition pathways in 2D vibronic spectra. For example, experimentally separating the measurement of R and NR data, achieved in other 2D techniques by controlling the wavevectors or relative phases of the input pulses, better separates pathway contributions to peak amplitudes. Here, amplitudes of overlapping pathways have been determined by subtracting the amplitudes of the corresponding R and NR neighboring pathways.

Figure 3.7 (a) shows the 2D VE spectrum for the ZZZZ (parallel) configuration. Panel (b) shows the 2D VE spectrum resulting from the difference of the ZYYZ and ZYZY configurations, hereafter referred to as ZYYZ-ZYZY. The pathways hidden in the ZZZZ data (a) are clearly seen in panel (b). While pathway $\mathsf{VII}^{\mathsf{i}}_{\mathsf{i,j}}$ is vanishingly weak in the ZZZZ data, it is has a similar magnitude to $\mathsf{VII}^{\mathsf{j}}_{\mathsf{j,i}}$ in the ZYYZ-ZYZY spectrum. The ZYYZ-ZYZY difference spectrum allows us access to pathways VI, previously completely hidden by pathways III and the τ_2 coherence pathways V in the $\omega_{eg} - \omega_k$ region. Additionally, as a result of the ZYYZ-ZYZY response there a sign change between the R and NR pathways as the order of the two dipole interactions switch and therefore the sign of θ^{signal}_{probe} also flips. Separating R and NR data by the sign of the 2D signal aids in differentiating spectral features. Figure 3.7 (c-e) demonstrates the effect of separating R from NR data. Specifically, in 2D VE spectroscopy, where there are more vibronic transitions and more τ_2 coherences, data separation and isolation are of great importance. In each τ_2 coherence the R data are offset in ω_3 from the NR and coincident with another pathway's location. All R data in the lower region (i.e., pathways V) are restricted to only two locations $[(\omega_i, \omega_{eg} - \omega_i),(\omega_j, \omega_{eg} - \omega_j)]$. NR data arises

in additional locations [$(\omega_i, \omega_{eg} - \omega_j)$,$(\omega_j, \omega_{eg} - \omega_i)$]. The additional separation of NR data allows for better data separation and amplitude measurements.

In the $(\omega_{eg} - \omega_k)$ region of the 2D VE spectrum, the two NR peaks $\mathsf{V^0_{i,j}}$ and $\mathsf{V^0_{j,i}}$ share the same amplitude with the R contributions, centered on top of the stronger peaks $\mathsf{V^0_{k,k}}$. The peak labelled $\mathsf{V^0_{i,i}}$ is equal to the pathway intensities $\mathsf{V^0_{i,i}} + \mathsf{V^0_{i,j}R}$ as those two pathways share spectral coordinates. The intensity of pathway $\mathsf{V^0_{i,j}R}$ is not directly observable in the spectrum. However, we can use the intensity of $\mathsf{V^0_{i,j}NR}$ instead because the two pathways share the same four dipole moments and are equal in intensity. The fact that the pathway $\mathsf{V^0_{i,j}NR}$ is well isolated allows us to make a direct measurement of that signal contribution. The total signal strength of the peak labelled $\mathsf{V^0_{i,i}}$ can be written as the intensity of pathways $\mathsf{V^0_{i,i}}+\mathsf{V^0_{i,j}NR}$ to distinguish the different contributions to signal observed at this (ω_1, ω_3) coordinate. To clarify the separation of pathway intensity and peak intensity, signal strength of peaks are denoted by spectral locations ($\mathbf{S}(\omega_1, \omega_3)$) and signal contributions of individual pathways are denoted by pathway symbols ($\mathbf{S}(\mathsf{N^{m_3}_{m_1,m_2}})$. The example discussed above is expressed in Eqn. 3.13.

$$\begin{aligned}\mathbf{S}(\omega_i, \omega_{eg} - \omega_i) &= \mathbf{S}(\mathsf{V^0_{i,i}}) + \mathbf{S}(\mathsf{V^0_{i,j}R}) \\ &\propto \mu^{0,i} \cdot \mu^{0,i} \cdot \mu^{i,0'} \cdot \mu^{i,0'} + \frac{1}{2}\mu^{0,i} \cdot \mu^{0,j} \cdot \mu^{j,0'} \cdot \mu^{i,0'}\end{aligned} \tag{3.13}$$

By way of example, pathways $\mathsf{I^0_{i,0}}$ and $\mathsf{II^i_{i,i}}$ are clearly overlapping and impacting the apparent intensity, making a comparison without fitting unfruitful. By only considering NR data, the negative tilt limits the extent to which the pathways overlap. Using the NR signal, measurement of $\mu^{e,g}/\mu^{i,i'} = \sqrt{\mathbf{S}(\mathsf{I^0_{i,0}})/\mathbf{S}(\mathsf{II^i_{i,i}})}$ improves from 2.61 to 1.48. We note that the value of the ratio obtained from the Hamiltonian is 1.40.

Vibronic pathways with four distinct dipoles, which always experience a coherence in τ_2, respond non-isotropically to magic angle experiments. Due to the four separate transition dipoles there is a non-zero angle subtended either by the two vibrational dipoles and/or by the two vibronic dipoles. The amplitude of the ZZZZ+2YYZZ signal falls as the cosine

of that subtended angle. Fortunately, the linear combination of geometries (ZYYZ-ZYZY) grows as the sine of that same angle (Eqns. 2.14 in Ch. 2). [62] Pathways for which this angle is zero respond isotropically under magic angle and ZZZZ+2YYZZ conditions. As a consequence of all τ_2 coherences involving the same two dipoles, normalized intensities in the ZYYZ-ZYZY combination are a function only of the transition dipoles which interact with the probe and signal fields. Thus, this linear combination not only enhances weak pathways by eliminating pathways with a τ_2 population, but can also be used as a metric to test the validity of assuming an isotropic response. Using the procedure outlined here, analysis of dipole orientations in Sec. 3.5.2 and signal amplitudes in Sec. 3.5.3 is restricted to pathways that follow the isotropic responses.

3.5 Discussion: Extracting Hamiltonian Parameters from 2D EV and 2D VE Polarization-Selective Spectra

In this section, we demonstrate how peak positions and amplitudes of the spectral features in the 2D EV and 2D VE spectra encode information about vibronic coupling parameters, vibronic dipole orientations and NCEs. Each of the following analyses can be performed in either 2D vibronic spectroscopy but a combined analysis provides additional molecular insight. For example, better peak separation in the ω_3 dimension in 2D EV enables accurate measurement of vibronic state energies, but sampling a broader range of vibronic transitions renders 2D VE substantially more sensitive to NCEs. We will demonstrate that signal positions in 2D vibronic spectroscopy report directly on Hamiltonian eigenstates. The comparisons of 2D signal amplitudes inform calculations of selected vibronic dipole strength, reporting on Huang-Rhys displacement and Duschinsky mixing. Measuring changes in dipole orientation gives additional insight into the extent of Duschinsky mixing. Finally, both 2D signal amplitude and anisotropy are revisited in the context of NCEs.

3.5.1 Signal Positions: Eigenstate Energies

Signal positions in 2D VE and 2D EV spectroscopy report on eigenstate energies and do not depend on complicating factors like the orientational response or relative amplitudes. The relatively narrow line widths of vibrational coherences manifest in peaks which are well separated along the detection axis in 2D EV spectroscopy. To highlight the advantages of 2D vibronic spectroscopic signals, this discussion assumes that Hamiltonian parameters for the ground electronic state, such as the bilinear coupling B_{ij} and mechanical anharmonicities (g_{iii} *and* g_{jjj}), have been determined by other means. We also assume the relative strengths of grounds state vibrational dipoles ($\mu^{0,i}/\mu^{0,j}$) are known. The ground state vibrational anharmonicity (Δ_k), may be deduced from 2D IR measurements, and is not observable in 2D EV spectroscopy. The excited state anharmonicity ($\Delta_{k'}$) can be found by comparing the ω_3 position of several pathways in 2D EV spectra. Pathways $\mathsf{I}^{\mathsf{k}}_{0,0}$ and $\mathsf{II}^{\mathsf{k}}_{0,0}$ appear at frequencies ω_k and $\omega_{k'}$ respectively. Table 3.2 relates measured and calculated eigenstate energies from ω_3 pathway position, or difference in position of two pathways, as labelled in Fig. 3.6. There is general agreement within the precision of the FFT. The 2D signal positions are directly sensitive to the Hamiltonian parameters which describe the model system. The energy splitting, $\Delta_{eg,k}$, reports on the strength of quadratic vibronic coupling (V_{kk}) for each mode. Additionally, ω_3 positions of 2D EV pathways $\mathsf{I}^{\mathsf{i}}_{0,0}$, $\mathsf{II}^{\mathsf{i}}_{0,0}$, $\mathsf{I}^{\mathsf{j}}_{0,0}$, and $\mathsf{II}^{\mathsf{j}}_{0,0}$ report $\omega_i = 1,834.4\ cm^{-1}$, $\omega_{i'} = 1,805.9\ cm^{-1}$, $\omega_j = 2,058.3\ cm^{-1}$, and $\omega_{j'} = 2,042.2\ cm^{-1}$, respectively.

Table 3.2: Measuring Eigenstate energies by signal positions measured in cm^{-1}. Hamiltonian values are taken as the difference of eigenstate energies of the diagonalized Hamiltonian. (Eqs. 3.2 and 3.4). Simulated values represent the difference in local extrema along ω_3 of peaks labeled in Fig. 3.6 (b).

	$\Delta_{eg,i}$	$\Delta_{eg,j}$	$\Delta_{i'}$	$\Delta_{j'}$	$\Delta_{i'j'}$
Simulated	-28.5	-16.1	-14.3	-36.8	-10.3
Hamiltonian	-28.24	-14.75	-14.99	-38.23	-10.79

For the case considered here, $B_{ij} = V_{ij} = 0$, and $\Delta_{eg,k} = V_{kk}$. We note that V_{ij} and V_{kk} collectively impact the eigenstate energies so measuring $\Delta_{eg,k}$ fails to recover V_{kk} in isolation. However, the error can be quantified since $\Delta_{i'j'}$ reports on the V_{ij}. Measuring values of $\Delta_{i'j'}$ on the same order of magnitude as Δ_{kk} informs the experimentalist about the relative strength of these two parameters. We also note that $\Delta_{i'j'}$ is a direct measure of the excited state Duschinsky mixing. It is important to note that several locations in the 2D EV spectrum report on the same energies. For example, pathways II and V share an ω_3 coordinate and the quantity $\Delta_{i'j'}$ affects signal positions for both vibrational modes. Therefore, $\Delta_{i'j'}$ can be measured as the difference in ω_3 positions of any combination of pathways II or V with any corresponding pathway VI. Figure 3.8 shows the simulated 2D EV spectra for a range of values for V_{jj}. The ω_3 position of pathways III along $\omega_3 = \omega_j$ remains unchanged as V_{jj} varies, shown by the two positive features at zero along the vertical axis for all plots in Fig. 3.8. When$|V_{jj}| >> 0$, the pathways IV $-$ VI are well removed from pathways III. The separation between III and other pathways enables direct amplitude comparisons of pathways III and I which is a measure of the mode specific Huang-Rhys parameter (D_k). The structure of the other three eigenstates move in unison, as shown by the three parallel sloped lines in Fig. 3.8 (a). Their relative positions are defined as $\Delta_{i'j'}$ and $\Delta_{j'}$, labelled in Fig. 3.8 (a), and are influenced primarily by V_{ij} and g_{jjj} respectively.

Vibrational anharmonicity in the excited state can be measured with transient 2D IR, however that is a fifth-order experiment [22,169–171] with substantially weaker signals. Here we can access the same information in a third-order experiment. In special cases, transient-IR spectroscopy can correctly measure V_{ii} or V_{jj}, with the stronger signal strengths associated with third-order spectroscopies. However, the correct interpretation of transient-IR measurements may suffer without the ω_1 resolution afforded by 2D EV as discussed previously, [62] complicating the direct link between signal positions and parameters in the vibronic Hamiltonian.

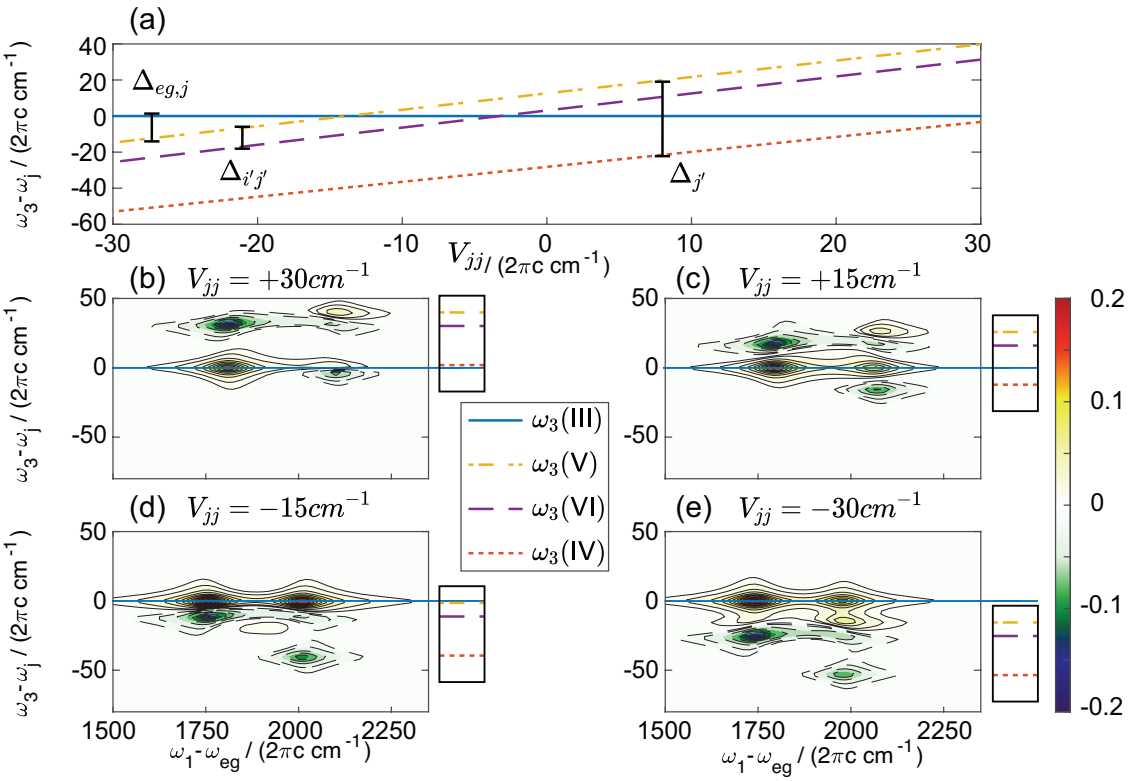

Figure 3.8: **Signal Position Dependence** (a) Calculated ω_3 positions of nearly overlapping pathways plotted as a function of the excited state frequency shifting (V_{jj}). The spectral effects of this shift are seen in the lower plots (b-e). A box showing the frequency of the three shifting energy levels, shown on right, moves as a single unit relative to the unshifting ground state frequency (blue line). As the system transitions from blue-shifted (b,c) to red-shifted (d,e) the spectrum becomes congested and difficult to decipher by eye. Similar molecular systems can present drastically different spectra, depending on the excited state vibrational energy shifts aiding or hindering pathway separation in ω_3. Besides V_{jj} all simulation parameters were held constant to those described at the beginning of this section. The ω_1 positions also shift corresponding to the shifting eigenstate energies. Labelled energy splittings combine to fully describe the energy of all measurable eigenstates for each mode. Contours at ±(0.01, 0.02, 0.04, 0.08, 0.12, 0.16, and 0.20). Plotted area corresponds to boxed region of Fig. 3.6 (b).

3.5.2 Anisotropy: Transition Dipole Orientation

Polarization-selective 2D VE and 2D EV data provides information about the orientation of vibrational and vibronic dipole moments in the molecular frame relative to the electronic

transition. The intensity of each nonlinear pathway in a 2D vibronic spectrum is the product of the orientational response ($\overleftrightarrow{\boldsymbol{Y}}_{\alpha}$) and the vibronic response ($\boldsymbol{R}_{\alpha}^{abcd}$). By comparing the amplitude of the same pathway in two different experimental polarization geometries, the vibronic response is eliminated and we gain information restricted to dipole orientations. Table 3.3 demonstrates the efficacy of angle extraction from 2D EV spectroscopy by summarizing the extraction of dipole angles for pathways $\mathsf{I}-\mathsf{IV}$ in the spectral simulations shown in Fig. 3.6. Pathways V and VI can exhibit the four angle dependence and are omitted.

Table 3.3: Summary of relative dipole orientations measured from 2D EV amplitudes. Angles $\theta_{a,b}^{c,d}$, determined by the anisotropy ,$r(\theta)$, represent the angle between vibronic dipoles $\mu^{a,b}$ and vibrational dipoles $\mu^{c,d}$. Signals with measured anisotropy values outside the range ($-0.2 \leq r \leq 0.4$) are marked by (*) and have an angle assigned by the corresponding extreme (0^o). Hamiltonian (Ham.) values follow from the diagonalization of the material Hamiltonian (Eqs. 3.2-3.5) and are calculated as the corresponding differences in angles found in Table 3.1.

Sym.	$r(\theta)$	$\mu^{a,b}$	$\mu^{c,d}$	$\theta_{a,b}^{c,d}$	Ham.
$\mathsf{I}_{0,0}^{\mathsf{i}}$	0.097	$\mu^{e,g}$	μ^{i}	45.3	45.0
$\mathsf{I}_{0,0}^{\mathsf{j}}$	0.401	$\mu^{e,g}$	μ^{j}	0.0*	0.0
$\mathsf{II}_{0,0}^{\mathsf{i}}$	0.203	$\mu^{e,g}$	$\mu^{i'}$	35.0	35.1
$\mathsf{II}_{0,0}^{\mathsf{j}}$	0.368	$\mu^{e,g}$	$\mu^{j'}$	13.4	12.5
$\mathsf{III}_{\mathsf{i},0}^{\mathsf{i}}$	0.279	$\mu^{0,i'}$	μ^{i}	26.6	37.7
$\mathsf{III}_{\mathsf{i},0}^{\mathsf{j}}$	0.396	$\mu^{0,i'}$	μ^{j}	4.4	7.3
$\mathsf{III}_{\mathsf{j},0}^{\mathsf{i}}$	0.239	$\mu^{0,j'}$	μ^{i}	31.2	42.8
$\mathsf{III}_{\mathsf{j},0}^{\mathsf{j}}$	0.403	$\mu^{0,j'}$	μ^{j}	0.0*	2.8
$\mathsf{IV}_{\mathsf{i},\mathsf{i}}^{2\mathsf{i}}$	0.348	$\mu^{0,i'}$	$\mu^{i',2i'}$	17.1	24.1
$\mathsf{IV}_{\mathsf{j},\mathsf{j}}^{2\mathsf{j}}$	0.399	$\mu^{0,j'}$	$\mu^{j',2j'}$	2.0	4.8

Table 3.3 accounts for determining the orientations of all three vibronic dipoles included in 2D EV spectroscopy via multiple pathways. Anisotropy was determined by the combination of parallel and crossed data: $r(\theta) = (ZZZZ - YYZZ)/(ZZZZ + 2YYZZ)$, using the extreme

of each peak to measure intensity. All angles were calculated directly from the anisotropy relationship: $r(\theta) = 1/5(3cos^2(\theta) - 1)$. Peaks with a measured anisotropy slightly in excess of physical bound (0.4) marked with an asterisk (*) and have angles assigned $\theta = 0$.

Each calculated angle is produced by the appropriate sum of angles between $\boldsymbol{\mu}^a$ and $\boldsymbol{\mu}^b$ in Table 3.1, thus calculated angles for pathways I and II match the values in Table 3.1. Comparing the extracted relative angles to the calculated angles, we note that the angle recovery is more accurate better separated pathways (I, II, IV) and less so for pathways III. Pathways III are often near pathways V, which can obscure the anisotropy of a single pathway. The extracted angles allow us to spatially map coupled vibronic coordinates on the molecular frame.

Measuring the reorientations of vibrational dipoles in the excited state gives insight into the extent of Duschinsky mixing. An approximation of the Duschinsky mixing can be made by considering how far modes i and j rotate in the molecular frame relative to the ground state vibrations normalized to the angle between the ground state vibrations ($\theta_{0,j}^{0,i}$ measured to be 45.3^o in Table 3.3). The ratio of angles ($\theta_{0',i'}^{0,i}/\theta_{0,j}^{0,i} = 10.3/45.3$) and ($\theta_{0',j'}^{0,j}/\theta_{0,j}^{0,i} = 13.4/45.3$) report on the extent of the excited state rotation. The measured values in table 3.3 lead to unitless quantities of 0.23 and 0.30 of θ_{norm} for modes i and j, respectively. These values correspond to an extracted V_{ij} of approximately 0.3, which is greater than -0.24, used in the simulation (see Fig. 3.4). The above ratios directly compare the orientations of the ground and excited state, and are therefore exclusively sensitive to Duschinsky mixing, excluding any ground state bilinear mixing.

3.5.3 Signal Amplitudes: Transition Dipole Strength

Just as comparing amplitudes of individual pathways normalized out the vibronic response to allow for orientational analysis, specific experimental polarizations can eliminate the orientational response for the analysis of dipole strengths through 2D peak amplitudes. Generally, 2D vibronic experiments performed at the magic angle or the linear combination of (ZZZZ+2YYZZ) signals produce the isotropic vibronic response, which is dependent only on

dipole strength. Forgoing any orientational response, the strength of the vibronic response for each vibronic pathway is proportional to the product of the four involved dipole moments. The following analyses (Eqs. 3.13-3.17) reference pathway symbols to reflect the intensity of a given pathway. For reference, pathways discussed below are listed in tables 3.4 and 3.5 along with (ω_1, ω_3) positions, pathway type: R, NR, absorptive, and the four transition dipoles that contribute to the amplitude.

Table 3.4: Pathway Dipoles of 2D EV Spectra

Pathway	Type	ω_1	ω_3	Contributing Dipoles			
$\mathsf{I}^{\mathsf{i}}_{0,0}$	ABS	ω_{eg}	ω_i	$\mu^{0,0'}$	$\mu^{0,0'}$	$\mu^{0,i}$	$\mu^{0,i}$
$\mathsf{II}^{\mathsf{i}}_{0,0}$	ABS	ω_{eg}	$\omega_{i'}$	$\mu^{0,0'}$	$\mu^{0,0'}$	$\mu^{0',i'}$	$\mu^{0',i'}$
$\mathsf{III}^{\mathsf{i}}_{\mathsf{i},0}$	ABS	$\omega_{eg} + \omega_{i'}$	ω_i	$\mu^{0,i'}$	$\mu^{0,i'}$	$\mu^{0,i}$	$\mu^{0,i}$
$\mathsf{III}^{\mathsf{j}}_{\mathsf{i},0}$	ABS	$\omega_{eg} + \omega_{i'}$	ω_j	$\mu^{0,i'}$	$\mu^{0,i'}$	$\mu^{0,j}$	$\mu^{0,j}$

The 2D EV and 2D VE spectra in Figs. 3.6 and 3.7 report peak amplitudes, distinct from pathway intensity. For well isolated 2D spectral regions, there is only one pathway contributing intensity to each peak. Elsewhere, multiple vibronic pathways share (ω_1, ω_3) coordinates (e.g. pathways $\mathsf{V}^{\mathsf{0}}_{\mathsf{i},\mathsf{i}}$ and $\mathsf{V}^{\mathsf{0}}_{\mathsf{i},\mathsf{j}}\mathsf{R}$). When multiple pathways combine constructively or destructively, effective contributions must be separated prior to dipole comparisons. As discussed in Sec. 2.6.4 of Chapter 2 [62], careful selection of τ_2 can eliminate the contributions of pathways which oscillate in τ_2. Separation of R and NR signals can also help to resolve spectrally overlapping pathways as shown earlier.

Calculating the ratio of signal intensities from different vibronic pathways produces useful information in comparing dipole strengths. We highlight four such comparisons here, though additional comparisons may be of interest, depending on the system of interest or specific experimental questions. First, 2D EV spectroscopy provides a direct measure to compare the vibrational dipole strength in the ground and excited states. Calculations for both modes may be made in a similar fashion but an example is given explicitly for mode i below.

Table 3.5: Pathway Dipoles of 2D VE Spectra

Pathway	Type	ω_1	ω_3	Contributing Dipoles			
$\mathsf{I}^{0}_{i,0}$	ABS	ω_i	ω_{eg}	$\mu^{0,i}$	$\mu^{0,i}$	$\mu^{0,0'}$	$\mu^{0,0'}$
$\mathsf{II}^{i}_{i,i}$	ABS	ω_i	$\omega_{eg} - \Delta_{eg,i}$	$\mu^{0,i}$	$\mu^{0,i}$	$\mu^{i,i'}$	$\mu^{i,i'}$
$\mathsf{III}^{i}_{i,0}$	ABS	ω_i	$\omega_{eg} + \omega_{i'}$	$\mu^{0,i}$	$\mu^{0,i}$	$\mu^{0,i'}$	$\mu^{0,i'}$
$\mathsf{III}^{i}_{j,0}$	ABS	ω_j	$\omega_{eg} + \omega_{i'}$	$\mu^{0,j}$	$\mu^{0,j}$	$\mu^{0,i'}$	$\mu^{0,i'}$
$\mathsf{V}^{0}_{i,i}$	ABS	ω_i	$\omega_{eg} - \omega_i$	$\mu^{0,i}$	$\mu^{0,i}$	$\mu^{i,0'}$	$\mu^{i,0'}$
$\mathsf{V}^{0}_{i,j}$	R	ω_i	$\omega_{eg} - \omega_i$	$\mu^{0,i}$	$\mu^{0,j}$	$\mu^{j,0'}$	$\mu^{i,0'}$
$\mathsf{V}^{0}_{i,j}$	NR	ω_i	$\omega_{eg} - \omega_j$	$\mu^{0,i}$	$\mu^{0,j}$	$\mu^{i,0'}$	$\mu^{j,0'}$
$\mathsf{VII}^{j}_{i,i}$	ABS	ω_i	$\omega_{eg} + (\omega_j - \omega_i) + \Delta_{eg,j}$	$\mu^{0,i}$	$\mu^{0,i}$	$\mu^{i,j'}$	$\mu^{i,j'}$
$\mathsf{VII}^{j}_{i,j}$	R	ω_i	$\omega_{eg} + (\omega_j - \omega_i) + \Delta_{eg,j}$	$\mu^{0,i}$	$\mu^{0,j}$	$\mu^{j,j'}$	$\mu^{i,j'}$
$\mathsf{VII}^{j}_{j,i}$	NR	ω_j	$\omega_{eg} + (\omega_j - \omega_i) + \Delta_{eg,j}$	$\mu^{0,j}$	$\mu^{0,i}$	$\mu^{j,j'}$	$\mu^{i,j'}$
$\mathsf{VII}^{i}_{i,j}$	R	ω_i	$\omega_{eg} - \Delta_{eg,i}$	$\mu^{0,i}$	$\mu^{0,j}$	$\mu^{j,i'}$	$\mu^{i,i'}$
$\mathsf{VII}^{i}_{i,j}$	NR	ω_j	$\omega_{eg} + (\omega_i - \omega_j) + \Delta_{eg,i}$	$\mu^{0,i}$	$\mu^{0,j}$	$\mu^{i,i'}$	$\mu^{j,i'}$

$$\frac{\mu^{i}}{\mu^{i'}} = \sqrt{\frac{\mathbf{S}(\mathsf{I}^{i}_{0,0})}{\mathbf{S}(\mathsf{II}^{i}_{0,0})}} \tag{3.14}$$

Because pathways $\mathsf{I}^{i}_{0,0}$ and $\mathsf{II}^{i}_{0,0}$ share the same vibronic dipoles, the ratio of their signal strength results in a comparison of their vibrational dipoles, and this provides a direct measurement of how the vibrational dipoles shift in strength in the different electronic states. Second, the determination of mode specific Huang-Rhys parameters is possible in both spectroscopies. The calculation relies on comparing the FC factors of transitions $\mu^{0,0'}$ and $\mu^{0,k'}$ and is assessed by a number of comparisons as shown below. Equations 3.15b and 3.15c respectively represent the comparisons that can be made in 2D VE and 2D EV to measure the D_k for each vibrational mode.

$$D_i = \left(\frac{\mu^{0,i'}}{\mu^{0,0'}}\right)^2 \tag{3.15a}$$

$$2D\ VE : D_i = \frac{\mathbf{S}(\mathsf{III}^{\mathsf{i}}_{\mathsf{i},0})}{\mathbf{S}(\mathsf{I}^{\mathsf{0}}_{\mathsf{i},0})} = \frac{\mathbf{S}(\mathsf{III}^{\mathsf{i}}_{\mathsf{j},0})}{\mathbf{S}(\mathsf{I}^{\mathsf{0}}_{\mathsf{j},0})} = \frac{\mathbf{S}(\mathsf{III}^{\mathsf{i}}_{\mathsf{i},0})}{\mathbf{S}(\mathsf{I}^{\mathsf{0}}_{\mathsf{j},0})}\left(\frac{\mu^j}{\mu^i}\right)^2 = \frac{\mathbf{S}(\mathsf{III}^{\mathsf{i}}_{\mathsf{j},0})}{\mathbf{S}(\mathsf{I}^{\mathsf{0}}_{\mathsf{i},0})}\left(\frac{\mu^i}{\mu^j}\right)^2 \tag{3.15b}$$

$$2D\ EV : D_i = \frac{\mathbf{S}(\mathsf{III}^{\mathsf{i}}_{\mathsf{i},0})}{\mathbf{S}(\mathsf{I}^{\mathsf{i}}_{\mathsf{0},0})} = \frac{\mathbf{S}(\mathsf{III}^{\mathsf{j}}_{\mathsf{i},0})}{\mathbf{S}(\mathsf{I}^{\mathsf{j}}_{\mathsf{0},0})} = \frac{\mathbf{S}(\mathsf{III}^{\mathsf{i}}_{\mathsf{i},0})}{\mathbf{S}(\mathsf{I}^{\mathsf{j}}_{\mathsf{0},0})}\left(\frac{\mu^j}{\mu^i}\right)^2 = \frac{\mathbf{S}(\mathsf{III}^{\mathsf{j}}_{\mathsf{i},0})}{\mathbf{S}(\mathsf{I}^{\mathsf{i}}_{\mathsf{0},0})}\left(\frac{\mu^i}{\mu^j}\right)^2 \tag{3.15c}$$

A key advantage to note in expressions 3.15 is the abundance of available comparisons. Each instance of pathways I and III can be related back to the Huang-Rhys parameter, enabling the averaging of multiple measurements in well defined spectra or an opportunity to still find this information within a restricted detection spectral window.

2D spectral amplitude also holds information about the level of Duschinsky mixing in the system. In 2D VE spectroscopy, pathways III and V share vibrational dipole moments allowing for a direct comparison of their vibronic dipoles to inform on this delocalization as shown in Eqn. 3.16. Signal strength of pathway V is determined using the method outlined in Eqn. 3.13.

$$\frac{\mu^{0,k'}}{\mu^{k,0'}} = \sqrt{\frac{\mathbf{S}(\mathsf{III}^{\mathsf{k}}_{\mathsf{k},0})}{\mathbf{S}(\mathsf{V}^{\mathsf{0}}_{\mathsf{k},\mathsf{k}})}} \tag{3.16}$$

As stated in Sec. 3.2.3, excited state bilinear coupling changes the measurement of displacement as the excited state coordinates are rotated and projected onto the ground state coordinates. Figure 3.9 shows how the comparison in Eqn. 3.16 may be used to approximate the level of Duschinsky mixing in a system. The trend in Fig. 3.9 provides useful information in multiple ways. First, in the unmixed limit the DHO. prediction ($\langle g;0|e;k'\rangle = \langle g;k|e;0'\rangle$) holds, so the ratio approaches unity for both modes. Second, anharmonicity plays only a minor role in the pertubative limit and therefore might be excluded from consideration in approximating the extent of mixing. Third, the sign of V_{ij} may be determined by comparing

the effect in both modes. As the excited state becomes further mixed, each mode experiences the oppositely signed effect. Positive values of V_{ij} increase the dipole ratio in the higher frequency mode and vice versa. Fourth, as a consequence of the third point, we are better equipped to distinguish between Duschinsky mixing and Herzberg–Teller coupling. Figure 3.5 shows Herzberg–Teller coupling increasing the intensity of all pathways with lower FC overlaps. Here, the oppositely signed effect in each mode allows us to attribute these intensity shifts to Duschinsky mixing altering the FC overlap, rather than an increased Q-dependence of the electronic dipole.

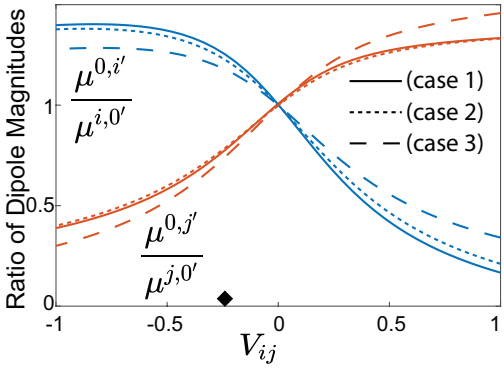

Figure 3.9: **Duschinsky Mixing Measured in Dipole Magnitude:** Ratio of $\mu^{0,k'}/\mu^{k,0'}$ as a function of Duschinsky mixing. Both modes respond in opposing manners for opposing signs of coupling. The parameter V_{ij} normalized to $|\omega_j - \omega_i|$. Only V_{ij} is varied in plot. Case 1) Represents the modeled molecular system. The parameters B_{ij}, V_i, V_j, g_{iii}, and g_{jjj} match the modelled molecular system. Case 2) demonstrates the low impact of anharmonicity on this measurement by varying only slightly from case 1. The parameters B_{ij}, V_i, and V_j match the modelled system but $g_{iii} = g_{jjj} = 0$. Case 3) Shows the effect the linear coupling terms V_i and V_j in harmonic oscillators. The parameter B_{ij} matches the simulation $g_{iii} = g_{jjj} = 0$. The parameters V_i and V_j are set such that $D_i = D_j = 0.5$ (Eqn. 3.6). Black diamond indicates the value of V_{ij} used in the model system calculation.

Another avenue by which we access a measure of the Duschinsky mixing is through the strength of dipoles in which the vibrational character changes. Thus, properties of the mode switching transition dipole ($\mu^{i,j'}$) also prove to be of interest. While these transitions are typically forbidden, 2D VE spectroscopy may be more sensitive to their detection. Ideally,

each ground electronic state vibrational mode would be compared to each electronically-excited vibrational mode. For example, a comparison of the FC factors in the transitions $\mu^{j,j'}$ and $\mu^{i,j'}$ could yield insight into the similarities of modes j and j'. Spectral congestion in the present simulated 2D VE spectrum affords one such comparison, shown in Eqn. 3.17. Any comparison of 2D VE pathways II and VII leads to further understanding of how the FC overlap between a single vibration in one state is split between the modes in the other electronic state.

$$\frac{\mu^{i,j'}}{\mu^{i,i'}} = \sqrt{\frac{\mathbf{S}(\mathsf{VII}^{\mathsf{j}}_{\mathsf{i,i}})}{\mathbf{S}(\mathsf{II}^{\mathsf{i}}_{\mathsf{i,i}})}} \tag{3.17}$$

Table 3.5 highlights that multiple pathways overlap and complicate this measurement; therefore, pathway amplitudes are determined by relationships like: $\mathbf{S}(\mathsf{VII}^{\mathsf{j}}_{\mathsf{i,i}}) = \mathbf{S}(\omega_i, \omega_{eg} + (\omega_j - \omega_i) + \Delta_{eg,j}) - \mathbf{S}(\mathsf{VII}^{\mathsf{j}}_{\mathsf{j,i}}\mathsf{NR})$. While poor peak definition of pathways $\mathsf{II}^{\mathsf{i}}_{\mathsf{i,i}}$ and $\mathsf{II}^{\mathsf{j}}_{\mathsf{j,j}}$ inhibits this comparison for the present system, the effect can be discussed qualitatively. The considerable strength of pathway $\mathsf{VII}^{\mathsf{j}}_{\mathsf{i,i}}$ and weak presence of pathway $\mathsf{II}^{\mathsf{j}}_{\mathsf{j,j}}$ are further evidence for excited state delocalization.

A summary of dipole strengths measured through ratio of pathway amplitudes is found in Table 3.6. Calculations of Eqn. 3.15b and 3.15c, found by four separate comparisons report the mean of the measured value. Pathways which are more well separated better recover the calculated values. The determination of D_j from 2D EV data is superior to that of the 2D VE data as pathways III in the 2D EV spectrum are isolated while pathways III in the 2D VE data contend with contributing amplitude from pathways IV and VI. Clearly the measurement from Eqn. 3.17 lacks accuracy due to the proximity of pathways I and II. Both Duschinsky mixing and Huang-Rhys displacement are of great interest to the electronic spectroscopy community, but are difficult to measure directly, requiring assistance from additional modeling. [123,140,142,153,172] Here, calculations of dipole orientation and dipole strength, demonstrate the sensitivity 2D vibronic spectroscopy to both effects.

Table 3.6: Dipole strengths measured from simulated spectra and determined from the relationships discussed above. Hamiltonian values refer to ratios of dipole strengths which result form material and interaction Hamiltonians.

Eqn. #	Mode	Relationship	Measured	Hamiltonian
15	i	$\mu^i/\mu^{i'}$	0.80	0.899
15	j	$\mu^j/\mu^{j'}$	1.50	1.567
16 b	i	D_i	0.60	0.523
16 b	j	D_j	0.42	0.303
16 c	i	D_i	0.46	0.523
16 c	j	D_j	0.29	0.303
17	i	$\mu^{0,i'}/\mu^{i,0'}$	1.67	1.964
17	j	$\mu^{0,j'}/\mu^{j,0'}$	1.16	1.394
18	i	$\mu^{i,j'}/\mu^{i,i'}$	1.73	0.689

3.5.4 Non-Condon Effects

Section 3.3 described a method by which NCEs could impact not only the magnitude but also the orientation of individual vibronic dipoles. This Section explores the consequences of that angular and magnitude dependence. As described in Eqn. 3.12, the NCEs depend on adjacent transition intensities. Figure 3.10 shows the isotropic amplitude and anisotropy parameter (r) for selected 2D VE pathways as a function of non-Condon expansion coefficients $\mu^{(1)}$ and $\mu^{(2)}$. Generally, the pathways show an increase in response to the intensity borrowing described by the first-order NCEs. Interestingly, the sign change from $\mu^{(1)}$ to $\mu^{(2)}$ is not always consistent. There are clear indications to the presence of NCEs; chief among them is the amplitude seen in pathway $\mathsf{VII}^{\mathsf{i}}_{\mathsf{j,j}}$ which is negligible under the Condon approximation due to the nearly zero FC overlap of states $|g;01\rangle, |e;1'0'\rangle$. Assigning strength of NCEs from individual pathways is non-trivial as first- and second-order effects can a single pathway in opposing ways. Unfortunately, an experiment cannot selectively measure a response with

and without NCEs. As a result, these effects should be understood through the most useful lens: their apparent effect on a normalized spectrum. Therefore, the weak presence of $\mu^{(2)}$ effects in the 2D VE pathways $\mathsf{II}^{j}_{j,j}$ and $\mathsf{VII}^{i}_{i,j}$, manifesting as a decrease in amplitude.

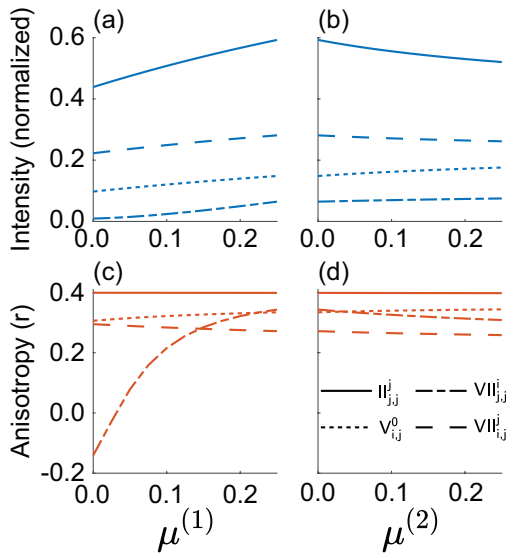

Figure 3.10: **Non-Condon Effects on Selected Pathways:** Pathway intensity is plotted in (a) and (b) for increasing first- ($\mu^{(1)}$) and second-order ($\mu^{(2)}$) NCEs, respectively. Pathway Anisotropy is plotted in (c) and (d) for the same conditions. In panels (a) and (c), $\mu^{(2)} = 0$. In panels (b) and (d), $\mu^{(1)} = 0.25$. These values of $\mu^{(1)}$ and $\mu^{(2)}$ map directly onto transitioning from case (i)-(iii) for each dipole in Fig. 3.5. Pathway intensity responds non-uniformly as the result of each expansion term. Only through NCEs does pathway $\mathsf{VII}^{j}_{i,j}$ have any measurable intensity. For some pathways, both first and second-order effect increase amplitude, others strengthen under first-order NCEs and weaken under second-order NCEs. The NCEs in anisotropy plots range from indiscernible for pathway $\mathsf{II}^{j}_{j,j}$, to slightly positive or negative for ($\mathsf{V}^{0}_{i,j}$, $\mathsf{VII}^{j}_{i,j}$), to drastic for pathway $\mathsf{VII}^{i}_{j,j}$.

Generally, the 2D VE spectrum experiences a larger shift in peak intensities as a function of NCEs because it samples many more electronic transitions within the vibronic progression than the 2D EV spectrum. For the system simulated here, the 2D EV spectrum is almost entirely insensitive to the second-order NCE whereas most pathways in the 2D VE spectrum measure some level of amplitude modulation. Of particular note, the 2D VE pathway $\mathsf{VII}^{i}_{i,j}$ has negligible intensity under the FC limit and, under $\mu^{(1)}$, has magnitude similar to allowed

transitions because they gain strength from neighboring allowed transitions. They respond weakly to $\mu^{(2)}$ because under that term of the expansion, they are gaining intensity from other forbidden transitions. The amplitudes of peaks arising from pathways VII do not necessarily confirm the presence of NCEs in and of themselves. While it is true that some pathways show enhanced sensitivity to NCEs, it is possible to encounter a system with significant overlap between $|g;10\rangle$, $|e;0'1'\rangle$ and $|g;01\rangle$, $|e;1'0'\rangle$. Such a system would have a highly mixed excited vibrational manifold in which the first mode loses much of its ground state character - an effect which should be detectable in the amplitudes and orientations of transitions discussed in Secs. 3.5.2 and 3.5.3. For example, effects in the relative FC amplitudes of 2D VE pathways $\mathsf{II}^{j}_{j,j}$ and $\mathsf{VII}^{i}_{i,j}$ are observed. In the absence of NCEs, the amplitude of pathway $\mathsf{VII}^{i}_{i,j}$ exceeds that of pathway $\mathsf{II}^{j}_{j,j}$, indicating a considerable Duschinsky rotation in the excited state vibrational manifold. However, if first-order NCEs do play a role, then the pathway VII intensities are expected to increase substantially. The reason for the increase is the fact that their forbidden vibronic transitions lie adjacent to allowed transitions with significant overlap (e.g. $|g;0,1\rangle \rightarrow |e;1'0'\rangle$ borrows intensity from $|g;0,1\rangle \rightarrow |e;0'0'\rangle$). As seen in the amplitudes of 2D VE pathways V, these are strong dipoles. Abnormal intensities for 2D VE pathways VII can be treated as an indication of NCEs, prompting further experimentation and consideration in more rigorous analyses.

3.6 Conclusions

In this chapter, we made use of a simple model material Hamiltonian with linear, quadratic, bilinear, and cubic perturbations, expanding on previous work to couple multiple vibrational modes of arbitrary frequency and orientation. Under the Born–Oppenheimer approximation, we described the relationships between Hamiltonian parameters and vibrational and vibronic dipole orientations, that account for the nuclear dependence of the electronic transitions cast in the molecular frame. Further, we tracked the orientational response as dipoles responded to first and second-order NCEs. Using the model Hamiltonian and the nonlinear orientational response functions detailed in chapter 2, polarization-selective 2D EV and 2D

VE spectra were simulated. The 2D peak positions, amplitudes and anisotropy were used to measure the relative orientation and amplitude of each dipole created by material Hamiltonian, the Huang-Rhys parameters and Duschinsky rotation. Finally, we elucidated how NCEs can both scale and rotate dipole moments through a complete treatment of the expanded vibronic dipole moment, and the surprising influence of the NCEs on the 2D vibronic spectra was discussed thoroughly. All of these pieces fit together to answer the question left open by Ch. 2, [62] where the discussion of the spectra was in the context of generalized eigenstates and transition dipole moments: What gives rise to these unique eigenstates? We identify the origin of those eigenstates and transition dipoles, and calculate their impact on 2D vibronic spectral observables. We then perform the analysis in reverse, starting with the 2D spectra to tease out the Hamiltonian parameters describing the physical and dynamical properties of the molecular system which generate these spectra. In doing so we provide an intuitive framework for future investigations to build molecular-level understanding with confidence in the information measurable by these 2D vibronic spectroscopies. In this study, two anharmonic vibrational modes are treated explicitly. However, the approach accommodates an arbitrary number of anharmonic oscillators, describing any number of vibrational coordinates including solvent interactions, and inter/intramolecular modes that are dark to the experiment. We expect that the inclusion of bath-induced population and coherence transfer processes will impact the extraction of angular information depending on the coupling between the system and the bath. The continued experimental development and use of 2D VE and 2D EV techniques will depend on the concurrent advances in theoretical treatments of vibronic coherent dynamics in simulating experimental 2D vibronic spectra.

Chapter 4

COHERENCE TRANSFER IN TWO-DIMENSIONAL ELECTRONIC-VIBRATIONAL SPECTROSCOPY

4.1 Introduction

This chapter reports on more recent developments in the field addressing the manifestations of coherence transfer, specifically in two-dimensional electronic-vibrational spectroscopy (2D EV). It describes recent work which outlines how the breakdown of the Born–Oppenheimer approximation leads to ultrafast τ_1 coherence transfer in the model proton transfer system 10-hydroxybenzo[h]quinoline (HBQ). The excited-state intramolecular proton transfer (ESIPT) has been well studied to undergo a barrierless transition in less than 15 fs [3, 173, 174], which agrees with in silico work [175]. This transfer is well under the time duration of well-compressed pulses used in current electronic and vibronic spectroscopies [23,36,110,116,176, 177], as vibronic spectroscopies are often limited by a bandwidth compression limit of both the electronically and vibrationally resonant pulses.

Typically a light–matter interaction prompts a change in the state of the system. Each additional pulse of light in an experiment constitutes another instance at which the state can change. Third-order nonlinear response theory assumes coherences and population states simply decay between light–matter interactions, limiting the number of possible states accessed during experimental time to those reached explicitly by the successive application of bra and ket side interactions of the related Feynman diagrams [40, 62, 63, 85, 126]. Additional states may be accessed during the experiment through coherence or population transfer events, in which the system progresses into a new coherence or population without the prompting of a light–matter interaction. This phenomenon has been observed and modeled in experiments ranging from purely vibrational coherence transfer [15], to vibronic

coherences of mixed electronic and vibrational character [178], and further discussed in the optical regime [179] Population transfers have been specifically leveraged in vibrational spectroscopy to enable isolation of specific subsets of ensembles for study [180]. Recently, work by Gaynor et al. [38] tracked the τ_2 dynamics of a vibronic coherence in a Ruthenium-centered solar cell dye molecule, $N3^{4-}$, partially reviewed in Sec. 2.6.2. This 3D EV experiment monitored multiple vibronic states over the course of τ_2. It used time–frequency analysis to show oscillations between those two coherences, each one growing and dying in time with the other. These results show how vibronic interactions are both utilized in molecular systems undergoing a host of excited state dynamics and are readily measured and tracked by these vibronic spectroscopies.

4.2 Born–Oppenheimer Approximation and Proton Transfer

The Born–Oppenheimer approximation is key to simplifying complex vibronic interactions and is commonly invoked to separate problems into distinct electronic and nuclear components. It states that nuclei are sufficiently large and therefore sufficiently slow-moving that they are effectively stationary on the timescale on which electrons move [158]. Pointedly, electronic structure calculations often assume a single averaged geometry of fixed nuclear coordinates. Even our own formalism is informed by the work of Ballhausen [159] which treats distinctly separable states as described in Sec. 3.1. This assumption has been incredibly successful and has been invoked consistently to help researchers, ourselves included, parse difficult problems, like developing models for these spectroscopies [40,62,63]. For light nuclei, specifically protons, which may undergo rapid motions, transfers, or tunneling events, a full quantum mechanical treatment is necessary [181–183].

A recent set of experiments explored the ESIPT of HBQ through the use of two- and three-dimensional Electronic-Vibrational spectroscopy. HBQ is used as a model for the ESIPT process because of its size, calculable tractability, solvent-dependent behavior, and chemical tunability. Among the analyses produced in those experiments is key evidence for HBQ violating the Born–Oppenheimer approximation seen through the origin of an excited

state emission (ESE) signal which arose from a τ_1 coherence transfer. The most intense features (excited state absorptions, ESAs) were measured at the red edge of the enol→enol* (E→E*) transition energy (shown in Fig. 4.1). An initially unexplained set of features arose at an energy lower than expected, which resulted in the following analysis.

The primary feature in the 2D EV spectrum is a series of ESA peaks centered in ω_1 just to the blue of $2.55 \times 10^4 \text{cm}^{-1}$. These positively going features are generated from a similar pathway in which, following both pump pulses promoting the system into the E* state and the ESIPT shifting the system into the keto* (K*) geometry, the probe pulse is absorbed. These ESA peaks report directly on the vibrational manifold of the K* state. Each peak within the column labeled ESA constitutes a different vibrational mode in the keto* state coupled to the excitation. These peaks coincide, in ω_1, with the red edge of the spectral bandwidth of the probe pulse and the red edge of the E→E* transition. The unexpected data then, come in the form of spectral intensity lower in ω_1 than the pump pulses' bandwidth. Any explanation must explain a τ_1 coherence energy gap that is not directly excitable via the pump pulse.

4.3 Coherence Transfer Observed in 2D EV spectra

The negatively going ESE signals spanning $\approx$ 2.40–2.47 $\times 10^4 \text{cm}^{-1}$ in ω_1, provide unique insight into the excited state enol to keto tautomerization process. The ESIPT has been well studied experimentally to proceed without barrier in less than 15 fs [3,4,173,174] which agrees with recent in silico work [175]. These signals originate from a coherence transfer occurring during τ_1 in experimental time, which is modulated by a high frequency mode.

Coherence and population transfer events have been discussed and observed in the vibrational [11], electronic [178, 184], and vibronic spectroscopies [38, 40, 62, 63]. They are generally observed in connection with long-duration transitions, tracked over hundreds or thousands of femtoseconds. These data result from a distinct process in which the coherence transfer enables the observation of the ESE signal. While ESE signals can be produced in EV spectroscopy, their origin is tied to accessing a vibrationally excited state, oscillating in

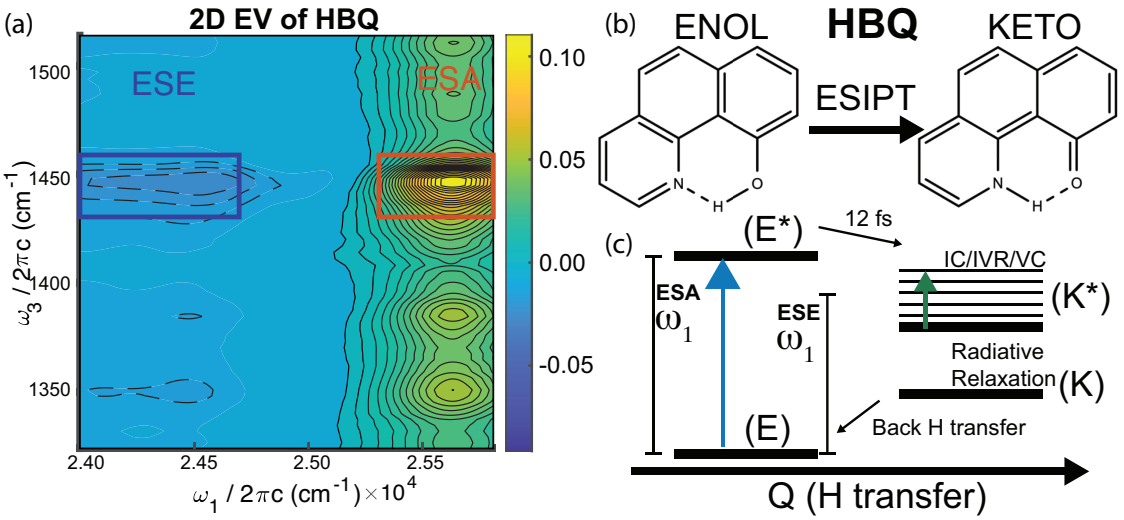

Figure 4.1: **HBQ structure and EV Surface (a)** Two-Dimensional Electronic-Vibrational spectrum of HBQ taken at τ_2=250 fs. The primary signals at ω_3= 1450 cm^{-1} form an ESE and ESA. Boxes relate to the integrated areas used in analysis represented in Fig. 4.2. **(b)** Structure of HBQ shown in the enol and keto forms, before and after ESIPT. **(c)** Simplified energy landscape of HBQ. The electronic excitation(blue arrow) is from (E)→(E*) states. The proton transfer occurs balistically on the order of 12 fs. The system is then probed (green arrow) in the (K*) electronic state while the system undergoes a series of intersystem crossings (IC), intramolecular vibrational relaxations (IVR) and vibrational Cooling (VC). Note that the frequency of the ESE is less than the (E,E*) energy gap.

ω_1 at frequencies higher than ω_{eg}. If it were not for the rapid transfer event, the system would not access a vibrationally hot state required for the emission process. This constitutes a direct observation of the Born–Oppenheimer approximation breaking down as the nuclear and electronic degrees of freedom are simultaneously and cooperatively undergoing this transfer. Not only are these nuclear degrees of freedom crucial to the production of the ESE signal, but also in modulating the transfer, seen in its oscillation over the course of τ_1.

Following a procedure similar to previous work [38], a sliding window FFT over τ_1 was performed with a 5 fs width, 1 fs two-sided hyperbolic tangent rise/decay, in 1 fs steps. This produced a time domain signal correlating to the regions of τ_1 which most strongly contribute to the EV signal. Both the ESA and ESE were fit, omitting the first 12 fs. The ESA fits a

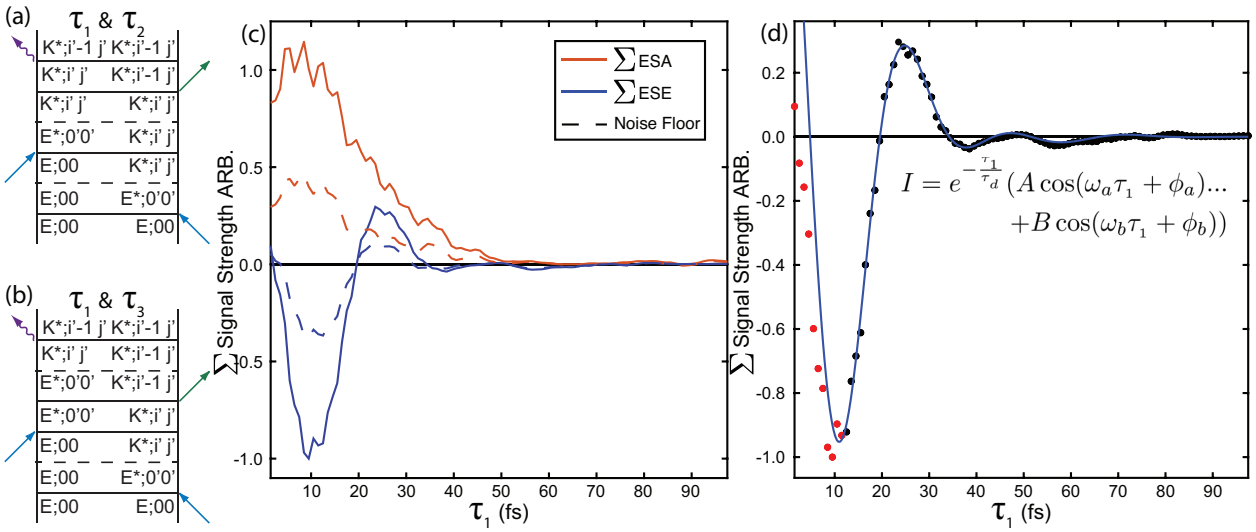

Figure 4.2: **Time Frequency Analysis of ESE Along τ_1:** Possible coherence transfer pathways are shown in **(a)** and **(b)** which might produce the negatively going features at ω_1=2.40–2.45×10^4 cm^{-1}. Coherence transfer occurs between the E* and K* states, which produces the lower frequency oscillation during τ_1. A second coherence transfer is required for the system to terminate in a population state. This can occur during in either τ_1 or τ_3 shown in (a) and (b) respectively. **(c)** τ_1 dependent signal contribution (details in text) of the ESE and ESA region. Dashed line shows the noise floor for each region, determined in the same manner as used for ω_2 beat maps. The ESA has an appreciable intensity at τ_1=0 and decays over that period. The ESE grows in over the first 12 fs and then clearly oscillates in τ_1. **(d)** Time domain fitting of the ESE signal shown in (c). Data omitted from the fit (related to the growth of the signal) is shown in red.

single exponential decay with a time constant of 13.1±0.5 fs. The ESE fit the decaying sum of two sinusoids (equation inset of Fig. 4.2 (d) with an equivalent time constant 12±2 fs and frequencies 755±50 cm^{-1} and 1405±90 cm^{-1}. the low-frequency mode Joo and co-workers attributed to the non-Born–Oppenheimer dynamics in 2020 [4].

Informed by modeling of the third-order response theory and accounting for all non-coherence transfer pathways [40, 62, 63], it is clear that these signals exclusively arise from a τ_1 coherence transfer producing an ESE of the excited state keto* state. Feynman pathways can be found in reference [62] and a discussion of how peaks move around in (ω_1, ω_3) space in reference [63]. Their negative sign eliminates the possibility of an ESA pathway. As, in a

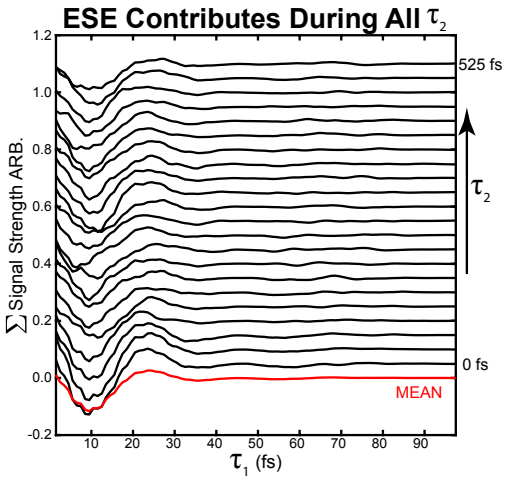

Figure 4.3: **τ_2 Dependence of ESE Signal in HBQ:** The general oscillatory behavior of the ESE along τ_1 is preserved throughout τ_2. Further the mean behavior of the system retains its phase of oscillation indicating this is primarily a τ_1 phenomenon which is only modulated by the system's behavior in τ_2 or τ_3.

GSB, $\boldsymbol{k}_1$ and $\boldsymbol{k}_2$ interact on the same side of the Feynman diagram and $\boldsymbol{k}_2$ returns the system to the ground state, the system must evolve in τ_1 at a frequency resonant with the $\boldsymbol{k}_2$ field. Thus, only the ESE pathway is capable of producing signals at this low ω_1 region. However, the ESE pathway is incapable of producing a low ω_1 frequency coherence in the absence of a population or coherence transfer. Proposed Feynman pathways involving a τ_1 and τ_2 or τ_3 coherence transfer are shown in Fig. 4.2 (a) and (b) respectively. The fit data shows a strong oscillation in τ_1 and that behavior is largely replicated along all of τ_2 (shown in Fig. 4.3), suggesting that this transfer occurs within the first few femtoseconds of experimental time. Finally, as seen in Fig. 4.2 (c) the ESE signal grows in during τ_1 in contrast to the initial amplitude seen in the ESA. This suggests that the ESE coherence is initiated as a transfer during τ_1. While this does occur within the IRF of the experiment, it happens on the same timescale on which others have observed the proton transfer [3, 4, 174]. The fact that each ESE arises at a probe frequency equivalent to an ESA peak indicates that both sets of peaks are reporting on the same vibrational manifold. This is consistent with the timeline that a τ_2

population transfer occurs during the ESA pathway. For all the data shown, we are probing the vibrational manifold which sits atop the electronically excited keto* form.

This is direct evidence of the Born–Oppenheimer approximation breaking down in ESIPT systems. This is not surprising, but instead rather encouraging, as these spectroscopies are specifically sensitive the coupling between nuclear and electronic degrees of freedom. The Born–Oppenheimer approximation assumes that coupling is negligible. Signals from outside the bandwidth of the pump pulses requires a sub-ensemble of the system to access states during τ_1 which are non-resonant with those energies. Further, the sign of these signals indicates a vibrational hot state proceeding though an ESE pathway. These two effects combine to restrict origin of these signals to electronic states which are strongly coupled to specific vibrational modes, but not necessarily optically accessible. In addition to directly reporting on coupling in the electronically excited manifold, this demonstrates the feasibility for future experiments to purposefully investigate dark electronic states in a pseudo-background free manner.

Chapter 5

X-RAY PUMP X-RAY PROBE TRANSIENT ABSORPTION SPECTROSCOPY: MODELING AND COMPUTATIONS

Relevant publications, with the permission of AIP publishing:

- [64] Chelsea E. Liekhus-Schmaltz, Phay J. Ho, Robert B. Weakly, Andrew Aquila, Robert W. Schoenlein, Munira Khalil, and Niranjan Govind. "Ultrafast X-ray pump X-ray probe transient absorption spectroscopy: A computational study and proposed experiment probing core-valence electronic correlations in solvated complexes", *Journal of Chemical Physics*, vol. 154, no. 21,p. 214107-9, 2021

5.1 Introduction

The advent of multicolor, ultrafast X-ray pulses at free electron lasers (FELs) such as the linac coherent light source (LCLS), offers the possibility of performing novel X-ray pump, X-ray probe (XPXP) spectroscopy experiments. X-ray pulses can now be separated by ∼30% of their photon energies, and future technologies will allow experimenters to arbitrarily tune the energy of one soft X-ray pulse and one hard X-ray pulse at the Tender X-ray Instrument at LCLS. [56, 185–188] XPXP experiments will therefore be able to measure an atomic site-specific electronic excitation with an atomic site-specific probe potentially tuned to a different element to directly measure charge flow in a molecule. For example, with sufficiently short (∼ 100 as) and intense pulses the X-ray pump can be used in a stimulated X-ray Raman measurement, creating a localized electronic excitation that can be probed with an X-ray pulse. [189–193] While pairs of different colored attosecond pulses are not currently demonstrated, longer X-ray pulses can also be used to generate novel, atomic site-specific excitations to study electronic dynamics.

Most XPXP spectroscopy experiments have been conducted on gas phase molecules using electron and or ion coincidence measurements. [194–199] These experiments have successfully studied the molecular dynamics of the selected gas phase molecules, and as a result, considerable effort has been made to extend these techniques into the liquid and solid phases. [200–204] Recent literature suggests that XPXP techniques [191, 205, 206] could be useful for studying solvated transition metal systems, which are common models for photocatalysis and photosynthesis.

Optical or IR pump, X-ray probe measurements have already proven that X-ray absorption spectroscopy is a useful tool for studying the transient electronic character in solvated transition metal complexes. [207–211] The limitation of these techniques lies in the pump energy. While optical pulses can be used to initiate charge transfer and measure subsequent changes in the valence electronic structure, they cannot initiate or measure changes in the local charge density around specific atoms. Instead, in an ultrafast, XPXP experiment, we can initiate complex orbital relaxations and electron motions by specifically ionizing the Fe atom for example and then monitor the changes via transmissive X-ray absorption near edge spectroscopy (XANES).

Femtosecond XPXP measurements provide the opportunity to extend these experiments to both shorter time scales by avoiding group velocity mismatch and by exciting novel electronic states to study detailed aspects of the electronic structure. Both benefiting and complicating this approach is the added layer of complexity brought by the X-ray pump pulse. X-ray pulses generate a core hole in the excited atom which is subsequently filled by higher-lying electrons via fluorescence and Auger–Meitner decay, resulting in the ejection of one or more electrons and a superposition of many electronic states after a few femtoseconds [212]. Probing this host of new electronic states gives researchers access to previously hidden electronic interactions; answering questions like: What role do core electrons play in electron transport processes? How do high-lying core electrons impact the ligand field splitting? The diversity of electronic states to be probed requires a knowledge of their distribution resulting from the cascade caused by the X-ray pump pulse.

While X-ray absorption and emission spectra of solvated systems have been successfully calculated using time-dependent density functional theory (TDDFT), [213–219] and electron cascades have been studied in liquid and solid samples, [220] electron cascades have not yet been studied in solvated transition metal systems to which most state-of-the-art electron cascade calculations are not readily applicable. In this chapter, we attempt to bridge this knowledge gap by utilizing an atomic electron cascade calculation [221, 222] to guide our TDDFT-based X-ray absorption near-edge spectroscopy (XANES) calculations.

5.2 Ground State Experimental and Calculated Spectra

We begin by examining the ground state Fe K-edge XANES spectra of $K_4Fe^{II}(CN)_6$ and $K_3Fe^{III}(CN)_6$ to establish the essential XANES features, which will be used as a baseline when describing the excited state Fe K-edge features in Sec. 5.5, where computational details can be found. Given that the X-ray pump will produce a highly ionized compound, we first compare ground state spectra of two analogous compounds, with the oxidation state of Fe varied between them to provide reference points for understanding the spectra to come. We present both experimental and calculated XANES spectra of $K_4Fe^{II}(CN)_6$ and $K_3Fe^{III}(CN)_6$. Experimental XANES data were taken at the Advanced Light Source (ALS) at beamline 10.3.2, and is reproduced from reference [216], where a more detailed experimental account can be found.

The experimental and calculated XANES spectrum of the Fe^{II} and Fe^{III} oxidation states of $K_4Fe^{II}(CN)_6$ are shown in Fig. 5.1. Both $K_4Fe^{II}(CN)_6$ and $K_3Fe^{III}(CN)_6$ have B peaks which are quadrupole transitions from the 1s to e_g orbitals and C peaks which correspond to primarily 1s to π^* orbital transitions (shown in detail in Fig. 5.2). $K_3Fe^{III}(CN)_6$ has an "A" peak, corresponding to a quadrupole transition from the 1s to t_{2g} orbital, which has a vacancy in this oxidation state. Both the A and C peaks are significantly modified by the change in oxidation state with the A peak appearing and the C peak blue shifting as the Fe oxidation state changes from II to III. The energy splitting between the A and B peaks is a key signature of the valency of the Fe atom in $Fe(CN)_6$ and is a direct measure

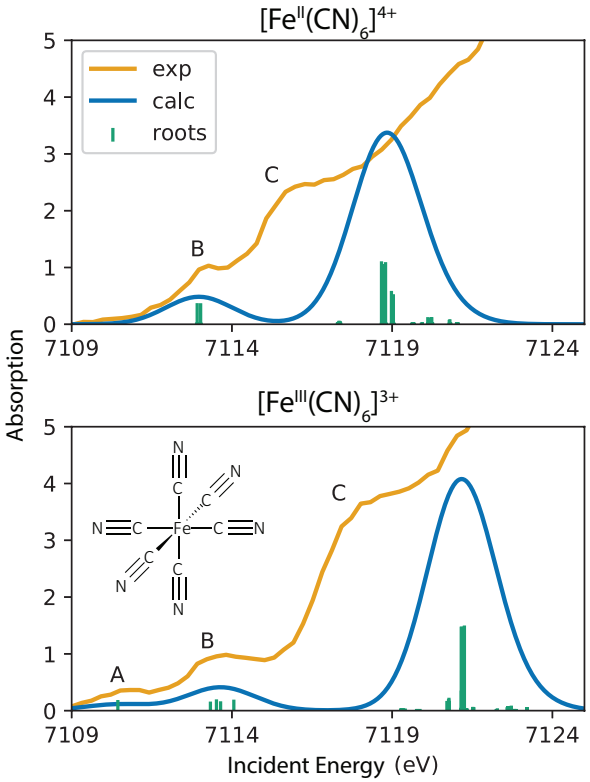

Figure 5.1: **Experimental and calculated Fe K-edge XANES of $K_4Fe^{II}(CN)_6$ and the complimentary complex $K_3Fe^{III}(CN)_6$.** Both oxidation states have B, and C peaks which correspond to a 1s to e_g and π^* transition. The A peak is only visible in the Fe^{III} oxidation state where there is a vacancy in the t_{2g} orbital. The calculated roots are broadened by 1.5 eV and scaled by 4×10^4 from the raw oscillator strength. Figure 5.2 shows these transitions in more detail. The experimental data are presented in arbitrary absorption units.

of the ligand-field splitting, which is 3.3 eV in the experimental spectrum and 3.2 eV in the calculated spectrum. [216]

While the position of the A and B peaks are well represented by the calculation, the C peak is less so. The lowest lying roots of the C peak are 1.4 eV removed from the experimental data and C peak maximum is further removed, more than 3 eV from the experiment. This discrepancy is largely due to the strong solvent interactions involved in the π^* orbitals,

which are not fully captured by the implicit solvent model. In our earlier work, [216] we have shown how the C peak is strongly dependent on the solvent. The C peak is therefore an important marker for probing solvent–solute interactions. All three of these peaks provide important insights into the valency, ligand-field splitting, and solvent–solute interactions. In the subsequent sections, we will show that the XPXP spectrum has similar peaks that provide additional measures of these properties and provide more opportunity to study these interactions.

5.3 Conceptual Experimental Overview

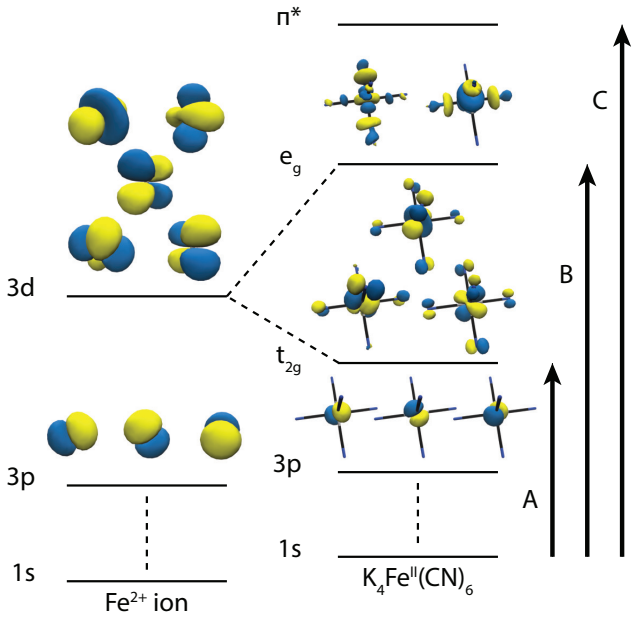

Figure 5.2: **Comparison of Atomic and Molecular Orbitals in the Fe Complex:** Atomic orbitals of the bare Fe^{2+} ion are compared with the $K_4Fe^{II}(CN)_6$ molecular orbitals. The 3p orbitals in the solvated system are well represented by the ion, while the 3d orbitals are strongly modulated by the ligands. Also shown are the electronic transitions involved in the XANES spectrum. We label the 1s to t_{2g} transition "A", the 1s to e_g transition "B", and the 1s to π^* transition "C". The splittings are not drawn to scale. Both sets of orbitals are drawn with the same isovalues. Orbitals of $K_4Fe^{II}(CN)_6$ are further scaled in unison to show the molecular frame and ligand contributions to e_g and t_{2g} molecular orbitals.

We will consider the following X-ray pump X-ray probe procedure: a femtosecond X-ray pump with photon energy above the Fe K-edge removes a 1s electron to initiate an electron cascade and an X-ray probe that is below the Fe K-edge observes the XANES signal. The calculated electron cascade informs the XANES calculations by reporting the type and distribution of both core and valence holes in the system as a function of time. While we can calculate the Fe K-edge XANES spectrum of $K_4Fe^{II}(CN)_6$, at this time, it is not straightforward to calculate the electron cascade of the solvated system. Therefore, to simplify our calculations, we have performed the electron cascade calculations on an isolated Fe^{2+} ion, which has the same charge as the Fe oxidation state and low-spin configuration as in $K_4Fe^{II}(CN)_6$ as described earlier. We then use the resulting electronic configurations to determine which configurations (holes) to consider as references in our XANES calculations.

The accuracy of this simplification is largely determined by the similarities and differences between the atomic and molecular orbitals. In Fig. 5.2 we show the 3p and 3d atomic and molecular orbitals of both the Fe^{2+} ion and $K_4Fe^{II}(CN)_6$ to compare the two. From visual inspection, we see that both 3p orbitals are very similar. This is because the 3p molecular orbital is completely composed of Fe atomic orbitals. The 3d molecular orbital shows obvious differences between the ion and molecule due to the octahedral metal–ligand coordination. In contrast to the 3p orbital, the Fe t_{2g} orbital is hybridized with the cyanide ligand orbitals. It is likely, therefore, that electron cascade processes that involve 3p and lower orbitals are well represented by the Fe^{2+} ion, while those processes that involve electrons in the 3d orbitals are less likely to be accurately modeled.

5.4 Monte-Carlo Simulations of Auger–Meitner Cascades

For the electron cascade dynamics, we used our previously developed on-the-fly Monte-Carlo rate equation method, [223, 224] which has been used to model nonlinear X-ray multiphoton processes and inner-shell relaxation in atoms and molecules. In this method, all electronic processes are treated as random quantum processes, where the probabilities are weighted by the transition rates. The rates are computed using the Hartree–Fock–Slater (HFS) elec-

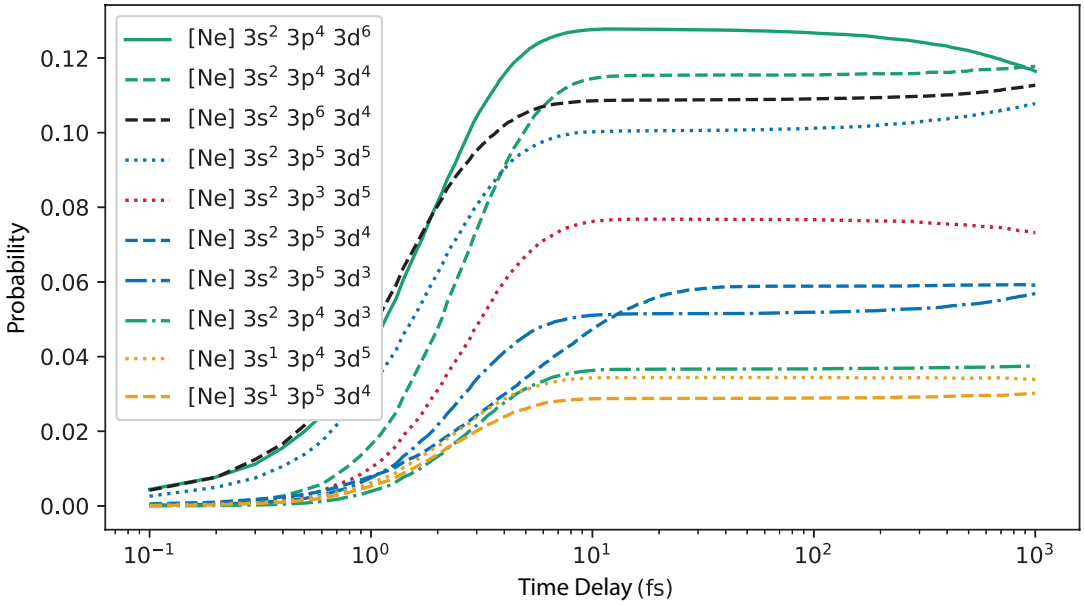

Figure 5.3: **Electron Configurations During Electron Cascade.** The probability of the top ten most likely electron configurations after 10 to 100 fs are shown above. Lines of the same color have the same lowest electron hole, and lines of the same style have the same highest electron hole. To prepare for the XANES portion of the calculation, we rely on the Monte-Carlo electron cascade calculation to identify which holes are the most relevant to a potential X-ray pump X-ray probe experiment. We see that 3p and 3d orbitals are the most likely places for an electron hole after 10 to 100 fs.

tronic structure method, which includes relativistic corrections and spin-orbit coupling terms, following the procedure outlined in reference [225]. We have used this method to study X-ray interaction with bromine ions. [226] Briefly, we first calculate the non-relativistic HFS energies and wave functions for all the occupied and unoccupied orbitals. From these wave functions and the HFS potential, the relativistic energy corrections (relativistic mass-velocity and Darwin corrections) and spin-orbit energies are computed. To compute the inner-shell decay rate, the non-relativistic HFS wave functions and orbital energies with relativistic and spin-orbit corrections are used. We note that these cross-sections and rates are calculated for spin-averaged electronic configurations, but they are sensitive to the occupation numbers

and energies of the individual spin-orbit orbitals.

We used 100,000 trajectories to obtain a converged time profile of the cascade dynamics. The following steps are repeated until the transitions cease. In our cascade dynamics simulations, each trajectory is started with a 1s hole in the Fe^{2+} ion in the low-spin electronic configuration to approximate the low-spin $K_4Fe^{II}(CN)_6$ complex and the rates of individual Auger–Meitner and fluorescence decay channels are computed. A random number is then generated to determine if an electronic transition takes place in a given time step. A transition occurs if the calculated probability of the transition is greater than the randomly generated number. If no electronic transition occurs, the time step is advanced and a new random number is generated. If a transition occurs, one decay channel is selected and the Auger–Meitner and fluorescence rates are computed for the new selected electronic configuration. The time step is then advanced and another random number is generated to determine if there is a transition. These steps are repeated until there are no more transitions. From the time history of these transitions, the time profile of all participating electronic configurations can be computed.

The result of the electron cascade calculation is shown in Fig. 5.3 where the top 10 most probable electronic configurations after 10 to 100 fs as displayed. These electronic states compose 75% of the total population at the start of 10 fs. We see that the original 1s hole has resulted in configurations with primarily 3p or 3d holes. Some of these configurations have additional lower lying holes in the 3s orbital. The probability of having a vacancy in 2s or 2p after 10 fs is small. The remaining states not shown in Fig. 5.3 also contain primarily 3s, 3p, and 3d holes. Overall, in the 10-100 fs window, more than 99% of the configurations has one of more 3p or 3d holes and about 17% of these configurations also have 3s hole. For the rest of our analysis we use the resulting population statistics to motivate studying the effect of several combinations of 3p and 3d holes on the XANES spectrum of $K_4Fe^{II}(CN)_6$.

5.5 Electronic Structure Calculations of Predicted States

All DFT and TDDFT-based XANES calculations were performed with the NWChem computational chemistry program. [213, 227, 228] The PBE0 exchange–correlation functional [229] was used as we have previously shown that this functional is sufficiently accurate to describe the overall structure, dynamics, and spectra over a wide energy range for solvated transition metal complexes. [216, 217] The COSMO (COnductor-like Screening MOdel) [230, 231] implicit solvation model with a dieletric constant of 80.1 was used to represent the water solvent instead of an explicit solvent representation to reduce the complexity of the model. All-electron calculations were performed using the 6-311G** basis set [232, 233] for the light atoms and the Sapporo-TZP-2012 basis for the Fe atom. [234] Previously converged geometries from reference [216] and tabulated in Appendix F were used and were kept fixed for all calculations.

Having identified 3p and 3d orbitals as the most important electron hole locations after a 1s ionization event, we now calculate the resulting XANES spectra of the solvated system with these reference hole configurations. The spectra we generate use the same geometry, basis set, and exchange-correlation as those in the ground state $K_4Fe^{II}(CN)_6$ calculation. The reference hole configurations are generated by converging the Kohn-Sham orbitals with specified molecular orbital occupancies using the "occup" block feature in NWChem, which are then used for XANES calculations. By using TDDFT, we acknowledge that the spectra can only be captured within the space of single excitations. However, we believe this approach can provide a first order estimate in combination with the appropriate reference. The final calculated XANES spectra of $K_4Fe^{II}(CN)_6$ in the ground state and five different excited electronic configurations that involve 3p and t_{2g} holes are shown in Fig. 5.4. Each XANES spectrum shows the characteristic B and C peaks that represent a 1s to e_g and π^* transitions, respectively.

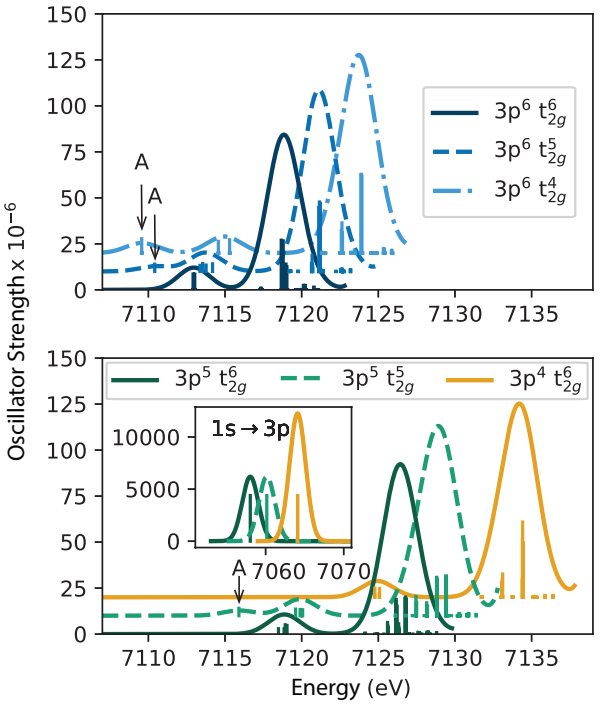

Figure 5.4: **Calculated XANES spectra of several electron configurations with 3p and t_{2g} holes.** The spectra are calculated using 100 roots, broadened by 1.5 eV, and shifted by 143.8 eV to match the $K_4Fe^{II}(CN)_6$ ground state XANES. The top panel shows the spectra of electronic configurations with filled 3p orbitals while the bottom panel shows the spectra of electronic configurations with at least one hole in the 3p orbitals. For easy visualization, we only plot the A, B, and C peak regions in the main figures. The A peaks are indicated by arrows. The inset shows the lower energy peaks caused by a 3p vacancy.

5.5.1 Valence Hole States

The first aspect we focus on is the appearance of new peaks in the spectra shown in Fig. 5.4. There are two main sets of additional peaks that appear, the A peak and a much stronger lower energy peak around 7060 eV. The A peak appears when there is a vacancy in the t_{2g} orbital as in the configurations [Ne] $3s^2\ 3p^6\ 3t_{2g}^5$, [Ne] $3s^2\ 3p^6\ t_{2g}^4$, and [Ne] $3s^2\ 3p^5\ t_{2g}^5$. The strength of the A transition also scales with the t_{2g} orbital vacancy, which can be seen by comparing [Ne] $3s^2\ 3p^6\ t_{2g}^5$ and [Ne] $3s^2\ 3p^6\ 3t_{2g}^4$. As well, the splitting between the A and

B peak increases with the orbital vacancy going from approximately 3.2 eV to 5.4 eV as the hole vacancy increases from 1 to 2.

Initial states with a hole in the t_{2g} orbital provide a unique opportunity to examine key chemical properties of $K_4Fe^{II}(CN)_6$. As in the ground state, the splitting between the A and B peak provides direct measurement of the splitting between the t_{2g} and e_g orbitals as well as a measurement of the Fe oxidation state. Measuring this splitting with different electron configurations, such as with or without a 3p hole provides the opportunity to examine how the ligand-field splitting is affected by interactions between the 3p and 3d electrons or the oxidation state of the Fe atom. The lower energy peaks around 7060 eV, which we will refer to as the 3p peaks, appear in the configurations [Ne] $3s^2\ 3p^5\ 3t_{2g}^6$, [Ne] $3s^2\ 3p^5\ 3t_{2g}^5$, and [Ne] $3s^2\ 3p^4\ 3t_{2g}^6$ where there is a 3p vacancy. Here, the transitions are much stronger since they are dipole allowed, compared to the A and B which are dipole forbidden. Again, the strength of the transition scales with the vacancy of the 3p orbital. As with the A peaks, the 3p peaks also shift with t_{2g} and 3p vacancy, once again providing a measure of the interaction between the 3p and t_{2g} electrons.

The electron configuration also affects the C peak. Removing electrons from the t_{2g} orbital blue shifts the broad C peak by approximately 2.5 eV, while removing a 3p electron causes an approximately 7.5 eV shift. As we saw in the ground state calculation, the C peak is sensitive to solvent–solute interactions. [216] Therefore, the size of the shifts reflects both the relative screening ability of the different orbitals on the excited 1s electron and changes in solvent–solute interactions due to the various charge states. The C peak can therefore measure not only the effect of the overall charge on solvent interactions as noted in earlier studies, but also the position of the charge within the total electronic state, depending on the hole position.

In an XPXP experiment, we expect that some portion of the states we have discussed above will contribute to the initial state since they would appear after approximately 10 fs, a time scale short enough that significant nuclear or valence electronic motion would not yet occur. We also see in Fig. 5.3 that the electron cascade does not significantly evolve after this

time, meaning that further changes would then be dominated by metal–ligand, or solute-solvent interactions. While we do not consider the evolution of these peaks as a function of pump–probe delay in this manuscript, the peaks that we identified in this discussion would be good candidates for monitoring in a time-evolving system.

5.5.2 3p Core Hole States

To consider the same states of interest from another perspective more robustly, we produce in Fig 5.5 the 1s→3p XANES spectra for both $K_4Fe^{II}(CN)_6$ (a) and $K_3Fe^{III}(CN)_6$ (b). The second oxidation state makes a convenient experiment, as it allows for comparing the electron cascade under varied initial conditions, with and without an added valence hole. While the Fe^{III} complex could be missing the peak corresponding to the [Ne] $3s^2\ 3p^5\ t_{2g}^6$ configuration, other peaks should be largely comparable. While the electron cascade could vary between the two oxidation states, that variance can be separated into two aspects. The first is radiative decay processes from the t_{2g}, which should vary by no more than $1/6^{\text{th}}$ due to the missing electron. The second is in Auger–Meitner and Coster–Kronig processes which could vary to a greater extent due to the necessary action of multiple electrons.

Noting the different scale in oscillator strength, these transitions show great promise for future exploration. Peaks generally lie to the blue of the atomic Kβ energy ≈7,058 eV. Just as the valence hole states shifted with each successive hole in the 3p, we see that behavior mirrored. For all [Ne] $3s^2\ 3p^5$ states, we observe an approximate blue shift in the 1s→3p transition energy of 2 eV. This is present in both oxidation states. Additionally, subsequent holes in the 3p, shift the 1s→3p transition energy substantially further, on the order of 10 eV. Given the lifetime broadening of 3p states in third row transitions metals is on the order of a single eV [235], an XPXP experiment should expect to spectrally separate and isolate these states, affording the separate study of each $3p^{n<6}$ state.

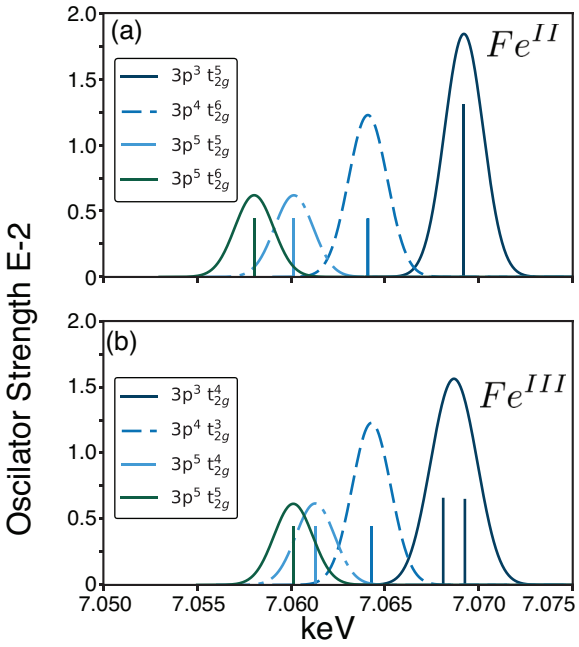

Figure 5.5: **Calculated shifts in 1s → 3p transition energy and oscillator strengths** for $K_4Fe^{II}(CN)_6$ (a) and $K_3Fe^{III}(CN)_6$ (b) for a selected sample of electronic states. All configurations listed in the inset have a filled [Ne] $3s^2$ core. The spectra are calculated using 100 roots, broadened by 1.5 eV, and shifted by 143.8 eV to match the $K_4Fe^{II}(CN)_6$ ground state XANES. Additional holes in the valence create a sequential blue-shift in the transition energy in both compounds.

5.6 Proposed Experimental Design

In consideration of the proposed experiment, it is prudent to underscore an easily overlooked outcome of the calculated XANES spectra. As seen in Fig. 5.4, a 3p core hole shifts the valence energies sufficiently so that peaks A of $3p^6\ 3d^n$ species are isolated from those which have a 3p core hole. Thus we are left with two separable experiments. Probing the red edge of the A-C region reports on species without 3p holes. Probing the 3p region reports on those species with a 3p hole. The C and 3p peaks and the splitting between the A and B peaks were identified in the previous section as useful measurements in an XPXP experiment. Given that the A, B, and C peaks are sensitive to the ligand-field splitting and the solute-solvent

interactions, an ideal experiment would measure the contributions of all three peaks in the excited electronic state simultaneously. The spectral congestion in the B-C region, shown in Fig. 5.4, limits that global resolution. We therefore explore the feasibility of measuring an individual A peak, spectrally isolated from that congestion, and by considering the strong signal strengths of dipole allowed transitions in the 3p region.

Of those electronic configurations containing an A peak, the [Ne] $3s^2$ $3p^6$ t_{2g}^4 configuration is both predicted by the electronic cascade and its A peak is generally well separated from the other calculated XANES transitions. Note in Fig. 5.4, that peaks A-C of electronic state with 3p holes are blue shifted from those with a full p shell. The A peak of configurations with additional holes in the 3p would be further blueshifted, removing them from the present consideration. Moreover, the splitting resulting from holes in the t_{2g} further redshifts the A peaks. These two interactions make [Ne] $3s^2$ $3p^6$ t_{2g}^4 configuration the most likely candidate for an individually resolved electronic state in the region. This provides the best opportunity to calculate the feasibility of the experiment in this region, neglecting more highly ionized species. Resolving 1s to 3p transitions is less dependent on signal size, as they are dipole allowed.

Both X-ray pulses would be focused onto a liquid-jet of the solvated sample. The first pulse would be tuned to above the Fe K-edge to remove a 1s electron and initiate the cascade and resulting dynamics. We assume a $\sim$10 fs delay between the two pulses, which represents the time at which most electron cascade dynamics conclude. While, certainly, some valence dynamics occur on this timescale there is a trade-off between capturing those dynamics and probing stationary configurations. The scale of this delay should be reconsidered with the realization of attosecond pulses but is necessary given the current technology available. It is considered to be a portion of the instrument response function of the experiment. Just as the experiment is limited in the short times scale ($<$10 fs) by the resolution of the electron cascade and the available femtosecond pulse durations, it is also limited on the long timescale ($>$100 fs) as nuclear dynamics dictate the molecular response. The assumption of fixed molecular geometry breaks down, as would the molecule itself.

The second pulse would be below the Fe K-edge and span the appropriate region of the XANES spectrum. Two spectrometers would be used to measure the signal. One would be downstream of the interaction region to measure the experimental spectrum and one would be a transmissive spectrometer upstream to measure the incoming X-ray pulses' shot-to-shot spectrum. [236] While the exact spectrum of the pump pulse is not a source of noise, the spectrum of the probe pulse is critical to extracting the spectroscopic signal. Such a configuration is best conducted in the CXI (Coherent X-ray Interaction) hutch at LCLS, [237] where we can make use of their liquid jet capabilities, the tight X-ray focus, and place the upstream spectrometer in the X-ray transport tunnel. We cannot generate a full expected experimental signal since we have not calculated all of the most likely electronic states predicted by the electron cascade. Instead, we can predict the expected signal contribution from electronic states in which we are most interested.

To generate the expected experimental signal, we assume an initial excitation rate of 10% and a 100 μm liquid jet with a 500 mM concentration of $K_4Fe^{II}(CN)_6$. We use the tabulated X-ray absorption properties of Fe to predict the absorption edge size. [238] We can then appropriately scale the calculated XANES spectrum and superimpose it on our scaled experimental ground state absorption edge, appropriately shifted with the B peak position to represent the change in the ionization energy. The resultant signal is shown in the lower panel of Fig. 5.6 for the [Ne] $3s^2 3p^6 t_{2g}^4$ electronic state where we have assumed that this state makes up 10% of the resultant initial electronic state. The corresponding ground state absorption spectrum generated from the same edge and the calculated XANES spectrum along with the absorption due to the water and cyanide ligands is shown in the upper panel of Fig. 5.6.

To observe this signal, we would measure a difference spectrum between the pumped and ground state spectrum. The uncertainty of a difference signal at the A peak energy can be estimated from the definition of the absorption absorption spectrum, $A(h\nu)$, relative to the measurement at the downstream spectrometer, M, and the measurement at the upstream

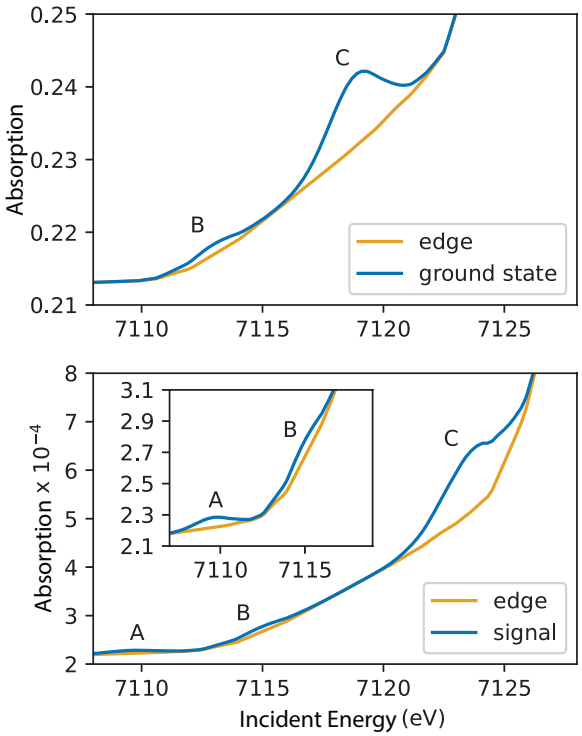

Figure 5.6: **Predicted Contributions to XPXP valence Signal.** The expected absorption signal from the [Ne] $3s^2$ $3p^6$ t_{2g}^4 electronic state, scaled for its expected ∼10% probability and ∼10% overall excitation rate is shown in the lower panel. Included is both the broadened signal and the absorption edge. The inset shows the A and B peak in more detail. The upper panel shows the ground state absorption using the same edge, the calculated spectrum, and the background absorption from the ligands and the solvent for comparison. This figure allows us to estimate the signal size in order to determine the averaging time necessary for a 120 Hz experiment. The absorption edge is the combined absorption of all atoms, including solvent, according to tabulated values. [238]

spectrometer, P, at photon energy $h\nu$:

$$M(h\nu) = P(h\nu)(1 - A(h\nu)). \tag{5.1}$$

The uncertainty of the difference spectrum is then given by

$$\delta A(h\nu) = A\sqrt{\left(\frac{\delta M}{M}\right)^2 + \left(\frac{\delta P}{P}\right)^2}. \tag{5.2}$$

Assuming shot-noise-limited detection consistent with photon counting, and that the $\frac{\delta M}{M} \approx \frac{\delta P}{P}$,

$$\delta\Delta A(h\nu) = 4A(h\nu)\sqrt{\frac{1}{N_{photons}(h\nu)}}, \tag{5.3}$$

where $N_{photons}(h\nu)$ is the number of photons in the X-ray probe at photon energy $h\nu$ over the bandwidth of one pixel.

For the measurement in question, we will estimate that $N_{photons}(h\nu) \approx 11000$ for each pulse, which is the pixel well depth of the ePix10k detector currently installed at the CXI hutch. From the upper panel of Fig. 5.6, we estimate that the total absorption A between 7110 and 7125 eV is 0.22. At 120 Hz, 4.5 hours of data collection will approximately provide the necessary number of photons to resolve the change in absorption of 6×10^{-6} at the A peak. Averaging over several pixels would reduce this averaging time. To resolve the ∼10 times larger C peak, only 2.7 minutes of data collection is necessary. With the prospect of LCLS-II coming online, which promises MHz repetition rates, measuring both the A and C peak are well within feasibility limits.

The same experiment can and should be conducted evaluating exclusively the 3p core states, due to their Superior dipole strength. The technical feature possibly preventing this experiment is the relative energetic distance between the valence edge and the 3p orbitals. Reaching sufficiently large energy separation utilizing the current methods of most FELs precludes that separation.

5.7 Conclusions

In order to fully exploit the unique element-specific capabilities of X-ray pump X-ray probe experiments in solvated molecular systems, it is essential to understand the specific electronic states resulting from electron cascades, and how these states are manifest in X-ray absorption spectra (as measured by the probe.) We have proposed combining an atomic electron cascade calculation with a TDDFT-based XANES calculation to accomplish this goal in a solvated model transition metal complex. The electron cascade calculation allowed us to identify

which molecular orbitals were most likely missing electrons after the cascade. We then calculated the XANES spectra of several electronic configurations with the corresponding holes. We believe this approach will be necessary for interpreting and predicting XPXP measurements, and the methodology laid out in this manuscript could be one way to attain these results.

We then evaluated how these different electron holes could be useful for measuring chemically relevant properties, such as the ligand-field splitting, and 3p and 3d electron interactions. From this we identified the A-B peak splitting and the C peak in the [Ne] $3s^2$ $3p^6$ t_{2g}^4 electron configuration as one potential target for experimental observation. We laid out an experimental plan that will allow us to test our computational approach and prediction, and showed that this experiment is currently feasible with present LCLS conditions. Understanding these interactions in model transition metal systems lays the ground work for studies on more complex interactions like those found in solvated cyanide-bridged mixed-valence bimetallic electron transport compounds involving, for example, a combination of 3d and 4d transition metal centers. As XPXP measurements continue to mature, they will provide new insight into not only solvated transition metal complexes, but solvated systems in general, and the computational and experimental techniques presented here can serve as a guide for that development.

Chapter 6

X-RAY PUMP X-RAY PROBE TRANSIENT ABSORPTION SPECTROSCOPY: EXPERIMENT AND ANALYSIS

6.1 Introduction

Femtosecond pump–probe spectroscopy utilizing a sequence of two time-delayed femtosecond light pulses is used extensively to understand complex chemical phenomena in the condensed phase following the development of high-intensity, commercially available, and tunable ultrafast laser systems. In these widely used experiments, the pump pulse acts as an ultrafast trigger for a non-equilibrium process on the system of interest's ground or electronically excited state and the probe pulse monitors the resultant state of the system as a function of the experimentally controlled time-delay between the pump and probe pulses. Pump–probe transient absorption experiments measure non-equilibrium species via their time-dependent electronic and vibrational spectra by resolving the spectral content in the probe pulse. For example, optical transient absorption experiments measure spectral signatures of transient excitonic states following photoexcitation of the sample with the pump pulse in complex systems. On the other hand, infrared transient absorption experiments measure vibrational spectra of photo-excited systems [239]. Femtosecond optical and infrared transient absorption spectroscopy in the condensed phase have resulted in new discoveries in many fields [16, 17, 97, 179, 240, 241].

The advent of third generation synchrotrons and the development of table-top X-ray sources has resulted in the development of transient X-ray spectroscopy for measuring the X-ray absorption and emission spectra of core electrons of complex samples in solution following optical excitation with an optical pump pulse [242–246]. X-ray spectroscopy is an element-specific probe of electronic and atomic structure and can measure coupled electronic

and nuclear motions with high spatial and temporal resolution in complex photochemical phenomena in solution. Femtosecond X-rays from X-ray free electron lasers (X-FELs) are allowing researchers to routinely measure X-ray absorption and emission spectra of transient species in solution on the 50 fs timescale [247–250].

The generation of tunable, high intensity, time-delayed, femtosecond X-ray pulse pairs has been recently demonstrated at various X-FELs around the world [56–61]. These technological developments have enabled X-ray pump X-ray probe experiments studying nuclear and electronic dynamics at different atomic sites in small molecules in the gas phase through various electron ionization detection schemes [251–253]. Two-pulse X-ray photon correlation techniques have measured non-equilibrium atomic correlations on short length scales in solutions and solid phase [254–258]. These experiments have measured simple lattices, nanoparticles, resonant Auger–Meitner processes, shifts in the periodic behavior of lattice solids, and even shifts in crystallographic measures of proteins [259, 260]. Additionally, nonlinear X-ray matter interactions with intense X-ray pulses have resulted in seeded stimulated emission signals at the Mn K-edge in concentrated solutions [201].

Valence-core interaction information could conceivably be accessed via a wide array of transitions and techniques, ranging from fluorescence or table-top experiments on K, L, or M holes, to multi-photon Resonant Inelastic X-ray scattering (RIXS) experiments. In resolving these interactions, each of the above approaches suffer fundamental limitations. Lifetimes of K and L holes are short-lived and have broad spectra, convoluting transitions. Alternatively, techniques that access the valence suffer from the dense continuum of states creating an overabundance of possible transitions to evaluate.

The use of Kβ fluorescence (3p electron filling a 1s hole, releasing an incoherent photon) has long been linked to the 3p–3d exchange interaction. The relative intensities of Kβ_1, Kβ_3, and Kβ' are tied to the spin and occupancy of the 3d shell [44–46]. This principle has informed a breadth of studies investigating spin states, oxidation states, and phase changes, [261–264], viewed through both Kβ and the comparison of various fluorescence channels and core holes [265, 266]. Additionally, there has been a proven use of K-shell

fluorescence as a reporter on oxidation and spin state [218, 267–270] and the use of transient X-ray Emission Spectroscopy (XES) spectroscopy to study excited state behavior [271–276].

Generally, L-edge spectroscopy has been used heavily to monitor the covalency, spin, and back-bonding in third row transition metals [43, 47–50]. In $L_{2/3}$-edge spectroscopy, the 2p orbital is localized to the metal so intensity is directly proportional to the metal d-character in the unoccupied valence orbitals of the metal [277, 278]. Direct measurement of the 3p–3d resonance [279, 280] reports the same breadth of states available to any edge-sensitive technique, where the density of states is high near the continuum. These interactions play a role in modifying core lifetimes [281]. Alternatively, a more direct assessment of the 3p–3d interactions has been made through the lens of directly resolving Auger–Meitner and super-Coster–Kronig events [282, 283].

Another proven method for measuring the 3p–3d interactions is M-edge spectroscopy [52]. Either steady-state or pump-probe experiments can report directly on the 3p electrons and the role they play in molecular behavior. Additionally, M-edge transitions are sufficiently low in energy to be accessed by table-top experiments [53, 54, 284]. Intrinsic to this detection is the same convolution of electronic states inherent to any X-ray absorption near edge structure (XANES) type measurement. Any spectroscopy which directly probes the continuum sees a dense manifold of close-lying transitions, nearly indistinguishable from one another, in combination forming a single complicated edge. Alternatively, in directly probing core hole states, we can limit the density of states to a tangible and calculable subset, allowing us to track individual electronic states as the ensemble evolves over time.

Experiments that have combined detection schemes have proven useful in collecting information about the same molecular behavior through multiple lenses. This ranges from RIXS [285–288], examining The 2p shell to resolve spectra which lend insight into a variety of molecular attributes or the combination of XES and scattering experiments correlating the energetic and real spaces [218, 289]. Both combining detection schemes, and utilizing multi-step (RIXS) processes improve molecular-level insight by resolving signals along additional axes.

We can further investigate systems by correlating pump and probe frequencies in the X-ray domain, building a road map to purely X-ray nonlinear spectroscopy. X-ray pump X-ray probe spectroscopies have been demonstrated on simple molecules in the gas phase [251]. Additionally, X-ray photons have been utilized to directly probe resonant Auger–Meitner processes [290]. Other proposed and theoretical work set the groundwork for two-color X-ray experiments in which each pulse is resonant with a different elemental edge [291] or in which multiple edges are monitored [175].

Any emission-based technique is necessarily broadened by the lifetime of the energetically lowest core hole involved, and is limited in the time frame of the experiment to that lifetime. Any technique, whether emission or absorption based, that directly involves a valence–core transition suffers from the dense continuum of states which exists at the edge, creating a convolution of peaks to unpack. Transient X-ray absorption spectroscopy has the distinct benefits of delivering relevant chemical information, in a spectrally isolated region, due to its core-to-core absorption probe, with narrow peak widths, temporal resolution limited by pulse duration, and experimental duration range limited only by the longest-lived core hole.

Recently, we proposed an ultrafast X-ray pump X-ray probe (XPXP) transient absorption experiment to measure core-valence electronic correlations in solvated chemical systems using the transition metal complex, $K_4Fe^{II}(CN)_6$, as an example system [64]. X-ray pump pulses generate a core hole in the Fe atom resulting in new electronic states that are probed by measuring their transient X-ray absorption spectra with the probe pulse. We combined atomic electron cascade calculations and excited-state time-dependent density functional theory (TDDFT) calculations to predict the changes in the X-ray probe transmission near the Fe K-edge following the X-ray pump interaction. This allowed us to understand how specific states resulting from electron cascades manifest in the X-ray absorption spectra, as interrogated by the probe. Even though the transient spectra computed within the TDDFT framework can only be captured within the space of single excitations, this approach provided a reasonable first-order estimate. The results revealed the advantages of measuring the transient X-ray absorption spectra of non-equilibrium Fe 3p hole states at $\approx$7.06 keV as

they are spectrally separated from the continuum states near the Fe K-edge and the 1s→3p transition is dipole-allowed. The computational study proposed a new experimental tool to probe the 3p–valence exchange interaction strength in solvated chemical systems. In response to the wide array of novel excited states, each orbital relaxes in energy due to the shift in shielding produced by new electron vacancies. The difference in how two individual orbitals relax gives a measure of their specific interaction strength. This chapter is the experimental realization of our previous theoretical work described above, and to the best of our knowledge, the work presented here is the first XPXP transient absorption experiment of molecules in solution.

6.2 Experimental Design

Figure 6.1 (a) depicts the generation of an energy tunable ≈10 fs XPXP pair, separated by a time delay (τ) coincident on a thin liquid jet (250 μm) containing an aqueous solution of either $K_4Fe^{II}(CN)_6$ or $K_3Fe^{III}(CN)_6$. The X-ray pump pulse centered above the Fe K-edge at 7.2 keV, ionizes the sample by removing a 1s electron from the Fe atom. The energy of the X-ray pump pulse (marked by the blue arrow in Fig. 6.1 (c) is chosen to ensure that fluctuations in its photon energy or spectral shape do not influence the character of the initially prepared ionized Fe state. The averaged width of the probe pulse is represented in Fig. 6.3 (a). Figure 6.1 (b) provides an example of an Auger–Meitner electron cascade and we stress that this is only one of a multitude of possible pathways explored by the system following the interaction with the X-ray pump pulse. The representative cascade pathway in Fig. 6.1 (b) proceeds in experimental time as follows: (1) a pump photon ejects a 1s electron to the continuum, (2) Kα fluorescence fills the 1s hole and emits a photon, (3) Auger–Meitner decay fills the new 2p hole while removing a 3p electron, (4) Coster–Kronig decay fills the 3s hole, ejecting a $3d_{t2g}$ electron, resulting in an electron configuration of $[Ne]3s^2 3p^{x=5} 3d_{t2g}^{y=4}$, and (5) following the Auger–Meitner electronic cascade, the second X-ray pulse centered at 7.06 keV probes the ensemble of resultant core-electronic excited states containing 3p holes. The X-ray probe pulse is spectrally resolved following the sample to measure the transient X-ray absorption

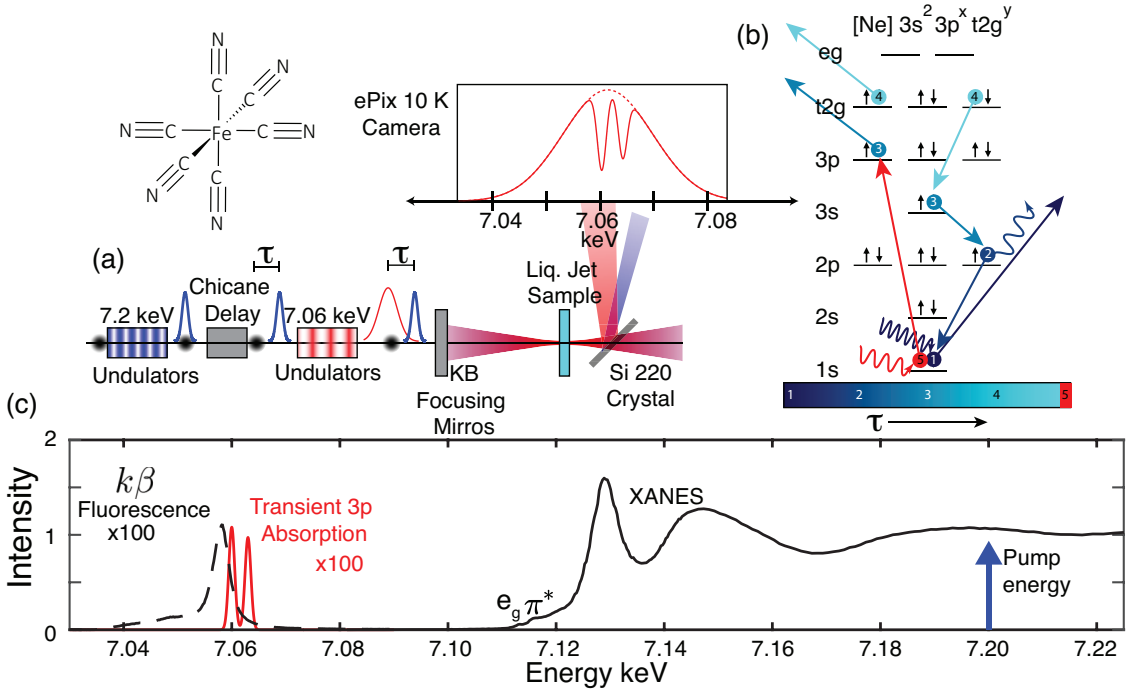

Figure 6.1: **Experimental Overview of the XPXP Experiment. (a)** Both the 7.20 keV X-ray pump (blue) and 7.060 keV X-ray probe (red) are generated collinearly by separate undulators from the same electron bunch (black haze). Insertion of a Chicane delay allows for the pump-probe timing to scan over experimental time (τ). Both beams are focused onto the thin liquid jet by a pair of Kirkpatrick–Baez (KB) mirrors before diffracting off a Si-220 analyzing crystal. The transmitted X-ray spectra are measured using an analyzer crystal and an X-ray detector (ePix 10K). Data reported here are collected at $\tau = 0$ fs. **(b)** Example of an Auger–Meitner cascade in the iron complexes following removal of a Fe 1s electron. The example shows that the 1s hole is quickly filled by various processes including fluorescence, Auger–Meitner decay, and Coster–Kronig decay events. The resultant electronic states have an electronic configuration of $[\mathrm{Ne}]3\mathrm{s}^2 3\mathrm{p}^x 3\mathrm{d}^y_{\mathrm{t2g}}$. Details of the cascade are provided in the text. After delay time, τ, the X-ray probe pulse, resonant with numerous 1s→3p transitions, interrogates the core electronic excited states formed following the X-ray pump interaction. **(c)** Equilibrium Fe K-edge X-ray absorption spectrum and Kβ X-ray emission spectrum of a 500 mM aqueous solution of $K_4Fe^{II}(CN)_6$. The X-ray absorption spectrum (solid black, normalized to the post-edge) displays weak pre-edge features of 1s→$3d_{eg}$ and 1s→ π^* transitions characteristic of an Fe^{II} complex as described in Ref. [216]. The X-ray pump pulse energy is picked to be far from the edge at 7.20 keV to remove a 1s electron from the sample. Transient 3p absorption features measured by the X-ray probe pulse are shown in red. See Appendix G for further details on the scaling of the X-ray absorption spectra, emission spectra, and transient signals.

spectrum (see Fig. 6.1 (a) and Fig. 6.1 (c)). The measured XPXP transient absorption spectra combined with simulations directly measure the oxidation state-dependent electronic cascade pathways and are sensitive the 3p–3d valence interaction strengths in Fe^{II} and Fe^{III} hexacyanoferrates dissolved in water.

Experiments were conducted in the Coherent X-ray Imaging (CXI) hutch at the Linac Coherent Light Source [292]. We utilize a pulse generation scheme similar to that used in previously published work by Kroll et al. [201], utilizing the split undulator method [56]. Two collinear X-ray pulses ($\approx$60 μJ each, 10 fs) were generated in a series of undulators from a single electron bunch with a chicane delay providing the experimental delay (τ) between the two pulses. As shown in Fig. 6.1 (a), The electron bunch is inefficiently lased in the first half of the undulators to produce the 7.20 keV pump pulse. The remaining electron energy is utilized in the second half of the undulators to produce the lower-energy 7.06 keV probe pulse. Data shown here are restricted to $\tau = 0$ fs. Absolute photon energies were determined by the in-hutch notch monochromator. The spectrometer calibration was performed by inserting a channel cut monochromator upstream at the XPP (X-ray Pump Probe) endstation [205]. The monochromator was tuned to multiple energies in the 7.06 keV region which presented as peaks in the resolved probe spectrum.

We measure the transmission of the probe pulse as a function of pump fluence, achieved by two focal conditions. In the first condition, we position the sample jet at the focus of the two beams. In the second, the sample is positioned upstream ($\Delta z = +2$ mm) to reduce the fluence of both pulses. As the response to this technique is linear with respect to the fluence of each pulse, small perturbations in the focal area create a $\Delta S \propto 1/\Delta z^4$ drop in signal strength.

The two focal conditions serve as "pump on" and "pump off" conditions as neither pulse can be uniquely blocked or eliminated without drastically impacting the energy, intensity, and temporal profile of the other pulse. The fact that both pulses are generated from the same electron bunch creates an intrinsic link between the character and intensity of the two pulses. Future experiments will take advantage of a non-collinear generation geometry,

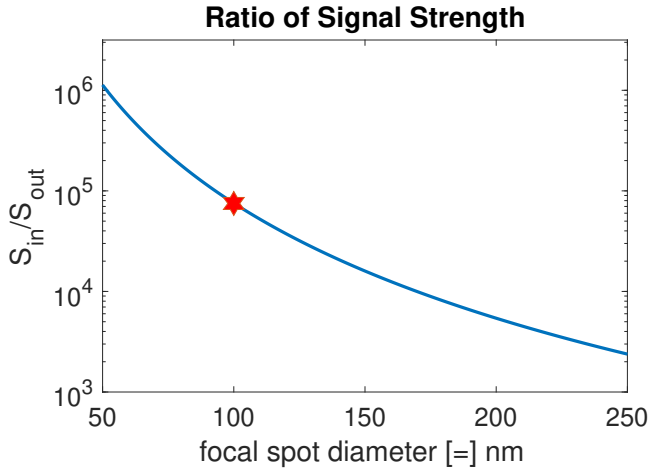

Figure 6.2: **Comparison of predicted signal strength:** In and out of focus experimental conditions. Experimental measures indicate an initial diameter of 100 nm (shown by red star). Experimental error in the diameter of a factor of 2 would still result in a drop of signal strength greater than 10^3.

generating pulses from distinct electron bunches, enabling direct chopping of the pump pulses either by mechanical means or through electron bunch control.

To show the efficacy of this approach we first consider that the experiment is bilinear, the signal strength in a given volume is proportional to the product of the pump and probe field strength. This bilinear relationship leads to the quartic relationship with displacement along the direction of travel ($\Delta z = 2$ mm), as seen in Eqn. 6.1, below

$$\begin{aligned} \frac{S_{out}}{S_{in}} &= \frac{Area_{in}^2}{Area_{out}^2} \\ &= \left(1 + \frac{\theta_h \cdot \Delta z}{D_h} + \frac{(\theta_h \cdot \Delta z)^2}{D_h^2}\right)\left(1 + \frac{\theta_v \cdot \Delta z}{D_v} + \frac{(\theta_v \cdot \Delta z)^2}{D_v^2}\right). \end{aligned} \tag{6.1}$$

In the above expression, D_h and D_v are the diameters of the focused beam in the horizontal and vertical dimensions. For the assumptions listed above, the change in signal strength is shown in Fig. 6.2.

Two sets of Kirkpatrick–Baez (KB) mirrors are positioned to independently adjust the focal plane (z) in both the horizontal and vertical dimensions of the beam profile. The two mirrors, at different distances from the focus (0.9 and 0.5 m), impart elliptical cones of

con/divergence from the focus ($\theta_h = 0.63$, $\theta_v = 1.02$ mrad) in the horizontal and vertical dimensions respectively. Imprint etchings [292] taken during the experiment indicate a focal diameter of 100 nm. Data are collected at 120 Hz., alternating 36,000 shots (5 minutes) in each fluence condition. Total shot counts for each spectrum are provided in Table 6.1.

The two complexes, potassium ferrocyanide ($K_4Fe^{II}(CN)_6$) and potassium ferricyanide ($K_3Fe^{III}(CN)_6$), were purchased from Sigma Aldrich and used without further purification. Aqueous 500 mM solutions were prepared by dissolving these complexes in ultrapure water. An HPLC pump was used to flow the solutions through a 250 μm (inner diameter) capillary. A catcher placed below the capillary refed the pump to enable closed-loop recirculation of the sample. Beam throughput was measured to be 3%. Assuming half of the beam is in the focal volume [269], the fluence from each pulse at the sample measured 1.1×10^{18} W/cm^2.

6.3 Data Processing and Analysis

The XPXP data were processed by separately averaging and subtracting the X-ray pumped and unpumped probe spectra to produce the ΔT/T spectra and error bounds in Fig. 6.6. Individual X-ray shots exhibiting abnormal characteristics in intensity or spectral distribution were excluded from the analysis. Additionally, each X-ray probe pixel underwent individual filtering to account for the shot-to-shot variation in spectral shape and central frequency of individual X-ray probe pulses. The XPXP signal is dependent on the X-ray pump and probe pulse fluence and the transient absorption signal is absent in pure water. (See Figs. 6.4 and 6.5.)

Data were filtered via three methods based off of (1) set bounds, (2) linearity between multiple diagnostics, and (3) instance counts of individual pixels. The total amount of data collected and displayed here is listed in Table 6.1. Descriptions of the filtering protocols follow. Bounds filters apply two conditions (listed below as [$\text{cond}_{\text{floor}}$, cond_{var}]) based on a single self-normalized diode or metric such that the mean of the metric is one. All shots which are either lower in normalized metric value than $\text{cond}_{\text{floor}}$, or deviate from the mean by cond_{var} number of standard deviations, are eliminated. Two photodiodes (10 mm x 10 mm

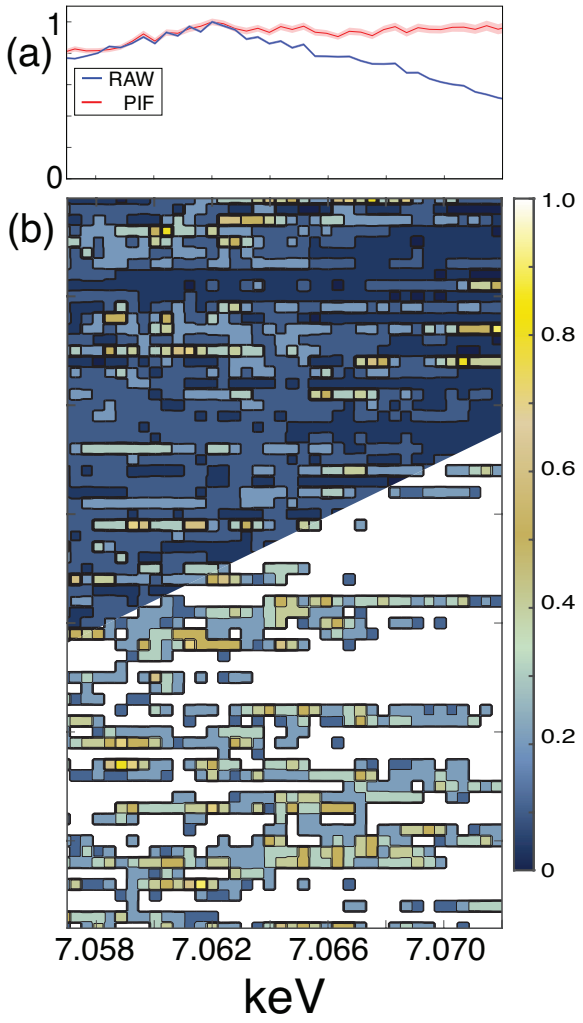

Figure 6.3: **Application of Pixel Instance Filter: (a)** Average probe spectrum pre (blue) and post (red) application of the pixel instance filter (PIF) over a randomly selected 1,000 shots detected through solvent only. Shaded areas represent standard error. **(b)** Sample of initial shots in the subset averaged in (a). Each row represents a single shot. The upper region is unfiltered data with small contributions (close to zero) in all shots. The lower region represents data following the application of the filter threshold. For a given vertical slice (pixel) there are fewer considered shots, increasing the value of standard error, but also giving a more true representation of the mean value across the spectrum.

Table 6.1: Total number of shots analyzed following bounds and linearity filters for each spectrum.

Substance	**Condition**	**Pumped**	**Unpumped**	**Figure**
Solvent	Full Fluence	28,050	27,584	6.4
Fe^{II}	Fe Foil Attenuated	88,351	29,715	6.5
Fe^{II}	Full Fluence	165,8355	174,422	6.6 a
Fe^{III}	Full Fluence	220,428	168,162	6.6 b

Hamamatsu Si PIN, Model: S3590, covered in light-blocking black kapton) collected scatter off the diamond chamber window. The Diodes were positioned directly downstream of the KB mirrors, ≈75 mm from the diamond window, oriented away from the liquid jet. One diode included an additional 100 μm thick Fe foil to block the pump pulse and measure only the probe pulse intensity.

1. (Low) Photon Intensity Diode (Upstream) [0.055, 2.3]

2. (High) Photon Intensity Diode (Upstream) [0.02, 2.2]

3. (High) Photon Energy (Upstream) [0.945, 2.2]

4. (Total Combined) Intensity Diode (Upstream) [0.2,2.2]

Linearity filters remove shots whose characteristics of expected linearity exceed the listed bounds for each diode or sensor by the listed fraction of the domain. If the data cover a span of 1,000 arbitrary units with a bound of 0.02, shots which deviate from the best fit line by more than 20 are removed.

1. X: (High) Photon Intensity Diode (Upstream),
   Y: Fluorescence Diode (Downstream)
   Bound: [0.5]

2. X: (Low) Photon Intensity Diode (Upstream),
   Y: (Low) Integrated Photon Energy Spectrum (Upstream)
   Bound: [0.09]

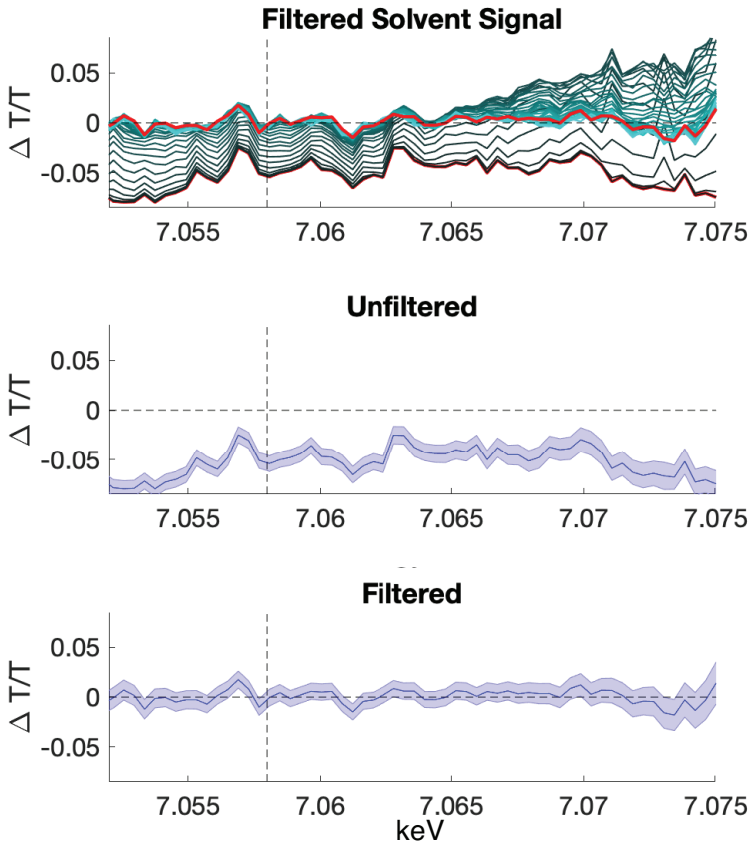

Figure 6.4: **Progressive Effect of Pixel Instance Filter Applied to Solvent Spectra: TOP:** Progressive effect of ΔT/T from PIF. Spectra correspond to evenly spaced thresholds between 0 $\rightarrow$1 in steps of 0.025. The lower red line corresponds to no filter applied. Upper red line corresponds to threshold = 0.78. **MIDDLE:** Solvent signal without filtering. **BOTTOM:** Solvent signal with final filter (Threshold = 0.78). Total signal disappears.

Two considerations in the spectral measurement of sase pulses are: (1) Due to the photon-energy fluctuations from pulse-to-pulse, the ensemble spectral width (averaged over many

pulses) exceeds the spectral width of an individual pulse, and (2) subsequent shots have little to no correlation in photon energy other than the same statistical average that all shots share in an ensemble. This creates a statistical illusion as the typical Gaussian profile indicates that each shot carries a small intensity in the wings. This is represented as a weak intensity measured at each shot. In reality, sase pulses are intense regardless of their deviation from the average photon energy. There are simply fewer shots with appreciable intensity in the wings. They are poorly sampled high-intensity readings rather than well-sampled low-intensity readings.

Figure 6.3 shows the effect of applying the pixel instance filter (PIF) on approximately 70 randomly selected shots. Pixels with low intensity are removed from analysis. This dramatically reduces the number of points that are considered in analysis, but also restricts the analysis to the subset of shots in which photons interact with the detector.

Each horizontal line in Fig. 6.3 (b) shows an individual pulse spectrum. The upper portion of the plot includes all of the data, but most of the pixels are nearly zero. If we remove the lowest values from each spectrum (lower portion) we see that each shot leaves the majority of the energy bandwidth relatively untouched. If we were to simply take the value of each pixel (energy bin) as its raw readout value we would be misrepresenting the spectrum of the pulse. By only considering the

For this reason, we filter (remove from analysis) each instance of a pixel that fails to reach a minimum threshold intensity, which scales with the average pulse intensity. This can be viewed as eliminating the pixel instances which contain no chemical information and windowing each shot to the most data-rich pixels. For instance, after the application of this filter, the pixel on the far right of Fig. 6.3 (b) would only consider the 6 shots in the lower panel and 3 in the upper panel with appreciable intensity. Its uncertainty would increase, changing from $\propto 1/\sqrt{70}$ to $\propto 1/\sqrt{9}$, but the 9 shots which are considered are the only 9 that carry any information. The increase in uncertainty is seen in panel (a) in which the red bounds of the PIF data are wider than those of the blue (raw) data. Further, the sloped shape of the spectrum disappears, depicting the wings of the spectrum as intense, but less

well sampled.

Figure 6.4 Show the effect of applying the PIF on solvent data scaling the threshold from 0→1, and at the final threshold. Note that this removes the apparent offset signal of $\approx 5\%$ and removes the false bias showing a positive signal at $h\nu > 7.065$ keV. A consequence of this data reduction is the increase in measurement uncertainty as discussed above. The elimination of uniform offset in sufficiently large data sets indicates the validity in considering the mean subtracted difference spectra for small data sets. Thus Fig. 6.5 shows data both with and without the mean subtracted. Threshold values were determined by an automated procedure, the rate of change in the difference signal was measured as a function of the threshold value and the smallest threshold with a negligible rate of change was selected.

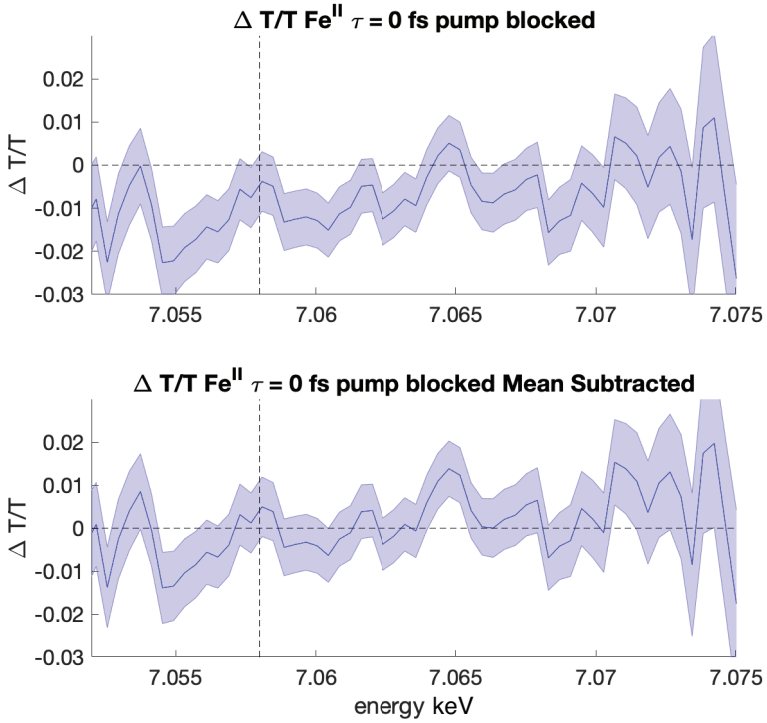

Figure 6.5: **XPXP Spectrum Measured by Filtering Pump with Fe Foil:** Spectrum collected with 10 μm Fe foil blocking beam path. This approximates a blocked pump pulse and results in greater uncertainty and the elimination of the signal.

Another method for performing this experiment would be to physically chop the pump pulse. As the character of the pump and probe are linked through the method used to produce both pulses, simply eliminating the pump undulators would alter the probe pulse, making comparisons ineffective. In this colinear geometry, one other option afforded the experimenter is to utilize the very absorption edge of study to block the pump. This can be achieved through the insertion of a thin foil of Fe, although it does not provide an expeditious method for performing this experiment.

Figure 6.5 shows data of the Fe^{II} complex with 10 μm Fe foil in front of the sample area, interacting with both pulses. The attenuation length of Fe foil is 24.38 and 3.2 μm at 7.062 and 7.200 keV respectively, leading to respective transmitted fluences of 66.35% and 4.4%. Assuming the bilinear intensity relationship discussed in Sec. 6.2 above, this corresponds to a 97% drop in signal strength seen as the elimination of both peaks.

6.4 Results

Figure. 6.6 displays the XPXP signal as a change in transmission of the X-ray probe spectrum following 1s excitation of the Fe atom in solvated Fe^{II} and Fe^{III} complexes by the X-ray pump. The data are measured at a nominal delay time of 0 fs between the two X-ray pulses. Both plots display the presence of transient 1s$\rightarrow$3p absorption features as two negative spectral features, blue shifted from the atomic Fe Kβ energy (vertical dashed line in Figs. 6.4 – 6.6 & 6.9). These transitions are a result of new core electronic excited states with 3p holes formed following the initial steps of an Auger–Meitner cascade (see Fig. 6.1 (b) for an example of electron cascade). The XPXP transient absorption signal is absent in pure water (see Fig. 6.4) and is dependent on the X-ray pump and probe pulse fluences (see Fig. 6.5).

The spectral features in the XPXP signal are fit using Gaussian lineshapes. The best fit is plotted as a solid red line in Fig. 6.6 and the peak amplitudes, positions and linewidths extracted from the fit are listed in Table 6.2. From the fits, we measure that XPXP transient signals in both Fe^{II} and Fe^{III} complexes exhibit two 1s$\rightarrow$3p transitions at $\approx$7,060 and $\approx$7,062 eV. The first peaks in the transient signals of the Fe^{II} and Fe^{III} complexes are blue-

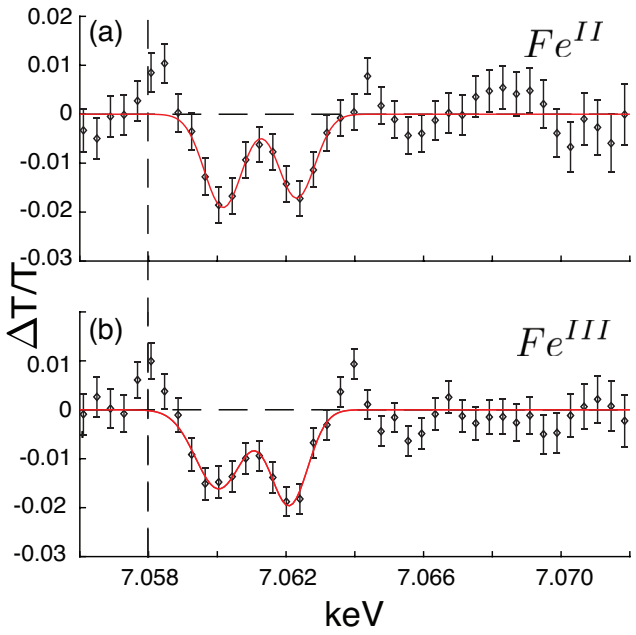

Figure 6.6: **Difference signal ($\Delta T/T$):** for both **(a)** $K_4Fe^{II}(CN)_6$ and **(b)** $K_3Fe^{III}(CN)_6$ taken at $\tau = 0$ fs. Negative peaks centered at ≈7.060 and ≈7.062 keV correspond to additional 1s→3p (Kβ) absorptions due to 3p holes resulting from the Auger–Meitner cascade, reducing transmission of the probe pulse. The fit line (red) consists of the sum of two Gaussians. Extracted values are shown in Table 6.2. The vertical dashed line represents the atomic Kβ line (7.058 keV). Error bars are calculated as the standard error for each pixel. See Sec. 6.3 for details.

shifted from the peaks of each Kβ X-ray emission signal (Fig. G.1) by 1.9 and 1.5 eV respectively.

The fits reveal that the overall transient signal in the Fe^{II} complex is blue-shifted with respect to the Fe^{III} signal. We note that this shift is within the 0.4 eV resolution of the detection spectrometer. The width of all the peaks in the transient spectra for both samples is ≈2 eV. The 1s→3p peaks in the XPXP signal are narrower compared to the Kβ emission peak because their width is limited by the non-radiative lifetime of the 3p hole rather than the lifetime of the 1s hole, making it easier to resolve individual electronic states in the transient absorption XPXP spectra. We compare the intensities of the spectral features by their integrated peak areas (see Table 6.2). We find that for the Fe^{II} sample, the peak at

7.060 keV is 15% more intense than the peak at 7.062 keV. In the case of the Fe^{III} sample, the peak at 7.060 keV is 3% more intense than the peak at 7.062 keV. Assuming similar dipole strengths for all 1s→$3p^5$ transitions, the integrated area of each peak corresponds to the relative population of that particular 3p state in the sample of interest. We also observe that the XPXP Fe^{III} data show overall greater intensity by 10% of the observed transitions relative to the Fe^{II} data and we attribute this to an initial additional hole in the $3d_{t2g}$ orbital, in agreement with previous calculations on the generalized case of 3p vacancy dependent M-edge spectroscopy [293]. In summary, the 1s→3p XPXP transient absorption spectra for the Fe^{II} and Fe^{III} complexes show remarkable similarities in the peak positions, integrated areas and lineshapes.

Table 6.2: Parameters of fits shown in XPXP spectra

Peak	**Center Frequency [eV]**	**Amplitude [%]**	**Width (FWHM) [eV]**	**Relative Integrated Amplitude [ARB.]**
Fe^{II}	7,060.170±0.005	-1.908±0.150	1.966±0.010	0.957
Fe^{II}	7,062.310±0.005	-1.717±0.150	1.933±0.010	0.832
Fe^{III}	7,060.04±0.017	-1.615±0.310	2.185±0.329	1.000
Fe^{III}	7,062.09±0.013	-1.946±0.330	1.958±0.251	0.968

6.5 Discussion

To aid the interpretation of the data shown in Fig. 6.6, we revisit the two computational approaches used in Ch. 5 to interrogate and track a specific subset of the cascade, the $3p^5$ hole states. The relevant application of the TDDFT work is shown in Fig. 6.9, and the time dependent propagation of those states via the MCMC simulation is shown in Fig. 6.7. Theoretical approaches for the on-the-fly Monte Carlo simulation of the electron cascade [223–225] and TDDFT calculations of the 3p hole state spectral signatures [213, 216, 228] have been outlined in previous work [64] and are described Ch.5. The present work builds

upon previous work via the consideration of the Fe^{III} electron cascade and in contrasting it with that of the Fe^{II} cascade.

6.5.1 MCMC: Possible Transient Core Excited States Probed in the XPXP Experiment

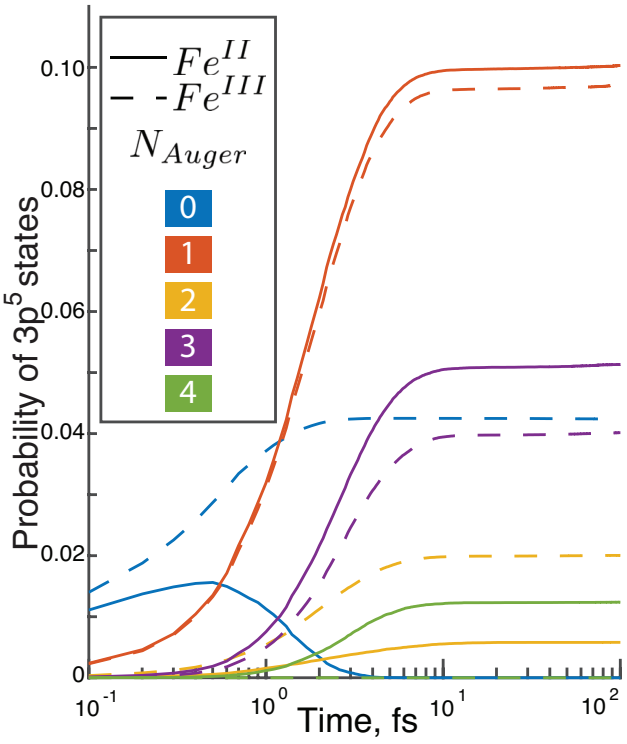

Figure 6.7: **Time-dependent probabilities of [Ne]$3s^2 3p^5 3d^y_{t2g}$ electronic states following 1s hole generation:** Monte-Carlo electron cascade calculations of atomic Fe^{II} (solid) and Fe^{III} (dashed) are shown above where the color corresponds to the same number of new holes (labeled N_{auger}) in the two species. The probabilities for each state are given with respect to all electronic configurations (including non-[Ne]$3s^2 3p^5 3d^y_{t2g}$ sates). At long times ($\geq$1 ps), [Ne]$3s^2 3p^5 3d^y_{t2g}$ states comprise 18% and 21% of all possible electronic states for Fe^{II} and Fe^{III} respectively. The electronic cascade is distinct for each species. For example, the dashed blue line shows that the $3p^5 3d^5$ configuration of Fe^{III} survives the cascade at times greater than 10 fs, while the solid blue line shows that the $3p^5 3d^6$ configuration of Fe^{II} does not.

To predict the transient electronic core-excited states created in the X-ray probe's spectral window (7060$\pm$10 eV) following the removal of a 1s core electron in the Fe atom by the

X-ray pump pulse, we perform an electron cascade Markov-Chain Monte-Carlo (MCMC) calculation, as described previously. The calculations serve as a starting point for understanding the spectral features seen in this X-ray pump X-ray probe experiment. Figure 6.7 shows the time evolution of all $3p^5$ electronic configurations in the Fe^{II} and Fe^{III} atomic systems produced by the MCMC simulations during the first 100 fs after ionization of a 1s electron. Lines of the same color represent states that have lost equivalent numbers of electrons through Auger–Meitner events (N_{Auger}) as indicated in the legend. For example, the solid and dashed blue lines (N_{Auger}=0) correspond to the initial $3d^6$ and $3d^5$ valence configurations for Fe^{II} and Fe^{III} atoms, respectively. Interestingly, we note that the probability of observing $[Ne]3s^23p^53d^6_{t2g}$ state of the Fe^{II} system decays to zero within 1 fs. Given the experimental X-ray pulse durations of 10 fs, we expect the largest contributions from $3p^5$ core excited states with 0, 1, and 3 Auger–Meitner events (N_{Auger} = 0, 1, and 3) depending on the starting oxidation state of the Fe atom. The relative contributions of each of the core-excited states will depend on their calculated probabilities as shown in Fig. 6.7.

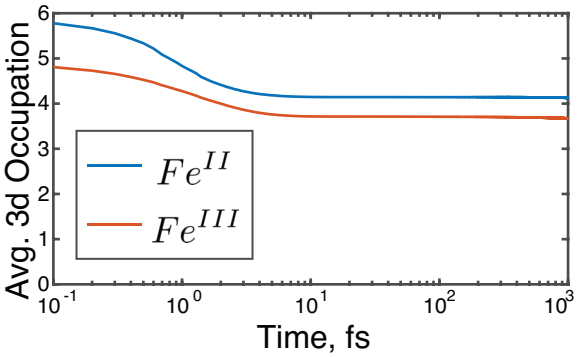

Figure 6.8: **MCMC Determined Average 3d Occupancy:** for both compounds for all [Ne] $3s^2$ $3p^5$ states from 1 as $\tau \rightarrow$1 ps.

We compare the published fluorescence yield values of the Fe atom with the probabilities obtained from the cascade simulation. Fluorescence spectra [218] of both complexes and integrated RIXS spectra [216] of the Fe^{II} complex collected at the Advanced Photon Source are presented in Figs. G.1 and G.2 in Appendix G for reference. Krause determined that

the fluorescence yield for Fe to be ≈30% [294], with relative intensities of Kα1:Kα2:Kβ to be 50:100:17, resulting in an estimated population of the Fe^{III} $[Ne]3s^23p^53d^5$ state to be approximately 3%, which is consistent with the simulation value of 4% in Fig. 6.7. Evidently, the $[Ne]3s^23p^53d^6$ state of the Fe^{II} complex is shorter lived. We note that this comparison relies on the approximation that the only channel for producing [Fe^{II} $3p^53d^6$] or [Fe^{III} $3p^53d^5$] states is through Kβ fluorescence and ignores the pathways of Kα fluorescence followed by L-edge fluorescence or corresponding Auger–Meitner processes. The MCMC simulation also predicts the average oxidation state during the first 10 fs (the duration of the sase pulses) of the electronic cascade to be $3d^{4.2}$ and $3d^{3.8}$ for the Fe^{II} and Fe^{III} respectively, shown in full time resolution in Fig. 6.8.

Figure 6.8 shows the average 3d occupancy over the full range of MCMC simulations (1 picosecond). Initially, at τ= 1 attosecond, both compounds retain valence occupations near that of the ground state. As time progresses, variations in their respective ensemble of Auger–Meitner cascades reduce the difference in valence occupation. Combining all the information gleaned from the electron cascade calculations, we would expect the following in the transient XPXP signal: (1) two or three spectral features representing distinct electronic states for the Fe^{II} and Fe^{III} samples, (2) similar but non-identical intensity of the spectral features, and (3) a lack of the $1s\rightarrow[Ne]3s^23p^53d^6_{t2g}$ peak in the Fe^{II} data.

6.5.2 TDDFT: Calculated XANES Support Measurement of 3p–3d Interactions

To further aid the interpretation of the data shown in Fig. 6.6, we also perform TDDFT calculations of 1s→3p absorption spectra for a variety of electronic configurations on separate geometries for both Fe^{II} and Fe^{III} compounds following the same computational protocol [64] and geometries [216] used previously, provided in Appendix F and discussed in Sec. 5.5. This approach guides the physical intuition for assigning peaks and trends in data and is summarized in Figs. 6.9 (a) & (b), which show calculated roots of the labeled electronic configurations relative to the atomic Kβ energy (dashed line). The excited state energies and oscillator strengths are provided in Table F.3 in Appendix F. Figure 6.9 (c) diagrammatically

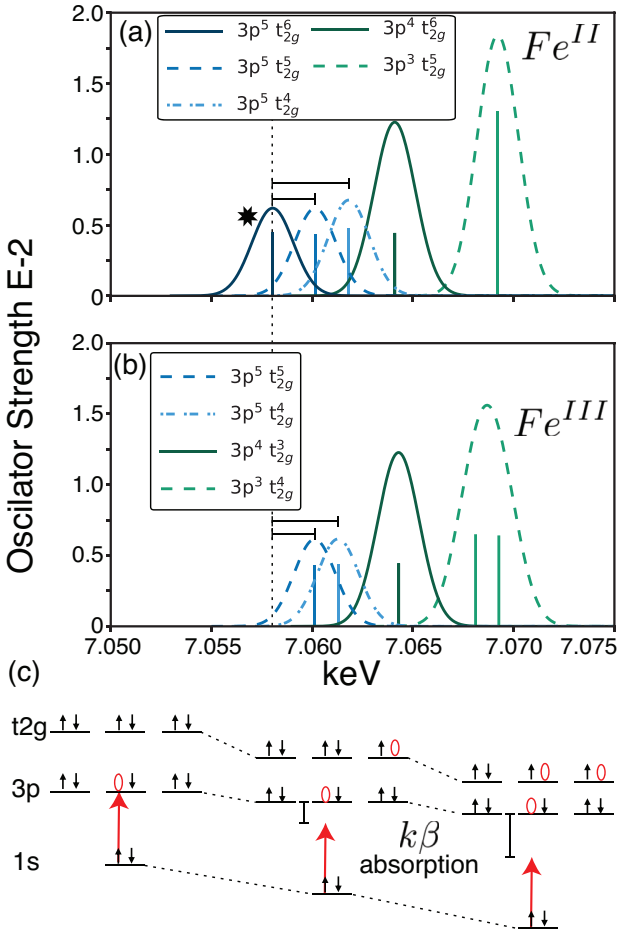

Figure 6.9: **Calculated shifts in 1s→3p transition energy and oscillator strengths** for **(a)** $K_4Fe^{II}(CN)_6$ and **(b)** $K_3Fe^{III}(CN)_6$ for a selected sample of electronic states. Starred transition is not observed in the data. All configurations listed in the inset have a filled [Ne] $3s^2$ core. Additional holes in the valence create a sequential blue-shift in the transition energy in both compounds. **(c)** Diagrammatic 1s→3p energy shift. Each additional hole (red oval) in the t_{2g} corresponds to a progressive increase of the 1s→3p transition energy. Shifts are also depicted for the first two peaks of the progressions shown in (a) and (b).

shows the progressive blue shift from the atomic Kβ energy. Each additional hole (open circle) correlates with the 3p orbital rising in energy above the atomic Kβ energy. In the process of all orbitals relaxing in the presence of the valence hole, the difference in response

between the 3p and valence shells gives the measure of the 3p–3d interaction strength.

The TDDFT calculations report that each progressive hole in the 3d valence shell produces a corresponding shift in the 1s→3p energy gap. For Fig. 6.9 (a) & (b) we see that in the $[Ne]3s^2 3p^{x<5} 3d^{y}_{t2g}$ configurations, each additional hole in the t_{2g} orbital corresponds to a +2 eV shift of the 1s→3p calculated transition. In the $[Ne]3s^2 3p^5 3d^{y}_{t2g}$ configurations, each additional hole in the t_{2g} corresponds to +2 eV shift of the 1s→3p calculated transition, which contains information about the strength of the 3p–3d interactions in the molecule under investigation. The TDDFT calculations reveal that spectra of the states with electronic configurations of the type $[Ne]3s^2 3p^{x<5} 3d^{y}_{t2g}$ correspond to spectral features ≈6 eV to the blue of the Kβ emission (7.058 keV). Further, we see that the peak from the 1s→$[Ne]3s^2 3p^5 3d^6_{t2g}$ configuration for the Fe^{II} species (starred in Fig. 6.9 (a)), would be located around the peak of the atomic Kβ emission line.

6.5.3 Unifying the Molecular Picture

Combining the electron cascade (Fig. 6.7) and the TDDFT calculations (Fig. 6.9), we assign the peaks at ≈7.060 and ≈7.062 keV in the Fe^{II} and Fe^{III} XPXP transient absorption spectra (Fig. 6.6) to 1s→$[Ne]3s^2 3p^5 3d^5_{t2g}$ and 1s→$[Ne]3s^2 3p^5 3d^4_{t2g}$ transitions, respectively. Both the MCMC electron cascade simulations and the TDDFT calculations confirm that the valence-hole-free state in the Fe^{II} complex does not survive the nominal 1s core lifetime, and we observe transitions to similar core excited states in both complexes. From the integrated area of the peaks in the XPXP data, we observe that the electron cascade in the Fe^{III} complex generates more highly ionized states in the relative populations of $3d^5_{t2g}$ and $3d^4_{t2g}$ states compared to the electron cascade in the Fe^{II} complex. A comparison of the TDDFT calculations and the XPXP experimental data reveals that excited states with configurations of $[Ne]3s^2 3p^{x<5} 3d^{y}_{t2g}$ are not formed in this experiment due to a lack of observed transitions above the noise in Fig. 6.6 for X-ray probe energies greater than 7.063 keV and the fact that the data are collected at zero nominal delay between the X-ray pump and probe pulses. We note that the lack of $3p^{x<5}$ holes may be caused by surrounding ligand or solvent electrons

contributing to the electron cascade and effectively quenching that signal by decreasing the $3p^{x<5}$ lifetime. Furthermore, for values of $x < 5$ the system necessarily undergoes additional decay events that are less likely to occur at these early experimental times. Based on the Monte-Carlo simulations, we anticipate their growth to require tens of femtoseconds and the collected data at $\tau = 0$ fs likely hides these states in the present experiment.

We consider the possibility that the peaks seen in the XPXP experimental signal could arise from the splitting of the $3p^5$ configurations via spin–orbit interactions. In reference calculations of $3p^5$ configurations, the 3p spin–orbit coupling was computed to be ≈1.3 eV for both Fe^{II} and Fe^{III} complexes [295]. Given that the 3p spin–orbit coupling is less than the linewidth and the energy separation of the observed peaks in the XPXP transient spectra shown in Fig. 6.6, we maintain the assignment of the observed peaks to the $1s\rightarrow[Ne]3s^23p^53d^5_{t2g}$ and $1s\rightarrow[Ne]3s^23p^53d^4_{t2g}$ transitions in solvated Fe^{II} and Fe^{III} complexes. Our combined femtosecond XPXP experimental data and simulation protocol provide a supporting experimental measure of the 3p–3d valence interaction strengths by resolving the 2 eV shift in the $1s\rightarrow3p$ transition as a function of the number of 3d holes in solvated Fe complexes.

6.6 Conclusions

In each of the exotic states produced during the cascade, core and valence electrons rearrange and relax in energy due to the constantly changing electrostatic shielding. This additionally includes shifts resulting from 3p–3d and 3d–3d coulomb and valence interactions, crystal field interactions, spin–orbit interactions, and the overlap of each of the electronic wavefunctions. Measuring the time-evolution of core–valence interactions is crucial for the understanding, accurate modeling, and prediction of electronic correlations in transition metal complexes used in catalytic, magnetic, and information-storage applications.

As discussed above, and shown schematically in Fig. 6.9 (c), we measure the $1s\rightarrow3p$ transition response, sensitive to the 3p–3d Coulomb and valence interactions as a function of the number of 3d holes and find a +2 eV shift per hole. Our ability to extract other interactions from the $1s\rightarrow3p^5$ spectral features is theoretically limited by the 3p non-radiative

lifetime broadening (1-2 eV) and currently by the experimental resolution of the spectrometer (0.40 eV) [235]. The experimental data were obtained during the experimental instrument response function (IRF) of 14 fs dictated by the convolution of the 10 fs X-ray pump and X-ray probe pulses. Given that the IRF is much longer than the core hole lifetime of the 1s electron ionized by the X-ray pump pulse, the transient X-ray absorption spectra are probing a near static population of core-excited states with varying 3d holes. With the generation of tunable hard X-ray pump and probe pulses with attosecond pulse lengths, the XPXP experiment described here would measure transient absorption spectra prior to Auger–Meitner decay and would be uniquely sensitive to state-specific time-evolving core–valence interactions (pure core electronic coherences).

The interpretation of the experimental XPXP transient absorption spectra in this study relies on the MCMC simulation of the electron cascade in isolated Fe^{II} and Fe^{III} atoms to model the effect of the X-ray pump pulse and the TDDFT calculations of the $1s \rightarrow 3p^5$ transitions for a select group of core-excited states in $Fe^{II}(CN)_6^{4-}$ and $Fe^{III}(CN)_6^{3-}$ complexes. Despite the atomic nature of the electron cascade calculations and the single excitation nature of TDDFT calculations, we were able to measure $1s \rightarrow 3p$ transition dipole sensitivity to the 3d hole density. We stress that the successful demonstration of a fs XPXP experiment of a solvated molecular system, as shown here, increases the urgency of developing theoretical tools to accurately model multi-pulse X-ray-matter interactions with complex molecules in solution. Such calculations will be crucial for understanding how electronic correlations, spin–orbit, ligand-field, and solute-solvent interactions are manifested in transient absorption spectra of X-ray core-excited molecular states. Along with theoretical developments, experimental developments in generating intense, multicolor, time-delayed attosecond pulse pairs in the hard X-ray regime will result in an extension of the fs XPXP spectroscopy presented here to a coherent multidimensional nonlinear X-ray experiment of complex molecular compounds in solution. See Appendix G for a non-exhaustive proposed list of possible improvements across experimental and theoretical treatments. An analogy is the development of third-order nonlinear coherent multidimensional optical and IR spectroscopy to measure

couplings between excitonic states and anharmonic vibrations, respectively, following the establishment of femtosecond optical pump-probe and IR pump-probe and transient grating experiments. Mukamel and co-workers have proposed several coherent multidimensional techniques in the X-ray regime to elucidate coherent electronic charge and energy transfer pathways [296–298]. With the availability of tunable attosecond hard X-ray pulses, it will be possible to create and collapse coherences within the 1s core hole lifetime, generating opportunities for investigating the coherences between specific core-excited electronic states of complex systems in solution.

BIBLIOGRAPHY

[1] G. R. Fleming and P. G. Wolynes, "Chemical dynamics in solution," *Physics Today*, vol. 43, no. 5, pp. 36–43, 1990.

[2] A. Nitzan, *Chemical dynamics in condensed phases: relaxation, transfer, and reactions in condensed molecular systems*. Oxford, New York, USA: Oxford University Press, first ed., 2006.

[3] C. H. Kim and T. Joo, "Coherent excited state intramolecular proton transfer probed by time-resolved fluorescence," *Physical Chemistry Chemical Physics*, vol. 11, no. 44, pp. 10266–10269, 2009.

[4] J. W. Kim, C. H. Kim, C. Burger, M. Park, M. F. Kling, D. E. Kim, and T. Joo, "Non-Born-Oppenheimer molecular dynamics observed by coherent nuclear wave packets," *Journal of Physical Chemistry Letters*, vol. 11, no. 3, pp. 755–761, 2020.

[5] T. Maiman, "Stimulated optical radiation in ruby," *Nature*, vol. 187, pp. 493–494, 1960.

[6] D. Strickland and G. Mourou, "Compression of amplified chirped optical pulses," *Optics Communications*, vol. 56, no. 3, pp. 219–221, 1985.

[7] P. Maine, D. Strickland, P. Bado, M. Pessot, and G. Mourou, "Generation of ultrahigh peak power pulses by chirped pulse amplification," *IEEE Journal of Quantum Electronics*, vol. 24, no. 2, pp. 398–403, 1988.

[8] S. Woutersen, Y. Mu, G. Stock, and P. Hamm, "Subpicosecond conformational dynamics of small peptides probed by two-dimensional vibrational spectroscopy," *Proceedings of the National Academy of Sciences*, vol. 98, no. 20, pp. 11254–11258, 2001.

[9] S. Woutersen, Y. Mu, G. Stock, and P. Hamm, "Hydrogen-bond lifetime measured by time-resolved 2D-IR spectroscopy: N-methylacetamide in methanol," *Chemical Physics*, vol. 266, no. 2-3, pp. 137–147, 2001.

[10] P. Hamm, M. Lim, W. F. DeGrado, and R. M. Hochstrasser, "Pump/probe self heterodyned 2D spectroscopy of vibrational transitions of a small globular peptide," *Journal of Chemical Physics*, vol. 112, no. 4, pp. 1907–1916, 2000.

[11] M. Khalil and A. Tokmakoff, "Signatures of vibrational interactions in coherent two-dimensional infrared spectroscopy," *Chemical Physics*, vol. 266, pp. 213–230, 5 2001.

[12] A. Tokmakoff, "Two-dimensional line shapes derived from coherent third-order nonlinear spectroscopy," *Journal of Physical Chemistry A*, vol. 104, pp. 4247–4255, 2000.

[13] M. T. Zanni, S. Gnanakaran, J. Stenger, and R. M. Hochstrasser, "Heterodyned two-dimensional infrared spectroscopy of solvent-dependent conformations of acetylproline-NH_2," *Journal of Physical Chemistry B*, vol. 105, no. 28, pp. 6520–6535, 2001.

[14] O. Golonzka, M. Khalil, N. Demirdöven, and A. Tokmakoff, "Coupling and orientation between anharmonic vibrations characterized with two-dimensional infrared vibration echo spectroscopy," *Journal of Chemical Physics*, vol. 115, no. 23, pp. 10814–10828, 2001.

[15] M. Khalil, N. Demirdöven, and A. Tokmakoff, "Vibrational coherence transfer characterized with Fourier-transform 2D IR spectroscopy," *Journal of Chemical Physics*, vol. 121, no. 1, pp. 362–373, 2004.

[16] D. M. Jonas, "Two-dimensional femtosecond spectroscopy," *Annual Review of Physical Chemistry*, vol. 54, no. 1, pp. 425–463, 2003.

[17] J. D. Hybl, A. A. Ferro, and D. M. Jonas, "Two-dimensional Fourier transform electronic spectroscopy," *Journal of Chemical Physics*, vol. 115, no. 14, pp. 6606–6622, 2001.

[18] K. A. Kitney-Hayes, A. A. Ferro, V. Tiwari, and D. M. Jonas, "Two-dimensional Fourier transform electronic spectroscopy at a conical intersection," *Journal of Chemical Physics*, vol. 140, no. 12, p. 124312, 2014.

[19] M. J. Nee, R. McCanne, K. J. Kubarych, and M. Joffre, "Two-dimensional infrared spectroscopy detected by chirped pulse upconversion," *Optics Letters*, vol. 32, no. 6, p. 713, 2007.

[20] C. R. Baiz, R. McCanne, M. J. Nee, and K. J. Kubarych, "Orientational dynamics of transient molecules measured by nonequilibrium two-dimensional infrared spectroscopy," *Journal of Physical Chemistry A*, vol. 113, no. 31, pp. 8907–8916, 2009.

[21] S. Draeger, S. Roeding, and T. Brixner, "Rapid-scan coherent 2D fluorescence spectroscopy," *Optics Express*, vol. 25, no. 4, p. 3259, 2017.

[22] M. S. Lynch, K. M. Slenkamp, M. Cheng, and M. Khalil, "Coherent fifth-order visible-infrared spectroscopies: Ultrafast nonequilibrium vibrational dynamics in solution," *Journal of Physical Chemistry A*, vol. 116, no. 26, pp. 7023–7032, 2012.

[23] F. D. Fuller and J. P. Ogilvie, "Experimental implementations of two-dimensional Fourier transform electronic spectroscopy," *Annual Review of Physical Chemistry*, vol. 66, no. 1, pp. 667–690, 2015.

[24] O. Golonzka and A. Tokmakoff, "Polarization-selective third-order spectroscopy of coupled vibronic states," *Journal of Chemical Physics*, vol. 115, no. 1, pp. 297–309, 2001.

[25] V. Tiwari, W. K. Peters, and D. M. Jonas, "Electronic energy transfer through non-adiabatic vibrational-electronic resonance. I. Theory for a dimer," *Journal of Chemical Physics*, vol. 147, p. 154308, 2017.

[26] V. Tiwari, W. K. Peters, and D. M. Jonas, "Electronic resonance with anticorrelated pigment vibrations drives photosynthetic energy transfer outside the adiabatic framework," *Proceedings of the National Academy of Sciences*, vol. 110, no. 4, pp. 1203–1208, 2013.

[27] V. Tiwari and D. M. Jonas, "Electronic energy transfer through non-adiabatic vibrational-electronic resonance. II. 1D spectra for a dimer," *Journal of Chemical Physics*, vol. 148, no. 8, p. 84308, 2018.

[28] S. T. Roberts, J. J. Loparo, and A. Tokmakoff, "Characterization of spectral diffusion from two-dimensional line shapes," *Journal of Chemical Physics*, vol. 125, no. 8, p. 6606, 2006.

[29] T. L. Courtney, Z. W. Fox, K. M. Slenkamp, and M. Khalil, "Two-dimensional vibrational-electronic spectroscopy," *Journal of Chemical Physics*, vol. 143, no. 15, p. 154201, 2015.

[30] T. L. Courtney, Z. W. Fox, L. Estergreen, and M. Khalil, "Measuring coherently coupled intramolecular vibrational and charge-transfer dynamics with two-dimensional vibrational-electronic spectroscopy," *Journal of Physical Chemistry Letters*, vol. 6, no. 7, pp. 1286–1292, 2015.

[31] J. D. Gaynor, A. Petrone, X. Li, and M. Khalil, "Mapping vibronic couplings in a solar cell dye with polarization-selective two-dimensional electronic-vibrational spectroscopy," *Journal of Physical Chemistry Letters*, vol. 9, no. 21, pp. 6289–6295, 2018.

[32] T. A. Oliver, N. H. Lewis, and G. R. Fleming, "Correlating the motion of electrons and nuclei with two-dimensional electronic-vibrational spectroscopy," *Proceedings of the National Academy of Sciences*, vol. 111, no. 28, pp. 10061–10066, 2014.

[33] N. H. Lewis and G. R. Fleming, "Two-dimensional electronic-vibrational spectroscopy of chlorophyll a and b," *Journal of Physical Chemistry Letters*, vol. 7, pp. 831–837, 2016.

[34] E. A. Arsenault, Y. Yoneda, M. Iwai, K. K. Niyogi, and G. R. Fleming, "The role of mixed vibronic Q_y-Q_x states in green light absorption of light-harvesting complex II," *Nature Communications*, vol. 11, p. 6011, 2020.

[35] N. H. Lewis, H. Dong, T. A. Oliver, and G. R. Fleming, "A method for the direct measurement of electronic site populations in a molecular aggregate using two-dimensional electronic-vibrational spectroscopy," *Journal of Chemical Physics*, vol. 143, no. 12, p. 124203, 2015.

[36] Z. W. Fox, T. J. Blair, R. B. Weakly, T. L. Courtney, and M. Khalil, "Implementation of continuous fast scanning detection in femtosecond Fourier-transform two-dimensional vibrational-electronic spectroscopy to decrease data acquisition time," *Review of Scientific Instruments*, vol. 89, no. 11, p. 113104, 2018.

[37] Z. W. Fox, T. J. Blair, and M. Khalil, "Determining the orientation and vibronic couplings between electronic and vibrational coordinates with polarization-selective two-dimensional vibrational-electronic spectroscopy," *Journal of Physical Chemistry Letters*, vol. 11, no. 4, pp. 1558–1563, 2020.

[38] J. D. Gaynor, J. Sandwisch, and M. Khalil, "Vibronic coherence evolution in multidimensional ultrafast photochemical processes," *Nature Communications*, vol. 10, no. 1, pp. 1–9, 2019.

[39] P. Bhattacharyya and G. R. Fleming, "Two-dimensional electronic-vibrational spectroscopy of coupled molecular complexes: a near-analytical approach," *Journal of Physical Chemistry Letters*, vol. 10, no. 9, pp. 2081–2089, 2019.

[40] J. D. Gaynor and M. Khalil, "Signatures of vibronic coupling in two-dimensional electronic-vibrational and vibrational-electronic spectroscopies," *Journal of Chemical Physics*, vol. 147, no. 9, p. 94202, 2017.

[41] H. Dong, N. H. Lewis, T. A. Oliver, and G. R. Fleming, "Determining the static electronic and vibrational energy correlations via two-dimensional electronic-vibrational spectroscopy," *Journal of Chemical Physics*, vol. 142, no. 17, p. 55101, 2015.

[42] E. I. Solomon and A. B. P. Lever, eds., *Inorganic electronic structure and spectroscopy volume I: Methodology*. N: John Wiley & Sons, 1999.

[43] E. I. Solomon and A. B. P. Lever, eds., *Inorganic electronic structure and spectroscopy volume II: Applicaitions and case studies*. John Wiley & Sons, 1999.

[44] K. Tsutsumi, "The X-ray non-diagram lines of Kβ' of some compouns of the iron group," *Journal of the Physical Society of Japan*, vol. 14, no. 12, pp. 1679–1706, 1959.

[45] K. Tsutsumi and H. Nakamori, "X-ray K emission spectra of chromium in various chromium compounds," *Journal of the Physical Society of Japan*, vol. 25, no. 5, pp. 1418–1423, 1968.

[46] K. Tsutsumi, H. Nakamori, and K. Ichikawa, "X-ray Mn Kβ emission spectra of manganese oxides and manganates," *Physical Review B*, vol. 13, no. 2, pp. 929–933, 1976.

[47] R. K. Hocking, S. DeBeer George, Z. Gross, F. A. Walker, K. O. Hodgson, B. Hedman, and E. I. Solomon, "Fe L- and K-edge XAS of low-spin ferric corrole: Bonding and reactivity relative to low-spin ferric porphyrin," *Inorganic Chemistry*, vol. 48, no. 4, pp. 1678–1688, 2009.

[48] R. K. Hocking, E. C. Wasinger, F. M. De Groot, K. O. Hodgson, B. Hedman, and E. I. Solomon, "Fe L-edge XAS studies of $K_4[Fe(CN)_6]$ and $K_3[Fe(CN)_6]$: A direct probe of back-bonding," *Journal of the American Chemical Society*, vol. 128, no. 32, pp. 10442–10451, 2006.

[49] R. K. Hocking, S. D. George, K. N. Raymond, K. O. Hodgson, B. Hedman, and E. I. Solomon, "Fe L-Edge X-ray absorption spectroscopy determination of differential orbital covalency of siderophore model compounds: Electronic structure contributions to high stability constants," *Journal of the American Chemical Society*, vol. 132, no. 11, pp. 4006–4015, 2010.

[50] E. C. Wasinger, F. M. De Groot, B. Hedman, K. O. Hodgson, and E. I. Solomon, "L-edge X-ray absorption spectroscopy of non-heme iron sites: Experimental determination of differential orbital covalency," *Journal of the American Chemical Society*, vol. 125, no. 42, pp. 12894–12906, 2003.

[51] M. O. Krause and J. H. Oliver, "Natural widths of atomic K and L levels, Kα X-ray lines and several KLL Auger lines," *Journal of Physical and Chemical Reference Data*, vol. 8, no. 2, pp. 329–338, 1979.

[52] F. M. Degroot and A. Kotani, *Core Level Spctroscopy of Solids*. Boca Raton, FL,: Taylor & Francis Group, 2008.

[53] J. Vura-Weis, C. M. Jiang, C. Liu, H. Gao, J. M. Lucas, F. M. De Groot, P. Yang, A. P. Alivisatos, and S. R. Leone, "Femtosecond $M_{2,3}$-edge spectroscopy of transition-metal oxides: Photoinduced oxidation state change in α-Fe_2O_3," *Journal of Physical Chemistry Letters*, vol. 4, no. 21, pp. 3667–3671, 2013.

[54] E. S. Ryland, M. F. Lin, M. A. Verkamp, K. Zhang, K. Benke, M. Carlson, and J. Vura-Weis, "Tabletop femtosecond M-edge X-ray absorption near-edge structure of FeTPPCl: metalloporphyrin photophysics from the perspective of the metal," *Journal of the American Chemical Society*, vol. 140, no. 13, pp. 4691–4696, 2018.

[55] T. X. Carroll, J. Hahne, T. D. Thomas, L. J. Sæthre, N. Berrah, J. Bozek, and E. Kukk, "Carbon 1s core-hole lifetime in CO_2," *Physical Review A - Atomic, Molecular, and Optical Physics*, vol. 61, no. 4, pp. 425031–425037, 2000.

[56] A. A. Lutman, R. N. Coffee, Y. Ding, Z. Huang, J. Krzywinski, T. Maxwell, M. Messerschmidt, and H. D. Nuhn, "Experimental demonstration of femtosecond two-color X-ray free-electron lasers," *Physical Review Letters*, vol. 110, 3 2013.

[57] T. Hara, Y. Inubushi, T. Katayama, T. Sato, H. Tanaka, T. Tanaka, T. Togashi, K. Togawa, K. Tono, M. Yabashi, and T. Ishikawa, "Two-colour hard X-ray free-electron laser with wide tunability," *Nature Communications*, vol. 4, pp. 2919–5, 2013.

[58] A. A. Lutman, F. J. Decker, J. Arthur, Chollet, Y. Feng, J. Hastings, Z. Huang, H. Lemke, H. D. Nuhn, A. Marinelli, J. L. Turner, S. Wakatsuki, J. Welch, and D. Zhu, "Demonstration of single-crystal self-seeded two-color X-ray free-electron lasers," *Physical Review Letters*, vol. 113, no. 25, pp. 254801–5, 2014.

[59] A. Marinelli, D. Ratner, A. A. Lutman, J. Turner, J. Welch, F. J. Decker, H. Loos, C. Behrens, S. Gilevich, A. A. Miahnahri, S. Vetter, T. J. Maxwell, Y. Ding, R. N. Coffee, S. Wakatsuki, and Z. Huang, "High-intensity double-pulse X-ray free-electron laser," *Nature Communications*, vol. 6, pp. 6369–6, 2015.

[60] W. Lu, B. Friedrich, T. Noll, K. Zhou, J. Hallmann, G. Ansaldi, T. Roth, S. Serkez, G. Geloni, A. Madsen, and S. Eisebitt, "Development of a hard X-ray split-and-delay line and performance simulations for two-color pump-probe experiments at the European XFEL," *Review of Scientific Instruments*, vol. 89, no. 6, p. 30010, 2018.

[61] E. Prat, P. Dijkstal, E. Ferrari, R. Ganter, P. Juranić, A. Malyzhenkov, S. Reiche, T. Schietinger, G. Wang, A. A. Haddad, S. Augustin, C. Bostedt, G. Knopp, J. Knurr,

A. S. Morillo-Candas, Z. Sun, and K. Schnorr, "Widely tunable two-color X-ray free-electron laser pulses," *Physical Review Research*, vol. 4, no. 2, p. L022025, 2022.

[62] J. D. Gaynor, R. B. Weakly, and M. Khalil, "Multimode two-dimensional vibronic spectroscopy. I. Orientational response and polarization-selectivity," *Journal of Chemical Physics*, vol. 154, p. 184201, 2021.

[63] R. B. Weakly, J. D. Gaynor, and M. Khalil, "Multimode two-dimensional vibronic spectroscopy II: Simulating and extracting vibronic coupling parameters from polarization-selective spectra," *Journal of Chemical Physics*, vol. 154, p. 184202, 2021.

[64] C. E. Liekhus-Schmaltz, P. J. Ho, R. B. Weakly, A. Aquila, R. W. Schoenlein, M. Khalil, and N. Govind, "Ultrafast X-ray pump X-ray probe transient absorption spectroscopy: A computational study and proposed experiment probing core-valence electronic correlations in solvated complexes," *Journal of Chemical Physics*, vol. 154, no. 21, p. 214107, 2021.

[65] J. D. Gaynor, *Correlated electronic and vibrational motion : A direct perspective through multidimensional electronic-vibrational spectroscopy.* PhD thesis, University of Washington, 2019.

[66] W. P. Aue, E. Bartholdi, and R. R. Ernst, "Two-dimensional spectroscopy. Application to nuclear magnetic resonance," *Journal of Chemical Physics*, vol. 64, no. 5, pp. 2229–2246, 1976.

[67] S. Mukamel, D. Abramavicius, L. Yang, W. Zhuang, I. V. Schweigert, and D. V. Voronine, "Coherent multidimensional optical probes for electron correlations and exciton dynamics: From NMR to X-rays," *Accounts of Chemical Research*, vol. 42, no. 4, pp. 553–562, 2009.

[68] N. S. Ginsberg, J. A. Davis, M. Ballottari, Y. C. Cheng, R. Bassi, and G. R. Fleming, "Solving structure in the CP29 light harvesting complex with polarization-phased 2D electronic spectroscopy," *Proceedings of the National Academy of Sciences*, vol. 108, no. 10, pp. 3848–3853, 2011.

[69] V. R. Policht, A. Niedringhaus, and J. P. Ogilvie, "Characterization of vibrational coherence in monomeric bacteriochlorophyll a by two-dimensional electronic spectroscopy," *Journal of Physical Chemistry Letters*, vol. 9, no. 22, pp. 6631–6637, 2018.

[70] T. Brixner, J. Stenger, H. a. M. Vaswani, M. Cho, R. E. Blankenship, and G. R. Fleming, "Two-dimensional spectroscopy of electronic couplings in photosynthesis," *Nature*, vol. 434, no. 7033, pp. 625–628, 2005.

[71] G. S. Schlau-Cohen, A. Ishizaki, T. R. Calhoun, N. S. Ginsberg, M. Ballottari, R. Bassi, and G. R. Fleming, "Elucidation of the timescales and origins of quantum electronic coherence in LHCII," *Nature Chemistry*, vol. 4, no. 5, pp. 389–395, 2012.

[72] G. S. Engel, T. R. Calhoun, E. L. Read, T. K. Ahn, T. Mančal, Y. C. Cheng, R. E. Blankenship, and G. R. Fleming, "Evidence for wavelike energy transfer through quantum coherence in photosynthetic systems," *Nature Letters*, vol. 446, no. 7137, pp. 782–786, 2007.

[73] E. Meneghin, A. Volpato, L. Cupellini, L. Bolzonello, S. Jurinovich, V. Mascoli, D. Carbonera, B. Mennucci, and E. Collini, "Coherence in carotenoid-to-chlorophyll energy transfer," *Nature Communications*, vol. 9, no. 1, p. 3160, 2018.

[74] O. Bixner, V. Lukeš, T. Mančal, J. Hauer, F. Milota, M. Fischer, I. Pugliesi, M. Bradler, W. Schmid, E. Riedle, H. F. Kauffmann, and N. Christensson, "Ultrafast photo-induced charge transfer unveiled by two-dimensional electronic spectroscopy," *Journal of Chemical Physics*, vol. 136, no. 20, p. 204503, 2012.

[75] D. B. Turner, K. W. Stone, K. Gundogdu, and K. A. Nelson, "Three-dimensional electronic spectroscopy of excitons in GaAs quantum wells," *Journal of Chemical Physics*, vol. 131, no. 14, p. 144510, 2009.

[76] A. Jha, H. G. Duan, V. Tiwari, P. K. Nayak, H. J. Snaith, M. Thorwart, and R. J. Dwayne Miller, "Direct observation of ultrafast exciton dissociation in lead iodide perovskite by 2D electronic spectroscopy," *ACS Photonics*, vol. 5, no. 3, pp. 852–860, 2018.

[77] D. B. Turner, P. Wen, D. H. Arias, and K. A. Nelson, "Coherent two-exciton dynamics measured using two-quantum rephasing two-dimensional electronic spectroscopy," *Physical Review B*, vol. 84, no. 16, p. 165321, 2011.

[78] A. Halpin, P. J. Johnson, R. Tempelaar, R. S. Murphy, J. Knoester, T. L. Jansen, and R. J. Dwayne Miller, "Two-dimensional spectroscopy of a molecular dimer unveils the effects of vibronic coupling on exciton coherences," *Nature Chemistry*, vol. 6, no. 3, pp. 196–201, 2014.

[79] D. Abramavicius, B. Palmieri, D. V. Voronine, F. Šanda, and S. Mukamel, "Coherent multidimensional optical spectroscopy of excitons in molecular aggregates; quasiparticle versus supermolecule perspectives," *Chemical Reviews*, vol. 109, no. 6, pp. 2350–2408, 2009.

[80] F. Milota, V. I. Prokhorenko, T. Mancal, H. Von Berlepsch, O. Bixner, H. F. Kauffmann, and J. Hauer, "Vibronic and vibrational coherences in two-dimensional electronic spectra of supramolecular J-aggregates," *Journal of Physical Chemistry A*, vol. 117, no. 29, pp. 6007–6014, 2013.

[81] Y. S. Kim and R. M. Hochstrasser, "Chemical exchange 2D IR of hydrogen-bond making and breaking," *Proceedings of the National Academy of Sciences*, vol. 102, no. 32, pp. 11185–11190, 2005.

[82] J. Kübel, G. Lee, S. A. Ooi, S. Westenhoff, H. Han, M. Cho, and M. Maj, "Ultrafast chemical exchange dynamics of hydrogen bonds observed via isonitrile infrared sensors: implications for biomolecular studies," *Journal of Physical Chemistry Letters*, vol. 10, no. 24, pp. 7878–7883, 2019.

[83] K. Kwak, J. Zheng, H. Cang, and M. D. Fayer, "Ultrafast two-dimensional infrared vibrational echo chemical exchange experiments and theory," *Journal of Physical Chemistry B*, vol. 110, no. 40, pp. 19998–20013, 2006.

[84] K. M. Slenkamp, M. S. Lynch, B. E. Van Kuiken, J. F. Brookes, C. C. Bannan, S. L. Daifuku, and M. Khalil, "Investigating vibrational anharmonic couplings in cyanide-bridged transition metal mixed valence complexes using two-dimensional infrared spectroscopy," *Journal of Chemical Physics*, vol. 140, no. 8, p. 84505, 2014.

[85] M. Khalil, N. Demirdöven, and A. Tokmakoff, "Coherent 2D IR spectroscopy: Molecular structure and dynamics in solution," *Journal of Physical Chemistry A*, vol. 107, no. 27, pp. 5258–5279, 2003.

[86] E. C. Fulmer, P. Mukherjee, A. T. Krummel, and M. T. Zanni, "A pulse sequence for directly measuring the anharmonicities of coupled vibrations: Two-quantum two-dimensional infrared spectroscopy," *Journal of Chemical Physics*, vol. 120, no. 17, pp. 8067–8078, 2004.

[87] T. A. Oudenhoven, Y. Joo, J. E. Laaser, P. Gopalan, and M. T. Zanni, "Dye aggregation identified by vibrational coupling using 2D IR spectroscopy," *Journal of Chemical Physics*, vol. 142, no. 21, p. 212449, 2015.

[88] J. D. Eaves, J. J. Loparo, C. J. Fecko, S. T. Roberts, A. Tokmakoff, and P. L. Geissler, "Hydrogen bonds in liquid water are broken only fleetingly," *Proceedings of the National Academy of Sciences*, vol. 102, no. 37, pp. 13019–13022, 2005.

[89] T. Brinzer, E. J. Berquist, Z. Ren, S. Dutta, C. A. Johnson, C. S. Krisher, D. S. Lambrecht, and S. Garrett-Roe, "Ultrafast vibrational spectroscopy (2D-IR) of CO_2

in ionic liquids: Carbon capture from carbon dioxide's point of view," *Journal of Chemical Physics*, vol. 142, p. 212425, jun 2015.

[90] M. L. Cowan, B. D. Bruner, N. Huse, J. R. Dwyer, B. Chugh, E. T. Nibbering, T. Elsaesser, and R. J. Miller, "Ultrafast memory loss and energy redistribution in the hydrogen bond network of liquid H_2O," *Nature*, vol. 434, no. 7030, pp. 199–202, 2005.

[91] S. Garrett-Roe, F. Perakis, F. Rao, and P. Hamm, "Three-dimensional infrared spectroscopy of isotope-substituted liquid water reveals heterogeneous dynamics," *Journal of Physical Chemistry B*, vol. 115, no. 21, pp. 6976–6984, 2011.

[92] M. C. Thielges and M. D. Fayer, "Protein dynamics studied with ultrafast two-dimensional infrared vibrational echo spectroscopy," *Accounts of Chemical Research*, vol. 45, no. 11, pp. 1866–1874, 2012.

[93] E. R. Andresen and P. Hamm, "Site-specific difference 2D-IR spectroscopy of bacteriorhodopsin," *Journal of Physical Chemistry B*, vol. 113, no. 18, pp. 6520–6527, 2009.

[94] M. Lim, P. Hamm, and R. M. Hochstrasser, "Protein fluctuations are sensed by stimulated infrared echoes of the vibrations of carbon monoxide and azide probes," *Proceedings of the National Academy of Sciences*, vol. 95, no. 26, pp. 15315–15320, 1998.

[95] H. T. Kratochvil, M. Maj, K. Matulef, A. W. Annen, J. Ostmeyer, E. Perozo, B. Roux, F. I. Valiyaveetil, and M. T. Zanni, "Probing the effects of gating on the ion occupancy of the K^+ channel selectivity filter using two-dimensional infrared spectroscopy," *Journal of the American Chemical Society*, vol. 139, no. 26, pp. 8837–8845, 2017.

[96] C. R. Baiz, Y. S. Lin, C. S. Peng, K. A. Beauchamp, V. A. Voelz, V. S. Pande, and A. Tokmakoff, "A molecular interpretation of 2D IR protein folding experiments with Markov state models," *Biophysical Journal*, vol. 106, no. 6, pp. 1359–1370, 2014.

[97] P. Hamm and M. T. Zanni, *Concepts and Methods of 2D infrared Spectroscopy*. Cambridge University Press, 2011.

[98] A. Tokmakoff, "Orientational correlation functions and polarization selectivity for nonlinear spectroscopy of isotropic media. II. Fifth order," *Journal of Chemical Physics*, vol. 105, no. 1, pp. 13–21, 1996.

[99] E. L. Read, G. S. Engel, T. R. Calhoun, T. Mančal, T. K. Ahn, R. E. Blankenship, and G. R. Fleming, "Cross-peak-specific two-dimensional electronic spectroscopy," *Proceedings of the National Academy of Sciences*, vol. 104, no. 36, pp. 14203–14208, 2007.

[100] M. T. Zanni, N. H. Ge, Yung Sam Kim, and R. M. Hochstrasser, "Two-dimensional IR spectroscopy can be designed to eliminate the diagonal peaks and expose only the crosspeaks needed for structure determination," *Proceedings of the National Academy of Sciences*, vol. 98, no. 20, pp. 11265–11270, 2001.

[101] E. Thyrhaug, K. Žídek, J. Dostál, D. Bína, and D. Zigmantas, "Exciton structure and energy transfer in the Fenna-Matthews-Olson complex," *Journal of Physical Chemistry Letters*, vol. 7, no. 9, pp. 1653–1660, 2016.

[102] D. M. Jonas, "Vibrational and nonadiabatic coherence in 2D electronic spectroscopy, the Jahn-Teller effect, and energy transfer," *Annual Review of Physical Chemistry*, vol. 69, pp. 327–352, 2018.

[103] S. Woutersen and P. Hamm, "Structure determination of trialanine in water using polarization sensitive two-dimensional vibrational spectroscopy," *Journal of Physical Chemistry B*, vol. 104, no. 47, pp. 11316–11320, 2000.

[104] M. T. Zanni, S. Gnanakaran, J. Stenger, and R. M. Hochstrasser, "Heterodyned two-dimensional infrared spectroscopy of solvent-dependent conformations of acetylproline-NH_2," *Journal of Physical Chemistry B*, vol. 105, no. 28, pp. 6520–6535, 2001.

[105] L. De Marco, W. Carpenter, H. Liu, R. Biswas, J. M. Bowman, and A. Tokmakoff, "Differences in the vibrational dynamics of H_2O and D_2O: observation of symmetric and antisymmetric stretching vibrations in heavy water," *Journal of Physical Chemistry Letters*, vol. 7, no. 10, pp. 1769–1774, 2016.

[106] M. Ji, M. Odelius, and K. J. Gaffney, "Large angular jump mechanism observed for hydrogen bond exchange in aqueous perchlorate solution," *Science*, vol. 328, no. 5981, pp. 1003–1005, 2010.

[107] P. L. Kramer, J. Nishida, C. H. Giammanco, A. Tamimi, and M. D. Fayer, "Observation and theory of reorientation-induced spectral diffusion in polarization-selective 2D IR spectroscopy," *Journal of Chemical Physics*, vol. 142, no. 18, p. 184505, 2015.

[108] L. P. Deflores, Z. Ganim, R. A. Nicodemus, and A. Tokmakoff, "Amide I-II 2D IR spectroscopy provides enhanced protein secondary structural sensitivity," *Journal of the American Chemical Society*, vol. 131, no. 9, pp. 3385–3391, 2009.

[109] J. D. Gaynor, T. L. Courtney, M. Balasubramanian, and M. Khalil, "Fourier transform two-dimensional electronic-vibrational spectroscopy using an octave-spanning mid-IR probe," *Optics Letters*, vol. 41, no. 12, p. 2895, 2016.

[110] Y. Song, A. Konar, R. Sechrist, V. P. Roy, R. Duan, J. Dziurgot, V. Policht, Y. A. Matutes, K. J. Kubarych, and J. P. Ogilvie, "Multispectral multidimensional spectrometer spanning the ultraviolet to the mid-infrared," *Review of Scientific Instruments*, vol. 90, no. 1, p. 013108, 2019.

[111] P. P. Roy, J. Shee, E. A. Arsenault, Y. Yoneda, K. Feuling, M. Head-Gordon, and G. R. Fleming, "Solvent mediated excited state proton transfer in indigo carmine," *Journal of Physical Chemistry Letters*, vol. 11, no. 10, pp. 4156–4162, 2020.

[112] E. A. Arsenault, Y. Yoneda, M. Iwai, K. K. Niyogi, and G. R. Fleming, "The role of mixed vibronic Q_y-Q_x states in green light absorption of light-harvesting complex II," *Nature Communications*, vol. 11, p. 6011, 2020.

[113] E. A. Arsenault, Y. Yoneda, M. Iwai, K. K. Niyogi, and G. R. Fleming, "Vibronic mixing enables ultrafast energy flow in light-harvesting complex II," *Nature Communications*, vol. 11, no. 1, pp. 1–8, 2020.

[114] N. H. Lewis, N. L. Gruenke, T. A. Oliver, M. Ballottari, R. Bassi, and G. R. Fleming, "Observation of electronic excitation eransfer through light harvesting complex II using two-dimensional electronic-vibrational spectroscopy," *Journal of Physical Chemistry Letters*, vol. 7, no. 20, pp. 4197–4206, 2016.

[115] T. A. Oliver and G. R. Fleming, "Following coupled electronic-nuclear motion through conical intersections in the ultrafast relaxation of β-Apo-8-carotenal," *Journal of Physical Chemistry B*, vol. 119, no. 34, pp. 11428–11441, 2015.

[116] E. C. Wu, Q. Ge, E. A. Arsenault, N. H. Lewis, N. L. Gruenke, M. J. Head-Gordon, and G. R. Fleming, "Two-dimensional electronic-vibrational spectroscopic study of conical intersection dynamics: An experimental and electronic structure study," *Physical Chemistry Chemical Physics*, vol. 21, no. 26, pp. 14153–14163, 2019.

[117] N. H. Lewis, H. Dong, T. A. Oliver, and G. R. Fleming, "Measuring correlated electronic and vibrational spectral dynamics using line shapes in two-dimensional electronic-vibrational spectroscopy," *Journal of Chemical Physics*, vol. 142, no. 17, p. 174202, 2015.

[118] M. Cho and G. R. Fleming, "Two-dimensional electronic-vibrational spectroscopy reveals cross-correlation between solvation dynamics and vibrational spectral diffusion," *Journal of Physical Chemistry B*, vol. 124, no. 49, pp. 11222–11235, 2020.

[119] Y. Song, A. Schubert, E. Maret, R. K. Burdick, B. D. Dunietz, E. Geva, and J. P. Ogilvie, "Vibronic structure of photosynthetic pigments probed by polarized two-dimensional electronic spectroscopy and ab initio calculations," *Chemical Science*, vol. 10, no. 35, pp. 8143–8153, 2019.

[120] G. M. Sando, K. G. Spears, J. T. Hupp, and P. T. Ruhoff, "Large electron transfer rate effects from the Duschinsky mixing of vibrations," *Journal of Physical Chemistry A*, vol. 105, no. 22, pp. 5317–5325, 2001.

[121] J. W. Kim, J. Jeon, T. H. Yoon, and M. Cho, "Two-dimensional electronic spectroscopy of bacteriochlorophyll a with synchronized dual mode-locked lasers," *Nature Communications*, vol. 11, no. 1, p. 6029, 2020.

[122] H. D. Zhang, Q. Qiao, R. X. Xu, and Y. Yan, "Effects of Herzberg-Teller vibronic coupling on coherent excitation energy transfer," *Journal of Chemical Physics*, vol. 145, no. 20, p. 204109, 2016.

[123] L. Paul, T. Moitra, K. Ruud, and S. Chakrabarti, "Strong Duschinsky mixing induced breakdown of Kasha's rule in an organic phosphor," *Journal of Physical Chemistry Letters*, vol. 10, no. 3, pp. 369–374, 2019.

[124] K. Huang and A. Rhys, "Theory of light absorption and non-radiative transitions in F-centres," *Proceedings of the Royal Society A*, vol. 204, no. 1078, pp. 406–423, 1950.

[125] S. Mukamel, *Principles of Nonlinear Optical Spectroscopy*. New York, USA: Oxford University Press, 1995.

[126] J. Sung and R. J. Silbey, "Four wave mixing spectroscopy for a multilevel system," *Journal of Chemical Physics*, vol. 115, no. 20, pp. 9266–9287, 2001.

[127] M. Cho, G. R. Fleming, and S. Mukamel, "Nonlinear response functions for birefringence and dichroism measurements in condensed phases," *Journal of Chemical Physics*, vol. 98, no. 7, pp. 5314–5326, 1993.

[128] B. J. Berne and R. Pecora, *Dynamic light scattering: With applications in chemistry, biology, and physics*. New York, USA: Dover, 2000.

[129] L. D. Favro, "Theory of the rotational Brownian motion of a free rigid body," *Physical Review*, vol. 119, no. 1, pp. 53–62, 1960.

[130] C. C. Wang and R. Pecora, "Time-correlation functions for restricted rotational diffusion," *Journal of Chemical Physics*, vol. 72, no. 10, pp. 5333–5340, 1980.

[131] R. M. Hochstrasser, "Two-dimensional IR-spectroscopy: Polarization anisotropy effects," *Chemical Physics*, vol. 266, no. 2-3, pp. 273–284, 2001.

[132] J. R. Lakowicz, *Principles of fluorescence spectroscopy*. New York, USA: Springer US, 2006.

[133] M. Lim, T. A. Jackson, and P. A. Anfinrud, "Binding of CO to myoglobin from a heme pocket docking site to form nearly linear Fe-C-O," *Science*, vol. 269, no. 5226, pp. 962–966, 1995.

[134] J. Bredenbeck, J. Helbing, and P. Hamm, "Transient two-dimensional infrared spectroscopy: Exploring the polarization dependence," *Journal of Chemical Physics*, vol. 121, no. 12, pp. 5943–5957, 2004.

[135] G. S. Schlau-Cohen, T. R. Calhoun, N. S. Ginsberg, M. Ballottari, R. Bassi, and G. R. Fleming, "Spectroscopic elucidation of uncoupled transition energies in the major photosynthetic light-harvesting complex, LHCII," *Proceedings of the National Academy of Sciences*, vol. 107, no. 30, pp. 13276–13281, 2010.

[136] D. Paleček, P. Edlund, E. Gustavsson, S. Westenhoff, and D. Zigmantas, "Potential pitfalls of the early-time dynamics in two-dimensional electronic spectroscopy," *Journal of Chemical Physics*, vol. 151, no. 2, p. 24201, 2019.

[137] M. K. Petti, J. S. Ostrander, E. R. Birdsall, M. B. Kunz, Z. T. Armstrong, A. M. Alperstein, and M. T. Zanni, "A proposed method to obtain surface specificity with pump-probe and 2D spectroscopies," *Journal of Physical Chemistry A*, vol. 124, no. 17, pp. 3471–3483, 2020.

[138] J. A. Myers, K. L. Lewis, P. F. Tekavec, and J. P. Ogilvie, "Two-color two-dimensional Fourier transform electronic spectroscopy with a pulse-shaper," *Optics Express*, vol. 16, no. 22, p. 17420, 2008.

[139] K. Wynne and R. M. Hochstrasser, "The theory of ultrafast vibrational spectroscopy," *Chemical Physics*, vol. 193, no. 3, pp. 211–236, 1995.

[140] J. Lu, Y. Lee, and J. M. Anna, "Extracting the frequency-dependent dynamic Stokes shift from two-dimensional electronic spectra with prominent vibrational coherences," *Journal of Physical Chemistry B*, vol. 124, no. 40, pp. 8857–8867, 2020.

[141] A. De Sio, X. T. Nguyen, and C. Lienau, "Signatures of strong vibronic coupling mediating coherent charge transfer in two-dimensional electronic spectroscopy," *Zeitschrift fur Naturforschung - Section A Journal of Physical Sciences*, vol. 74, no. 8, pp. 721–737, 2019.

[142] A. De Sio, E. Sommer, X. T. Nguyen, L. Groß, D. Popović, B. T. Nebgen, S. Fernandez-alberti, S. Pittalis, C. A. Rozzi, E. Molinari, E. Mena-Osteritz, P. Bäuerle, T. Frauenheim, S. Tretiak, and C. Lienau, "Intermolecular conical interactions in molecular aggregates," *Nature Nanotechnology*, vol. 16, pp. 63–68, 2021.

[143] J. E. Laaser and M. T. Zanni, "Extracting structural information from the polarization dependence of one- and two-dimensional sum frequency generation spectra," *Journal of Physical Chemistry A*, vol. 117, no. 29, pp. 5875–5890, 2013.

[144] C. R. Baiz, B. Błasiak, J. Bredenbeck, M. Cho, J.-H. Choi, S. A. Corcelli, A. G. Dijkstra, C.-J. Feng, S. Garrett-Roe, N.-H. Ge, M. W. D. Hanson-Heine, J. D. Hirst, T. L. C. Jansen, K. Kwac, K. J. Kubarych, C. H. Londergan, H. Maekawa, M. Reppert, S. Saito, S. Roy, J. L. Skinner, G. Stock, J. E. Straub, M. C. Thielges, K. Tominaga, A. Tokmakoff, H. Torii, L. Wang, L. J. Webb, and M. T. Zanni, "Vibrational spectroscopic map, vibrational spectroscopy, and intermolecular interaction," *Chemical Reviews*, vol. 120, no. 15, pp. 7152–7218, 2020.

[145] M. S. Child and R. T. Lawton, "Local and normal vibrational states: A harmonically coupled anharmonic-oscillator model," *Faraday Discussions of the Chemical Society*, vol. 71, pp. 273–285, 1981.

[146] T. L. C. Jansen, S. Saito, J. Jeon, and M. Cho, "Theory of coherent two-dimensional vibrational spectroscopy," 2019.

[147] E. L. Sibert, "Modeling vibrational anharmonicity in infrared spectra of high frequency vibrations of polyatomic molecules," *Journal of Chemical Physics*, vol. 150, no. 9, p. 90901, 2019.

[148] A. Tokmakoff and M. D. Fayer, "Frequency-frequency correlation functions and apodization in two-dimensional infrared vibrational echo spectroscopy: A new approach," *Journal of Chemical Physics*, vol. 103, no. 8, pp. 2810–2826, 1995.

[149] E. R. Smith, D. A. Farrow, and D. M. Jonas, "Response functions for dimers and square-symmetric molecules in four-wave-mixing experiments with polarized light," *Journal of Chemical Physics*, vol. 123, no. 4, p. 044102, 2005.

[150] A. Jain, A. S. Petit, J. M. Anna, and J. E. Subotnik, "Simple and efficient theoretical approach to compute 2D optical spectra," *Journal of Physical Chemistry B*, vol. 123, no. 7, pp. 1602–1617, 2019.

[151] T. Kunsel, V. Tiwari, Y. A. Matutes, A. T. Gardiner, R. J. Cogdell, J. P. Ogilvie, and T. L. Jansen, "Simulating fluorescence-detected two-dimensional electronic spectroscopy of multichromophoric systems," *Journal of Physical Chemistry B*, vol. 123, no. 2, pp. 394–406, 2019.

[152] A. Baiardi, J. Bloino, and V. Barone, "General time dependent approach to vibronic spectroscopy including Franck-Condon, Herzberg-Teller, and Duschinsky effects," *Journal of Chemical Theory and Computation*, vol. 9, no. 9, pp. 4097–4115, 2013.

[153] M. Toutounji, "Spectroscopy of vibronically coupled and Duschinskcally rotated polyatomic molecules," *Journal of Chemical Theory and Computation*, vol. 16, no. 3, pp. 1690–1698, 2020.

[154] G. J. Small, "Herzberg-Teller vibronic coupling and the Duschinsky effect," *Journal of Chemical Physics*, vol. 54, no. 8, pp. 3300–3306, 1971.

[155] K. Polley and R. F. Loring, "Two-dimensional vibronic spectra from classical trajectories," *Journal of Chemical Physics*, vol. 150, no. 16, p. 164114, 2019.

[156] P. Bhattacharyya and G. R. Fleming, "The role of resonant nuclear modes in vibrationally assisted energy transport: The LHCII complex," *Journal of Chemical Physics*, vol. 153, no. 4, p. 44119, 2020.

[157] S. Woutersen and P. Hamm, "Nonlinear two-dimensional vibrational spectroscopy of peptides," *Journal of Physics: Condensed Matter*, vol. 14, no. 39, pp. R1035–R1062, 2002.

[158] M. Born and R. Oppenheimer, "Zur Quantentheorie der Molekeln," *Annalen der Physik*, vol. 389, no. 20, pp. 457–484, 1927.

[159] C. Ballhausen and A. Hansen, "Electronic spectra," *Annual Review of Biomedical Engineering*, vol. 23, pp. 15–38, 1972.

[160] J. C. Vallet, A. J. Boeglin, J. P. Lavoine, and A. A. Villaeys, "Vibronic mode couplings in adsorbed molecules analyzed by doubly resonant sum-frequency generation," *Physical Review A*, vol. 53, no. 6, pp. 4508–4518, 1996.

[161] C. Cohen-Tannoudji and B. Diu, *Quantum mechanics*. Paris: Wiley-Interscience, 1977.

[162] D. L. Tonks and J. B. Page, "General theory of vibrational mode mixing and frequency shifts in resonance Raman scattering," *Chemical Physics Letters*, vol. 79, no. 2, pp. 247–252, 1981.

[163] Q. Peng, Y. Yi, Z. Shuai, and J. Shao, "Excited state radiationless decay process with Duschinsky rotation effect: Formalism and implementation," *Journal of Chemical Physics*, vol. 126, no. 11, p. 114302, 2007.

[164] D. Harris and M. Bertolucci, *Symmetry and spectroscopy: An introduction to vibrational and electronic spectroscopy.* new Yok: Dover, 1989.

[165] J. Hollas, *Modern spectrscopy.* West Sussex, England: John Wiley & Sons, 2nd ed., 1992.

[166] G. Fischer, *Vibronic coupling: The interactions between electronic and nuclear motions.* London: Academic Press, 1984.

[167] T. Azumi and K. Matsuzaki, "What does the term "vibronic coupling" mean?," *Photochemistry and Photobiology*, vol. 25, no. 3, pp. 315–326, 1977.

[168] G. Herzberg and E. Teller, "Fluctuation structure of electron transfer in multiatomic molecules," *Z. Phys. Chem.*, vol. 21, no. 410-446, 1933.

[169] A. Tokmakoff, "Orientational correlation functions and polarization selectivity for nonlinear spectroscopy of isotropic media. I. Third order," *Journal of Chemical Physics*, vol. 105, no. 1, pp. 1–12, 1996.

[170] J. Bredenbeck, J. Helbing, and P. Hamm, "Labeling vibrations by light: Ultrafast transient 2D-IR spectroscopy tracks vibrational modes during photoinduced charge transfer," *Journal of the American Chemical Society*, vol. 126, no. 4, pp. 990–991, 2004.

[171] E. C. Fulmer, F. Ding, and M. T. Zanni, "Heterodyned fifth-order 2D-IR spectroscopy of the azide ion in an ionic glass," *Journal of Chemical Physics*, vol. 122, no. 3, p. 94202, 2005.

[172] T. J. Zuehlsdorff, H. Hong, L. Shi, and C. M. Isborn, "Nonlinear spectroscopy in the condensed phase: The role of Duschinsky rotations and third order cumulant contributions," *Journal of Chemical Physics*, vol. 153, no. 4, p. 44127, 2020.

[173] P. T. Chou, Y. C. Chen, W. S. Yu, Y. H. Chou, C. Y. Wei, and Y. M. Cheng, "Excited-state intramolecular proton transfer in 10-hydroxybenzo[h]quinoline," *Journal of Physical Chemistry A*, vol. 105, no. 10, pp. 1731–1740, 2001.

[174] W. Chansen, R. Salaeh, C. Prommin, K. Kerdpol, R. Daengngern, and N. Kungwan, "Theoretical study on influence of geometry controlling over the excited-state intramolecular proton transfer of 10-hydroxybenzo[h]quinoline and its derivatives," *Computational and Theoretical Chemistry*, vol. 1113, pp. 42–51, 8 2017.

[175] C. M. Loe, C. Liekhus-Schmaltz, N. Govind, and M. Khalil, "Spectral signatures of ultrafast excited-state intramolecular proton transfer from computational multi-edge transient X-ray absorption spectroscopy," *Journal of Physical Chemistry Letters*, vol. 12, no. 40, pp. 9840–9847, 2021.

[176] J. D. Gaynor, T. L. Courtney, M. Balasubramanian, and M. Khalil, "Fourier transform two-dimensional electronic-vibrational spectroscopy using an octave-spanning mid-IR probe," *Optics Letters*, vol. 41, no. 12, p. 2895, 2016.

[177] L. Whaley-Mayda, A. Guha, S. B. Penwell, and A. Tokmakoff, "Fluorescence-encoded infrared vibrational spectroscopy with single-molecule sensitivity," *Journal of the American Chemical Society*, vol. 143, no. 8, pp. 3060–3064, 2021.

[178] V. R. Policht, A. Niedringhaus, R. Willow, P. D. Laible, D. F. Bocian, C. Kirmaier, D. Holten, T. Mančal, and J. P. Ogilvie, "Hidden vibronic and excitonic structure and vibronic coherence transfer in the bacterial reaction center," *Sci. Adv*, vol. 8, p. 953, 3 2022.

[179] M. Cho, "Coherent two-dimensional optical spectroscopy," *Chemical Reviews*, vol. 108, no. 4, pp. 1331–1418, 2008.

[180] L. M. Kiefer and K. J. Kubarych, "NOESY-like 2D-IR spectroscopy reveals non-Gaussian dynamics," *Journal of Physical Chemistry Letters*, vol. 7, no. 19, pp. 3819–3824, 2016.

[181] L. Zhao, Z. Tao, F. Pavošević, A. Wildman, S. Hammes-Schiffer, and X. Li, "Real-time time-dependent nuclear-electronic orbital approach: Dynamics beyond the Born-Oppenheimer approximation," *Journal of Physical Chemistry Letters*, vol. 11, no. 10, pp. 4052–4058, 2020.

[182] P. E. Schneider, F. Pavošević, and S. Hammes-Schiffer, "Diagonal Born-Oppenheimer corrections within the nuclear-electronic orbital framework," *Journal of Physical Chemistry Letters*, vol. 10, no. 16, pp. 4639–4643, 2019.

[183] S. Hammes-Schiffer, "Theoretical perspectives on non-Born-Oppenheimer effects in chemistry," *Philosophical Transactions of the Royal Society A: Mathematical, Physical and Engineering Sciences*, vol. 380, no. 2223, 2022.

[184] A. S. Sardjan, F. P. Westerman, J. P. Ogilvie, and T. L. Jansen, "Observation of ultrafast coherence transfer and degenerate states with polarization-controlled two-dimensional electronic spectroscopy," *Journal of Physical Chemistry B*, vol. 124, no. 42, pp. 9420–9427, 2020.

[185] A. Marinelli, D. Ratner, A. A. Lutman, J. Turner, J. Welch, F.-J. Decker, H. Loos, C. Behrens, S. Gilevich, A. A. Miahnahri, S. Vetter, T. J. Maxwell, Y. Ding, R. Coffee, S. Wakatsuki, and Z. Huang, "High-intensity double-pulse X-ray free-electron laser," *Nature Communications*, vol. 6, no. 1, p. 6369, 2015.

[186] Y. Ding, C. Behrens, R. N. Coffee, F. J. Decker, P. Emma, C. Field, W. Helml, Z. Huang, P. Krejcik, J. Krzywinski, H. Loos, A. Lutman, A. Marinelli, T. J. Maxwell, and J. Turner, "Generating femtosecond X-ray pulses using an emittance-spoiling foil in free-electron lasers," *Applied Physics Letters*, vol. 107, no. 19, pp. 1–6, 2015.

[187] I. Inoue, T. Osaka, T. Hara, and M. Yabashi, "Two-color X-ray free-electron laser consisting of broadband and narrowband beams," *Journal of Synchrotron Radiation*, vol. 27, pp. 1720–1724, 2020.

[188] R. W. Schoenlein, A. Aquila, D. Cocco, G. L. Dakovski, D. M. Fritz, J. B. Hastings, P. A. Heimann, M. P. Minitti, T. Osipov, and W. F. Schlotter, "New science opportunities and experimental approaches enabled by high repetition rate soft X-ray lasers," in *X-Ray Free Electron Lasers: Applications in Materials, Chemistry and Biology*, ch. 23, pp. 434–457, The Royal Society of Chemistry, 2017.

[189] A. Picón, J. Mompart, and S. H. Southworth, "Stimulated Raman adiabatic passage with two-color X-ray pulses," *New Journal of Physics*, vol. 17, p. 083038, 2015.

[190] D. Cho and S. Mukamel, "Stimulated X-ray raman imaging of conical intersections," *Journal of Physical Chemistry Letters*, vol. 11, pp. 33–39, 2020.

[191] T. Heinz, O. Shpyrko, D. Basov, N. Berrah, P. Bucksbaum, T. Devereaux, D. Fritz, K. Gaffney, O. Gessner, V. Gopalan, Z. Hasan, A. Lanzara, T. Martinez, A. Millis, S. Mukamel, M. Murnane, K. Nelson, R. Prasankumar, D. Reis, K. Schafer, G. Scholes, Z.-X. Shen, A. Stolow, H. Wen, M. Wolf, D. Xiao, L. Young, B. Garrett, L. Horton, H. Kerch, J. Krause, T. Settersten, L. Wilson, K. Runkles, T. Anderson, G. Chui, and E. Rutherford, "Basic Energy Sciences Roundtable: Opportunities for Basic Research at the Frontiers of XFEL Ultrafast Science," Tech. Rep. 1616251, 2017.

[192] T. Driver, S. Li, E. G. Champenois, J. Duris, D. Ratner, T. J. Lane, P. Rosenberger, A. Al-Haddad, V. Averbukh, T. Barnard, N. Berrah, C. Bostedt, P. H. Bucksbaum, R. N. Coffee, L. F. DiMauro, L. Fang, D. Garratt, A. Gatton, Z. Guo, G. Hartmann,

D. Haxton, W. Helml, Z. Huang, A. LaForge, A. Kamalov, M. F. Kling, J. Knurr, M.-F. Lin, A. A. Lutman, J. P. MacArthur, J. P. Marangos, M. Nantel, A. Natan, R. Obaid, J. T. O'neal, N. H. Shivaram, A. Schori, P. Walter, A. L. Wang, T. J. Wolf, A. Marinelli, and J. P. Cryan, "Attosecond transient absorption spooktroscopy: A ghost imaging approach to ultrafast absorption spectroscopy," *Physical Chemistry Chemical Physics*, vol. 22, pp. 2704–2712, 2020.

[193] J. Duris, S. Li, T. Driver, E. G. Champenois, J. P. MacArthur, A. A. Lutman, Z. Zhang, P. Rosenberger, J. W. Aldrich, R. Coffee, G. Coslovich, F. J. Decker, J. M. Glownia, G. Hartmann, W. Helml, A. Kamalov, J. Knurr, J. Krzywinski, M. F. Lin, J. P. Marangos, M. Nantel, A. Natan, J. T. O'Neal, N. Shivaram, P. Walter, A. L. Wang, J. J. Welch, T. J. Wolf, J. Z. Xu, M. F. Kling, P. H. Bucksbaum, A. Zholents, Z. Huang, J. P. Cryan, and A. Marinelli, "Tunable isolated attosecond X-ray pulses with gigawatt peak power from a free-electron laser," *Nature Photonics*, vol. 14, no. 1, pp. 30–36, 2020.

[194] C. E. Liekhus-Schmaltz, I. Tenney, T. Osipov, A. Sanchez-Gonzalez, N. Berrah, R. Boll, C. Bomme, C. Bostedt, J. D. Bozek, S. Carron, R. Coffee, J. Devin, B. Erk, K. R. Ferguson, R. W. Field, L. Foucar, L. J. Frasinski, J. M. Glownia, M. Gühr, A. Kamalov, J. Krzywinski, H. Li, J. P. Marangos, T. J. Martinez, B. K. McFarland, S. Miyabe, B. Murphy, A. Natan, D. Rolles, A. Rudenko, M. Siano, E. R. Simpson, L. Spector, M. Swiggers, D. Walke, S. Wang, T. Weber, P. H. Bucksbaum, and V. S. Petrovic, "Ultrafast isomerization initiated by X-ray core ionization," *Nature Communications*, vol. 6, p. 8199, 2015.

[195] J. C. Castagna, B. Murphy, J. Bozek, and N. Berrah, "X-ray split and delay system for soft x-rays at LCLS," *Journal of Physics: Conference Series*, vol. 425, no. 15, p. 152021, 2013.

[196] A. Rudenko and D. Rolles, "Time-resolved studies with FELs," *Journal of Electron Spectroscopy and Related Phenomena*, vol. 204, pp. 228–236, Oct. 2015.

[197] L. Fang, T. Osipov, B. F. Murphy, A. Rudenko, D. Rolles, V. S. Petrovic, C. Bostedt, J. D. Bozek, P. H. Bucksbaum, and N. Berrah, "Probing ultrafast electronic and molecular dynamics with free-electron lasers," *Journal of Physics B: Atomic, Molecular and Optical Physics*, vol. 47, no. 12, p. 124006, 2014.

[198] N. Berrah and L. Fang, "Chemical analysis: Double core-hole spectroscopy with free-electron lasers," *Journal of Electron Spectroscopy and Related Phenomena*, vol. 204, pp. 284–289, 2015.

[199] C. S. Lehmann, A. Picón, C. Bostedt, A. Rudenko, A. Marinelli, D. Moonshiram, T. Osipov, D. Rolles, N. Berrah, C. Bomme, M. Bucher, G. Doumy, B. Erk, K. R. Ferguson, T. Gorkhover, P. J. Ho, E. P. Kanter, B. Krässig, J. Krzywinski, A. A. Lutman, A. M. March, D. Ray, L. Young, S. T. Pratt, and S. H. Southworth, "Ultrafast x-ray-induced nuclear dynamics in diatomic molecules using femtosecond x-ray-pump–x-ray-probe spectroscopy," *Physical Review A*, vol. 94, no. 1, p. 013426, 2016.

[200] M. L. Grünbein, L. Foucar, A. Gorel, M. Hilpert, M. Kloos, K. Nass, G. N. Kovacs, C. M. Roome, R. L. Shoeman, M. Stricker, S. Carbajo, W. Colocho, S. Gilevich, M. Hunter, J. Lewandowski, A. Lutman, J. E. Koglin, T. J. Lane, T. van Driel, J. Sheppard, S. L. Vetter, J. L. Turner, R. B. Doak, T. R. M. Barends, S. Boutet, A. L. Aquila, F.-J. Decker, I. Schlichting, and C. A. Stan, "Observation of shock-induced protein crystal damage during megahertz serial femtosecond crystallography," *Physical Review Research*, vol. 3, no. 1, p. 013046, 2021.

[201] T. Kroll, C. Weninger, F. D. Fuller, M. W. Guetg, A. Benediktovitch, Y. Zhang, A. Marinelli, R. Alonso-Mori, A. Aquila, M. Liang, J. E. Koglin, J. Koralek, D. Sokaras, D. Zhu, J. Kern, J. Yano, V. K. Yachandra, N. Rohringer, A. A. Lutman, and U. Bergmann, "Observation of seeded Mn Kβ stimulated X-ray emission using two-color X-ray free-electron laser pulses," *Physical Review Letters*, vol. 125, no. 3, p. 037404, 2020.

[202] I. Inoue, Y. Inubushi, T. Sato, K. Tono, T. Katayama, T. Kameshima, K. Ogawa, T. Togashi, S. Owada, Y. Amemiya, T. Tanaka, T. Hara, and M. Yabashi, "Observation of femtosecond X-ray interactions with matter using an X-ray–X-ray pump–probe scheme," *Proceedings of the National Academy of Sciences*, vol. 113, no. 6, pp. 1492–1497, 2016.

[203] T. Pardini, J. Alameda, A. Aquila, S. Boutet, T. Decker, A. Gleason, S. Guillet, P. Hamilton, M. Hayes, R. Hill, J. Koglin, B. Kozioziemski, J. Robinson, K. Sokolowski-Tinten, R. Soufli, and S. Hau-Riege, "Delayed onset of nonthermal melting in single-crystal silicon pumped with hard X- rays," *Physical Review Letters*, vol. 120, no. 26, p. 265701, 2018.

[204] W. Roseker, S. Lee, M. Walther, F. Lehmkühler, B. Hankiewicz, R. Rysov, S. O. Hruszkewycz, G. B. Stephenson, M. Sutton, P. H. Fuoss, M. Sikorski, A. Robert, S. Song, and G. Grübel, "Double-pulse speckle contrast correlations with near Fourier transform limited free-electron laser light using hard X-ray split-and-delay," *Scientific Reports*, vol. 10, no. 1, p. 5054, 2020.

[205] M. Chollet, R. Alonso-Mori, M. Cammarata, D. Damiani, J. Defever, J. T. Delor, Y. Feng, J. M. Glownia, J. B. Langton, S. Nelson, *et al.*, "The x-ray pump–probe

instrument at the linac coherent light source," *Journal of synchrotron radiation*, vol. 22, no. 3, pp. 503–507, 2015.

[206] R. N. Coffee, J. P. Cryan, J. Duris, W. Helml, S. Li, and A. Marinelli, "Development of ultrafast capabilities for x-ray free-electron lasers at the linac coherent light source," *Philosophical Transactions of the Royal Society A*, vol. 377, no. 2145, p. 20180386, 2019.

[207] Y. Ogi, Y. Obara, T. Katayama, Y.-I. Suzuki, S. Y. Liu, N. C.-M. Bartlett, N. Kurahashi, S. Karashima, T. Togashi, Y. Inubushi, K. Ogawa, S. Owada, M. Rubešová, M. Yabashi, K. Misawa, P. Slavíček, and T. Suzuki, "Ultraviolet photochemical reaction of $[Fe(III)(C_2O_4)_3]^{3-}$ in aqueous solutions studied by femtosecond time-resolved X-ray absorption spectroscopy using an X-ray free electron laser," *Structural Dynamics*, vol. 2, no. 3, p. 034901, 2015.

[208] G. Vankó, A. Bordage, M. Pápai, K. Haldrup, P. Glatzel, A. M. March, G. Doumy, A. Britz, A. Galler, T. Assefa, D. Cabaret, A. Juhin, T. B. van Driel, K. S. Kjær, A. Dohn, K. B. Møller, H. T. Lemke, E. Gallo, M. Rovezzi, Z. Németh, E. Rozsályi, T. Rozgonyi, J. Uhlig, V. Sundström, M. M. Nielsen, L. Young, S. H. Southworth, C. Bressler, and W. Gawelda, "Detailed characterization of a nanosecond-lived excited state: X-ray and theoretical investigation of the quintet state in photoexcited $[Fe(terpy)_2]^{2+}$," *The Journal of Physical Chemistry C*, vol. 119, no. 11, pp. 5888–5902, 2015.

[209] H. T. Lemke, C. Bressler, L. X. Chen, D. M. Fritz, K. J. Gaffney, A. Galler, W. Gawelda, K. Haldrup, R. W. Hartsock, H. Ihee, J. Kim, K. H. Kim, J. H. Lee, M. M. Nielsen, A. B. Stickrath, W. Zhang, D. Zhu, and M. Cammarata, "Femtosecond X-ray absorption spectroscopy at a hard X-ray free electron laser: Application to spin crossover dynamics," *The Journal of Physical Chemistry A*, vol. 117, no. 4, pp. 735–740, 2013.

[210] M. L. Shelby, P. J. Lestrange, N. E. Jackson, K. Haldrup, M. W. Mara, A. B. Stickrath, D. Zhu, H. T. Lemke, M. Chollet, B. M. Hoffman, X. Li, and L. X. Chen, "Ultrafast excited state relaxation of a metalloporphyrin revealed by femtosecond X-ray absorption spectroscopy," *Journal of the American Chemical Society*, vol. 138, no. 28, pp. 8752–8764, 2016.

[211] N. A. Miller, A. Deb, R. Alonso-Mori, B. D. Garabato, J. M. Glownia, L. M. Kiefer, J. Koralek, M. Sikorski, K. G. Spears, T. E. Wiley, D. Zhu, P. M. Kozlowski, K. J. Kubarych, J. E. Penner-Hahn, and R. J. Sension, "Polarized XANES monitors femtosecond structural evolution of photoexcited vitamin B12," *Journal of the American Chemical Society*, vol. 139, no. 5, pp. 1894–1899, 2017.

[212] P. Weightman, "X-ray-excited Auger and photoelectron spectroscopy," *Reports on Progress in Physics*, vol. 45, no. 7, pp. 753–814, 1982.

[213] K. Lopata, B. E. Van Kuiken, M. Khalil, and N. Govind, "Linear-response and real-time time-dependent density functional theory studies of core-level near-edge X-ray absorption," *Journal of Chemical Theory and Computation*, vol. 8, no. 9, pp. 3284–3292, 2012.

[214] B. E. Van Kuiken, M. Valiev, S. L. Daifuku, C. Bannan, M. L. Strader, H. Cho, N. Huse, R. W. Schoenlein, N. Govind, and M. Khalil, "Simulating Ru L_3-edge X-ray absorption spectroscopy with time-dependent density functional theory: Model complexes and electron localization in mixed-valence metal dimers," *Journal of Physical Chemistry A*, vol. 117, no. 21, pp. 4444–4454, 2013.

[215] Y. Zhang, S. Mukamel, M. Khalil, and N. Govind, "Simulating valence-to-core x-ray emission spectroscopy of transition metal complexes with time-dependent density functional theory," *Journal of chemical theory and computation*, vol. 11, no. 12, pp. 5804–5809, 2015.

[216] M. Ross, A. Andersen, Z. W. Fox, Y. Zhang, K. Hong, J. H. Lee, A. Cordones, A. M. March, G. Doumy, S. H. Southworth, M. A. Marcus, R. W. Schoenlein, S. Mukamel, N. Govind, and M. Khalil, "Comprehensive experimental and computational spectroscopic study of hexacyanoferrate complexes in water: From infrared to X-ray wavelengths," *Journal of Physical Chemistry B*, vol. 122, no. 19, pp. 5075–5086, 2018.

[217] A. M. March, G. Doumy, A. Andersen, A. Al Haddad, Y. Kumagai, M. F. Tu, J. Bang, C. Bostedt, J. Uhlig, D. R. Nascimento, T. A. Assefa, Z. Németh, G. Vankó, W. Gawelda, N. Govind, and L. Young, "Elucidation of the photoaquation reaction mechanism in ferrous hexacyanide using synchrotron X-rays with sub-pulse-duration sensitivity," *Journal of Chemical Physics*, vol. 151, no. 14, p. 144306, 2019.

[218] E. Biasin, Z. W. Fox, A. Andersen, K. Ledbetter, K. S. Kjær, R. Alonso-Mori, J. M. Carlstad, M. Chollet, J. D. Gaynor, J. M. Glownia, K. Hong, T. Kroll, J. H. Lee, C. Liekhus-Schmaltz, M. Reinhard, D. Sokaras, Y. Zhang, G. Doumy, A. M. March, S. H. Southworth, S. Mukamel, K. J. Gaffney, R. W. Schoenlein, N. Govind, A. A. Cordones, and M. Khalil, "Direct observation of coherent femtosecond solvent reorganization coupled to intramolecular electron transfer," *Nature Chemistry*, vol. 13, no. 4, pp. 343–349, 2021.

[219] E. Biasin, D. R. Nascimento, B. I. Poulter, B. Abraham, K. Kunnus, A. T. Garcia-Esparza, S. H. Nowak, T. Kroll, R. W. Schoenlein, R. Alonso-Mori, M. Khalil, N. Govind, and D. Sokaras, "Revealing the bonding of solvated Ru complexes with

valence-to-core resonant inelastic X-ray scattering," *Chemical Science*, vol. 12, no. 10, pp. 3713–3725, 2021.

[220] N. Timneanu, C. Caleman, J. Hajdu, and D. van der Spoel, "Auger electron cascades in water and ice," *Chemical Physics*, vol. 299, pp. 277–283, 2004.

[221] A. G. Kochur, A. I. Dudenko, V. L. Sukhorukov, and I. D. Petrov, "Direct hartree-fock calculation of multiple xe^{i+} ion production through inner shell vacancy de-excitations," *Journal of Physics B: Atomic, Molecular and Optical Physics*, vol. 27, no. 9, pp. 1709–1721, 1994.

[222] A. G. Kochur, A. I. Dudenko, P. V. Demekhin, and V. L. Sukhorukov, "Direct Hartree-Fock calculation of the cascade decay production of multiply charged ions following inner-shell ionization of Ne, Ar, Kr and Xe," *Journal of Physics B: Atomic, Molecular and Optical Physics*, vol. 28, no. 3, pp. 387–402, 1995.

[223] P. J. Ho, C. Bostedt, S. Schorb, and L. Young, "Theoretical tracking of resonance-enhanced multiple ionization pathways in X-ray free-electron laser pulses," *Physical Review Letters*, vol. 113, no. 25, pp. 1–5, 2014.

[224] P. J. Ho, E. P. Kanter, and L. Young, "Resonance-mediated atomic ionization dynamics induced by ultraintense X-ray pulses," *Physical Review A - Atomic, Molecular, and Optical Physics*, vol. 92, no. 6, 2015.

[225] F. Herman and S. Skillman, *Atomic structure calculations*. Englewood Cliffs, New Jersey: Englewood Cliffs, NJ: Prentice-Hall, 1963.

[226] A. E. A. Fouda, P. J. Ho, R. W. Dunford, E. P. Kanter, B. Krassing, L. Young, E. R. Peterson, L. Pan, D. R. Beck, and S. H. Southworth, "Resonant X-ray absorption of strong-field-ionized CF_3Br," *Journal of Physics B: Atomic, Molecular and Optical Physics*, vol. 53, p. 244009, 2020.

[227] M. Valiev, E. Bylaska, N. Govind, K. Kowalski, T. Straatsma, H. V. Dam, D. Wang, J. Nieplocha, E. Aprà, T. Windus, and W. de Jong, "Nwchem: A comprehensive and scalable open-source solution for large scale molecular simulations," *Computer Physics Communications*, vol. 181, no. 9, pp. 1477 – 1489, 2010.

[228] E. Aprà, E. J. Bylaska, W. A. De Jong, N. Govind, K. Kowalski, T. P. Straatsma, M. Valiev, H. J. Van Dam, Y. Alexeev, J. Anchell, V. Anisimov, F. W. Aquino, R. Atta-Fynn, J. Autschbach, N. P. Bauman, J. C. Becca, D. E. Bernholdt, K. Bhaskaran-Nair, S. Bogatko, P. Borowski, J. Boschen, J. Brabec, A. Bruner, E. Cauët, Y. Chen, G. N. Chuev, C. J. Cramer, J. Daily, M. J. Deegan, T. H. Dunning, M. Dupuis, K. G. Dyall,

G. I. Fann, S. A. Fischer, A. Fonari, H. Früchtl, L. Gagliardi, J. Garza, N. Gawande, S. Ghosh, K. Glaesemann, A. W. Götz, J. Hammond, V. Helms, E. D. Hermes, K. Hirao, S. Hirata, M. Jacquelin, L. Jensen, B. G. Johnson, H. Jónsson, R. A. Kendall, M. Klemm, R. Kobayashi, V. Konkov, S. Krishnamoorthy, M. Krishnan, Z. Lin, R. D. Lins, R. J. Littlefield, A. J. Logsdail, K. Lopata, W. Ma, A. V. Marenich, J. Martin Del Campo, D. Mejia-Rodriguez, J. E. Moore, J. M. Mullin, T. Nakajima, D. R. Nascimento, J. A. Nichols, P. J. Nichols, J. Nieplocha, A. Otero-De-La-Roza, B. Palmer, A. Panyala, T. Pirojsirikul, B. Peng, R. Peverati, J. Pittner, L. Pollack, R. M. Richard, P. Sadayappan, G. C. Schatz, W. A. Shelton, D. W. Silverstein, D. M. Smith, T. A. Soares, D. Song, M. Swart, H. L. Taylor, G. S. Thomas, V. Tipparaju, D. G. Truhlar, K. Tsemekhman, T. Van Voorhis, A. Vázquez-Mayagoitia, P. Verma, O. Villa, A. Vishnu, K. D. Vogiatzis, D. Wang, J. H. Weare, M. J. Williamson, T. L. Windus, K. Woliński, A. T. Wong, Q. Wu, C. Yang, Q. Yu, M. Zacharias, Z. Zhang, Y. Zhao, and R. J. Harrison, "NWChem: Past, present, and future," *Journal of Chemical Physics*, vol. 152, no. 18, p. 184102, 2020.

[229] C. Adamo and V. Barone, "Toward reliable density functional methods without adjustable parameters: The PBE0 model," *Journal of Chemical Physics*, vol. 110, no. 13, pp. 6158–6170, 1999.

[230] A. Klamt and G. Schüürmann, "COSMO: a new approach to dielectric screening in solvents with explicit expressions for the screening energy and its gradient," *Journal of the Chemical Society, Perkin Transactions 2*, vol. 0, no. 5, pp. 799–805, 1993.

[231] D. M. York and M. Karplus, "A smooth solvation potential based on the conductor-like screening model," *Journal of Physical Chemistry A*, vol. 103, no. 50, pp. 11060–11079, 1999.

[232] R. Krishnan, J. S. Binkley, R. Seeger, and J. A. Pople, "Self-consistent molecular orbital methods. XX. A basis set for correlated wave functions," *Journal of Chemical Physics*, vol. 72, no. 1, pp. 650–654, 1980.

[233] A. D. McLean and G. S. Chandler, "Contracted Gaussian basis sets for molecular calculations. I. Second row atoms, Z=11-18," *Journal of Chemical Physics*, vol. 72, no. 10, pp. 5639–5648, 1980.

[234] T. Noro, M. Sekiya, and T. Koga, "Segmented contracted basis sets for atoms H through Xe: Sapporo-(DK)-nZP sets (n = D, T, Q)," *Theoretical Chemistry Accounts*, vol. 131, no. 2, p. 1124, 2012.

[235] L. I. Yin, I. Adler, T. Tsang, M. H. Chen, D. A. Ringers, and B. Crasemann, "Widths of atomic M-shell vacancy states and quasiatomic aspects of radiationless transitions in solids," *Physical Review A*, vol. 9, no. 3, pp. 1070–1080, 1974.

[236] D. Zhu, M. Cammarata, J. M. Feldkamp, D. M. Fritz, J. B. Hastings, S. Lee, H. T. Lemke, A. Robert, J. L. Turner, and Y. Feng, "A single-shot transmissive spectrometer for hard X-ray free electron lasers," *Applied Physics Letters*, vol. 101, no. 3, p. 34103, 2012.

[237] M. Liang, G. J. Williams, M. Messerschmidt, M. M. Seibert, P. A. Montanez, M. Hayes, D. Milathianaki, A. Aquila, M. S. Hunter, J. E. Koglin, D. W. Schafer, S. Guillet, A. Busse, R. Bergan, W. Olson, K. Fox, N. Stewart, R. Curtis, A. A. Miahnahri, and S. Boutet, "The coherent X-ray imaging instrument at the Linac coherent light source," *Journal of Synchrotron Radiation*, vol. 22, no. 3, pp. 514–519, 2015.

[238] B. L. Henke, E. M. Gullikson, and J. C. Davis, "X-ray interactions: photoabsorption, scattering, transmission, and reflection at e=50-30000 ev, z=1-92," *Atomic Data and Nuclear Data Tables*, vol. 54, no. 2, pp. 181–342, 1993.

[239] P. A. Anfinrud, C. Han, and R. M. Hochstrasser, "Direct observations of ligand dynamics in hemoglobin by subpicosecond infrared spectroscopy," *Proceedings of the National Academy of Sciences of the United States of America*, vol. 86, no. 21, pp. 8387–8391, 1989.

[240] Y. Tanimura and S. Mukamel, "Two-dimensional femtosecond vibrational spectroscopy of liquids," *The Journal of Chemical Physics*, vol. 99, no. 12, pp. 9496–9511, 1993.

[241] S. Mukamel, "Multidimensional femtosecond correlation spectroscopies of electronic and vibrational excitations," *Annual Review of Physical Chemistry*, vol. 51, pp. 691–729, 2000.

[242] R. W. Schoenlein, T. Elsaesser, K. Holldack, Z. Huang, H. Kapteyn, M. Murnane, and M. Woerner, "Recent advances in ultrafast X-ray sources," *Philosophical Transactions of the Royal Society A: Mathematical, Physical and Engineering Sciences*, vol. 377, p. 20180384, 2019.

[243] L. X. Chen, W. i. J. H. Jäger, G. Jennings, D. J. Gosztota, A. Munkholm, and J. P. Hessler, "Capturing a photoexcited molecular structure through time-domain X-ray absorption fine structure," *Science*, vol. 292, no. 5515, pp. 262–264, 2001.

[244] M. Saes, C. Bressler, R. Abela, D. Grolimund, S. L. Johnson, P. A. Heimann, and M. Chergui, "Observing photochemical transients by ultrafast X-ray absorption spectroscopy," *Physical Review Letters*, vol. 90, no. 4, p. 4, 2003.

[245] M. Khalil, M. A. Marcus, A. L. Smeigh, J. K. McCusker, H. H. Chong, and R. W. Schoenlein, "Picosecond X-ray absorption spectroscopy of a photoinduced iron(II) spin crossover reaction in solution," *Journal of Physical Chemistry A*, vol. 110, no. 1, pp. 38–44, 2006.

[246] T. Lee, Y. Jiang, C. G. Rose-Petruck, and F. Benesch, "Ultrafast tabletop laser-pump-X-ray probe measurement of solvated Fe(CN_6^{4-}," *Journal of Chemical Physics*, vol. 122, no. 8, p. 084506, 2005.

[247] U. Bergmann, J. Kern, R. W. Schoenlein, P. Wernet, V. K. Yachandra, and J. Yano, "Using X-ray free-electron lasers for spectroscopy of molecular catalysts and metalloenzymes," *Nature Reviews Physics*, vol. 3, no. 4, pp. 264–282, 2021.

[248] P. M. Kraus, M. Zürch, S. K. Cushing, D. M. Neumark, and S. R. Leone, "The ultrafast X-ray spectroscopic revolution in chemical dynamics," *Nature Reviews Chemistry*, vol. 2, no. 6, pp. 82–94, 2018.

[249] E. H. Choi, Y. Lee, J. Heo, and H. Ihee, "Reaction dynamics studied via femtosecond X-ray liquidography at X-ray free-electron lasers," *Chemical Science*, vol. 13, no. 29, pp. 8457–8490, 2022.

[250] P. Wernet, "Chemical interactions and dynamics with femtosecond X-ray spectroscopy and the role of X-ray free-electron lasers," *Philosophical Transactions of the Royal Society A: Mathematical, Physical and Engineering Sciences*, vol. 377, no. 2145, p. 29, 2019.

[251] A. Picón, C. S. Lehmann, C. Bostedt, A. Rudenko, A. Marinelli, T. Osipov, D. Rolles, N. Berrah, C. Bomme, M. Bucher, G. Doumy, B. Erk, K. R. Ferguson, T. Gorkhover, P. J. Ho, E. P. Kanter, B. Krässig, J. Krzywinski, A. A. Lutman, A. M. March, D. Moonshiram, D. Ray, L. Young, S. T. Pratt, and S. H. Southworth, "Hetero-site-specific X-ray pump-probe spectroscopy for femtosecond intramolecular dynamics," *Nature Communications*, vol. 7, p. 11652, 2016.

[252] L. Fang, H. Xiong, E. Kukk, and N. Berrah, "X-ray pump-probe investigation of charge and dissociation dynamics in methyl iodine molecule," *Applied Sciences*, vol. 7, no. 5, 2017.

[253] M. Ilchen, P. Schmidt, N. M. Novikovskiy, G. Hartmann, P. Rupprecht, R. N. Coffee, A. Ehresmann, A. Galler, N. Hartmann, W. Helml, Z. Huang, L. Inhester, A. A. Lutman, J. P. MacArthur, T. Maxwell, M. Meyer, V. Music, H. D. Nuhn, T. Osipov, D. Ray, T. J. Wolf, S. Bari, P. Walter, Z. Li, S. Moeller, A. Knie, and P. V. Demekhin,

"Site-specific interrogation of an ionic chiral fragment during photolysis using an X-ray free-electron laser," *Communications Chemistry*, vol. 4, no. 1, 2021.

[254] Y. Shinohara, T. Osaka, I. Inoue, T. Iwashita, W. Dmowski, C. W. Ryu, Y. Sarathchandran, and T. Egami, "Split-pulse X-ray photon correlation spectroscopy with seeded X-rays from X-ray laser to study atomic-level dynamics," *Nature Communications*, vol. 11, no. 1, pp. 1–7, 2020.

[255] W. Roseker, S. O. Hruszkewycz, F. Lehmkühler, M. Walther, H. Schulte-Schrepping, S. Lee, T. Osaka, L. Strüder, R. Hartmann, M. Sikorski, S. Song, A. Robert, P. H. Fuoss, M. Sutton, G. B. Stephenson, and G. Grübel, "Towards ultrafast dynamics with split-pulse X-ray photon correlation spectroscopy at free electron laser sources," *Nature Communications*, vol. 9, no. 1, pp. 1–6, 2018.

[256] I. Inoue, Y. Inubushi, T. Sato, K. Tono, T. Katayama, T. Kameshima, K. Ogawa, T. Togashi, S. Owada, Y. Amemiya, T. Tanaka, T. Hara, and M. Yabashi, "Observation of femtosecond X-ray interactions with matter using an X-ray-X-ray pump-probe scheme," *Proceedings of the National Academy of Sciences*, vol. 113, no. 6, pp. 1492–1497, 2016.

[257] N. L. Opara, I. Mohacsi, M. Makita, D. Castano-Diez, A. Diaz, P. Juranić, M. Marsh, A. Meents, C. J. Milne, A. Mozzanica, C. Padeste, V. Panneels, M. Sikorski, S. Song, H. Stahlberg, I. Vartiainen, L. Vera, M. Wang, P. R. Willmott, and C. David, "Demonstration of femtosecond X-ray pump X-ray probe diffraction on protein crystals," *Structural Dynamics*, vol. 5, no. 5, 2018.

[258] K. R. Ferguson, M. Bucher, T. Gorkhover, S. Boutet, H. Fukuzawa, J. E. Koglin, Y. Kumagai, A. A. Lutman, A. Marinelli, M. Messerschmidt, K. Nagaya, J. Turner, K. Ueda, G. J. Williams, P. H. Bucksbaum, and C. Bostedt, "Transient lattice contraction in the solid-to-plasma transition," *Science Advances*, vol. 2, no. 1, pp. 1–6, 2016.

[259] T. Pardini, J. Alameda, A. Aquila, S. Boutet, T. Decker, A. E. Gleason, S. Guillet, P. Hamilton, M. Hayes, R. Hill, J. Koglin, B. Kozioziemski, J. Robinson, K. Sokolowski-Tinten, R. Soufli, and S. P. Hau-Riege, "Delayed onset of nonthermal melting in single-crystal silicon pumped with hard X-rays," *Physical Review Letters*, vol. 120, no. 26, p. 265701, 2018.

[260] N. J. Hartley, J. Grenzer, L. Huang, Y. Inubushi, N. Kamimura, K. Katagiri, R. Kodama, A. Kon, W. Lu, M. Makita, T. Matsuoka, S. Nakajima, N. Ozaki, T. Pikuz,

A. V. Rode, D. Sagae, A. K. Schuster, K. Tono, K. Voigt, J. Vorberger, T. Yabuuchi, E. E. McBride, and D. Kraus, "Using diffuse scattering to observe X-ray-driven nonthermal melting," *Physical Review Letters*, vol. 126, no. 1, pp. 1–6, 2021.

[261] G. Peng, F. M. Degroot, K. Hamalainen, J. Moore, X. Wang, M. Grush, J. B. Hastings, D. P. Siddons, W. H. Armstrong, O. C. Mullins, and S. P. Cramer, "High-resolution manganese X-ray fluorescence spectroscopy. Oxidation-state and spin-state Sensitivity," *Journal of the American Chemical Society*, vol. 116, pp. 2914–2920, 1994.

[262] B. Heremsmeier, C. Fadley, M. O. Krause, J. Jimenez-Mier, and P. Gerard, "Direct evidenece from gas-phase atomic spectra for an unscreened intra-atomic origin of outer-core multiplet splittings in solid manganese compounds," *Physical Review Letters*, vol. 61, no. 22, pp. 2592–2595, 1988.

[263] F. de Groot, S. Pizzini, and A. Fontaine, "Local-spin-selective X-ray absorption and X-ray magnetic circular dichroism of MnP," *Physical Review B*, vol. 51, no. 2, p. 51, 1995.

[264] I. S. Lyubutin, A. G. Gavriliuk, and V. V. Struzhkin, "High-spin-low-spin transition and the sequence of the phase transformations in the $BiFeO_3$ crystal at high pressures," *Journal of Experimental and Theoretical Physics Letters*, vol. 88, no. 8, pp. 524–530, 2008.

[265] X. Wang, F. M. de Groot, and S. P. Cramer, "Spin-polarized X-ray emission of transition-metal ions: A comparison via and detection," *Physical Review B - Condensed Matter and Materials Physics*, vol. 56, no. 8, pp. 4553–4564, 1997.

[266] C. Suzuki, J. Kawai, J. Y. Tanizawa, H. Adachi, S. Kawasaki, M. Takano, and T. Mukoyama, "Local spin moment of $LaCoO_3$ probed by a core hole," *Chemical Physics*, vol. 241, pp. 17–27, feb 1999.

[267] M. E. Reinhard, M. W. Mara, T. Kroll, H. Lim, R. G. Hadt, R. Alonso-Mori, M. Chollet, J. M. Glownia, S. Nelson, D. Sokaras, K. Kunnus, T. B. v. Driel, R. W. Hartsock, K. S. Kjaer, C. Weninger, E. Biasin, L. B. Gee, K. O. Hodgson, B. Hedman, U. Bergmann, E. I. Solomon, and K. J. Gaffney, "Short-lived metal-centered excited state initiates iron-methionine photodissociation in ferrous cytochrome c," *Nature Communications*, vol. 12, no. 1, p. 1086, 2021.

[268] S. Lafuerza, A. Carlantuono, M. Retegan, and P. Glatzel, "Chemical sensitivity of Kβ and Kα X-ray emission from a systematic investigation of iron compounds," *Inorganic Chemistry*, vol. 59, no. 17, pp. 12518–12535, 2020.

[269] T. Fransson, R. Alonso-Mori, R. Chatterjee, M. H. Cheah, M. Ibrahim, R. Hussein, M. Zhang, F. Fuller, S. Gul, I. S. Kim, P. S. Simon, I. Bogacz, H. Makita, C. De Lichtenberg, S. Song, A. Batyuk, D. Sokaras, R. Massad, M. Doyle, A. Britz, C. Weninger, A. Zouni, J. Messinger, V. K. Yachandra, J. Yano, J. Kern, and U. Bergmann, "Effects of X-ray free-electron laser pulse intensity on the Mn K β $_{1,3}$ X-ray emission spectrum in photosystem II - A case study for metalloprotein crystals and solutions," *Structural Dynamics*, vol. 8, no. 6, 2021.

[270] C. Liekhus-Schmaltz, Z. W. Fox, A. Andersen, K. S. Kjaer, R. Alonso-Mori, E. Biasin, J. Carlstad, M. Chollet, J. D. Gaynor, J. M. Glownia, K. Hong, T. Kroll, J. H. Lee, B. I. Poulter, M. Reinhard, D. Sokaras, Y. Zhang, G. Doumy, A. M. March, S. H. Southworth, S. Mukamel, A. A. Cordones, R. W. Schoenlein, N. Govind, and M. Khalil, "Femtosecond X-ray spectroscopy directly quantifies transient excited-state mixed valency," *Journal of Physical Chemistry Letters*, vol. 13, pp. 378–386, 2022.

[271] X. C. Lin, "Probing transient molecular structures in photochemical processes using laser-initiated time-resolved X-ray absorption spectroscopy," *Annual Review of Physical Chemistry*, vol. 56, pp. 221–254, 2005.

[272] H. Tatsuno, K. S. Kjær, K. Kunnus, T. C. B. Harlang, C. Timm, M. Guo, P. Chàbera, L. A. Fredin, R. W. Hartsock, M. E. Reinhard, S. Koroidov, L. Li, A. A. Cordones, O. Gordivska, O. Prakash, Y. Liu, M. G. Laursen, E. Biasin, F. B. Hansen, P. Vester, M. Christensen, K. Haldrup, Z. Németh, D. Sárosiné Szemes, Bajnóczi, G. Vankó, T. B. Van Driel, R. Alonso-Mori, J. M. Glownia, S. Nelson, M. Sikorski, H. T. Lemke, D. Sokaras, S. E. Canton, A. O. Dohn, K. B. Møller, M. M. Nielsen, K. J. Gaffney, K. Wärnmark, V. Sundström, P. Persson, and J. Uhlig, "Hot branching dynamics in a light-harvesting iron carbene complex revealed by ultrafast X-ray emission spectroscopy," *Angewandte Chemie*, vol. 132, no. 1, pp. 372–380, 2020.

[273] M. W. Mara, R. G. Hadt, M. E. Reinhard, T. Kroll, H. Lim, R. W. Hartsock, R. Alonso-Mori, M. Chollet, J. M. Glownia, S. Nelson, D. Sokaras, K. Kunnus, K. O. Hodgson, B. Hedman, U. Bergmann, K. J. Gaffney, and E. I. Solomon, "Metalloprotein entatic control of ligand-metal bonds quantified by ultrafast X-ray spectroscopy," *Science*, vol. 356, no. 6344, pp. 1276–1280, 2017.

[274] W. Zhang, R. Alonso-Mori, U. Bergmann, C. Bressler, M. Chollet, A. Galler, W. Gawelda, R. G. Hadt, R. W. Hartsock, T. Kroll, K. S. Kjær, K. Kubiek, H. T. Lemke, H. W. Liang, D. A. Meyer, M. M. Nielsen, C. Purser, J. S. Robinson, E. I. Solomon, Z. Sun, D. Sokaras, T. B. Van Driel, G. Vankó, T. C. Weng, D. Zhu, and K. J. Gaffney, "Tracking excited-state charge and spin dynamics in iron coordination complexes," *Nature*, vol. 509, no. 7500, pp. 345–348, 2014.

[275] W. Zhang, K. S. Kjær, R. Alonso-Mori, U. Bergmann, M. Chollet, L. A. Fredin, R. G. Hadt, R. W. Hartsock, T. Harlang, T. Kroll, K. Kubiček, H. T. Lemke, H. W. Liang, Y. Liu, M. M. Nielsen, P. Persson, J. S. Robinson, E. I. Solomon, Z. Sun, D. Sokaras, T. B. Van Driel, T. C. Weng, D. Zhu, K. Wärnmark, V. Sundström, and K. J. Gaffney, "Manipulating charge transfer excited state relaxation and spin crossover in iron coordination complexes with ligand substitution," *Chemical Science*, vol. 8, no. 1, pp. 515–523, 2016.

[276] A. M. March, T. A. Assefa, C. Boemer, C. Bressler, A. Britz, M. Diez, G. Doumy, A. Galler, M. Harder, D. Khakhulin, Z. Németh, M. Pápai, S. Schulz, S. H. Southworth, H. Yavaş, L. Young, W. Gawelda, and G. Vankó, "Probing transient valence orbital changes with picosecond valence-to-core X-ray emission spectroscopy," *Journal of Physical Chemistry C*, vol. 121, no. 5, pp. 2620–2626, 2017.

[277] S. J. George, M. D. Lowery, E. I. Solomon, and S. P. Cramer, "Copper L-edge spectral studies: A direct experimental probe of the ground-state covalency in the blue copper site in plastocyanin," 1993.

[278] R. K. Hocking, E. C. Wasinger, Y. L. Yan, F. M. Degroot, F. A. Walker, K. O. Hodgson, B. Hedman, and E. I. Solomon, "Fe L-edge X-ray absorption spectroscopy of low-spin heme relative to non-heme Fe complexes: Delocalization of Fe d-electrons into the porphyrin ligand," *Journal of the American Chemical Society*, vol. 129, no. 1, pp. 113–125, 2007.

[279] J. Barth, F. Gerken, and C. Kunz, "Experimental study of the 3p-3d intershell interaction in Ca, Sc, Ti, V, and Cr metals," *Physical Review B*, vol. 31, no. 4, pp. 2022–2028, 1985.

[280] R. Bruhn, B. Sonntag, and H. W. Wolff, "3p excitations of atomic and metallic Fe, Co, Ni and Cu," *Journal of Physics B: Atomic and Molecular Physics*, vol. 12, no. 2, pp. 203–212, 1979.

[281] M. Ohno and G. A. Van Riessen, "Hole-lifetime width: A comparison between theory and experiment," *Journal of Electron Spectroscopy and Related Phenomena*, vol. 128, no. 1, pp. 1–31, 2003.

[282] H. Höchst and M. K. Kelly, "Resonant valence-band photoemission from rhodium," *Physical Review B*, vol. 30, no. 4, pp. 1708–1710, 1984.

[283] Y. Hikosaka, P. Lablanquie, T. Kaneyasu, J. Adachi, H. Tanaka, I. H. Suzuki, M. Ishikawa, and T. Odagiri, "Super-Coster-Kronig decay of Kr 3p core-hole states

studied by multielectron coincidence spectroscopy," *Physical Review A*, vol. 103, no. 4, 2021.

[284] Z. H. Loh, M. Khalil, R. E. Correa, and S. R. Leone, "A tabletop femtosecond time-resolved soft X-ray transient absorption spectrometer," *Review of Scientific Instruments*, vol. 79, no. 7, 2008.

[285] L. J. Ament, M. Van Veenendaal, T. P. Devereaux, J. P. Hill, and J. Van Den Brink, "Resonant inelastic X-ray scattering studies of elementary excitations," *Reviews of Modern Physics*, vol. 83, no. 2, pp. 705–767, 2011.

[286] K. Kunnus, L. Li, C. J. Titus, S. J. Lee, M. E. Reinhard, S. Koroidov, K. S. Kjær, K. Hong, K. Ledbetter, W. B. Doriese, G. C. O'Neil, D. S. Swetz, J. N. Ullom, D. Li, K. Irwin, D. Nordlund, A. A. Cordones, and K. J. Gaffney, "Chemical control of competing electron transfer pathways in iron tetracyano-polypyridyl photosensitizers," *Chemical Science*, vol. 11, no. 17, pp. 4360–4373, 2020.

[287] R. M. Jay, S. Eckert, B. E. Van Kuiken, M. Ochmann, M. Hantschmann, A. A. Cordones, H. Cho, K. Hong, R. Ma, J. H. Lee, G. L. Dakovski, J. J. Turner, M. P. Minitti, W. Quevedo, A. Pietzsch, M. Beye, T. K. Kim, R. W. Schoenlein, P. Wernet, A. Föhlisch, and N. Huse, "Following metal-to-ligand charge-transfer dynamics with ligand and spin specificity using femtosecond resonant inelastic X-ray scattering at the nitrogen K-edge," *Journal of Physical Chemistry Letters*, vol. 12, no. 28, pp. 6676–6683, 2021.

[288] K. Kunnus, M. Guo, E. Biasin, C. B. Larsen, C. J. Titus, S. J. Lee, D. Nordlund, A. A. Cordones, J. Uhlig, and K. J. Gaffney, "Quantifying the steric effect on metal–ligand bonding in Fe carbene photosensitizers with Fe 2p3d resonant inelastic X-ray scattering," *Inorganic Chemistry*, vol. 61, no. 4, pp. 1961–1972, 2022.

[289] K. Kunnus, M. Vacher, T. C. Harlang, K. S. Kjær, K. Haldrup, E. Biasin, T. B. van Driel, M. Pápai, P. Chabera, Y. Liu, H. Tatsuno, C. Timm, E. Källman, M. Delcey, R. W. Hartsock, M. E. Reinhard, S. Koroidov, M. G. Laursen, F. B. Hansen, P. Vester, M. Christensen, L. Sandberg, Z. Németh, D. S. Szemes, Bajnóczi, R. Alonso-Mori, J. M. Glownia, S. Nelson, M. Sikorski, D. Sokaras, H. T. Lemke, S. E. Canton, K. B. Møller, M. M. Nielsen, G. Vankó, K. Wärnmark, V. Sundström, P. Persson, M. Lundberg, J. Uhlig, and K. J. Gaffney, "Vibrational wavepacket dynamics in Fe carbene photosensitizer determined with femtosecond X-ray emission and scattering," *Nature Communications*, vol. 11, no. 1, 2020.

[290] A. Picón, P. J. Ho, G. Doumy, and S. H. Southworth, "Optically-dressed resonant Auger processes induced by high-intensity X-rays," *New Journal of Physics*, vol. 15, no. 16, p. 83057, 2013.

[291] D. R. Nascimento, Y. Zhang, U. Bergmann, and N. Govind, "Near-edge X-ray absorption fine structure spectroscopy of heteroatomic core-hole states as a probe for nearly indistinguishable chemical environments," *Journal of Physical Chemistry Letters*, vol. 11, no. 2, pp. 556–561, 2020.

[292] M. Liang, G. J. Williams, M. Messerschmidt, M. M. Seibert, P. A. Montanez, M. Hayes, D. Milathianaki, A. Aquila, M. S. Hunter, J. E. Koglin, D. W. Schafer, S. Guillet, A. Busse, R. Bergan, W. Olson, K. Fox, N. Stewart, R. Curtis, A. A. Miahnahri, and S. Boutet, "The coherent X-ray imaging instrument at the Linac Coherent Light Source," *Journal of Synchrotron Radiation*, vol. 22, pp. 514–519, 2015.

[293] L. C. Davis and L. A. Feldkamp, "Interpretation of 3p-core-excitation spectra in Cr, Mn, Fe, Co, and Ni," *Solid State Communications*, vol. 19, no. 5, pp. 413–416, 1976.

[294] M. O. Krause, "Atomic radiative and radiationless yields for K and L shells," *Journal of Physical and Chemical Reference Data*, vol. 8, no. 2, pp. 307–327, 1979.

[295] G. Van der Laan, "$M_{2/3}$ absorption spectroscopy of 3d transition metal compounds," *Journal of Physics: Condensed Matter*, vol. 3, pp. 7443–7454, 1991.

[296] D. Healion, Y. Zhang, J. D. Biggs, N. Govind, and S. Mukamel, "Entangled valence electron-hole dynamics revealed by stimulated attosecond X-ray Raman scattering," *Journal of Physical Chemistry Letters*, vol. 3, no. 17, pp. 2326–2331, 2012.

[297] S. Mukamel, D. Healion, Y. Zhang, and J. D. Biggs, "Multidimensional attosecond resonant X-ray spectroscopy of molecules: Lessons from the optical regime," *Annual Review of Physical Chemistry*, vol. 64, pp. 101–127, 2013.

[298] S. M. Cavaletto, D. R. Nascimento, Y. Zhang, N. Govind, and S. Mukamel, "Resonant stimulated X-ray Raman spectroscopy of mixed-valence manganese complexes," *Journal of Physical Chemistry Letters*, vol. 12, pp. 5925–5931, 2021.

[299] Andrei Tokmakoff, *Time dependent quantum mechanics & spectroscopy*. Libretexts, 2019.

[300] Z. Chen, D. J. Higley, M. Beye, M. Hantschmann, V. Mehta, O. Hellwig, A. Mitra, S. Bonetti, M. Bucher, S. Carron, T. Chase, E. Jal, R. Kukreja, T. Liu, A. H. Reid, G. L. Dakovski, A. Föhlisch, W. F. Schlotter, H. A. Dürr, and J. Stöhr, "Ultrafast

self-induced X-Ray transparency and loss of magnetic diffraction," *Physical Review Letters*, vol. 121, p. 137403, 9 2018.

[301] D. J. Higley, Z. Chen, M. Beye, M. Hantschmann, A. H. Reid, V. Mehta, O. Hellwig, G. L. Dakovski, A. Mitra, R. Y. Engel, T. Maxwell, Y. Ding, S. Bonetti, M. Bucher, S. Carron, T. Chase, E. Jal, R. Kukreja, T. Liu, A. Föhlisch, H. A. Dürr, W. F. Schlotter, and J. Stöhr, "Stimulated resonant inelastic X-ray scattering in a solid," *Communications Physics*, vol. 5, no. 83, 2022.

Appendix A

THE LINEAR COUPLING PARAMETER $\left(V^1\right)$

A.1 Introduction

The linear coupling parameter is used in the material Hamiltonian of the vibronic modeling work to allow for coupling between electronic states [40, 62, 63]. This serves as a next order adaptation to the bilinear coupling Hamiltonian commonly utilized to describe coupled vibrational modes in 2D IR spectroscopy [11,14,97]. The effect is to offset the excited potential energy surface enabling non-zero Franck–Codon (FC) overlap between non-equivalent quanta of vibrations. This is akin to the displaced harmonic oscillator (DHO) model commonly used to explain vibronic progressions in electronic spectra [124,125]. A cursory explanation of this parameter of the Hamiltonian is provided in Ch. 3, but elaborated upon here in the one-mode picture for clarity.

There are two motivating questions that spur an explanation of this coupling parameter (represented as V^1). 1) What are the different representations of the linear coupling parameter? i.e. can we distinguish the various representations to clarify the V^1 various definitions and avoid confusion? 2) What is the relationship between V^1 and unitless displacement along a vibrational coordinate (q)? And, can that be related to λ, the reorganization energy which defines the commonly used stokes shift in fluorescence or the horizontal displacement operator, $\hat{D}$ from the DHO. model?

The formulae which form the important results of this appendix are: Eqn. A.18 defines the unitless displacement along (q) as a function of FC overlap through the relative intensities in a vibronic progression. Eqn. A.19-A.21 relate the strength of V^1 directly to the reorganization energy. Eqn. A.22 describes the effect on ω_{eg} due to using a linear coupling instead of a horizontal displacement operator.

A.2 Representations of V^1

This discussion can occur outside of the multi-mode picture. Mode-specific subscripts are dropped. There is an important distinction in the representation basis used to describe this parameter. Because the concept of a linear coupling parameter, some have found it convenient to utilize the position basis, while others expressed the Hamiltonian in the momentum basis.

Work by Vallet et al. [160] defined the annihilation & creation operators in the momentum basis. Written in terms of α those are:

$$\alpha^\dagger \equiv \frac{1}{\sqrt{2}}\left(\hat{P} + \mathrm{i}\hat{Q}\right) \tag{A.1}$$

$$\alpha \equiv \frac{1}{\sqrt{2}}\left(\hat{P} - \mathrm{i}\hat{Q}\right) \tag{A.2}$$

The annihilation and creation operators may also be written in the position basis, as done by Cohen-Tannoudji and co-workers [161], Tonks and Page [162], and this group [40, 65]. Written in terms of β those are:

$$\beta^\dagger \equiv \frac{1}{\sqrt{2}}\left(\hat{Q} - \mathrm{i}\hat{P}\right) \tag{A.3}$$

$$\beta \equiv \frac{1}{\sqrt{2}}\left(\hat{Q} + \mathrm{i}\hat{P}\right) \tag{A.4}$$

for completeness:

$$\hat{Q} = \frac{i}{\sqrt{2}}\left(\alpha - \alpha^\dagger\right) \tag{A.5}$$

$$\hat{P} = \frac{1}{\sqrt{2}}\left(\alpha + \alpha^\dagger\right) \tag{A.6}$$

$$\hat{Q} = \frac{1}{\sqrt{2}}\left(\beta^\dagger + \beta\right) \tag{A.7}$$

$$\hat{P} = \frac{\mathrm{i}}{\sqrt{2}}\left(\beta^{\dagger} - \beta\right) \tag{A.8}$$

Vallet defines the linear coupling parameter as follows in Eqn. 3 of their work, Where L_f is described as equivalent to V^1 [160]. The subscript f indexes over an arbitrary number of modes, similar to subscripts i and j in Ch. 3.

$$L_f A_f \equiv \mathrm{i}\left(\alpha_f - \alpha_f^{\dagger}\right) \tag{A.9}$$

This would indicate that the coefficient L_f could be treated in the complex plane. However this is in the momentum basis. Rewriting the Vallet equation in the position (β) basis shows,

$$\begin{aligned} A_f &= \mathrm{i}\left(\alpha_f - \alpha_f^{\dagger}\right) \\ &= \frac{\mathrm{i}}{\sqrt{2}}\left(\hat{P} - \mathrm{i}\hat{Q}\right) - \frac{\mathrm{i}}{\sqrt{2}}\left(\hat{P} + \mathrm{i}\hat{Q}\right) \\ &= \frac{-2\mathrm{i}^2}{\sqrt{2}}\hat{Q} \\ &= \beta^{\dagger} + \beta. \end{aligned} \tag{A.10}$$

The operator we use turns out to be $\frac{V^1\mathrm{i}}{\sqrt{2}}(\beta^{\dagger} - \beta)$. This corresponds to using the operator $V^1\hat{P}$ rather than our stated equation $V^1\hat{Q}$. While this seems to be a discrepancy, all the observable parameters are unchanged by this difference ($\omega_{eg}, \phi_{mixing}$, FC Overlap). The effect of this operator is to translate the exited state potential surface both horizontally along the q coordinate, and vertically along the ω_{eg} axis. The result is slanted translation rather than the purely horizontal shift resulting from applying the displacement operator described below. However, FC factors are independent of vertical offset and a relationship between the displacement value and V^1 can be determined analytically.

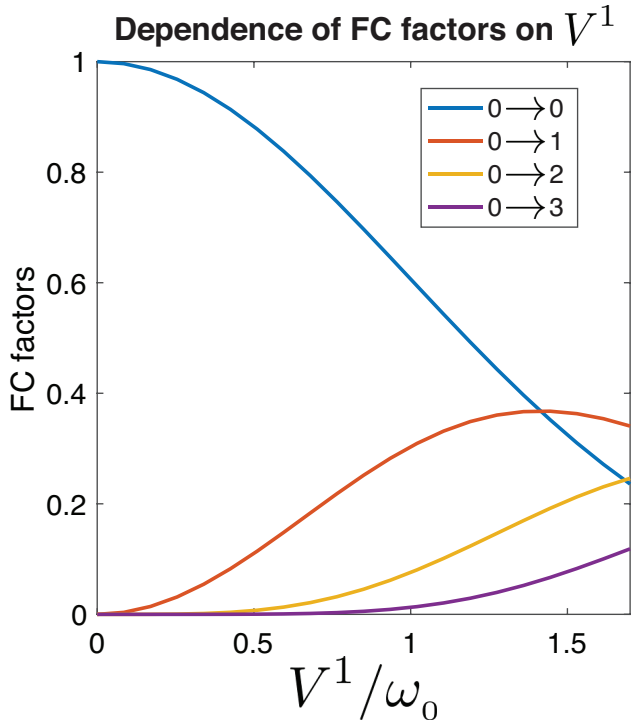

Figure A.1: **Franck–Condon overlap factors:** as a function of V^1 normalized to the vibrational frequency (ω_0).

A.3 Analytical Expression for Franck–Condon Factors

Note: Some approaches define λ as the extent of horizontal displacement which creates the stokes shift, equivalent to this descriptions definition of d. For clarity, here λ is refers to the reorganization energy, half the stokes shift, not the horizontal shift.

Below is a derivation of an analytical expression for relative intensities of FC factors as a function of D. First, we define the displacement operator where (d) is the displacement along the vibrational coordinate (q). D is not the operator $\hat{D}$; it is the dimensionless square displacement along q defined by:

$$D \equiv \frac{d^2 m\omega_0}{2\hbar} \tag{A.11}$$

$$\hat{D} = \mathrm{e}^{\frac{-i\hat{P}d}{\hbar}} \tag{A.12}$$

$$\hat{H}_e = \hat{D}\hat{H}_g\hat{D}^\dagger \tag{A.13}$$

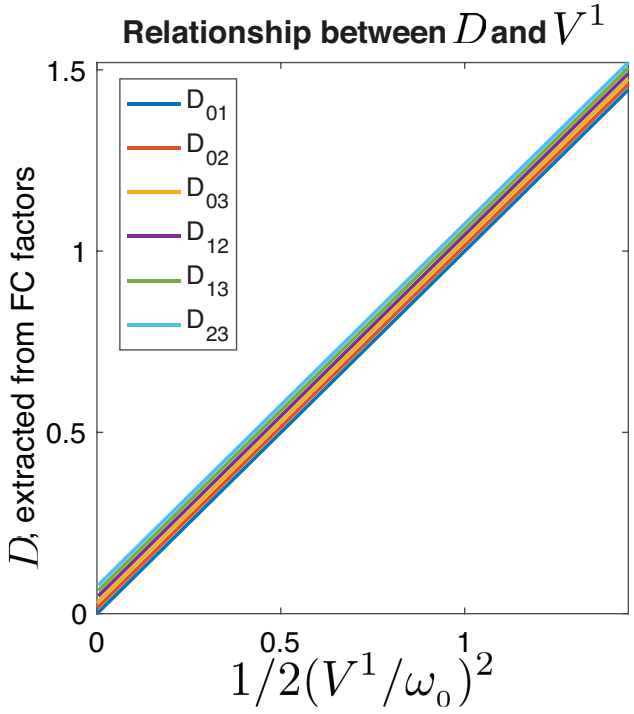

Figure A.2: **The unitless displacement:** D calculated as a function of FC factors according to Eqn. A.18. Note the X-axis gives the conversion between V^1 and D so each transition follows the line $Y = X$, equivalent to Eqn. A.19. Progressive transitions are slightly offset to show all lines.

The spectrum in frequency space is expressed in general as σ in Eqn. A.14, and specifically in Eqn. A.16, which gives the stick spectrum of absorbance and fluorescence for a single molecule.

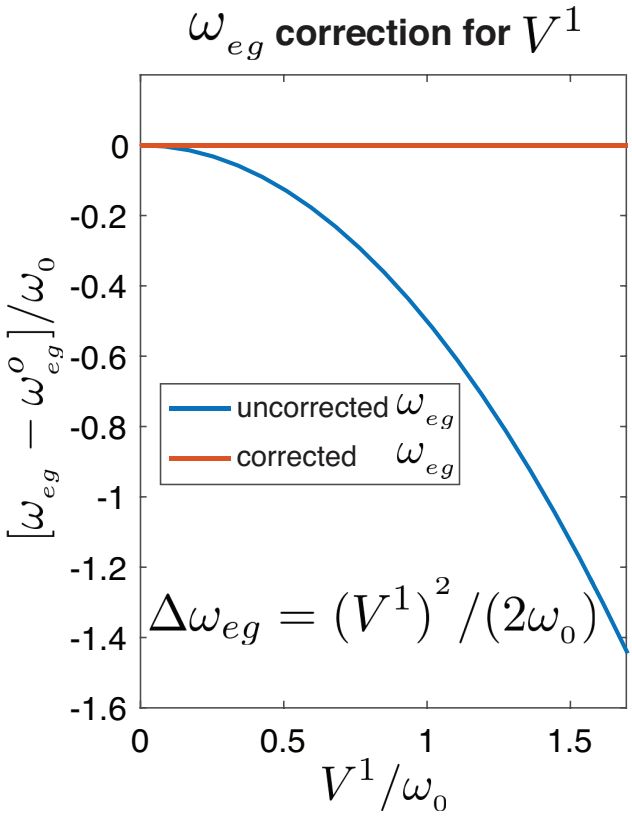

Figure A.3: $\boldsymbol{\omega_{eg}}$ **correction term:** electronic transition energy both directly calculated with the effects of V^1 and corrected by a $\lambda/\hbar$.

$$\begin{aligned}\sigma(\omega) &= \int_{-\infty}^{\infty} dt \mathrm{e}^{i\omega t} C_{\mu\mu}(t) \\ &= |\mu_{eg}|^2 \mathrm{e}^{-D} \int_{-\infty}^{\infty} dt e^{i\omega t} \mathrm{e}^{-i\omega_{eg} t} \mathrm{e}^{D\mathrm{e}^{-i\omega t}}\end{aligned} \tag{A.14}$$

Because $\mathrm{e}^{D\mathrm{e}^{-i\omega t}}$ has nested exponentials, it must be expressed as a Taylor expansion (Eqn. A.15) summed over the indexing variable (ν). Here each level ν represents raising the frequency by one quantum of ω_0. These represent transitions from the vibrational and electronic ground state, $|G, 0\rangle$, to the ν^{th} vibrationally excited state of the excited state, $|E, \nu\rangle$. This approach follows that found in reference [299].

$$\mathrm{e}^{De^{-i\omega t}} = \sum_{\nu=0}^{\infty} \frac{1}{\nu!} D^{\nu} \exp[-i\omega_0 t]^{\nu} \tag{A.15}$$

$$\sigma(\omega) = |\mu_{eg}|^2 \sum_{\nu=0}^{\infty} \frac{\mathrm{e}^{-D}}{\nu!} D^{\nu} \delta(\omega - \omega_{eg} \pm \nu\omega_0) \tag{A.16}$$

Taking the ratio between combinations of ν in Eqn. A.16 yields the FC factors between transitions a and b.

$$\begin{aligned} FC_{a,b} \rightarrow |\langle a|b\rangle|^2 &= \frac{\sigma_a}{\sigma_b} \\ &= \frac{b!}{a!} D^{a-b} \end{aligned} \tag{A.17}$$

Figure A.1 describes the FC factors as a function of V^1. This is done by explicit calculation of FC factors from the matrix representation of the mixed states. These values are what we use to calculate D. With an undisplaced harmonic oscillator in the excited state the FC factors for all transitions except $(0 \rightarrow 0)$ are zero. As the strength of the coupling increases, the excited state potential shifts in q and so the overlap with other states increases. As the parameter reaches a normalized value of 1, a vibronic progression is clearly visible.

Equation A.17 can be reworked to express the unitless displacement D as a function of the FC factors.

$$D = \left(\frac{\sigma_a a!}{\sigma_b b!} \right)^{\left(\frac{1}{a-b}\right)} \tag{A.18}$$

Taking the FC factors from Fig. A.1, D can be plotted rather than the FC factors by use of Eqn. A.18. This is plotted in Fig. A.2. Note that the transformation of V^1 to D is applied in the X-axis, so the plotted lines follow the line $Y = X$. The relationship is described in Eqn. A.19. These two relationships form the basis of exchanging the linear coupling parameter with the DHO. model, and the reorganization energy (λ).

$$D = \left(\frac{1}{\sqrt{2}} \frac{V^1}{\omega_o} \right)^2 \tag{A.19}$$

Given the definition of λ,

$$\lambda \equiv D\hbar\omega_o \tag{A.20}$$

where ω_o is the frequency of the harmonic oscillator. This is equivalent to ω_j^o in our expressions. We can relate the linear coupling parameter directly to the reorganization energy.

$$\lambda = \frac{\left(V^1\right)^2\hbar}{2\omega_o} \tag{A.21}$$

Finally, we come to the difference between the displacement operator and the linear perturbation, calculating shifts in ω_{eg}. As the strength of V^1 increases, the effect on the electronic transition energy is increased. As seen in Fig. A.3, this difference is proportional to the square of the coupling parameter. More directly:

$$\Delta\omega_{eg} = \frac{\lambda}{\hbar} = \frac{\left(V^1\right)^2}{2\omega_o} \tag{A.22}$$

Appendix B

MATLAB SCRIPTS

B.1 Vibrational-Electronic Response Functions

Following are the orientation-independent dephasing functions for multimode 2D VE peaks assuming homogeneous dynamics in the molecular ensemble. Note the naming convention used here for peaks 6_pop or 6_coh does not reflect the change in naming convention between the simulation code and the published notation. Pathways VII_coh in the published notation refer to peaks 7 in the simulation code. Pathways VII in the published notation refer to pathways 8 in the simulation code. Here functions are named consistently with the simulation code.

t1 = τ_1 axis

t2 = τ_2 value

t3 = τ_3 axis

lambdai = parameter relating fluctuations in ground and excited state vibrations (i)

C_egeg = correlation function of electronic transition frequency

C_egvi = vibronic correlation function mode (i)

C_vivi = ground state vibrational correlation function for mode (i)

C_vivj = ground state vibrational correlation function for mixed (i,j)

```
function [ F ] = F_VE1( t1, t3, lambda, C_egeg, C_egv, C_vv )
F = exp(-((C_vv).*t1 + (C_egeg).*t3));
end
```

```
function [ F ] = F_VE2( t1, t3, lambda, C_egeg, C_egv, C_vv )
F = exp(-((C_vv).*t1 + ...
    (C_egeg + C_egv*(2*lambda-2) + C_vv*(lambdaˆ2-2*lambda+1)).*t3));
end

function [ F ] = F_VE3_R( t1, t3, lambda, C_egeg, C_egv, C_vivi, C_vivi )
F = exp(-((C_vivi).*t1 + ...
    (C_egeg + C_egv*(2*lambda) + C_vjvj*(lambdaˆ2)).*t3));
end

function [ F ] = F_VE3_NR( t1, t3, lambda, C_egeg, C_egv, C_vivi, C_vjvj )
F = exp(-((C_vivi).*t1 + ...
    (C_egeg + C_egv*(2*lambda) + C_vjvj*(lambdaˆ2)).*t3));
end

function [ F ] = F_VE4( t1, t3, lambda, C_egeg, C_egv, C_vv )
F = exp(-((C_vv).*t1 + ...
    (C_egeg + 2*C_egv*(2*lambda-1) + C_vv*(4*lambdaˆ2-4*lambda+1)).*t3));
end

function [ F ] = F_VE5_R( t1, t2, t3, lambda, C_egeg, C_egv, C_vivi, C_vjvj, C_vivj )
F = exp(-((C_vivi).*t1 + ...
    (C_vivi+C_vjvj-2*C_vivj).*t2 + ...
    (C_egeg - 2*C_egv + C_vivi).*t3));
end
```

```
function [ F ] = F_VE5_NR( t1, t2, t3, ...
    lambda, C_egeg, C_egv, C_vivi, C_vjvj, C_vivj )
F = exp(-((C_vivi).*t1 + ...
    (C_vivi+C_vjvj-2*C_vivj).*t2 + ...
    (C_egeg - 2*C_egv + C_vjvj).*t3));
end

function [ F ] = F_VE6( t1, t2, t3, ...
    lambdai, lambdaj, C_egeg, C_egvi, C_egvj, C_vivi, C_vjvj, C_vivj)
F = exp(-((C_vivi).*t1 + ...
    (C_egeg + C_egvi*(2*lambdai-2) + C_egvj*(2*lambdaj) +...
    C_vivi*(lambdaiˆ2-2*lambdai+1) + C_vjvj*(lambdajˆ2) + ...
    C_vivj*(2*lambdai*lambdaj-2*lambdaj)).*t3));
end

function [ F ] = F_VE7_R( t1, t2, t3, ...
    lambdai, lambdaj, C_egeg, C_egvi, C_egvj, C_vivi, C_vjvj, C_vivj)
F = exp(-((C_vivi).*t1 + ...
    (C_vivi+C_vjvj-2*C_vivj).*t2 + ...
    (C_egeg + C_egvi*(2*lambdai-2) + C_egvj*(2*lambdaj) +...
    C_vivi*(lambdaiˆ2-2*lambdai+1) + C_vjvj*(lambdajˆ2) + ...
    C_vivj*(2*lambdai*lambdaj-2*lambdaj)).*t3));
end
```

```
function [ F ] = F_VE7_NR( t1, t2, t3, lambdai, lambdaj,...
    C_egeg, C_egvi, C_egvj, C_vivi, C_vjvj, C_vivj)
F = F_VE7_R( t1, t2, t3, lambdaj, lambdai, ...
    C_egeg, C_egvj, C_egvi, C_vjvj, C_vivi, C_vivj);
end

function [ F ] = F_VE8_R( t1, t2, t3, lambdak,...
    C_egeg, C_egvi, C_egvj, C_egvk, C_vivi, C_vjvj, C_vkvk, C_vivj, C_vivk, C_vjvk)
F = exp(-((C_vivi).*t1 + ...
    (C_vivi+C_vjvj-2*C_vivj).*t2 + ...
    (C_egeg + lambdak.^2*(C_vkvk) + ...
    2*lambdak*(C_egvk-C_vivk) + ...
    -2*C_egvi + C_vivi).*t3));
end

function [ F ] = F_VE8_NR( t1, t2, t3, lambdak,...
    C_egeg, C_egvi, C_egvj, C_egvk, C_vivi, C_vjvj, C_vkvk, C_vivj, C_vivk, C_vjvk)
F = exp(-((C_vivi).*t1 + ...
    (C_vivi+C_vjvj-2*C_vivj).*t2 + ...
    (C_egeg + lambdak.^2*(C_vkvk) + ...
    2*lambdak*(C_egvk-C_vjvk) + ...
    -2*C_egvj + C_vjvj).*t3));
end
```

B.2 Electronic-Vibrational Response Functions

Following are the orientation-independent dephasing functions for multimode 2D EV peaks assuming homogeneous dynamics in the molecular ensemble.

t1 = τ_1 axis

t3 = τ_3 axis

lambda = parameter relating fluctuations in ground and excited state vibrations.

C_egeg = correlation function of electronic transition frequency

C_egv = vibronic correlation function

C_vv = ground state vibrational correlation function

```
function [ F ] = F_EV1( t1, t3, lambda, C_egeg, C_egv, C_vv )
    F = exp(-(C_egeg.*t1 + C_vv.*t3));
    end

function [ F ] = F_EV2( t1, t3, lambda, C_egeg, C_egv, C_vv )
    F = exp(-(C_egeg.*t1 + (lambdaˆ2.*C ).*t3));
    end

function [ F ] = F_EV3( t1, t3, lambda, C _egeg, C _egv, C _vv )
    F = exp(-((C _egeg + 2*lambda*C_egv + lambdaˆ2*C_vv).*t1 + (C_vv).*t3));
    end

function [ F ] = F_VE4( t1, t3, lambda, C_egeg, C_egv, C)
    F = exp(-((C_vv).*t1 + (C_egeg + 2*C_egv*(2*lambda-1) + C_vv*(4*lambdaˆ2-...
    4*lambda+1)).*t3));
    end
```

```
function [ F ] = F_VE5_NR( t1, t2, t3, lambda, C_egeg, C_egv, C_vivi, C_vjvj, C_vivj )
    F = exp(-((C_vivi).*t1 + (C_vivi+C_vjvj-2*C_vivj).*t2 + (C_egeg - 2*C_egv + C_vjvj).*t3));
    end

function [ F ] = F_VE5_R( t1, t2, t3, lambda, C_egeg, C_egv, C_vivi, C_vjvj, C_vivj )
    F = exp(-((C_vivi).*t1 + (C_vivi+C_vjvj-2*C_vivj).*t2 + (C_egeg - 2*C_egv + C_vivi).*t3));
    end
```

Appendix C

VIBRONIC RESPONSE FUNCTIONS

C.1 Dephasing Functions

Representative dephasing functions are given for each pathway type in 2D EV and 2D VE spectroscopies. The dephasing functions include only the block of pathways corresponding to resonant vibrations with mode i (i.e., in $\omega_3 \approx \omega_i$ for 2D EV and $\omega_1 \approx \omega_i$ for 2D VE). An analogous set of functions are easily defined for the block of pathways corresponding to the resonant interaction with vibration j. Rephasing or non-rephasing is specified for the pathways involved in a τ_2-coherence since these pathways are spectrally separated. Absorptive pathways with equal rephasing and non-rephasing contributions have equivalent dephasing functions for both rephasing and non-rephasing components. Those functions are denoted $F^{a,b,c,d}_{(N_R,N_{NR})}$.

Electronic-Vibrational

Pathway $\mathsf{I}^{\mathsf{i}}_{0,0}$:

$$-ln\big[F^{g0,gi,g0,e0'}_{(3,4)}(\tau_3,\tau_2,\tau_1)\big] = \Gamma_{\nu_i,\nu_i}\tau_3 + \Gamma_{eg,eg}\tau_1 \tag{C.1}$$

Pathway $\mathsf{II}^{\mathsf{i}}_{0,0}$:

$$-ln\big[F^{g0,e0',ei',e0'}_{(1,2)}(\tau_3,\tau_2,\tau_1)\big] = \lambda_i^2\Gamma_{\nu_i,\nu_i}\tau_3 + \Gamma_{eg,eg}\tau_1 \tag{C.2}$$

Pathway $\mathsf{III}^{\mathsf{i}}_{\mathsf{i},0}$:

$$\begin{aligned} -ln\big[F^{g0,gi,g0,ei'}_{(3,4)}(\tau_3,\tau_2,\tau_1)\big] &= \Gamma_{\nu_i,\nu_i}\tau_3 \\ &\quad + \big[\Gamma_{eg,eg} + 2\lambda_i\Gamma_{eg,\nu_i} + \lambda_i^2\Gamma_{\nu_i,\nu_i}\big]\tau_1 \end{aligned} \tag{C.3}$$

Pathway $\mathsf{III}^{\mathsf{i}}_{\mathsf{j},0}$:

$$\begin{aligned} -ln\big[F^{g0,gi,g0,ej'}_{(3,4)}(\tau_3,\tau_2,\tau_1)\big] &= \Gamma_{\nu_i,\nu_i}\tau_3 \\ &\quad + \big[\Gamma_{eg,eg} + 2\lambda_j\Gamma_{eg,\nu_j} + \lambda_j^2\Gamma_{\nu_j,\nu_j}\big]\tau_1 \end{aligned} \tag{C.4}$$

Pathway $\mathsf{IV}^{\mathsf{2i}}_{\mathsf{i},\mathsf{i}}$:

$$\begin{aligned} -ln\big[F^{g0,ei',e2i',ei'}_{(1,2)}(\tau_3,\tau_2,\tau_1)\big] &= \lambda_i^2\Gamma_{\nu_i,\nu_i}\tau_3 \\ &\quad + \big[\Gamma_{eg,eg} + 2\lambda_i\Gamma_{eg,\nu_i} + \lambda_i^2\Gamma_{\nu_i,\nu_i}\big]\tau_1 \end{aligned} \tag{C.5}$$

Pathway $\mathsf{V}^{\mathsf{0}}_{\mathsf{i},\mathsf{i}}$:

$$\begin{aligned} -ln\big[F^{g0,ei',e0',ei'}_{(2,1)}(\tau_3,\tau_2,\tau_1)\big] &= \lambda_i^2\Gamma_{\nu_i,\nu_i}\tau_3 \\ &\quad + \big[\Gamma_{eg,eg} + 2\lambda_i\Gamma_{eg,\nu_i} + \lambda_i^2\Gamma_{\nu_i,\nu_i}\big]\tau_1 \end{aligned} \tag{C.6}$$

Pathway $\mathsf{VI}^{\mathsf{ij}}_{\mathsf{j},\mathsf{j}}$:

$$\begin{aligned} -ln\big[F^{g0,ej',ei'j',ej'}_{(1,2)}(\tau_3,\tau_2,\tau_1)\big] &= \lambda_i^2\Gamma_{\nu_i,\nu_i}\tau_3 \\ &\quad + \big[\Gamma_{eg,eg} + 2\lambda_j\Gamma_{eg,\nu_j} + \lambda_j^2\Gamma_{\nu_j,\nu_j}\big]\tau_1 \end{aligned} \tag{C.7}$$

Pathways involved in τ_2-coherences:

Pathway $\mathsf{V}^{\mathsf{0}}_{\mathsf{i},\mathsf{j}}$ (NR):

$$\begin{aligned} -ln\big[F_1^{g0,ej',e0',ei'}(\tau_3,\tau_2,\tau_1)\big] &= \lambda_i^2\Gamma_{\nu_i,\nu_i}\tau_3 \\ &\quad + \big[\lambda_i^2\Gamma_{\nu_i,\nu_i} + \lambda_j^2\Gamma_{\nu_j,\nu_j} - 2\lambda_i\lambda_j\Gamma_{\nu_i,\nu_j}\big]\tau_2 \\ &\quad + \big[\Gamma_{eg,eg} + 2\lambda_i\Gamma_{eg,\nu_i} + \lambda_i^2\Gamma_{\nu_i,\nu_i}\big]\tau_1 \end{aligned} \tag{C.8}$$

Pathway $\mathsf{V}^{\mathsf{0}}_{\mathsf{j},\mathsf{i}}$ (R):

$$\begin{aligned} -ln\big[F_2^{g0,ei',e0',ej'}(\tau_3,\tau_2,\tau_1)\big] &= \lambda_i^2\Gamma_{\nu_i,\nu_i}\tau_3 \\ &\quad + \big[\lambda_i^2\Gamma_{\nu_i,\nu_i} + \lambda_j^2\Gamma_{\nu_j,\nu_j} - 2\lambda_i\lambda_j\Gamma_{\nu_i,\nu_j}\big]\tau_2 \\ &\quad + \big[\Gamma_{eg,eg} + 2\lambda_j\Gamma_{eg,\nu_j} + \lambda_j^2\Gamma_{\nu_j,\nu_j}\big]\tau_1 \end{aligned} \tag{C.9}$$

Pathway $\mathsf{VI}^{\mathsf{ij}}_{\mathsf{i,j}}$ (NR):

$$\begin{aligned} -ln\big[F_2^{g0,ej',ei'j',ei'}(\tau_3,\tau_2,\tau_1)\big] &= \lambda_i^2\Gamma_{\nu_i,\nu_i}\tau_3 \\ &+ \big[\lambda_i^2\Gamma_{\nu_i,\nu_i} + \lambda_j^2\Gamma_{\nu_j,\nu_j} - 2\lambda_i\lambda_j\Gamma_{\nu_i,\nu_j}\big]\tau_2 \\ &+ \big[\Gamma_{eg,eg} + 2\lambda_i\Gamma_{eg,\nu_i} + \lambda_i^2\Gamma_{\nu_i,\nu_i}\big]\tau_1 \end{aligned} \tag{C.10}$$

Pathway $\mathsf{VI}^{\mathsf{ij}}_{\mathsf{j,i}}$ (R):

$$\begin{aligned} -ln\big[F_1^{g0,ei',ei'j',ej'}(\tau_3,\tau_2,\tau_1)\big] &= \lambda_i^2\Gamma_{\nu_i,\nu_i}\tau_3 \\ &+ \big[\lambda_i^2\Gamma_{\nu_i,\nu_i} + \lambda_j^2\Gamma_{\nu_j,\nu_j} - 2\lambda_i\lambda_j\Gamma_{\nu_i,\nu_j}\big]\tau_2 \\ &+ \big[\Gamma_{eg,eg} + 2\lambda_j\Gamma_{eg,\nu_j} + \lambda_j^2\Gamma_{\nu_j,\nu_j}\big]\tau_1 \end{aligned} \tag{C.11}$$

Vibrational-Electronic

Pathway $\mathsf{I}^{\mathsf{0}}_{\mathsf{i,0}}$:

$$-ln\big[F_{(3,4)}^{g0,e0',g0,gi}(\tau_3,\tau_2,\tau_1)\big] = \Gamma_{eg,eg}\tau_3 + \Gamma_{\nu_i,\nu_i}\tau_1 \tag{C.12}$$

Pathway $\mathsf{II}^{\mathsf{i}}_{\mathsf{i,i}}$:

$$\begin{aligned} -ln\big[F_{(1,2)}^{g0,gi,ei',gi}(\tau_3,\tau_2,\tau_1)\big] &= \big[\Gamma_{eg,eg} + 2(\lambda_i-1)\Gamma_{eg,\nu_i} \\ &+ (\lambda_i-1)^2\Gamma_{\nu_i,\nu_i}\big]\tau_3 \\ &+ \Gamma_{\nu_i,\nu_i}\tau_1 \end{aligned} \tag{C.13}$$

Pathway $\mathsf{III}^{\mathsf{j}}_{\mathsf{i,0}}$:

$$\begin{aligned} -ln\big[F_{(3,4)}^{g0,ej',g0,gi}(\tau_3,\tau_2,\tau_1)\big] &= \big[\Gamma_{eg,eg} + 2\lambda_j\Gamma_{eg,\nu_j} \\ &+ \lambda_j^2\Gamma_{\nu_j,\nu_j}\big]\tau_3 \\ &+ \Gamma_{\nu_i,\nu_i}\tau_1 \end{aligned} \tag{C.14}$$

Pathway $\mathsf{IV}^{\mathsf{2i}}_{\mathsf{i,i}}$:

$$\begin{aligned} -ln\big[F_{(1,2)}^{g0,gi,e2i',gi}(\tau_3,\tau_2,\tau_1)\big] &= \big[\Gamma_{eg,eg} + 2(2\lambda_i-1)\Gamma_{eg,\nu_i} \\ &+ (2\lambda_i-1)\Gamma_{\nu_i,\nu_i}\big]\tau_3 \\ &+ \Gamma_{\nu_i,\nu_i}\tau_1 \end{aligned} \tag{C.15}$$

Pathway $\mathsf{V}^{0}_{i,i}$:

$$\begin{aligned} -ln\big[F^{g0,gi,e0',gi}_{(1,2)}(\tau_3,\tau_2,\tau_1)\big] &= \big[\Gamma_{eg,eg} - 2\Gamma_{eg,\nu_i} + \Gamma_{\nu_i,\nu_i}\big]\tau_3 \\ &\quad + \Gamma_{\nu_i,\nu_i}\tau_1 \end{aligned} \tag{C.16}$$

Pathway $\mathsf{VI}^{ij}_{i,i}$:

$$\begin{aligned} -ln\big[F^{g0,gi,ei'j',gi}_{(1,2)}(\tau_3,\tau_2,\tau_1)\big] &= \big[\Gamma_{eg,eg} + \Gamma_{eg,\nu_i}(2\lambda_i - 2) \\ &\quad + \Gamma_{eg,\nu_j}(2\lambda_j) + \Gamma_{\nu_i,\nu_i}(\lambda_i^2 - 2\lambda_i + 1) \\ &\quad + \Gamma_{\nu_j,\nu_j}(\lambda_j^2) + \Gamma_{\nu_i,\nu_j}(2\lambda_i\lambda_j - 2\lambda_j)\big]\tau_3 \\ &\quad + \Gamma_{\nu_i,\nu_i}\tau_1 \end{aligned} \tag{C.17}$$

Pathway $\mathsf{VII}^{j}_{i,i}$:

$$\begin{aligned} -ln\big[F^{g0,gi,ej',gi}_{(1,2)}(\tau_3,\tau_2,\tau_1)\big] &= \big[\Gamma_{eg,eg} + \lambda_j^2\Gamma_{\nu_j,\nu_j} \\ &\quad + 2\lambda_j(\Gamma_{eg,\nu_j} - \Gamma_{\nu_i,\nu_j}) \\ &\quad + \Gamma_{\nu_i,\nu_i} - 2\Gamma_{eg.\nu_i}\big]\tau_3 \\ &\quad + \Gamma_{\nu_i,\nu_i}\tau_1 \end{aligned} \tag{C.18}$$

Pathways involved in τ_2-coherences:

Pathway $\mathsf{V}^{0}_{i,j}$ (R):

$$\begin{aligned} -ln\big[F^{g0,gj,e0',gi}_{1}(\tau_3,\tau_2,\tau_1)\big] &= \big[\Gamma_{eg,eg} - 2\Gamma_{eg,\nu_i} + \Gamma_{\nu_i,\nu_i}\big]\tau_3 \\ &\quad + \big[\Gamma_{\nu_i,\nu_i} + \Gamma_{\nu_j,\nu_j} - 2\Gamma_{\nu_i,\nu_j}\big]\tau_2 \\ &\quad + \Gamma_{\nu_i,\nu_i}\tau_1 \end{aligned} \tag{C.19a}$$

pathway $\mathsf{V}^{0}_{i,j}$ (NR):

$$\begin{aligned} -ln\big[F^{g0,gj,e0',gi}_{2}(\tau_3,\tau_2,\tau_1)\big] &= \big[\Gamma_{eg,eg} - 2\Gamma_{eg,\nu_j} + \Gamma_{\nu_j,\nu_j}\big]\tau_3 \\ &\quad + \big[\Gamma_{\nu_j,\nu_j} + \Gamma_{\nu_i,\nu_i} - 2\Gamma_{\nu_j,\nu_i}\big]\tau_2 \\ &\quad + \Gamma_{\nu_i,\nu_i}\tau_1 \end{aligned} \tag{C.19b}$$

pathway $\mathsf{VI}^{\mathsf{ij}}_{\mathsf{i,j}}$ (R):

$$\begin{aligned}-ln\big[F_1^{g0,gj,ei'j',gi}(\tau_3,\tau_2,\tau_1)\big] = \big[&\Gamma_{eg,eg} + \Gamma_{eg,\nu_i}(2\lambda_i - 2)\\ &+ \Gamma_{eg,\nu_j}(2\lambda_j) + \Gamma_{\nu_i,\nu_i}(\lambda_i^2 - 2\lambda_i + 1)\\ &+ \Gamma_{\nu_j,\nu_j}(\lambda_j^2) + \Gamma_{\nu_i,\nu_j}(2\lambda_i\lambda_j - 2\lambda_j)\big]\tau_3\\ &+ \big[\Gamma_{\nu_i,\nu_i} + \Gamma_{\nu_j,\nu_j} - 2\Gamma_{\nu_i,\nu_j}\big]\tau_2\\ &+ \Gamma_{\nu_i,\nu_i}\tau_1\end{aligned} \tag{C.20a}$$

pathway $\mathsf{VI}^{\mathsf{ij}}_{\mathsf{i,j}}$ (NR):

$$\begin{aligned}-ln\big[F_2^{g0,gj,ei'j',gi}(\tau_3,\tau_2,\tau_1)\big] = \big[&\Gamma_{eg,eg} + \Gamma_{eg,\nu_j}(2\lambda_j - 2)\\ &+ \Gamma_{eg,\nu_i}(2\lambda_i) + \Gamma_{\nu_j,\nu_j}(\lambda_j^2 - 2\lambda_j + 1)\\ &+ \Gamma_{\nu_i,\nu_i}(\lambda_i^2) + \Gamma_{\nu_i,\nu_j}(2\lambda_i\lambda_j - 2\lambda_i)\big]\tau_3\\ &+ \big[\Gamma_{\nu_j,\nu_j} + \Gamma_{\nu_i,\nu_i} - 2\Gamma_{\nu_i,\nu_j}\big]\tau_2\\ &+ \Gamma_{\nu_i,\nu_i}\tau_1\end{aligned} \tag{C.20b}$$

pathway $\mathsf{VII}^{\mathsf{j}}_{\mathsf{i,j}}$ (R):

$$\begin{aligned}-ln\big[F_1^{g0,gj,ej',gi}(\tau_3,\tau_2,\tau_1)\big] = \big[&\Gamma_{eg,eg} + \lambda_j^2\Gamma_{\nu_j,\nu_j}\\ &+ 2\lambda_j(\Gamma_{eg,\nu_j} - \Gamma_{\nu_i,\nu_j})\\ &+ \Gamma_{\nu_i,\nu_i} - 2\Gamma_{eg.\nu_i}\big]\tau_3\\ &+ \big[\Gamma_{\nu_i,\nu_i} + \Gamma_{\nu_j,\nu_j} - 2\Gamma_{\nu_i,\nu_j}\big]\tau_2\\ &+ \Gamma_{\nu_i,\nu_i}\tau_1\end{aligned} \tag{C.21a}$$

pathway $\mathsf{VII}^{\mathsf{j}}_{\mathsf{i,j}}$ (NR):

$$\begin{aligned}-ln\big[F_2^{g0,gj,ej',gi}(\tau_3,\tau_2,\tau_1)\big] = \big[&\Gamma_{eg,eg} + \lambda_j^2\Gamma_{\nu_j,\nu_j}\\ &+ 2\lambda_j(\Gamma_{eg,\nu_j} - \Gamma_{\nu_j,\nu_j})\\ &+ \Gamma_{\nu_j,\nu_j} - 2\Gamma_{eg.\nu_j}\big]\tau_3\\ &+ \big[\Gamma_{\nu_j,\nu_j} + \Gamma_{\nu_i,\nu_i} - 2\Gamma_{\nu_i,\nu_j}\big]\tau_2\\ &+ \Gamma_{\nu_i,\nu_i}\tau_1\end{aligned} \tag{C.21b}$$

C.2 Molecular Orientational Response Functions

Case I

$$\boldsymbol{Y}_{ZYYZ}(\theta) = \frac{1}{30}\big[3cos^2(\theta) - 1\big] \tag{C.22}$$

$$\boldsymbol{Y}_{ZYZY}(\theta) = \frac{1}{30}\big[3cos^2(\theta) - 1\big] \tag{C.23}$$

Case II

$$\boldsymbol{Y}_{ZYYZ}(\theta_a, \theta_b) = \frac{1}{60}\big[3cos(2(\theta_a - \theta_b)) + 1\big] \tag{C.24}$$

$$\boldsymbol{Y}_{ZYZY}(\theta_a, \theta_b) = \frac{1}{60}\big[3cos(2(\theta_a - \theta_b)) + 1\big] \tag{C.25}$$

Case III

$$\begin{aligned}\boldsymbol{Y}_{ZYYZ}(\theta_1, \theta_2, \theta_3, \theta_4) = \frac{1}{20}\big[&cos(\theta_1 + \theta_2 - \theta_3 - \theta_4) \\ &+ cos(\theta_1 - \theta_2 + \theta_3 - \theta_4)\big] \\ &- \frac{1}{30}\big[cos(\theta_1 - \theta_2 - \theta_3 + \theta_4)\big]\end{aligned} \tag{C.26}$$

$$\begin{aligned}\boldsymbol{Y}_{ZYZY}(\theta_1, \theta_2, \theta_3, \theta_4) = \frac{1}{20}\big[&cos(\theta_1 + \theta_2 - \theta_3 - \theta_4) \\ &+ cos(\theta_1 - \theta_2 - \theta_3 + \theta_4)\big] \\ &- \frac{1}{30}\big[cos(\theta_1 - \theta_2 + \theta_3 - \theta_4)\big]\end{aligned} \tag{C.27}$$

Appendix D

PATHWAY LABELS AND ANGLE DEPENDENCE

In all cases, the $\theta_{a,b}^{c,d}$ angles are such that $a = 0$ and $b = 0'$ because they are all defined with respect to the $\boldsymbol{\mu}^{0,0'}$ dipole moment. Therefore, the subscript (0,0') is omitted and only superscripts, (c,d) are given for the dipole moment forming the angle with $\boldsymbol{\mu}^{0,0'}$.

D.1 2D Electronic-Vibrational Pathways

Table D.1: 2D EV GSB Pathways: Dephasing Functions (R):R_3, (NR):R_4

Pathway Symbol	Type	Function	Vibronic States				Angles				$\omega_1 - \omega_{eg}$	ω_3
			$\|a\rangle$	$\|b\rangle$	$\|c\rangle$	$\|d\rangle$	θ_1	θ_2	θ_3	θ_4		
$I^i_{0,0}$	R+NR	$F_3 + F_4$	$\|g;0,0\rangle$	$\|g;1,0\rangle$	$\|g;0,0\rangle$	$\|e;0',0'\rangle$	(0,i)	–	–	–	0	ω_i
$I^j_{0,0}$	R+NR	$F_3 + F_4$	$\|g;0,0\rangle$	$\|g;0,1\rangle$	$\|g;0,0\rangle$	$\|e;0',0'\rangle$	(0,j)	–	–	–	0	ω_j
$III^i_{i,0}$	R+NR	$F_3 + F_4$	$\|g;0,0\rangle$	$\|g;1,0\rangle$	$\|g;0,0\rangle$	$\|e;1',0'\rangle$	(0,i')	(0,i)	–	–	$\omega_{i'}$	ω_i
$III^j_{i,0}$	R+NR	$F_3 + F_4$	$\|g;0,0\rangle$	$\|g;0,1\rangle$	$\|g;0,0\rangle$	$\|e;1',0'\rangle$	(0,i')	(0,j)	–	–	$\omega_{i'}$	ω_j
$III^i_{j,0}$	R+NR	$F_3 + F_4$	$\|g;0,0\rangle$	$\|g;1,0\rangle$	$\|g;0,0\rangle$	$\|e;0',1'\rangle$	(0,j')	(0,i)	–	–	$\omega_{j'}$	ω_i
$III^j_{j,0}$	R+NR	$F_3 + F_4$	$\|g;0,0\rangle$	$\|g;0,1\rangle$	$\|g;0,0\rangle$	$\|e;0',1'\rangle$	(0,j')	(0,j)	–	–	$\omega_{j'}$	ω_j

Table D.2: 2D EV ESE Pathways: Dephasing Functions (R):R_2, (NR):R_1

Pathway Symbol	Type	Function	Vibronic States				Angles				$\omega_1 - \omega_{eg}$	ω_3
			$\|a\rangle$	$\|b\rangle$	$\|c\rangle$	$\|d\rangle$	θ_1	θ_2	θ_3	θ_4		
$V^0_{i,i}$	R+NR	$F_1 + F_2$	$\|g;0,0\rangle$	$\|e;1',0'\rangle$	$\|e;0',0'\rangle$	$\|e;1',0'\rangle$	(0,i')	(0',i')	–	–	$\omega_{i'}$	$\omega_{i'}$
$V^0_{i,j}$	R	F_2	$\|g;0,0\rangle$	$\|e;0',1'\rangle$	$\|e;0',0'\rangle$	$\|e;1',0'\rangle$	(0,i')	(0,j')	(0',j')	(0',i')	$\omega_{i'}$	$\omega_{i'}$
$V^0_{i,j}$	NR	F_1	$\|g;0,0\rangle$	$\|e;0',1'\rangle$	$\|e;0',0'\rangle$	$\|e;1',0'\rangle$	(0,i')	(0,j')	(0',i')	(0',j')	$\omega_{i'}$	$\omega_{j'}$
$V^0_{j,i}$	R	F_2	$\|g;0,0\rangle$	$\|e;1',0'\rangle$	$\|e;0',0'\rangle$	$\|e;0',1'\rangle$	(0,j')	(0,i')	(0',i')	(0',j')	$\omega_{j'}$	$\omega_{j'}$
$V^0_{j,i}$	NR	F_1	$\|g;0,0\rangle$	$\|e;1',0'\rangle$	$\|e;0',0'\rangle$	$\|e;0',1'\rangle$	(0,j')	(0,i')	(0',j')	(0',i')	$\omega_{j'}$	$\omega_{i'}$
$V^0_{j,j}$	R+NR	$F_1 + F_2$	$\|g;0,0\rangle$	$\|e;0',1'\rangle$	$\|e;0',0'\rangle$	$\|e;0',1'\rangle$	(0,j')	(0',j')	–	–	$\omega_{j'}$	$\omega_{j'}$

Table D.3: 2D EV ESA Pathways: Dephasing Functions (R):R_1^*, (NR):R_2^*

Pathway Symbol	Type	Function	Vibronic States				Angles				$\omega_1 - \omega_{eg}$	ω_3
			$\|a\rangle$	$\|b\rangle$	$\|c\rangle$	$\|d\rangle$	θ_1	θ_2	θ_3	θ_4		
$II^i_{0,0}$	R+NR	$F_1 + F_2$	$\|g;0,0\rangle$	$\|e;0',0'\rangle$	$\|e;1',0'\rangle$	$\|e;0',0'\rangle$	(0',i')	–	–	–	0	$\omega_{i'}$
$II^j_{0,0}$	R+NR	$F_1 + F_2$	$\|g;0,0\rangle$	$\|e;0',0'\rangle$	$\|e;0',1'\rangle$	$\|e;0',0'\rangle$	(0',j')	–	–	–	0	$\omega_{j'}$
$IV^{2i}_{i,i}$	R+NR	$F_1 + F_2$	$\|g;0,0\rangle$	$\|e;1',0'\rangle$	$\|e;2',0'\rangle$	$\|e;1',0'\rangle$	(0,i')	(i',2i')	–	–	$\omega_{i'}$	$\omega_{i'} - \Delta_{i'}$
$IV^{2j}_{j,j}$	R+NR	$F_1 + F_2$	$\|g;0,0\rangle$	$\|e;0',1'\rangle$	$\|e;0',2'\rangle$	$\|e;0',1'\rangle$	(0,j')	(j',2j')	–	–	$\omega_{j'}$	$\omega_{j'} - \Delta_{j'}$
$VI^{ij}_{i,i}$	R+NR	$F_1 + F_2$	$\|g;0,0\rangle$	$\|e;1',0'\rangle$	$\|e;1',1'\rangle$	$\|e;1',0'\rangle$	(0,i')	(i',i'j')	–	–	$\omega_{i'}$	$\omega_{j'} - \Delta_{i'j'}$
$VI^{ij}_{i,j}$	R	F_1	$\|g;0,0\rangle$	$\|e;0',1'\rangle$	$\|e;1',1'\rangle$	$\|e;1',0'\rangle$	(0,i')	(0,j')	(j',i'j')	(i',i'j')	$\omega_{i'}$	$\omega_{j'} - \Delta_{i'j'}$
$VI^{ij}_{i,j}$	NR	F_2	$\|g;0,0\rangle$	$\|e;0',1'\rangle$	$\|e;1',1'\rangle$	$\|e;1',0'\rangle$	(0,i')	(0,j')	(i',i'j')	(j',i'j')	$\omega_{i'}$	$\omega_{i'} - \Delta_{i'j'}$
$VI^{ij}_{j,i}$	R	F_1	$\|g;0,0\rangle$	$\|e;1',0'\rangle$	$\|e;1',1'\rangle$	$\|e;0',1'\rangle$	(0,j')	(0,i')	(i',i'j')	(j',i'j')	$\omega_{j'}$	$\omega_{i'} - \Delta_{i'j'}$
$VI^{ij}_{j,i}$	NR	F_2	$\|g;0,0\rangle$	$\|e;1',0'\rangle$	$\|e;1',1'\rangle$	$\|e;0',1'\rangle$	(0,j')	(0,i')	(j',i'j')	(i',i'j')	$\omega_{j'}$	$\omega_{j'} - \Delta_{i'j'}$
$VI^{ij}_{j,j}$	R+NR	$F_1 + F_2$	$\|g;0,0\rangle$	$\|e;0',1'\rangle$	$\|e;1',1'\rangle$	$\|e;0',1'\rangle$	(0,j')	(j',i'j')	–	–	$\omega_{j'}$	$\omega_{i'} - \Delta_{i'j'}$

D.2 2D Vibrational-Electronic Pathways

Table D.4: 2D VE GSB Pathways: Dephasing Functions (R):R_3, (NR):R_4

Pathway Symbol	Type	Function	Vibronic States				Angles				ω_1	$\omega_3 - \omega_{eg}$
			$\|a\rangle$	$\|b\rangle$	$\|c\rangle$	$\|d\rangle$	θ_1	θ_2	θ_3	θ_4		
$I^i_{i,i}$	R+NR	$F_3 + F_4$	$\|g;0,0\rangle$	$\|e;0',0'\rangle$	$\|g;0,0\rangle$	$\|g;1,0\rangle$	(0,i)	–	–	–	ω_i	0
$I^j_{j,j}$	R+NR	$F_3 + F_4$	$\|g;0,0\rangle$	$\|e;0',0'\rangle$	$\|g;0,0\rangle$	$\|g;0,1\rangle$	(0,j)	–	–	–	ω_j	0
$III^i_{i,0}$	R+NR	$F_3 + F_4$	$\|g;0,0\rangle$	$\|e;1',0'\rangle$	$\|g;0,0\rangle$	$\|g;1,0\rangle$	(0,i)	(0,i')	–	–	ω_i	$\omega_{i'}$
$III^j_{i,0}$	R+NR	$F_3 + F_4$	$\|g;0,0\rangle$	$\|e;0',1'\rangle$	$\|g;0,0\rangle$	$\|g;1,0\rangle$	(0,i)	(0,j')	–	–	ω_i	$\omega_{j'}$
$III^i_{j,0}$	R+NR	$F_3 + F_4$	$\|g;0,0\rangle$	$\|e;1',0'\rangle$	$\|g;0,0\rangle$	$\|g;0,1\rangle$	(0,j)	(0,i')	–	–	ω_j	$\omega_{i'}$
$III^j_{j,0}$	R+NR	$F_3 + F_4$	$\|g;0,0\rangle$	$\|e;0',1'\rangle$	$\|g;0,0\rangle$	$\|g;0,1\rangle$	(0,j)	(0,j')	–	–	ω_j	$\omega_{j'}$

Table D.5: 2D VE ESA Pathways: Dephasing Functions (R):R_1^*, (NR):R_2^*

Pathway Symbol	Type	Function	Vibronic States				Angles				ω_1	$\omega_3 - \omega_{eg}$
			$\|a\rangle$	$\|b\rangle$	$\|c\rangle$	$\|d\rangle$	θ_1	θ_2	θ_3	θ_4		
$II^i_{i,i}$	R+NR	F_1+F_2	$\|g;0,0\rangle$	$\|g;1,0\rangle$	$\|e;1',0'\rangle$	$\|g;1,0\rangle$	(0,i)	(i,i')	–	–	ω_i	$\Delta_{eg,i}$
$II^j_{j,j}$	R+NR	F_1+F_2	$\|g;0,0\rangle$	$\|g;0,1\rangle$	$\|e;0',1'\rangle$	$\|g;0,1\rangle$	(0,j)	(0,j')	–	–	ω_j	$\Delta_{eg,j}$
$IV^{2i}_{i,i}$	R+NR	F_1+F_2	$\|g;0,0\rangle$	$\|g;1,0\rangle$	$\|e;2',0'\rangle$	$\|g;1,0\rangle$	(0,i)	(i,2i')	–	–	ω_i	$\omega_{i'}+\Delta_{eg,i}-\Delta_i$
$IV^{2j}_{j,j}$	R+NR	F_1+F_2	$\|g;0,0\rangle$	$\|g;0,1\rangle$	$\|e;0',2'\rangle$	$\|g;0,1\rangle$	(0,j)	(j,2j')	–	–	ω_j	$\omega_{j'}+\Delta_{eg,j}-\Delta_j$
$V^0_{i,i}$	R+NR	F_1+F_2	$\|g;0,0\rangle$	$\|g;1,0\rangle$	$\|e;0',0'\rangle$	$\|g;1,0\rangle$	(0,i)	(i,0')	–	–	ω_i	$-\omega_i$
$V^0_{i,j}$	R	F_1	$\|g;0,0\rangle$	$\|g;0,1\rangle$	$\|e;0',0'\rangle$	$\|g;1,0\rangle$	(0,i)	(0,j)	(j,0')	(i,0')	ω_i	$-\omega_i$
$V^0_{i,j}$	NR	F_2	$\|g;0,0\rangle$	$\|g;0,1\rangle$	$\|e;0',0'\rangle$	$\|g;1,0\rangle$	(0,i)	(0,j)	(i,0')	(j,0')	ω_i	$-\omega_j$
$V^0_{j,i}$	R	F_1	$\|g;0,0\rangle$	$\|g;1,0\rangle$	$\|e;0',0'\rangle$	$\|g;0,1\rangle$	(0,j)	(0,i)	(i,0')	(j,0')	ω_j	$-\omega_j$
$V^0_{j,i}$	NR	F_2	$\|g;0,0\rangle$	$\|g;1,0\rangle$	$\|e;0',0'\rangle$	$\|g;0,1\rangle$	(0,j)	(0,i)	(j,0')	(i,0')	ω_j	$-\omega_i$
$V^0_{j,j}$	R+NR	F_1+F_2	$\|g;0,0\rangle$	$\|g;0,1\rangle$	$\|e;0',0'\rangle$	$\|g;0,1\rangle$	(0,j)	(j,0')	–	–	ω_j	$-\omega_j$
$VI^{ij}_{i,i}$	R+NR	F_1+F_2	$\|g;0,0\rangle$	$\|g;1,0\rangle$	$\|e;1',1'\rangle$	$\|g;1,0\rangle$	(0,i)	(i,i'j')	–	–	ω_i	$\omega_{j'}+\Delta_{eg,i}-\Delta_{i'j'}$
$VI^{ij}_{i,j}$	R	F_1	$\|g;0,0\rangle$	$\|g;0,1\rangle$	$\|e;1',1'\rangle$	$\|g;1,0\rangle$	(0,i)	(0,j)	(j,i'j')	(i,i'j')	ω_i	$\omega_{j'}+\Delta_{eg,i}-\Delta_{i'j'}$
$VI^{ij}_{i,j}$	NR	F_2	$\|g;0,0\rangle$	$\|g;0,1\rangle$	$\|e;1',1'\rangle$	$\|g;1,0\rangle$	(0,i)	(0,j)	(i,i'j')	(j,i'j')	ω_i	$\omega_{i'}+\Delta_{eg,j}-\Delta_{i'j'}$
$VI^{ij}_{j,i}$	R	F_1	$\|g;0,0\rangle$	$\|g;1,0\rangle$	$\|e;1',1'\rangle$	$\|g;0,1\rangle$	(0,j)	(0,i)	(i,i'j')	(j,i'j')	ω_j	$\omega_{i'}+\Delta_{eg,j}-\Delta_{i'j'}$
$VI^{ij}_{j,i}$	NR	F_2	$\|g;0,0\rangle$	$\|g;1,0\rangle$	$\|e;1',1'\rangle$	$\|g;0,1\rangle$	(0,j)	(0,i)	(j,i'j')	(i,i'j')	ω_j	$\omega_{j'}+\Delta_{eg,i}-\Delta_{i'j'}$
$VI^{ij}_{j,j}$	R+NR	F_1+F_2	$\|g;0,0\rangle$	$\|g;0,1\rangle$	$\|e;1',1'\rangle$	$\|g;0,1\rangle$	(0,j)	(j,i'j')	–	–	ω_j	$\omega_{i'}+\Delta_{eg,j}-\Delta_{i'j'}$
$VII^i_{j,j}$	R+NR	F_1+F_2	$\|g;0,0\rangle$	$\|g;0,1\rangle$	$\|e;1',0'\rangle$	$\|g;0,1\rangle$	(0,j)	(j,i')	–	–	ω_j	$\omega_i-\omega_j+\Delta_{eg,i}$
$VII^i_{i,j}$	R	F_1	$\|g;0,0\rangle$	$\|g;0,1\rangle$	$\|e;1',0'\rangle$	$\|g;1,0\rangle$	(0,i)	(0,j)	(j,i')	(i,i')	ω_i	$\Delta_{eg,i}$
$VII^i_{i,j}$	NR	F_2	$\|g;0,0\rangle$	$\|g;0,1\rangle$	$\|e;1',0'\rangle$	$\|g;1,0\rangle$	(0,i)	(0,j)	(i,i')	(j,i')	ω_i	$\omega_i-\omega_j+\Delta_{eg,i}$
$VII^i_{j,i}$	R	F_1	$\|g;0,0\rangle$	$\|g;1,0\rangle$	$\|e;1',0'\rangle$	$\|g;0,1\rangle$	(0,j)	(0,i)	(i,i')	(j,i')	ω_j	$\omega_i-\omega_j+\Delta_{eg,i}$
$VII^i_{j,i}$	NR	F_2	$\|g;0,0\rangle$	$\|g;1,0\rangle$	$\|e;1',0'\rangle$	$\|g;0,1\rangle$	(0,j)	(0,i)	(j,i')	(i,i')	ω_j	$\Delta_{eg,i}$
$VII^j_{i,i}$	R+NR	F_1+F_2	$\|g;0,0\rangle$	$\|g;1,0\rangle$	$\|e;0',1'\rangle$	$\|g;1,0\rangle$	(0,i)	(i,j')	–	–	ω_i	$\omega_j-\omega_i+\Delta_{eg,j}$
$VII^j_{i,j}$	R	F_1	$\|g;0,0\rangle$	$\|g;0,1\rangle$	$\|e;0',1'\rangle$	$\|g;1,0\rangle$	(0,i)	(0,j)	(j,j')	(i,j')	ω_i	$\omega_j-\omega_i+\Delta_{eg,j}$
$VII^j_{i,j}$	NR	F_2	$\|g;0,0\rangle$	$\|g;0,1\rangle$	$\|e;0',1'\rangle$	$\|g;1,0\rangle$	(0,i)	(0,j)	(i,j')	(j,j')	ω_i	$\Delta_{eg,j}$
$VII^j_{j,i}$	R	F_1	$\|g;0,0\rangle$	$\|g;1,0\rangle$	$\|e;0',1'\rangle$	$\|g;0,1\rangle$	(0,j)	(0,i)	(i,j')	(j,j')	ω_j	$\Delta_{eg,j}$
$VII^j_{j,i}$	NR	F_2	$\|g;0,0\rangle$	$\|g;1,0\rangle$	$\|e;0',1'\rangle$	$\|g;0,1\rangle$	(0,j)	(0,i)	(j,j')	(i,j')	ω_j	$\omega_j-\omega_i+\Delta_{eg,j}$

Appendix E

TECHNICAL NOTES ON THE COLLECTION OF TWO-DIMENSIONAL VIBRONIC SPECTROSCOPIC DATA

Relevant publications, with the permission of AIP publishing:

- [36] Zachary W. Fox, Tyler J. Blair, Robert B. Weakly, Trevor L. Courtney, and Munira Khalil. "Implementation of continuous fast scanning detection in femtosecond Fourier-transform two-dimensional vibrational-electronic spectroscopy to decrease data acquisition time", *Journal of Chemical Physics*, Vol. 89, no. 11, p. 113104-7, 2018

E.1 Introduction

The following Appendix provides a series of technical notes about specific steps for calibration, timing verification, and modifications in 2D VE, but also contains relevant information for performing other types of experiments (2D EV, 2D IR, pump-probe) regardless of the laboratory setting. This represents the collection process at the time of writing. Much of the lab's operation is set by what worked when the system was developed. Improvements are always desired, but not at the cost of delaying or preventing actual science from taking place. Conventions like chopping notation are like the order of the alphabet. It does not matter whether it is (high)-(low) or (low)-(high), what matters is that every piece of software that is written agrees. Unless otherwise stated, "probe" refers to any approximately electronically resonant field, detected in the CCD. "Pump" refers to the MIR. If at any point the flipped experiment is discussed (T-IR), the language used will revert to energy-based names, visible and MIR, rather than pump and probe.

E.2 OPA and DFG

There are several benchmark values of power. Below is a short list of benchmark readings for the lab and the corresponding detector.

1. Benchmark power for first pass: 1.1 mW OPHIR

2. Benchmark power for second pass: 160 mW OPHIR

3. Benchmark DFG power: 5 mV coherent, when spectrally centered at 2,100 cm^{-1}

For alignment of the OPA, a level white light path is crucial. This can be achieved by moving the secondary height-only marker or iris around the OPA to check beam height while setting the white light path. Tilting though the BBO changes the angle of interaction with the crystal and thereby the wavelengths of signal/idler. Following the OPA, at the signal/idler splitting optic, the signal is transmitted and the idler is reflected. This can be confirmed by collecting the separate lines of light, independently doubling them in a crystal and detecting the output. Part of optimization of DFG amplitude is HeNe-IR overlap. After drastic pointing changes, this can have a huge impact even at the near field, so make sure not to skip this step early in the optimization. This step will need to be performed again if the collimating lens is adjusted.

After a large realignment of the OPA, the signal and idler are most likely poorly overlapped. To solve this and enable spatial overlap in the DFG crystal one can utilize a small trick. The green/red outputs are good indicators of the OPA process occurring, but they are poorly aligned with the signal/idler because they are produced by a different process with different vector math. Much closer to the signal/idler overlap are two weak beams which pass through a long pass filter stored by the output of the OPA. The two beams roughly correlate with 800 nm + signal (bluish) and 800 nm + idler (reddish, usually faint). As an added benefit they have the correct polarization to split at the T shaped signal/idler overlap area. This means that they can be used as close proxies for overlap and recover DFG. Remember

that these are not actually the signal and idler so additional spatial overlap tuning may be required following the initial DFG signal. Additionally, to ensure a high quality MIR beam mode, it is more important that the two colored paths are parallel than is their overlap, as neither path is perfectly collinear with the corresponding signal/idler output.

E.3 Stages and XPS

All stages in lab are controlled through the XPS. Following the XPS D installation, the intranet address of the XPS controlled was changed. The address is 192.168.254.254. Additionally, the network address was changed; it is 192.168.0.150. Stage calibration is only necessary for the XMS stages, which were calibrated at the factory, and whose calibration files must be associated with the correct stage in the XPS interface. Sec. 1.3 of the XPS configuration manual covers stages and can be found at:

https://www.newport.com/mam/celum/celum_assets/resources

E.3.1 Stage Installation

Proper stage installation ensures each stage is properly calibrated and moves according to the encoder position correctly. This is a crucial step to ensuring the equipment can be trusted, requiring the calibration files for S1-S3. The .txt files are stored local to the lab machine and to the XPS interface. Additionally, the values of those .txt files are included here in Table E.1. If completely reinstalling the stages, the .ini files need to be edited by hand to ensure they calibrate correctly so included are backups of the stage.ini and system.ini files from February 2022. Below are most helpful bits of the email exchange teaching how to install stages and modify the stages.ini file.

In the stages.ini of each stage you'll have to modify the following parameters:

PositionerMappingFileName =
PositionerMappingLineNumber = 0

PositonerMappingMaxPositionError = 0

For the XMS50_5427:

PositionerMappingFileName = xms50_5427.txt
PositionerMappingLineNumber = 26
PositonerMappingMaxPositionError = 0.001005; Unit

Note that in addition to a calibration file each of the XMS stages has a different value for "PositionMappingMaxPositonError". They are listed below.

- xms50_4411 = 0.0005584; Unit
- xms50_5428 = 0.002880; Unit
- xms50_4975 = 0.000664; Unit

E.3.2 Stage motion

There are several common errors which occur in stage motion. If a stage attempts to move a great distance or take a step scan while set to fast-scanning speed, the XPS will send an order to move to a starting position but the stage will take an error inducing amount of time as the stage will not report its arrival and the system time out. Below is a short list of benchmark speeds for the lab stages.

1. General speed is 300 mm/s.
2. Fast-Scanning speed is 0.06 mm/s, for sampling at 1 kHz.

Table E.1: Delay Stage Calibration Values

XMS50_4411.txt		**XMS50_4975.txt**		**XMS_5428.txt**	
Stage Positon	Calibration	Stage Positon	Calibration	Stage Positon	Calibration
-25.0000000	-0.0002455	-25.000000	-0.000664	-25.000000	-0.002750
-22.8029080	-0.0002846	-23.005657	-0.000493	-23.248709	-0.002848
-20.8760360	-0.0004167	-21.003971	-0.000390	-20.661063	-0.002880
-18.6592970	-0.0002975	-18.602756	-0.000250	-18.831536	-0.002615
-16.5949940	-0.0001992	-16.612152	-0.000225	-16.466803	-0.002071
-14.6093520	-0.0000673	-14.370035	-0.000295	-14.586042	-0.001574
-12.6400020	-0.0000474	-12.606116	-0.000154	-12.400919	-0.001199
-10.4346520	0.0000298	-10.542429	0.000048	-10.434179	-0.001219
-8.3438370	0.0000607	-8.429038	0.000154	-8.630769	-0.001340
-6.1876810	0.0000105	-5.974049	0.000354	-6.395479	-0.001305
-4.2953420	0.0000526	-4.050078	0.000290	-4.059328	-0.001018
-1.9313820	0.0000307	-2.189208	0.000157	-1.815120	-0.000487
0.0000000	0.0000000	0.000000	0.000000	-0.059045	-0.000032
0.0095010	0.0000005	0.137599	0.000043	0.000000	0.000000
2.2193560	0.0000345	2.093242	0.000138	2.012817	0.000247
3.9262910	0.0000447	4.224710	0.000368	4.302222	0.000182
5.8551720	0.0001454	5.919279	0.000498	6.436503	-0.000094
8.4348340	0.0001265	8.500087	0.000541	8.170100	-0.000113
10.6145870	0.0000297	10.379911	0.000399	10.605926	0.000127
12.2929040	0.0000457	12.574682	0.000248	12.374548	0.000491
14.5765540	-0.0000814	14.474231	0.000219	14.297111	0.000844
16.6129420	-0.0000967	16.722017	0.000279	16.522926	0.001005
18.7053100	-0.0001680	18.744959	0.000440	18.736548	0.000723
20.9708720	-0.0003365	20.961088	0.000530	20.778289	0.000495
22.7816920	-0.0004552	23.136320	0.000649	22.998793	0.000448
25.0000000	-0.0005584	25.000000	0.000575	25.000000	0.000749

To be properly accessed by the legacy .VI control system, each stage name follows a naming convention. The naming convention for stages is S#.S# where S stands for "single axis". This does not apply to spindle advance screws e.g. A6.A6 used for raster scan.

Note that the positive vs negative direction for each stage is relatively arbitrary, and the relationship between stage direction, and the sign of experimental time should be checked before performing any experiment which is non-symmetric about τ=0. For purposes of

pulses characterization, FFT over τ_1 pulses overlap produces a symmetric signal. For that reason it makes no difference whether the FFT is taken over positive or negative values of τ_1. Therefore, fast-scan collected characterization of MIR pulses simply analyzes whichever direction allows for a longer time axis. The best practice is to scan from $\pm$100 fs to $\approx \mp$ 2 ps as it provides the most averaging over a long time axis.

E.4 Detector Parameters

For an overview of information flow in the VE experiment, read the 2018 paper [36] on the implementation of fast scanning.

E.4.1 CCD CH. 8 timing

This value/setting should very rarely change. Only after a major change like replacing a laser, installing a new probe, moving the fiber at the detector's slit, switching to free space detection, etc. should this be required, but this should be checked before collecting data.

The channel 8 trigger sent out from the tower is the TDG generated delay signal for the CCD relative to the TDG signal sent to the DAQ acquisition. This is actually telling the CCD when during its 1 millisecond collection time to clear the pixels of charge and read out their values. A setting of CH. 8=200 μs means that the CCD will wait for 200 μs after the trigger signal. It is crucial that the system is configured in such a way that the pulse of light arrives during that time.

Method #1: Establishing approximate CH. 8 timing

This method is approximately represented in Fig. E.1, and is an initial method for setting timing, which must then be verified. Chop both the pump and the probe. Block the pump and detect the probe in the CCD in chopped mode. (This should just look like the spectrum, or its negative depending on whether the chopper is 180^o out of phase. The pump must be chopped because that is the "chop" signal that the CCD acquire VI looks for. Scan CH. 8 timing by small increments until a poorly chopped spectrum is achieved, e.g. middle panel of Fig. E.1. This occurs when the pulse arrives halfway through the CCD charge clearing

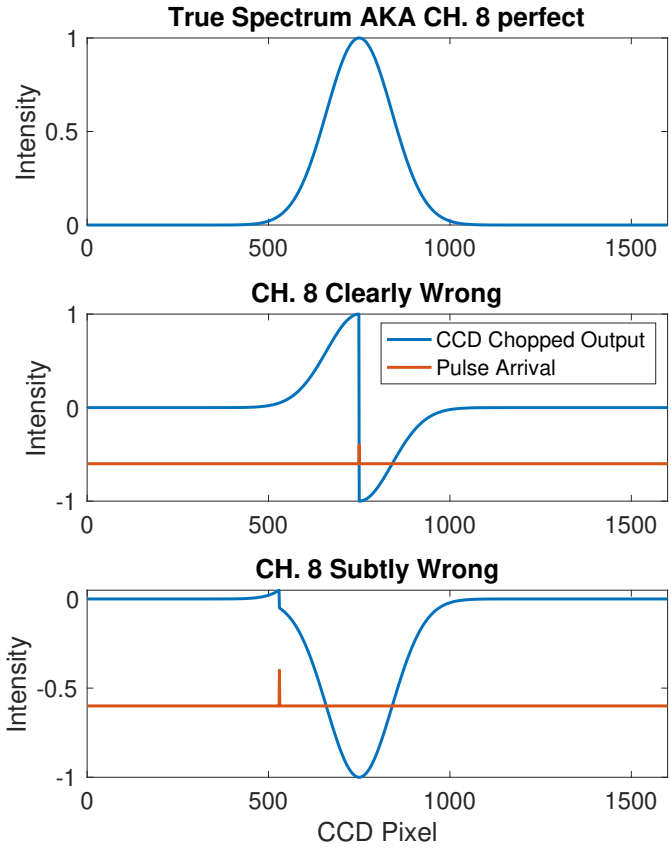

Figure E.1: **Example of CH. 8 timings:** as described by method #1. Each progressive pane shows a shift in CH.8 timing. Sometimes it is much more subtle than this and hard to determine the timing.

and is similar to the rolling shutter effect. Treat the 1,000 μs range of the CH. 8 timing as the same as the 360^o of phase in a chopper, moving by 500 μs ensures that charge is cleared as far away from the pulse arrival as possible. Note that the rate of charge clearance is approximately 30 pixels/μs. Also note that Fig. E.1 does not show timing within the duration of the pulse, rather it is showing the pulse arriving during the pixel charge clearing process.

Method #2: Double-Chop, Testing CH. 8 Timing

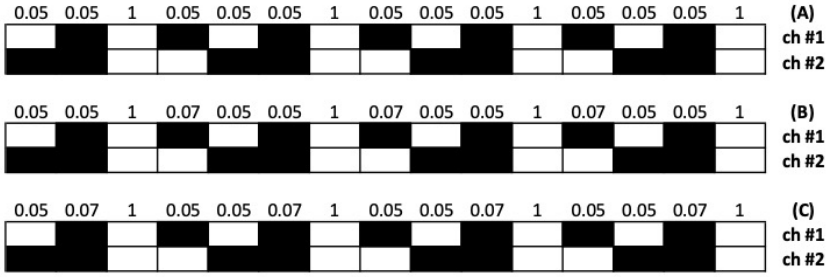

Figure E.2: **Double-Chopped Ch. 8 Timings** Power readings of the CCD with two choppers on a single line (ch #1, #2). Performing a double chop of the probe line while detecting the CCD ensures that one can tell the difference between (A) perfectly timing the trigger, and (B/C) triggering a bit too early or late as to create a small amount of bleed-through on either adjacent shot. Simple chopping makes that difficult.

This method is approximately represented in Fig. E.2. It should be used to verify the selection of CH. 8 timing as it will show if any pulse intensity is accidentally binned into adjacent shots. Keep the pump blocked. Move both choppers to the probe line and phase them both. Change one chopper to run at half speed (250 Hz). This can be done directly by setting it to run at the appropreiate sub-harmonic. See manual for further detail if needed. This can also be accomplished by passing a 1 kHz TDG trigger through the box car integrator and taking the output of alternating shots to produce a 500 Hz trigger for the second chopper, so that it runs at 250 Hz. Collect VE fast-scanned data so that there are shot-by-shot intensities. Make sure to select the "save raw data" button. As shown in Fig. E.2, properly timed pixel clearance results in only 1 out of 4 shots holding any intensity. Intensity on either shot adjacent to the "main" shot indicates charge bleed through.

E.4.2 CCD Offset

Data collection is performed in batches, usually 60,000 shots (1 minute) at a time. While the DAQ board is triggered by the Regen output, that only tells the DAQ when the shots are coming similar to a metronome. If the goal is to have the DAQ board and the CCD to collect

the same 60,000 shots, the system requires orchestration to tell them when to start, or select the down beat. Because the CCD and the DAQ board have non-negligible communication times, i.e. it takes more than a millisecond for them to send, process, and react to signals, one of them must say when to start and then wait for the other. In this case the CCD is the conductor. It sends a "FIRE" signal to start the collection and then must wait for the rest of the system to start before it starts collecting data itself. The "offset" is how many shots it waits before starting.

This would be difficult to measure if only measuring a signal chopped at 500 Hz. In that case all even numbers look the same and all odd numbers look the same. It is possible play a small trick by unsyncing the chopper so that there is some randomness in which shots get through. This can be seen in Fig. E.3.

1. Remove the trigger from the probe chopper, trigger it internally, and set the frequency to an awfully prime value (733.4 Hz).

2. Set up a photodiode (PD) to see the probe after the chopper. Picking off some of the light so that both the PD and the CCD will see light on each shot which passes the chopper.

3. Replace the BNC for the MCT, InGaSe, or any single channel detector in the DAQ with one from the PD.

4. In the fast-scan Collect VI press the button to "Save Raw Data".

5. Collect a small number of shots (10,000) for a variety of CCD offset values.

6. Access the raw data and plot the PD vs the summed CCD intensity against shot index. Keep in mind that MCT data is generally negative and detrended before saved.

7. Adjust the CCD offset to ensure the CCD and DAQ collect the same shots and index them similarly.

NOTE: This needs to be redone before alignment, especially if the CH. 8 timing has changed. Make sure to change the CH. 8 timing and then adjust the offest. Not the other way around

Note: Provided that chopping is well determined, this does not apply to step scanning as adjacent shots in step scans don't require individual binning along τ_1. In that case the offset can be simply changed between an even or odd number, an offset of 1 is the same as 3, but this can ruin fast-scanning if it hasn't been accounted for.

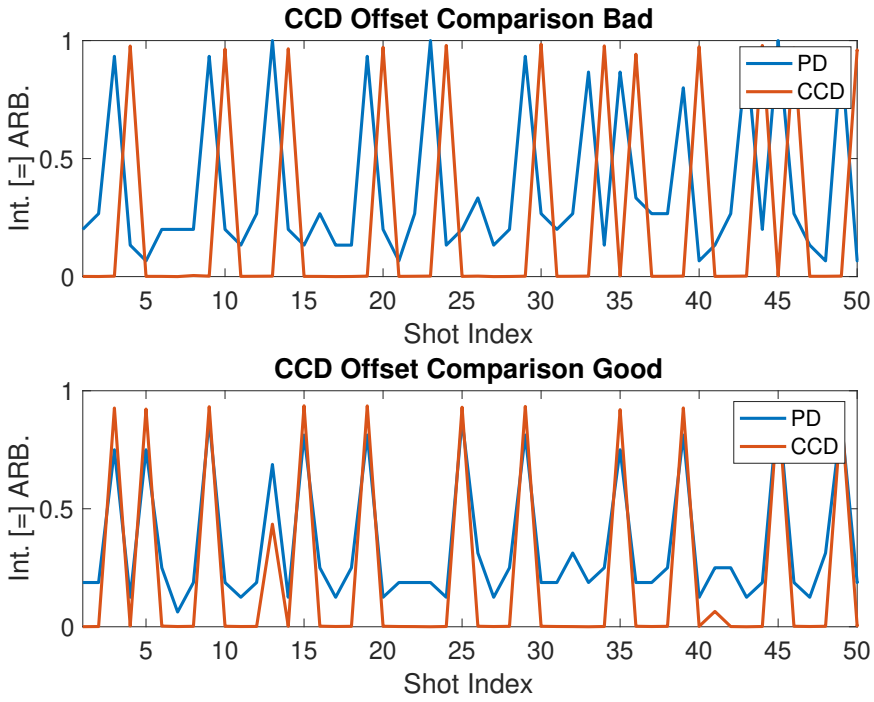

Figure E.3: **Example of Good and bad offset plots** measured on the CCD. These were taken from two separate runs with the same offset but different CH. 8 timings, underscoring the importance of setting the CH. 8 timing first.

E.5 Choppers

E.5.1 Chopper Phase

Chopper phase can be set by the usual method of observing the chopped intensity from a PD or other single channel detectors (e.g. the coherent) on an oscilloscope. Generally it will block alternating shots; vary the phase until it blocks half of every shot and move 90^o away. The remaining question is $\pm 90^o$. Whether the motion is $+90^o$ or -90^o determines whether the chopper end up in phase or 180^o out of phase. This difference will only impact the sign of the data. Specifically for 2D VE fast-scan collected data, there is a software solution to this, which is discussed below.

Subtracting unpumped data from pumped data and then mathematically switching the sign after is not a problem in Step scanned or chop acquired data but is a problem in fast-scanned acquired data. This is addressed in a separate note in Sec. E.5.2.

As of the writing of this Apendix all chopped CCD collection VIs performed a chop calculation which is equivalent to (low)-(high). There is no guarantee that someone won't write something new or change the logic in one of them but not the other to fit their purposes for a single day and forget about it. 1) Please don't do that. 2) Always check to make sure that didn't happen

E.5.2 Fast-Scan Acquired Chopped Data

There is a subtle but important difference in the way chopping for fast-scan data is performed compared to step scanned chopped data. In step-scanned data the system simply takes the (lows)-(highs) of the chopper signal. This works exactly the way one would anticipate and is perfectly valid. For the same reason that CCD offset doesn't matter too much for these types of scans (the τ_1 stage is stationary and adjacent shots all correspond to the same experimental time) it does not matter whether the subtraction is done with the preceding or following shots.

This would not matter in fast-scanning either, except the system subtracts the mean of

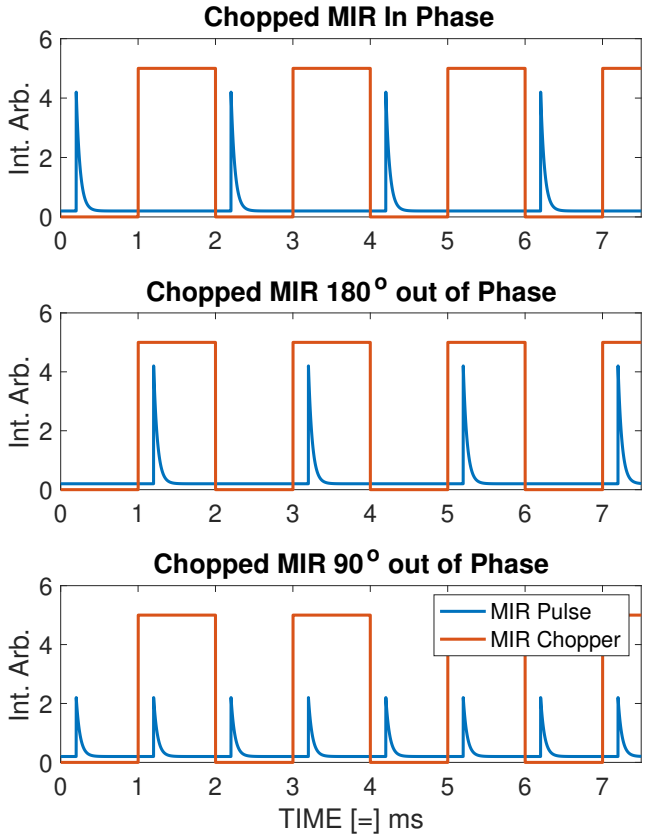

Figure E.4: **Chopper phase for the MIR light** as expected from the .m scripts which handle the initial data processing. Note this has no bearing on the sign of the signal seen in the acquire CCD VI which only looks at the chopped value. Here the calculation is performed (low)-(high).

both preceding and following blocked shots from each pumped shot. This is valid because unpumped shots don't have a value of τ_1 associated with them and so both adjacent shots are theoretically equivalent. Taking their mean distributes shot-to-shot laser fluctuations across more pumped shots and reduces noise overall. Getting the sign of the phase wrong by 180^o means that the system would be binning τ_1 based exclusively off of the blocked shots and then averaging out multiple pumped shots which have different values of τ_1. That is a bad idea. This logic is performed in the .m file called to bin time *VeFastScanFileFinder.m*

starting at line #99.

To fix that problem the value of the chopper output (0 or 5) is simply ignored. It is technically just there for diagnostics. Chopped value is actually determined by an automated evaluation the 'MCT_data' which can tell when light is and is not on the single channel detector. By comparing the mean value of the first 20 shots (odds vs evens) the .m script determines which ones carry the pump transmitted data. It does the subtraction of prior and following shots as described above but it doesn't matter if choppers are 180^o out of phase for the fast-scanned collected 2DVE.

E.5.3 Choppers CH. 7 timing

IMPORTANT NOTE: CHANGING THE CH. 7 TIMING REQUIRES RE-ESTABLISHING THE PHASE OF BOTH CHOPPERS.

CH. 7 is the trigger output that is sent to the both of the choppers. It also generally triggers the oscilloscope associated with the bright output single channel MCT. This is important because it can be used to artificially delay the square wave that the chopper generates.

This might seem like a convention problem, just never change it and it will never be an issue. However, there is good reason to temporarily change this timing, especially if detecting a spectrally dispersed MIR pulse. This timing can be used to change the trigger sent to FPAS so the acquire timing output is better centered around the probe pulse. This reduces noise because it allows for the shrinking of the integration gate (shown in orange in Fig. E.5). Reducing noise in the collection of the probe pulse might yield one of the best returns on effort in optimizing an experiment.

Changing CH. 7 will automatically change the phase of both choppers related to the proportion of change in CH. 7 timing.

$$\frac{\Delta\phi_{\text{chop}}}{360^o} = \frac{\Delta T_{\text{CH.7}}}{1\text{ms}} \tag{E.1}$$

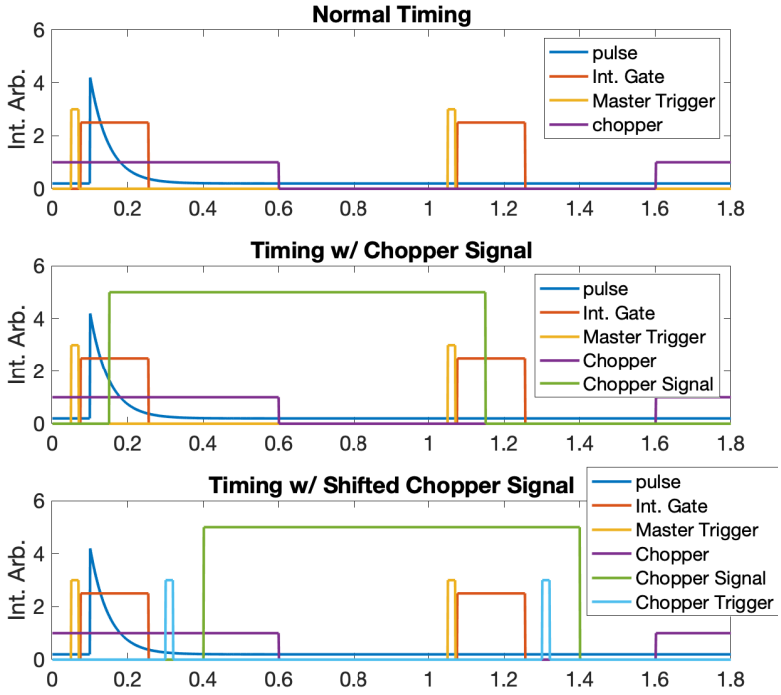

Figure E.5: **Ch.7 Timing Delay in FPAS.** Delaying the timing of the chopper signal enables the movement of the chopper signal switch outside of the integration gate.

Delaying the chopper square wave gives the leeway to move the ≈1-3 μs. This is not much but it solves the integration gate issue in the FPAS. The integration gate in the FPAS should cover the response curve of the MCT array. However, if the chopper wave is directly on top of the true trigger, the integration gate will always see some of both chopper up and chopper down. By delaying it slightly the integration gate can be safely extended.

E.6 Prism Compressor

There are two distance-related degrees of freedom related to the P_2 position and the length of the delay stage (L), both of which change both the compression of the pulse and the τ_2 of the experiment. While focused on the compression of the pulse, it can be easy to lose track

of the τ_2 direction and magnitude. Those delays are listed below.

- 1 mm of material in P_2 changes τ_2 delay by $\approx$ 5.3 ps.
- 1 mm of dist increase in L changes τ_2 delay by $\approx$13.3 ps.

The prism compressor for the 400 nm probe line relies on Brewster's angle interactions so it requires P interactions. To account for S vs. P polarization, at the exchange point between each region of the table (each box), the light is labelled as S or P, along with a description of that orientation relative to the table.

Appendix F

TDDFT GEOMETRIES AND ROOTS

Table F.1: Converged Geometries of $K_4Fe^{II}(CN)_6$ [=] Å

Atom	X	Y	Z
Fe	0.00000000	0.00000000	0.00000000
C	-1.81917027	-0.03335831	-0.71926660
N	-2.91104648	-0.05028038	-1.14336000
C	-0.26363647	1.81748256	0.66107639
N	-0.39650765	2.91674740	1.04361053
C	-0.65245477	-0.72431645	1.71356864
N	-1.01949658	-1.14265108	2.74378932
C	0.26492194	-1.81715092	-0.66122605
N	0.39946334	-2.91608401	-1.04407649
C	0.65377106	0.72497185	-1.71283131
N	1.02222110	1.14453278	-2.74209377
C	1.81942656	0.03289085	0.71938992
N	2.91151676	0.04957108	1.14269602

Table F.2: Converged Geometries of $K_3Fe^{III}(CN)_6$ [=] Å

Atom	X	Y	Z
Fe	0.00000000	0.00000000	0.00000000
C	1.66434078	0.87659818	-0.59439314
N	2.65503328	1.38456560	-0.93290973
C	0.86003876	-0.55780875	1.68189365
N	1.37242765	-0.88008464	2.67574262
C	-0.47522468	1.68896229	0.89877624
N	-0.75605374	2.69018114	1.42127310
C	-0.86020289	0.55931993	-1.68139135
N	-1.37281553	0.88364520	-2.67454402
C	0.47285518	-1.68909585	-0.89889251
N	0.75091419	-2.69077309	-1.42192322
C	-1.66433206	-0.87600171	0.59530378
N	-2.65485687	-1.38303558	0.93556623

Table F.3: Root Frequencies and Strengths: 1s→3p XANES for $K_4Fe^{II}(CN)_6$ and $K_3Fe^{III}(CN)_6$ in H_2O, represented in calculations/figures in chapters 5 and 6. Roots are scaled in the plot by corresponding hole density.

Geometry	**Configuration**	**Energy [eV]**	**Osc. Strength E-3**
Fe^{II}	$3p^5\ t2g^6$	7058.036	8.762
	$3p^5\ t2g^5$	7060.150	8.755
	$3p^5\ t2g^4$	7061.816	9.574
	$3p^4\ t2g^6$	7064.089	8.656
	$3p^4\ t2g^6$	7064.101	8.696
	$3p^3\ t2g^5$	7069.212	8.684×3
Fe^{III}	$3p^5\ t2g^5$	7060.121	8.698
	$3p^5\ t2g^4$	7061.286	8.733
	$3p^4\ t2g^3$	7064.281	8.674
	$3p^4\ t2g^3$	7064.293	8.696
	$3p^3\ t2g^4$	7068.109	8.676×1.5
	$3p^3\ t2g^4$	7069.264	8.566×1.5

Appendix G

XPXP EXPERIMENT: SUPPLEMENTAL SPECTRA AND DESIGN CONSIDERATIONS

G.1 Additional Spectra

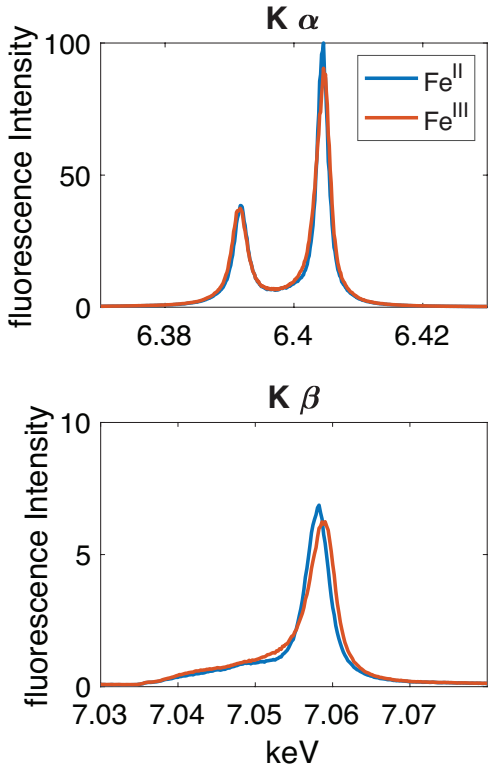

Figure G.1: Fluorescence data for Fe^{II} and Fe^{III}, displayed in counts. Peaks (at highest) intensity in the order [$k\alpha$ 1; $k\alpha$ 2; $k\beta$] for Fe^{II} = [37,120; 96,447; 6,626], Fe^{III} = [36,097; 87,230; 6,022]. hν for $k\beta$ is 7.0583 keV and 7.0590 keV respectively. ratio of total intensity $\frac{K\alpha}{K\beta}$ = 13.7 and 13.5 respectively. See previous publication for detection information [218]. Counts, in arbitrary units, match count units displayed in RIXS spectra shown in Fig. G.2.

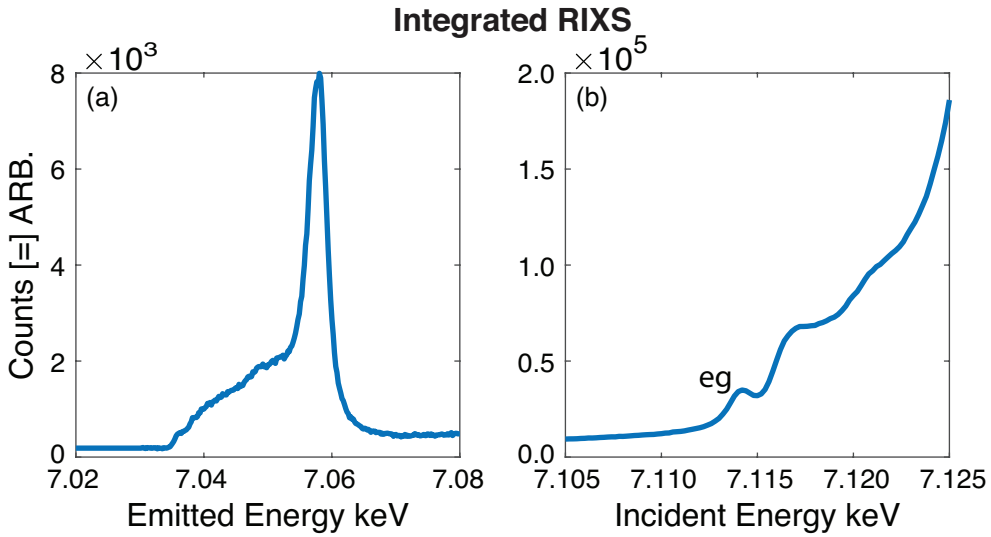

Figure G.2: Integrated RIXS spectra of 400 mM $K_4Fe^{II}(CN)_6$, see previous publication for detection information [216]. Count units are arbitrary, but consistent between the two plots.

The intensity of the eg peak in Fig. G.2 (b) and Kβ fluorescence in Fig. G.1 (b) are used as the ratio of intensities represented in Fig. 6.1 in Ch. 6. Additionally, The transient 3p absorption intensity in Fig. 6.1 is scaled so that the integral of a single 1s→3p root is equivalent to $1/6^{th}$ the integrated Kβ fluorescence. In practice the relative oscillator strengths of the 1s→3p transitions are more than three orders of magnitude stronger than those of the 1s→3d transitions.

G.2 Future Experimental Design Considerations

Future studies should focus on systems which undergo more complicated processes, like metal-to-metal charge transfer. Understanding the basic results of these measurements on simpler systems is key to understanding larger ones. Below, potential progressive improvements and augmentations for this experiment are enumerated.

1. **Attosecond Time Resolution:** If these two peaks arise from the same electronic state, they will grow in on the same timescale as the cascade occurs. Noting that the number of Auger–Meitner events corresponds directly to the hole density in the 3d, we expect peaks that correspond to different 3d hole populations to grow in with a different time profile.

2. **Pump–Probe Delay Resolution:** In the absence of attosecond resolution, we collect multiple data points as a function of pump-probe delay scanned over the duration of the cascade (<1 ps). The shift hypothesis would predict both peaks to vary in time.

3. **Increased Spectral Bandwidth:** If the Shift hypothesis is more correct, then we should not see absorption features to the red of Kβ. If the 3p orbitals are splitting, more than blue-shifting, for large 3d hole populations we expect to see peaks expanding around the Kβ line. The bandwidth available to this experiment precluded drawing conclusion for energies distant from the 7.06 keV. Increasing the spectral range of the experiment would permit such observation.

4. **Single Shot Measurement:** The shot-to-shot variation in FEL SASE pulses, necessitates single-shot measurements, comparing the probe spectrum prior to and post-interaction. This eliminates the need to compare spectra of dissimilar sase pulses. This could be accomplished by splitting the pulse in half and passing each path through the sample and blank paths before resolving them jointly with the same crystal and spectrometer as has been done for solid samples at lower energies (Co L3- edge) [300, 301].

5. **Pump–Probe Geometry:** In lieu of a single shot measurement, spatial separation of the two pulses will allow for the direct chopping of the pump pulse. This would also ease the technical difficulty of achieving the single-shot measurement. Such configurations will become available with the advent of LCLS-II.

6. **Monte-Carlo simulations in explicit ligand field:** Simulations are currently limited to an atomistic view. This misses two key aspects of the physical process. 1) the effect of the ligand field splitting which will change the relative rates at which electrons leave the 3d orbitals. 2) the high-lying ligand and bonding electrons themselves which could contribute to the cascade directly.

7. **Multiconfigurational and spin-orbit accounted XANES:** Computations currently inform the type of XANES signals produced by these exotic electronic configurations. Resolving specific electronic states requires an approach that can describe the ensemble of states generated.

8. **Simplify Cascade Behavior:** Performing this experiment on a dissociating iron salt or another metal with fewer 3d electrons could provide the computational simulations with a simpler initial problem to solve.

9. **Synthetic Tuning:** By synthetically tuning the ligand field surrounding the iron atom we could modulate the interaction strength between the 3d and 3p orbitals. Observing whether the peaks shift together relative to the Kβ energy or modulate their speak separation would differentiate 3p-3d interactions from the 3p splitting.

10. **Simultaneously Detect Seeded Emission:** Given the experimental similarity required for the detection of a stimulated emission signal [201], simultaneous experiments would combine the experimental insights of both experiments.

VITA

Robert B. Weakly was born in Snohomish, WA in 1991. He graduated from Snohomish Senior High School in 2009 and began his undergraduate work at Colorado State University. There, he studied chemistry and applied physics, receiving separate Bachelor of Science degrees in May 2014. He taught physics and chemistry at the high school level in both Portland, OR, and Sandy, UT for three years while completing his Master of Arts degree in teaching which was awarded in August 2016 from the University of Portland. Upon starting graduate studies at the University of Washington in August 2017, he joined the Khalil research group and remained there through the completion of his Doctor of Philosophy in chemistry in November 2022.